STUDYING THE EFFECT OF HYDRAULIC HYSTERESIS WITH AIR ENTRAPMENT ON SOLUTE TRANSPORT AND SLOPE STABILITY UNDER DIFFERENT CLIMATIC CONDITIONS

MOAMENBELLAH MOUSTAFA

A THESIS SUBMITTED TO THE FACULTY OF GRADUATE STUDIES IN PARTIAL FULFILLMENT OF THE REQUIREMENTS FOR THE DEGREE OF MASTER OF APPLIED SCIENCE

GRADUATE PROGRAM IN CIVIL ENGINEERING

YORK UNIVERSITY

TORONTO, ONTARIO

January, 2024

Abstract

Hysteresis, a natural phenomenon, characterizes distinct hydraulic responses during drying and wetting events, influenced by the soil-water characteristic curve (SWCC). Hysteresis in the SWCC refers to the phenomenon where the moisture retention characteristics of soil are different during wetting and drying processes. Air entrapment, another intrinsic aspect of hydraulic hysteresis, occurs upon soil rewetting following drainage or drying. The interplay between unsaturated soils and the atmosphere is significantly shaped by naturally occurring intermittent climatic conditions, leading to frequent cycles of soil drying and wetting. This dynamic climatic behavior induces significant alterations and reversals in soil suction and moisture saturation states.

Understanding the interplay between hysteresis and air entrapment is crucial for accurately capturing hydraulic responses under intermittent and nonmonotonic water flow. Both phenomena significantly influence water movement within the porous medium and the water balance at the ground surface. Despite their importance, it is common in numerical hydrological modeling to neglect hysteresis, with a nonhysteretic drying curve exclusively representing the complex water flow during drying and wetting cycles. Even when hysteresis is considered, the effect of air entrapment is often disregarded in numerical studies.

This research explores the combined impact of hydraulic hysteresis and air entrapment on solute transport and slope stability problems. Two solute transport scenarios were studied using a land-climate interaction (LCI) approach: 1-D salt transport at an oilfield brine site and 2-D subsurface drip irrigation systems with solute pulse inputs. Additionally, the study assessed the stability of a typical highway road embankment in Ontario, considering the influence of hysteresis and air

entrapment while applying the LCI. The research employed numerical modeling techniques to simulate variably saturated water flow, solute transport, and slope stability under intermittent LCI analyses, utilizing multi-year climatic data records comprising precipitation and potential evaporation. To improve the accuracy of slope stability assessments, this thesis introduces an equation for ensuring that widely used slope stability software such as SLOPE/W, which traditionally relies on a nonhysteretic unsaturated shear strength framework, appropriately accounts for the influences of hysteresis and air entrapment in the final results.

Comparisons between hysteretic and nonhysteretic analyses, referencing both drying and wetting curves, revealed that hysteresis increased actual water fluxes entering the soil surface. The inclusion of air entrapment further amplified these fluxes, with the increase in fluxes proportionate to the volume of air entrapment. In solute transport scenarios, the consideration of both hysteresis and air entrapment increased advective solute fluxes, leading to deeper solute migration. Neglecting hysteresis resulted in either excessive retardation or acceleration of solute migration, depending on the nonhysteretic curve used as a reference. Additionally, neglecting the effect of air entrapment in the hysteretic analysis caused considerable retardation effects on solute migration. In 1-D salt transport scenarios, the incorporation of hysteresis and air entrapment in simulations led to a notable increase in penetration depth, reaching up to 40% compared to nonhysteretic simulations based on drying curve. When examining 2-D solute transport from a subsurface drip irrigation system, the presence of hysteresis alone elevated the bottom boundary solute discharge by 16%. In certain cases, the inclusion of air entrapment along with hysteresis further intensified this increase, reaching up to 33%. The simulation of nonhysteretic wetting branches, particularly when considering air entrapment, resulted in a significant surge in solute discharge, reaching as high as 64%. In slope stability analyses, both

hysteresis and, more significantly, air entrapment estimated substantially lower suction strength and lower factor of safety (FOS) values compared to nonhysteretic drying curve results. In numerous cases, the inclusion of air entrapment in hysteretic simulations even triggered potential slope failures, contrasting with simulations neglecting air entrapment, where the slope exhibited greater stability. The inclusion of both hysteresis and air entrapment, in some instances, led to a reduction in FOS values by up to 21% relative to simulations based on nonhysteretic drying curve.

This thesis establishes the equal importance of hysteresis and air entrapment. Neglecting both effects can substantially lead to improper assessments of solute fate and slope stability conditions.

Acknowledgments

I am deeply grateful for the opportunity to express my sincerest thanks to Dr. Rashid Bashir, my esteemed advisor, who has been an invaluable mentor throughout my transformative years: from undergraduate studies, all the way to my graduate studies. His unwavering support, guidance, patience, advice, and encouragement over the years have left a lasting mark on both my professional and personal growth and views. I will forever cherish the countless opportunities he has provided me. Dr. Bashir's mentorship has profoundly shaped me as an engineer and as an individual, and I will remain forever indebted to him. His influence will undoubtedly continue to resonate in my journey ahead. Additionally, his expertise and contributions have been instrumental in bringing this thesis and work to fruition. My heartfelt appreciation extends to my family for their unwavering support, resilience, and patience throughout this pivotal chapter of my life. Their belief in me has been an anchor during both challenges and triumphs. Furthermore, I extend my gratitude to Dr. Mathew Perras for his assistance in improving this thesis. Most importantly, I am immensely grateful to almighty Allah for the abundant blessings bestowed upon me, surpassing my wildest imagination. AlhamduliAllah.

Table of Content

List of Figures

List of Abbreviations and Symbols

${}^{\Delta}\psi^{dw}$	Soil suction at the reversal from drying to wetting curve within the hysteresis loop
${}^{\Delta}\psi^{wd}$	Soil suction at the reversal from wetting to drying curve within the hysteresis loop
$(\sigma_n - u_a)$	Net normal stress
$\lvert q \rvert$	Absolute value of Darcian fluid flux density
${}^{\Delta}\bar{\bar{S}}^{dw}$	Apparent saturation of water at the reversal from drying to wetting curve within the hysteresis loop
${}^{\Delta}\bar{\bar{S}}^{wd}$	Apparent saturation of water at the reversal from wetting to drying curve within the hysteresis loop
${}^{\Delta}\bar{S}_w$	Effective water saturation at the reversal from initial drying curve to wetting scanning curve
Δ	Reversal from drying to wetting curve or wetting to drying curve within the hysteresis loop
AE	Actual evaporation
AEV	Air entry value
APE	Artificial pumping error
BC	Boundary condition
BF	Bottom flux
C	Solute concentration in the liquid phase
C'	Effective cohesion
COM	Center of mass of solute

CS1	Cross-section 1
Cs-137	Caesium-137
CS2	Cross-section 2
D_{ij}^{w}	Hydrodynamic dispersion coefficient tensor in the liquid phase
D_L	Longitudinal dispersivity
D_T	Transverse dispersivity
D_w	Molecular diffusion coefficient in free water
DC	Initial drying curve
E	Water flux rate (either maximum infiltration or maximum evaporation rate)
FEM	Finite element method
g	Gravitational acceleration (9.81 m/s^2)
h	Pressure head
h_A	Minimum allowable pressure head under prevailing soil conditions
H_r	Relative humidity of air
h_S	Maximum pressure head
H1D	HYDRUS-1D
HC	Hysteretic SWCC without air entrapment (closed hysteresis loop)
HCF	Hydraulic conductivity function
HC-TA$_{15\%}$	Hysteretic SWCC with 15% degree of air entrapment
HC-TA$_{25\%}$	Hysteretic SWCC with 25% degree of air entrapment

ij	Indicial notation for Einstein's summation convention
k	Hydraulic conductivity
$k(\psi)$	Hydraulic conductivity function
k_s	Saturated hydraulic conductivity
l	Constant parameter equal to 0.5
LCI	Land-climate interaction
LE	Limit equilibrium formulation
m	Empirical fitting van Genuchten (1980) parameter
M	Water's molecular weight (0.018015 kg/mol)
MDC	Main drying curve
MWC	Main wetting curve
n	Fitting van Genuchten (1980) parameter relating to the pore-size distribution
NI	Net infiltration
PDE	Partial differential equation
q_i	i-th component of the volumetric flux density
R	Gas constant
RO	Runoff
S	Water sink or source term
$\bar{\bar{S}}(\psi)$	Apparent saturation of water describing an arbitrary scanning curve as a function of soil suction

$\bar{\bar{S}}^{d}(\psi)$	Apparent saturation of water as a function of soil suction and hydraulic parameter of the drying curve
$\bar{\bar{S}}^{w}(\psi)$	Apparent saturation of water as a function of soil suction and hydraulic parameter of the wetting curve
$\bar{S}_a$	Effective saturation of air
$\bar{S}_{ar}$	Effective residual saturation of the air of an arbitrary wetting scanning curve
$\bar{S}_{at}$	Effective saturation of entrapped air
$\bar{S}_{ar}^{w}$	Maximum effective residual saturation of air of the main wetting curve
$\bar{S}_w$	Effective saturation of water
$\bar{\bar{S}}_w$	Apparent saturation of the water
S_a	Actual air saturation
S_e	Effective degree of saturation
S_m	Irreducible saturation of water
S_w	Actual water saturation
SS	Suction strength
SWCC	Soil-water characteristic curve
SWRC	Soil-water retention curve
t	Time
T	Temperature
TA	Trapped air
TMI	Thornthwaite moisture index

u	Pore-velocity
vG	van Genuchten (1980)
VWC	Volumetric water content
WC	Main wetting curve of closed hysteresis loop
WC-TA$_{15\%}$	Main wetting curve/branch of hysteresis loop with 15% degree of air entrapment
WC-TA$_{25\%}$	Main wetting curve/branch of hysteresis loop with 25% degree of air entrapment
x, y	Horizontal and vertical direction of the flow, respectively
x_i	Spatial coordinate
α	Fitting van Genuchten (1980) parameter relating to the inverse of air entry value
δ_{ij}	Kronecker delta function
θ	Volumetric water content
θ_r^*	Volumetric water content at which the suction strength becomes zero
θ_r	Residual water content
θ_s	Saturated volumetric water content
τ_w	Tortuosity factor in the liquid phase
ϕ'	Effective angle of internal friction
ψ	Soil suction or matric suction (i.e., negative pore-pressure)

CHAPTER 1: Introduction

The present thesis follows a sandwich format, in which each chapter (3 through 5) comprise standalone papers with a consistent structure, including an abstract, introduction, literature review, model setup, results and discussion, and summary and concluding remarks. In each chapter, the literature review provides a comprehensive overview of previous research on the impact of hysteresis, as well as air entrapment (if applicable). The current chapter, chapter 1, starts with the motivation for this research and the corresponding objectives as well as the thesis layout.

1.1 Motivation for Research

Hysteresis and air entrapment are commonly ignored when performing numerical modelling of water flow in variably saturated soils. Evidence from the literature suggests that the consideration of hydraulic hysteresis in variably saturated flow is expected to provide better representation of the field conditions. Considering that the accurate representation of flow in variably saturated environments is essential for modeling of various geotechnical/geoenvironmental analysis and design problems such as subsurface solute transport, and slope stability assessments. Thus, neglecting hysteresis may lead to inaccurate assessment and improper design considerations not only for flow but also for solute transport and slope stability problems.

Hydraulic hysteresis in variably saturated soils can have a significant impact on the transport of solutes. This is because hysteresis affects the water content and flow dynamics in the soil, which in turn influences the movement of solutes. During wetting and drying cycles, the soil moisture content changes, causing the hydraulic conductivity and diffusivity to vary. As a result, solute

transport can exhibit hysteresis, with the breakthrough curve (BTC) during wetting being different from that during drying. This phenomenon is particularly pronounced in soils with a high degree of heterogeneity and non-uniformity, as well as in soils with low permeability. The effects of hydraulic hysteresis on solute transport can be observed in several ways. First, the transport of conservative solutes, such as tracers, can exhibit hysteresis, with the arrival time and peak concentration being different during wetting and drying. Second, the transport of reactive solutes, such as contaminants, can be affected by changes in the redox conditions and microbial activity that occur during wetting and drying cycles. Third, the spatial distribution of solutes can be altered by the non-uniformity of flow patterns that result from hysteresis. Incorporating hydraulic hysteresis into numerical models of solute transport can improve the accuracy of predictions by accounting for the complex interactions between water flow and solute transport. This is particularly important in geoenvironmental applications, such as groundwater contamination and remediation, where accurate predictions of solute transport are crucial for effective decision-making.

Hydraulic hysteresis can also play a significant role in the stability of slopes, especially those in variably saturated soils. Hysteresis affects the water content and pore pressure distribution within the slope, which in turn influences the shear strength and deformation behavior of the soil. During wetting and drying cycles, the soil moisture content changes, causing the hydraulic conductivity to vary leading to changes in pore water pressure and the stress state within the soil mass. When the slope is subjected to loading, such as the weight of the soil itself or external forces, these changes in stress state can lead to shear failure and slope instability. Incorporating hydraulic hysteresis into numerical models of slope stability can improve the accuracy of predictions by accounting for the complex interactions between water flow and soil mechanics. This is

particularly important in geotechnical applications, such as the design of embankments, dams, tailings dams, and retaining structures, where slope stability is a critical consideration.

Although many studies have investigated the hysteresis phenomenon in hydraulic characteristics, most of these studies have not considered the air entrapment phenomenon that occurs simultaneously. Moreover, many of these studies have drawn conclusions based on simplified infiltration boundary conditions, rather than intermittent atmospheric boundary conditions using actual climatic data. Additionally, most of these studies have only compared hysteretic results with those obtained from wetting characteristics. As a result, it is likely that many findings may underestimate the impact of hysteresis or draw conclusions about specific hysteretic behavior that does not apply to all situations.

This thesis recognizes those gaps and works on bridging them. Thus, the thesis objectives are as follow:

1.2 Thesis Objective

The primary goal of this thesis is to thoroughly investigate and underscore the significant impact of hydraulic hysteresis with air entrapment on influencing solute transport and slope stability. The study seeks to place particular emphasis on situating these influences within realistic site conditions, with a specific focus on their effects under intermittent atmospheric boundary conditions. Furthermore, the thesis strives to ensure an unbiased comparison by contrasting the results obtained from models that incorporate hysteresis with those derived from nonhysteretic models, considering both nonhysteretic drying and wetting curves.

Another crucial objective is to bring attention to the often-overlooked influence of air entrapment by comparing cases that account for air entrapment with those that neglect it. Additionally, the thesis aims to explore the effects of varying degrees of air entrapment volumes on the simulation results.

To achieve these objectives, several efforts have been undertaken, including:

1. Conducting a literature review of previous studies on the topic of hydraulic hysteresis, air entrapment, solute transport, and slope stability to establish a basis for the research;
2. Developing numerical models that incorporate hydraulic hysteresis and air entrapment to simulate solute transport and slope stability under varying atmospheric conditions;
3. Conducting a series of simulations to investigate the effects of hydraulic hysteresis and air entrapment on solute transport and slope stability, with a focus on their influence under intermittent atmospheric conditions;
4. Comparing the results obtained from hysteresis-inclusive models to those obtained from nonhysteretic models by referring to both the nonhysteretic drying and wetting curves;
5. Comparing the simulation results of the thesis's cases that include air entrapment to those that neglect it; and
6. Exploring the effects of varying degrees of air entrapment volumes on the simulation results.

Overall, the thesis aims to improve our understanding of the role of hydraulic hysteresis and air entrapment in solute transport and slope stability under varying atmospheric conditions. By doing so, the research contributes to the development of more accurate and reliable numerical models that can lead to better geotechnical engineering practices.

1.3 Thesis Outline

This section outlines the main themes of chapter 2 through 6 of the current research, as follows:

1.3.1 Chapter 2

Chapter 2 provides background information on variably saturated water flow such as: and governing equation for water flow, in variably saturated porous medium, atmospheric flux boundary, soil-water characteristic curve (SWCC), and unsaturated hydraulic conductivity function (HCF). Then, the focus of this chapter switches to defining in greater detail, hydraulic hysteresis as well as importance of hydraulic hysteresis in the analysis and design of geotechnical/geoenvironmental problems. The chapter also discusses the hysteresis model used in this research and explains how its algorithm includes hysteresis and air entrapment in the hydraulic functions. The chapter ends with a brief introduction of solute transport and slope stability under unsaturated soil framework and their potential hysteretic response.

1.3.2 Chapter 3

Chapter 3 focuses on solute (salt) transport in the one-dimensional domain. This chapter starts with a literature review on the effect of hysteresis and air entrapment on solute transport. A hysteresis model for flow and transport was developed and validated against published results. This chapter concludes with quantifying the effect of hysteresis and air entrapment on the vertical transport of salt in an unsaturated soil for two different climatic conditions.

1.3.3 Chapter 4

Chapter 4 focuses on solute transport in the two-dimensional domain. A numerical solute transport study has been selected from the literature. This study was extended to incorporate hysteresis and air entrapment and quantify their effect on simulation results for intermittent atmospheric boundary conditions.

The study involves the transport of inert solute, which originates from a subsurface drip irrigation source. This study was subdivided into three different cases corresponding to three different boundary conditions (BC):

- A pre-determined (in time) (i.e., controlled) irrigation BC, with no water exchange at the soil-atmosphere boundary. In which the irrigation inputs are user-dependent entries, meaning that irrigation is not triggered by changes of the soil suction.
- A triggered irrigation BC, in which the water-solute flux inputs are only activated upon a specified soil suction is reached/triggered. Moreover, soil suction, hence irrigation is influenced by the interaction of land-climate (i.e., by the water exchange at the soil-atmosphere boundary).
- A pre-determined/controlled irrigation BC, with consideration of water exchange at the soil-atmosphere boundary.

This chapter concludes with quantifying the effect of hysteresis and air entrapment on solute transport within 2-D domain for actual atmospheric conditions.

1.3.4 Chapter 5

Chapter 5 focuses on slope stability under unsaturated soil framework. This chapter also provides a literature review on the effect of hysteresis on the stability of slopes. A typical highway road embankment in Ontario was selected from the literature. Limit equilibrium involving the method of slices was utilized to obtain a factor of safety for the stability state of the embankment. The concept of unsaturated shear strength was employed, to obtain a factor of safety that is more representable of the unsaturated moisture conditions as well as the hysteretic effects. An equation was proposed and accordingly applied in this chapter, in which corrects the pore-water pressure/soil suction to include the effect of hysteresis and air entrapment in the unsaturated shear strength; the correction was specifically made for slope stability software that neglects both effects. This chapter concludes with quantifying the effect of hysteresis and air entrapment on the stability of highway road embankment under two contrasting climatic conditions.

1.3.5 Chapter 6

Chapter 6 presents with a summary and conclusion of the entire thesis, which was sub-divided based on the main chapters of the thesis.

CHAPTER 2: Background Information

This chapter introduces relevant concepts like unsaturated saturated water flow in porous medium and the supporting constitutive models such as the soil-water characteristic curve (SWCC) and hydraulic conductivity function (HCF). It also briefly introduces atmospheric flux boundary condition and how it is implemented through the interaction of the atmosphere with the unsaturated soils. An in-depth discussion then follows on hydraulic hysteresis and air entrapment, importance of its inclusion, and how it can be parameterized in numerical modelling. In addition, chapter 2 introduces the hysteresis model used in the current research as well as explaining how its algorithm is used to describe hysteresis and air entrapment effects in numerical modelling. Chapter 2 ends with describing saturated-unsaturated advective-dispersive partial differential equation (PDE) for solute transport in porous media. The basic limit equilibrium concepts for slope stability assessments under an unsaturated soil framework and their connection with hysteresis and air entrapment effects is also presented.

2.1 Partial Differential Equation (PDE) for Unsaturated Flow

In the unsaturated soil framework, there are three phases that dictate the water flow in the domain: liquid phase or water, solid phase or soil, and gas phase or air. Air presence in the porous medium creates the state-variable known as the matric suction or the negative pressure head, which is the difference of pore-air pressure and pore-water pressure. Total suction, which is the summation of matric suction and osmotic suction, becomes the state variable when taking the effect of osmosis into consideration (Fredlund et al. 2012).

The above-mentioned state variables, along with the water content of the medium, dictate the pressure gradient which in return influences the water flow within the variably saturated medium. To mathematically estimate the unsaturated hydraulic response and the changes in the state variables, the Richards' partial differential equation (PDE) can be used (Richards 1931). The PDE combines the mass balance equation for water fluxes and the Darcy-Buckingham flux law, and can be expressed in two-dimension as follows:

$$\frac{\partial \theta}{\partial t} = \frac{\partial}{\partial x}\left[k(\psi)\left(\frac{\partial \psi}{\partial x} + 1\right)\right] + \frac{\partial}{\partial z}\left[k(\psi)\left(\frac{\partial \psi}{\partial z} + 1\right)\right] - S \qquad \text{[Eq. 2.1]}$$

where θ is volumetric water content [$L^3 L^{-3}$], t is time [T], x, y is the direction of the flow (horizontal and vertical direction) [L], $k(\psi)$ is hydraulic conductivity as function of soil suction or S_e from the SWCC [$L T^{-1}$], ψ is soil suction (i.e., negative pore-pressure) [kPa], and S is water sink or source term [$L^3 L^{-3} T^{-1}$].

To solve the Richards' PDE, two important functional relationship namely, soil-water characteristic curve (SWCC) and unsaturated hydraulic conductivity function (HCF) must be known. Hence in later sections, efforts have been allocated in explaining those constitutive models (i.e., SWCC and HCF) in greater depth. In addition, to solve the PDE, the boundary condition must be established, of which a soil-atmosphere boundary (i.e., atmospheric flux boundary) is a special type. The upcoming section explains the atmospheric boundary condition; in a brief summary, this type of BC limits the potential meteoric water fluxes into actual values while, simultaneously, considering water content/pressure head changes.

2.2 Atmospheric Flux Boundary

One of the driving factors in estimating the amount of water flowing within the soil domain, is to know the water fluxes that enter or exit the system through the soil-atmosphere boundary. Across the soil-atmosphere interface, the potential water flux is exclusively controlled by precipitation, and potential evaporation (PE), where PE itself is a function of temperature, relative humidity, wind speed, and net radiation. To account for the interaction of unsaturated soil with the atmosphere, system-dependent boundary conditions can be used (Šimůnek 2022, Šimůnek et al. 2022). System-dependent boundary conditions are a type of boundary condition where flux, pressure, or gradient cannot be defined a priori. They are often used in applications where the flux or pressure head along the boundary cannot be accurately known, and where the system's behavior is highly dependent on the hydraulic condition (mainly water content and pressure head) of the system being modeled as well as the external climatic factors.

The type of boundary conditions at the soil-atmosphere boundary can vary between a prescribed flux and prescribed head, and these conditions may change depending on various factors. Two scenarios in which this may occur are when the precipitation rate exceeds the soil's infiltration capacity, and when the evaporative demand exceeds the soil's ability to supply water for evaporation. In the first scenario, when the precipitation rate is higher than the soil's infiltration capacity, excess water can either accumulate on the soil surface, leading to ponding or result in instantaneous runoff. In this case, the infiltration rate is controlled by the soil's infiltration capacity rather than the precipitation rate. As a result, the boundary condition at the soil surface may switch from prescribed flux to prescribed head. The second scenario occurs when the evaporative demand exceeds the soil's ability to supply water for evaporation. This may happen when the soil moisture near the surface is less than the evaporative demand. In this case, the potential evaporation rate is

reduced to an actual evaporation rate, which is controlled by the moisture availability at the soil surface. The boundary condition at the soil surface may switch from prescribed flux to prescribed head as a result.

Neuman et al. (1974) represented the system-dependent boundary conditions mathematically, by limiting the potential rate of the flux, E [L/T]. The term E can either be the maximum infiltration or evaporation rate. The following two conditions must be satisfied:

$$\left|k(h)\left(\frac{\partial h}{\partial x}+1\right)\right| \leq E \qquad \text{[Eq. 2.2]}$$

and,

$$h_A \leq h \leq h_S \qquad \text{[Eq. 2.3]}$$

where h is pressure head of the soil surface, h_A is minimum allowed pressure head under prevailing soil conditions, in which the equilibrium between atmospheric water and soil water is achieved, and h_S is maximum pressure head, at which runoff or maximum accumulation of water occur. The minimum pressure head at the soil surface, h_A, can be calculated from the relative humidity of air, H_r [-], using method by Feddes et al. (1974):

$$h_A = \frac{RT}{Mg}\ln(H_r) \qquad \text{[Eq. 2.4]}$$

where M is the water molecular weight (0.018015 kg mol^{-1}), g is the gravitational acceleration (9.81 m s^{-2}), and R is the gas constant [J mol^{-1} K^{-1}], and T is the temperature [K].

2.3 Hydraulic Functions: SWCC and HCF

The state of the negative pressure head in the pores is influenced by the degree of saturation, which is the ratio between volumetric water content and the total volume of the pores. This functional

relationship, between the soil suction (ψ) and volumetric water content (θ), is non-unique of the soil type and is referred to as the soil-water characteristic curve (SWCC) (Pham et al. 2005), or less commonly known as the soil-water retention curve (SWRC). The SWCC is a constitutive relationship that is required to solve the Richards' PDE; this constitutive model captures the unique hydraulic behavior for different unsaturated soil types.

There are several empirical models that have been proposed to mathematically describe the SWCC. One of the most commonly known and used SWCC models in geotechnical engineering is the van Genuchten (1980), and can be written as follows:

$$S_e = \frac{1}{[1+(|\alpha\psi|^n)]^m}; \quad m = 1 - \frac{1}{n}; \qquad \text{[Eq. 2.5]}$$

$$S_e = \frac{(\theta - \theta_r)}{(\theta_s - \theta_r)}; \qquad \text{[Eq. 2.6]}$$

where θ_r is residual volumetric water content [L^3 L^{-3}], θ_s is saturated volumetric water content [L^3 L^{-3}], S_e is effective degree of saturation [L^3 L^{-3}], α is fitting parameter related to the inverse of air entry value (AEV) [1/(M L^{-1} T^{-2})], n is fitting parameter related to the pore-size distribution [-], and m is empirical fitting parameter [-].

The SWCC can also be used to estimate the hydraulic conductivity function (HCF) with dependency on either θ or ψ in an unsaturated state (Parker and Lenhard 1987, Pham et al. 2005). van Genuchten (1980) obtained the predictive HCF equation by combining the empirical fitting parameters from the SWCC with the Mualem (1976) model. Mualem's model employs a statistical pore-size distribution to describe the hydraulic conductivity function. The HCF equation for the van Genuchten (1980) model can be written as:

$$k = k_s S_e^{\,l} \left[1 - \left(1 - S_e^{\frac{1}{m}}\right)^m\right]^2 \quad \text{[Eq. 2.7]}$$

where k is hydraulic conductivity as a function of S_e [L T^{-1}], k_s is saturated hydraulic conductivity [L T^{-1}], S_e is effective degree of saturation [L^3 L^{-3}], m is empirical fitting parameter from the van Genuchten (1980) SWCC [-], and l is pore interaction parameter which can be taken as 0.5 for a wide range of soils [-].

The SWCC is what dictate the unsaturated hydraulic response of different soils; Figure 2.1 shows typical nonhysteretic drainage (i.e., drying) SWCCs for different textural soils: sand, silt, and clay. It is evident that different textural soils exhibit different SWCC shape and suction/moisture content values; these are dictated by the grain-size distribution, and the associated pore-size distribution which in return depends on: soil structure, compaction, and organic matter, among others. Of the general shape, at zero suction, where the pore-water pressure and pore-air pressure are equal, the SWCC exhibits a fully saturated state (i.e., volumetric water content is at maximum, θ_s). Negative pressure, also known as suction or tension, can indeed exist in soil pores even when the soil is fully saturated with water. Moreover, the suction that is required to transition from a fully saturated state to an unsaturated state is known as the air entry value (AEV) or air-entry pressure (AEP). More precisely, the AEV is the point where water starts to drain out of soil pores and admitting air. The value of the AEV varies depending on the size of the largest pore (from the pore-size distribution). Additionally, beyond the AEV, the rate of water drainage and soil suction changes are similarly dependent on the aforementioned factors. A residual water content, θ_r, is reached where the amount of retained water remain unchanged upon subjecting the soil to a specific high suction level or continuous drainage of the pores. This is the minimum amount of water that can be held in the soil and is typically a very small fraction of the soil's total porosity.

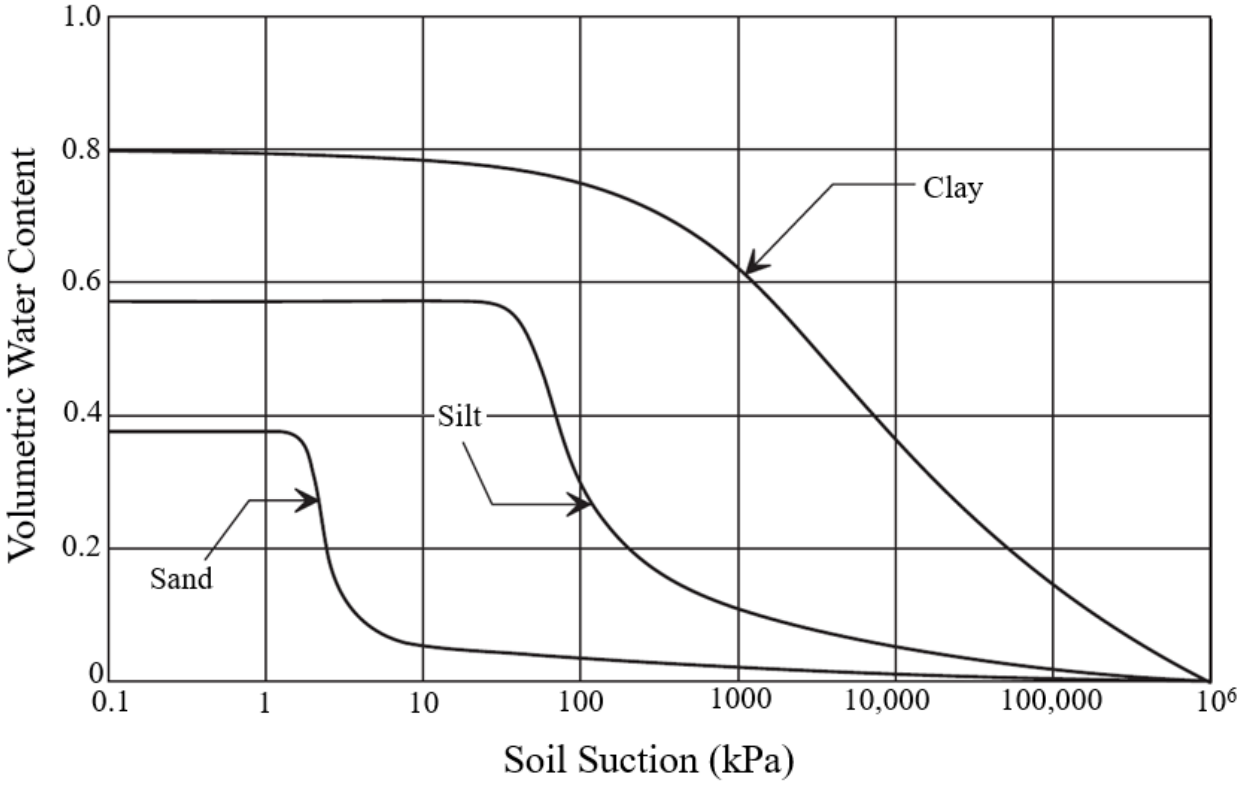

Figure 2.1 Main boundary drying curves for sand, silt, and clay soil [Modified from (Fredlund et al. 2012)]

2.4 Hysteresis in the Hydraulic Functions

As previously mentioned, the SWCCs shown in Figure 2.1 represent the main drainage curve and are nonhysteretic, meaning that they follow a unique path when the soil undergoes drying. However, in reality, the SWCC is hysteretic, which means that the relationship between soil suction and water content can differ depending on whether the soil is being wetted or dried. In general, when a soil starts to drain from a state of complete saturation, it follows the initial drainage curve, also known as the initial drying curve. This curve represents the relationship between soil suction and water content as the soil dries out. On the other hand, if a soil starts to wet from a

completely dry condition (i.e., residual saturation), it follows a new branch of the SWCC with a lower suction. This branch is called the main wetting curve or main imbibition curve, and it represents the relationship between soil suction and water content as the soil becomes wet.

More specifically, hysteretic SWCC, which means that the relationship between water content and soil suction is different for wetting rather than drying. This results in the formation of a hysteresis loop or envelope (Figure 2.2), where the water content at any given suction is always lower during wetting than during drying (Pham et al. 2005), except at residual water content and full saturation (only when the air entrapment is neglected), where the wetting and drying branches converge. Different branches within the hysteresis envelope have been identified and named based on their location (starting point) and status (drying or wetting) within the envelope

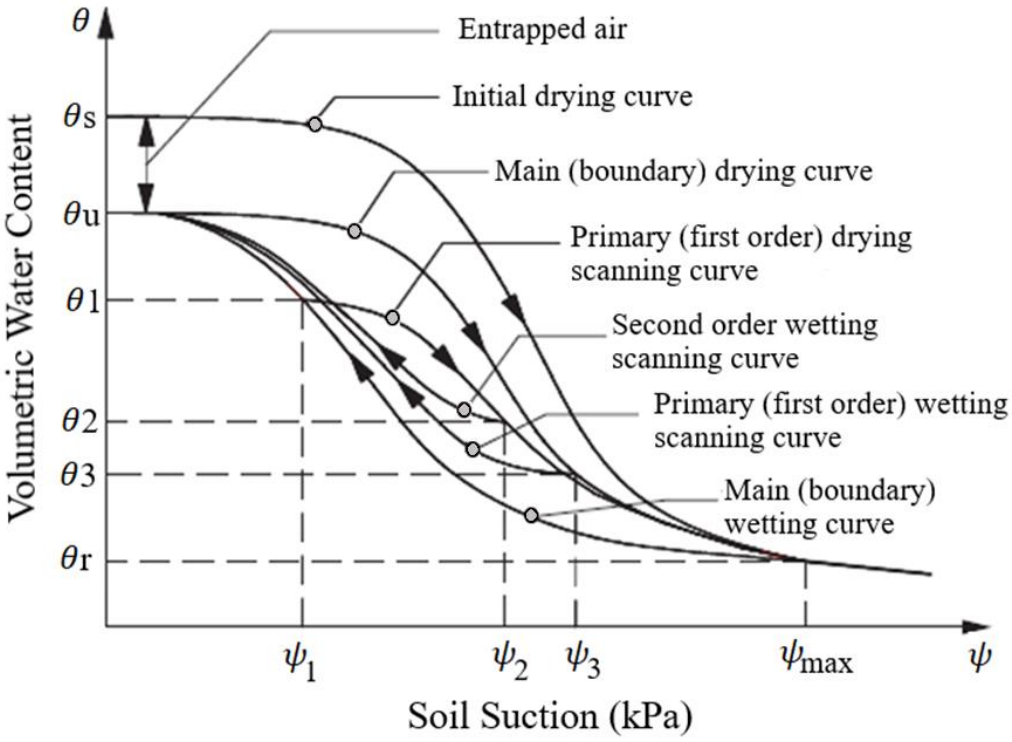

Figure 2.2 Typical hysteretic SWCC which presents different branches within the hysteresis loop [Modified from (Pham et al. 2005)]

(Figure 2.2). The initial drying curve is measured by drying the soil from complete saturation without any air entrapment and continues until residual water content is achieved. Any subsequent wetting of a completely dry soil creates the main boundary wetting curve, which ends at zero soil suction where the water content in most instances is lower than that of the initial drying curve due to air entrapment. If the soil dries from a zero-suction state at the main wetting curve, a new path is created, which is referred to as the main drying curve. Additionally, infinite orders of wetting scanning and drying scanning curves can form within the hysteresis loop, depending on the reversals from drying to wetting or wetting to drying. Water content within the hysteresis envelope can vary widely depending on the path it follows and the history of reversal points. This variability is attributed to irregularities of the soil's void passages (known as the "ink-bottle" effect), variations in contact angle (which is greater in advancing water fronts than in receding), air entrapment (which depends on the path and history of reversals), and aging caused by the soil's wetting and drying history (Haines 1930, Klausner 1991).

In most geotechnical applications, when carrying out numerical modeling of variably saturated water flow and solute transport, the SWCC is commonly assumed to be monotonic or nonhysteretic (Kool and Parker 1987, Bashir et al. 2015). It is a common practice to assume hydraulic characteristics based on the drying curve, to mathematically represent any non-monotonic water flow (i.e., either drying or wetting events). This can pose inaccuracies in estimating the water flow during wetting events or during cyclic drying-wetting events. Even when hysteresis was being modelled in some applications, the inclusion of air entrapment is commonly ignored.

Royer and Vachaud (1975) suggested that one reason for disregarding hysteresis is the notion that local hysteretic effects are overshadowed by the spatial variability of hydraulic properties.

However, challenging this viewpoint, Stauffer and Dracos (1984) provided evidence of a rapid groundwater recharge response, attributing it to the hysteresis in SWCC of unsaturated soils. Also, Vereecken et al. (1995) found that hysteresis and heterogeneity are as important in influencing the water flow within the domain. Kool and Parker (1987) argued that disregarding hysteresis is, in most cases, not based on the knowledge that hysteresis effects are negligible, but rather due to expedient analysis, motivated by the lack of data required for the calibration of hysteresis model. Hysteresis is ignored on the basis of the added labor and expenses for acquiring additional hydraulic properties for the wetting branch within the hysteresis loop (Mitchell and Mayer 1998). Mitchell and Mayer (1998) discussed that modelling transient water flow in the unsaturated soil is already a complex process, in which consideration of hysteresis further complicates the effort and computational times. In the past, engineers encountered challenges related to hysteresis inclusion, primarily because powerful computers and high storage capacity were not readily accessible. However, given the significant advancements in computational power in today's technologies, the incorporation of hysteresis should no longer pose an issue. Disregarding hysteresis in numerical modelling of variably saturated water flow have proven to result in considerable errors in the predicted fluid front and distribution (Gillham et al. 1976, Hoa et al. 1977, Kool and Parker 1987, Kaluarachchi and Parker 1987, Parker and Lenhard 1987). In addition, based on the result of Beese and van der Ploeg (1976), they suggested that the prediction of the water balance under atmospheric boundary conditions is improved when hysteresis is considered. Bashir et al. (2016) assessed the water balance and moisture conditions under intermittent atmospheric boundary conditions by comparing hysteretic simulations with main drying and main wetting curve. The results suggested that hysteretic simulations varied compared to drying and wetting curves, where the deviations between fluxes

of different simulations are a function of the climate type. In addition, the deviations varied for different climate types.

The assumption that the SWCC is nonhysteretic can only be described for cases where continuous monotonic water flow occurs; that is when soil pores experience either continuous wetting or drying events. However, this is not applicable in most geotechnical applications. Even so, hysteresis could develop during monotonic water flow. For example, during gravity drainage, the pores of the upper part of the soil undergo drainage and are represented by the drying curve. In the meanwhile, the pores of the lower part of the soil are, hence, wetting and is represented by the wetting curve. Thus, different parts of the subsurface simultaneously follow different branches, and the formation of the hysteresis loop becomes inevitable. For monotonic and non-monotonic flow cases such as in gravity drainage or capillary rise, the degree of hysteretic effects becomes a function of the hydraulic properties.

Additionally, the degree of hysteretic effects is further dictated by the natural climatic conditions existing at the soil-atmosphere interface, which is mostly found to be intermittent. The interaction of intermittent climatic records, consisting of precipitation and evaporation, result in transient and non-monotonic water flow (Russo et al. 1989). As a result, the field's soil pores would undergo frequent cycles of drying and wetting reversals, producing hysteresis loop and higher orders of scanning curves. The water content distribution in that case would depend on the path it follows and the preceding history of wetting and drying events (Haines 1930). Hysteresis in the SWCC must be considered in a variably saturated water flow problems to accurately capture the hydraulic responses during non-monotonic water flow within the porous medium.

The upcoming sections explain how the effect of hysteresis with air entrapment can be accounted for, through hysteresis models, in numerical modelling for variably saturated water flow problems. Procedures for obtaining the required set of the hysteresis van Genuchten (1980) parameters have also been presented.

2.5 Hysteresis Model by Parker and Lenhard (1987)

Hysteresis models have been the focus of a number of research to mathematically describe the hysteretic effects on the θ-ψ-k relationship. There are numerous hysteresis models such as theoretical and empirical models that have been developed over the years. The main focus of such models is to describe the scanning curves from the main boundary curves of the hysteresis loop. Earlier studies of theoretical and empirical models have been well-documented (Mualem 1974, Scott et al. 1983).

Hysteresis models that have been developed based on theoretical approach utilizes the domain theory of capillary hysteresis [e.g., (Topp 1971, Mualem 1974, 1984)]. These type of models have shown to claim universal validity (Kool and Parker 1987). In the domain theory, the porous medium is viewed as a collection of the pore domains (Kool and Parker 1987). The characteristics of the collective domains are representative of wetting and drying radii of pores. The distribution of radii governs the hysteretic behavior in the porous medium. Models based on the domain theory are complex and are not easy to implement (Kool and Parker 1987). This type of approach has not been considered and applied in the current research; therefore, it has not been any further discussed.

A simpler form of hysteresis models is the empirically based models. They have gained wide acceptance among engineers that studied the hysteretic effects. Empirical models assume that the

scanning curve in the θ-ψ-k relationship can be predicted by scaling the main boundary curve of the hysteresis loop. Kool and Parker (1987) stated that to model hysteretic flow using empirically based models, it would require knowledge of at least the main drying curve, main wetting curve, and hydraulic conductivity function of the porous medium. Several empirical hysteresis models have been proposed based on the scaling method and have been commonly applied in several hysteresis studies [e.g., (Scott et al. 1983, Jaynes 1984, Kool and Parker 1987, Lenhard et al. 1991)]

One of the commonly used hysteresis models is by Parker and Lenhard (1987), which is described and used for applications by Lenhard et al. (1991). The HYDRUS software packages implement this model (Šimůnek et al. 2022), hence it was used in the current research. The Parker and Lenhard (1987) model couples the scaling procedure of the scanning curve with empirical interpolation scheme. It estimates the drying and wetting scanning curves by rescaling the initial drying and main wetting curves, respectively. It combines the parametrizations of the van Genuchten (1980) θ-ψ-k model with the empirical scaling procedure proposed by Scott et al. (1983). Additionally, Parker and Lenhard (1987) considered the prediction of air entrapment volume for the wetting scanning curves using interpolation scheme. The model's general procedures are similar to Kool and Parker (1987) which incorporated air entrapment model proposed by Land (1968) given from Aziz and Settari (1979). The difference between Kool and Parker (1987) and Parker and Lenhard (1987), is that the latter resolves the so-called artificial pumping error (APE). The APE is the non-closure of the SWCC scanning loops which can possibly cause mass balance errors. This particularly occurs during a cyclic pressure head condition that is analogous to, motion-like, groundwater oscillation (Klute and Heermann 1974, Jaynes 1984, Kool and Parker 1987, Viaene et al. 1994, Šimůnek et al. 1999). Werner and

Lockington (2006) studied a hypothetical simulation of Kool and Parker (1987) model where artificial pumping error occurred (i.e., non-closure at the reversal points). An illustration of the APE is shown in Figure 2.3. As shown, Kool and Parker (1987) model failed to achieve a full closure between point 4 and point 2.

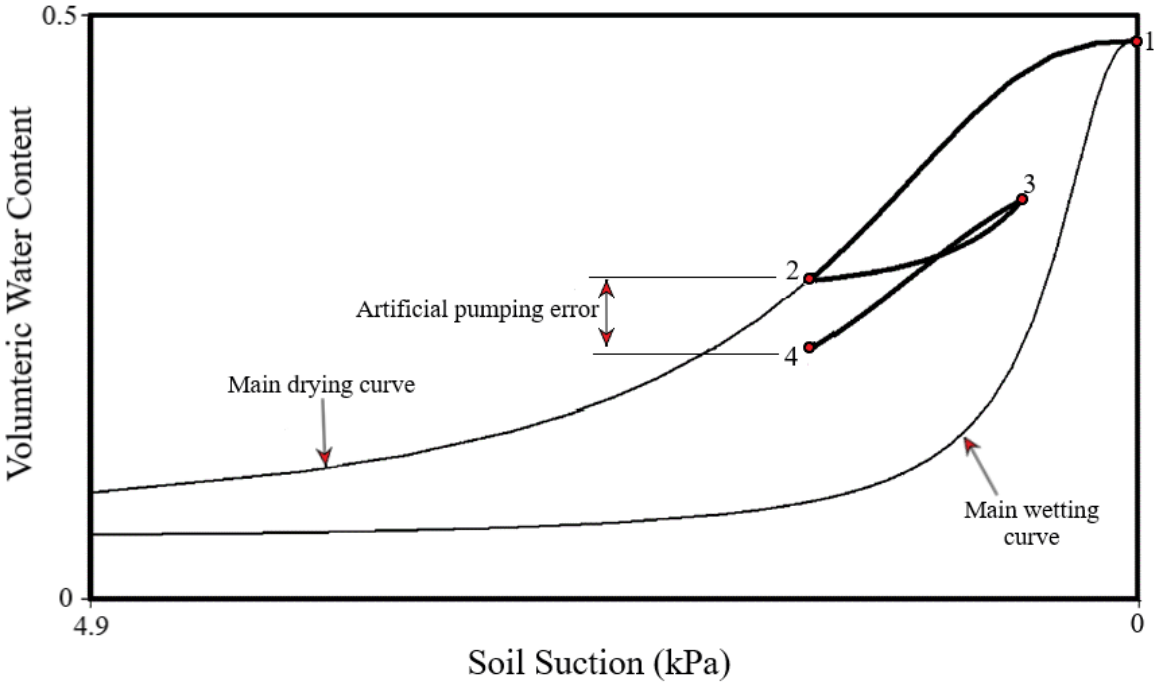

Figure 2.3 Hysteretic SWCC of a hypothetical simulation of cyclic capillary pressure, using the model by Kool and Parker (1987) [Modified from Werner and Lockington (2006)]

In order to solve the issue with the APE, Parker and Lenhard (1987) proposed a model which enforces full closure of the scanning hysteresis loop. This can be achieved by storing a history of reversal points and scaling the scanning curves to pass through them. Parker and Lenhard (1987) and Lenhard et al. (1991) have shown that their model provides a simple and convenient means for implementing a hysteretic water flow response in numerical modelling. It has provided

considerable improvement involving accuracies in the prediction with minimal data inputs. This model, by Parker and Lenhard (1987), was implemented in the current research, and is discussed in greater details in the coming sections.

2.5.1 Parametrization of vG's SWCC in the Hysteresis Model

The main drainage and wetting curves can be expressed in the form of vG function (van Genuchten 1980). The set of vG parameters describing the drying branch of SWCC are $\{\theta_s^d, \theta_r^d, \alpha^d, n^d\}$ and main wetting branch are $\{\theta_s^w, \theta_r^w, \alpha^w, n^w\}$. The superscript, w, denote to the vG parameter for the wetting curve, and d, is related to the drying curve. However, the number of the unknown parameters can be reduced by imposing some experimentally driven constraints on the vG parameters. For example, Kool and Parker (1987), Pham et al. (2005), and Likos et al. (2014) reported that the n parameter, related to the pore-size distribution, is the approximately equal for both drying and wetting curves, hence imposing the constraint, $n^w = n^d = n$. In addition, based on their findings, a similar constraint can be imposed on the residual water content, where $\theta_r^w = \theta_r^d = \theta_r$. Kool and Parker (1987) stated that imposing such constraints did not lead to any loss of accuracy in the results, except for soils with extremely narrow pore-size distribution. Consequently, this reduces the number of unknown parameters to six unknowns, and the parameters set describing the hysteresis loop becomes $\{\theta_s^d, \theta_r, \alpha^d, n\}$ for the drying curve, and $\{\theta_s^w, \theta_r, \alpha^w, n\}$ for the wetting curve. Now, with θ_s^w and α^w are the only controlling parameters of the hysteresis SWCC. In its simplest form, a closed hysteresis loop can be achieved by assuming $\theta_s^w = \theta_s^d = \theta_s$, meaning that air entrapment is negligible. The number of unknown parameters further reduce to five. However, the assumption of negligible air entrapment might not be reasonable for field conditions. It is expected that the presence air

entrapment would impose considerable effects on the water flow response (Stauffer and Dracos 1984, Fayer and Hillel 1986a, 1986b).

In several experiments including those of Hopmans and Dane (1986), the relationship, $\theta_s^w < \theta_s^d$, is mostly found to be true during rewetting of the pores in which the volume of trapped air (TA) is larger than zero ($TA > 0$). Thus, considering negligible air entrapment may not lead to an accurate assessment in most cases. The parameter θ_s^w can be estimated through the following: $\theta_s^w = (1 - TA) * \theta_s^d$, for some TA ranges that can be obtained from the literature through their experimental efforts. For example, Lu et al. (2013) reported that the average degree of air entrapment (i.e., ratio between the volume of entrapped air and the porosity, as a percentage) is 15% and can range from 2% to 35% for wide range of soils. Based on experimental studies, Pham et al. (2005) suggested that $\theta_s^w/\theta_s^d = 0.90 \pm 0.05$ is a reasonable approximation of trapped air volume in geotechnical engineering practices. Likos et al. (2014) measured the vG parameters of the main wetting curve based on a suite of 25 soils; they found that $\theta_s^w/\theta_s^d = 0.87 \pm 0.11$ for cohesive soils, $\theta_s^w/\theta_s^d = 0.81 \pm 0.08$ for cohesionless soils, and $\theta_s^w/\theta_s^d = 0.85 \pm 0.10$ based on all soils. The average and the standard deviation values of θ_s^w/θ_s^d, are found comparable between different studies. Thus, the ratio of θ_s^w/θ_s^d can be used to further reduce the number of unknown parameters. The vG parameter, α^w, that is inversely related to the air entry pressure of the main wetting curve, can also be derived from α^d. Kool and Parker (1987) and Likos et al. (2014) reported that $\alpha^w \approx 2\alpha^d$; where α^d is the related to the air entry value and pertains to drying curves, and α^w pertains to wetting curves.

Those constraints were used in the current research to reduce the number of unknown parameters in the hysteresis model. Thus, the vG parameters of the initial drying curve were only required to

be obtained. For this research, the vectors describing the hysteresis loop became $\{\theta_s^d, \theta_r, \alpha^d, n\}$ for the initial drying curve and $\{\theta_s^d(1 - TA), \theta_r, 2\alpha^d, n\}$ for the main wetting curve. On the other hand, to describe the scanning curves within the hysteresis loop a hysteresis model by Parker and Lenhard (1987) was used. This model has been elaborated upon in another publication by Lenhard et al. (1991), which the present research references. Detailed descriptions and explanation of the model's algorithm are presented in the following section.

2.5.2 Description of Hysteresis Model by Parker and Lenhard (1987)

Parker and Lenhard (1987) (also explained through Lenhard et al. (1991)) model employs the concept of apparent saturation rather than effective or actual saturation. This approach can encapsulate the entrapment effect of a discontinuous non-wetting fluid, such as trapped air, within an air-water system. A similar approach was previously implemented by Fayer and Hillel (1986a) to study the entrapment of air in soil pores and its impact on water movement in soil. The concept of apparent saturation separates the discontinuous air phase (i.e., entrapped air inside the wetting fluid or water) from the continuous air phase. The mathematical definition of the apparent saturation is as follows:

$$\bar{\bar{S}}_w = \bar{S}_w + \bar{S}_{at} \qquad \text{[Eq. 2.8]}$$

where $\bar{\bar{S}}_w$ is the apparent saturation of the water, and it is the summation of the effective saturation of water ($\bar{S}_w$) and the effective saturation of entrapped air ($\bar{S}_{at}$). The double overbar is indicative of apparent saturation, and the single overbar indicates effective saturation concept. The use of apparent saturation is only applicable when water, in the two-phase system, is always continuous, hence will not become entrapped by the nonwetting fluid (i.e., air). Also, with the

use of apparent saturation, the emulsified or trapped air is accounted for as part of the wetting fluid (i.e., water). The effective saturation of water and air, respectively is defined as the following:

$$\bar{S}_w = \frac{S_w - S_m}{1 - S_m}; \quad \text{[Eq. 2.9]}$$

$$\bar{S}_a = \frac{S_a}{1 - S_m} \quad \text{[Eq. 2.10]}$$

where S_w and S_a are the actual water and air saturations, respectively, and S_m is the irreducible saturation of water. The effective, apparent, and actual saturations can equalize when the zero suction is achieved exclusively on the initial drying curve (i.e., when the volume of trapped air volume is zero). When employing the concept of apparent saturation, the hysteretic θ-ψ relationship closes at zero capillary head (i.e., soil suction), as well as at infinite capillary head (see Figure 2.4). Parker and Lenhard (1987) and Lenhard et al. (1991) parametrically described the van Genuchten (1980) of the main drying and wetting curve, respectively, as:

$$\bar{\bar{S}}^w(\psi) = [1 + (\alpha^w \psi)^n]^{-m} \quad \text{[Eq. 2.11]}$$

$$\bar{\bar{S}}^d(\psi) = [1 + (\alpha^d \psi)^n]^{-m} \quad \text{[Eq. 2.12]}$$

To describe scanning curves, $\bar{\bar{S}}(\psi)$, the empirical model by Lenhard et al. (1991) rescales the main boundary curves to pass back through appropriate reversal points. Consider an arbitrary wetting scanning curve that begins at point ($^{\Delta}\bar{\bar{S}}^{dw}$, $^{\Delta}\psi^{dw}$) corresponding to the most recent reversal from drying to wetting, and consider an end point ($^{\Delta}\bar{\bar{S}}^{wd}$, $^{\Delta}\psi^{wd}$) corresponding to the

reversal from wetting to drying on the preceding drying curve. The equation, which rescales the main wetting curve by interpolating between the reversal points, is as follows:

$$\bar{\bar{S}}(\psi) = \frac{[\bar{\bar{S}}^{w}(\psi) - \bar{\bar{S}}^{w}({}^{\Delta}\psi^{wd})][{}^{\Delta}\bar{\bar{S}}^{dw} - {}^{\Delta}\bar{\bar{S}}^{wd}]}{\bar{\bar{S}}^{w}({}^{\Delta}\psi^{dw}) - \bar{\bar{S}}^{w}({}^{\Delta}\psi^{wd})} + {}^{\Delta}\bar{\bar{S}}^{wd} \qquad \text{[Eq. 2.13]}$$

where the superscript, Δ, denoted to the reversal point. The superscript "dw" signifies the transition from drying to wetting, while the superscript "wd" indicates the reversal from wetting to drying. So, ${}^{\Delta}\psi^{dw}$ describes the pressure head at the reversal point from drying to wetting, and the saturation value at that point is ${}^{\Delta}\bar{\bar{S}}^{dw}$. The same descriptions reversely apply to ${}^{\Delta}\bar{\bar{S}}^{wd}$ and ${}^{\Delta}\psi^{wd}$ where reversal occurs from wetting to drying. Equation [2.11] is used to calculate the value of the functions $\bar{\bar{S}}^{w}({}^{\Delta}\psi^{wd})$ for $\psi = {}^{\Delta}\psi^{wd}$ and $\bar{\bar{S}}^{w}({}^{\Delta}\psi^{dw})$ for $\psi = {}^{\Delta}\psi^{dw}$.

A similar procedure is used to rescale the main drying curve. For an arbitrary drying scanning curve that begins at point (${}^{\Delta}\bar{\bar{S}}^{wd}$, ${}^{\Delta}\psi^{wd}$) which corresponds to the most recent reversal from wetting to drying, and ends at point (${}^{\Delta}\bar{\bar{S}}^{dw}$, ${}^{\Delta}\psi^{dw}$) which corresponds to the reversal from drying to wetting on the preceding wetting curve, The equation is as follows:

$$\bar{\bar{S}}(\psi) = \frac{[\bar{\bar{S}}^{d}(\psi) - \bar{\bar{S}}^{d}({}^{\Delta}\psi^{dw})][{}^{\Delta}\bar{\bar{S}}^{wd} - {}^{\Delta}\bar{\bar{S}}^{dw}]}{\bar{\bar{S}}^{d}({}^{\Delta}\psi^{wd}) - \bar{\bar{S}}^{d}({}^{\Delta}\psi^{dw})} + {}^{\Delta}\bar{\bar{S}}^{dw} \qquad \text{[Eq. 2.14]}$$

where the of values of the functions $\bar{\bar{S}}^{d}({}^{\Delta}\psi^{dw})$ and $\bar{\bar{S}}^{d}({}^{\Delta}\psi^{wd})$ are given by Eq. [2.12] with $\psi = {}^{\Delta}\psi^{dw}$ and $\psi = {}^{\Delta}\psi^{wd}$, respectively.

To better explain the use of the equations, consider the hysteretic SWCC, using the apparent saturation concept, for a hypothetical problem as shown in Figure 2.4:

- Path 1-2 lies along the main drying curve and is described by Eq. [2.12] and Eq. [2.14], where the starting point, point 1, becomes (${}^{\Delta}\bar{\bar{S}}^{wd}$, ${}^{\Delta}\psi^{wd}$) = (1,0). The end point of the path becomes (${}^{\Delta}\bar{\bar{S}}^{dw}$, ${}^{\Delta}\psi^{dw}$).
- Path 2-3 is a primary wetting scanning curve and is described by Eq. [2.11] and Eq. [2.13]. So that (${}^{\Delta}\bar{\bar{S}}^{dw}$, ${}^{\Delta}\psi^{dw}$) corresponds to point 2, and (${}^{\Delta}\bar{\bar{S}}^{wd}$, ${}^{\Delta}\psi^{wd}$) corresponds to the previous reversal point (i.e., point 1) which is equal to (1,0).
- Path 3-4, which is a segment on the drying branch of the closed loop 2-3-2, is described by Eq. [2.12] and Eq. [2.14]. So that (${}^{\Delta}\bar{\bar{S}}^{wd}$, ${}^{\Delta}\psi^{wd}$) corresponds to point 3, and (${}^{\Delta}\bar{\bar{S}}^{dw}$, ${}^{\Delta}\psi^{dw}$) corresponds to point 2.
- Path 4-5, which is a segment on the wetting branch of the closed loop 3-4-3, is described by Eq. [2.11] and Eq. [2.13]. So that (${}^{\Delta}\bar{\bar{S}}^{dw}$, ${}^{\Delta}\psi^{dw}$) corresponds to point 4, and (${}^{\Delta}\bar{\bar{S}}^{wd}$, ${}^{\Delta}\psi^{wd}$) corresponds to the previously stored point 3. If path 4-5 were to continue wetting till reaching point 3, then beyond that path 2-3 would resume, and the memory storage of the loop 3-4-3 would not be needed.

As implied from Figure 2.4, storage of the reversal points is needed to achieve full closure of the hysteresis loop. It is unreasonable to store all reversal points when high orders of scanning curves are achieved; such large storage of data is deemed impractical in numerical modelling. So, Lenhard et al. (1991) suggested that a maximum number of 5-7 reversal points are sufficient for the storage. Parker and Lenhard (1987) argued that beyond the second and third order, the scanning curve, $\bar{\bar{S}}(\psi)$, can regarded as nonhysteretic until achieving full closure. They found that the hysteresis effects are dampened beyond the 3rd order of scanning curves.

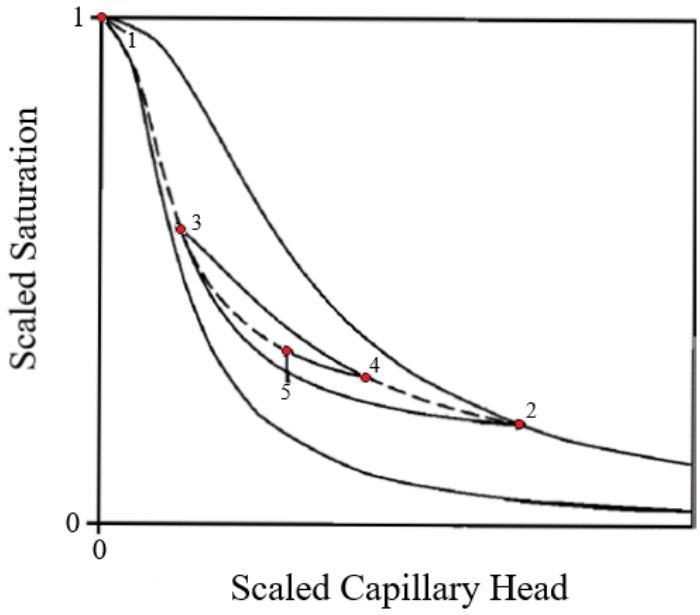

Figure 2.4 Hypothetical scaled or apparent saturation paths using $\bar{\bar{S}}(\psi)$ functionals [Modified from (Parker and Lenhard 1987)]

2.5.2.1 Air Entrapment Consideration by Parker and Lenhard (1987)

To account for the effect of air entrapment in the hysteresis model, Parker and Lenhard (1987) integrated an algorithm proposed by Land (1968). Land predicted the volume of trapped air after wetting from a point along the initial drying curve to full apparent saturation = 1 (i.e., zero suction). This was done through an interpolation scheme. To do so, the effective or actual saturation must be converted back. Only the maximum saturation of the trapped air, $\bar{S}_{ar}^{w}$, (shown in Figure 2.5) is needed to transform hysteresis loop from apparent values to actual values. The effective water saturation at the reversal points from initial drying curve to wetting scanning curve is denoted by ${}^{\Delta}\bar{S}_{w}$. Figure 2.5 illustrate the values of these points on the effective saturation of the hysteretic θ-ψ relation.

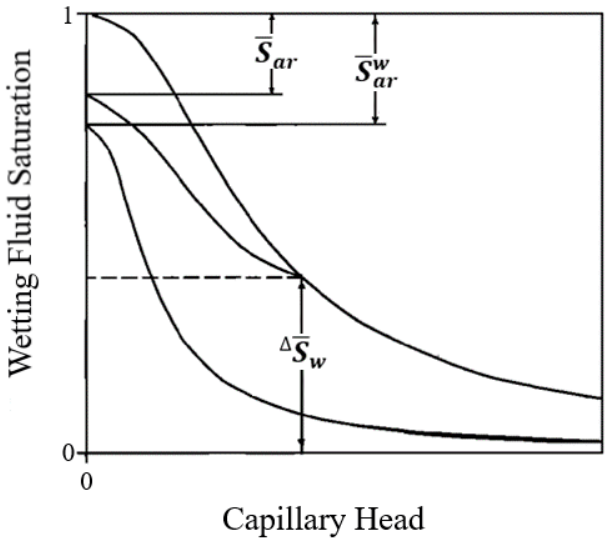

Figure 2.5 Hypothetical wetting of effective saturation paths in an air-water phase system, showing initial drying curve and main wetting curve [Modified from (Parker and Lenhard 1987)]

Land's (1968) algorithm, as described by Lenhard et al. (1991), is as follows:

$$\bar{S}_{ar} = \frac{1 - {}^{\Delta}\bar{S}_w}{1 + R(1 - {}^{\Delta}\bar{S}_w)}; \quad R = \frac{1}{\bar{S}^{w}_{ar}} - 1 \qquad \text{[Eq. 2.15]}$$

where $\bar{S}_{ar}$ is the effective residual saturation of the air of an arbitrary wetting scanning curve originating from ${}^{\Delta}\bar{S}_w$, $\bar{S}^{w}_{ar}$ is the maximum effective residual saturation of air of the main wetting curve. These effective residual saturations are the amount of trapped air at zero suction. A linear interpolation method was employed by Lenhard et al. (1991) to estimate effective saturation of trapped air ($\bar{S}_{at}$) of an intermediate point between ${}^{\Delta}\bar{S}_w$=$\bar{\bar{S}}_w$ and $\bar{\bar{S}}_w$=1. At ${}^{\Delta}\bar{S}_w$=$\bar{\bar{S}}_w$, $\bar{S}_{at}$=0, and at $\bar{\bar{S}}_w$=1, $\bar{S}_{at}$=$\bar{S}_{ar}$, the following equation is obtained when linearly interpolating between the two (Lenhard et al. 1991):

$$\bar{S}_{at} = \bar{S}_{ar}\left(\frac{\bar{\bar{S}}_w - {}^{\Delta}\bar{S}_w}{1 - {}^{\Delta}\bar{S}_w}\right); \quad \text{for} \quad \bar{\bar{S}}_w \geq {}^{\Delta}\bar{S}_w \qquad \text{[Eq. 2.16]}$$

In summary, the previous sections presented a procedural summary of the Lenhard et al. (1991) model. The procedure involves scaling of the scanning curves from the main boundary curves of the hysteresis loop. Also, it presented a general procedure of how air entrapment is accounted for in the model. The current research utilized the Lenhard et al. (1991) model through HYDRUS software package to describe the hysteretic characteristics and entrapment of air in the studied variably saturated water flow problems.

2.6 Solute Transport under Variably Saturated Medium with Consideration of Hydraulic Hysteresis

The partial differential equation (PDE) governing two-dimensional transport of a single-phase, inert, and non-adsorbing solute during transient water flow in a variably saturated rigid porous medium, can be expressed as follows (Šimůnek and van Genuchten 1995):

$$\frac{\partial}{\partial t}(\theta C) = \frac{\partial}{\partial x_i}\left(\theta D_{ij}^{w} \frac{\partial C}{\partial x_j}\right) - \frac{\partial}{\partial x_i}(q_i\, C); \qquad \text{[Eq. 2.17]}$$

where the dispersion coefficient tensor for the liquid phase, D_{ij}^{w}, is given by (Bear 1972):

$$\theta D_{ij}^{w} = D_T|q|\delta_{ij} + (D_L - D_T)\frac{q_j q_i}{|q|} + \theta D_w \tau_w \delta_{ij} \qquad \text{[Eq. 2.18]}$$

where C is solute concentration in the liquid phase [M L^{-3}], x_i is the spatial coordinates [L], where $x_1 = x$ and $x_2 = z$, ij are indicial notation used for Einstein's summation convention ($i, j = 1,2$), q_i is the i-th component of the volumetric flux density [L T^{-1}], D_{ij}^{w} is the dispersion coefficient tensor or the hydrodynamic dispersion coefficient tensor in the liquid phase [L^2 T^{-1}], D_w is the molecular diffusion coefficient in free water [L^2 T^{-1}], τ_w is the tortuosity factor in the

liquid phase [-], $|q|$ is the absolute value of the Darcian fluid flux density [L T^{-1}], δ_{ij} is the Kronecker delta function (δ_{ij}=1 if $i=j$, and δ_{ij}=0 if $i \neq j$), and D_L and D_T are the longitudinal and transverse dispersivities, respectively [L].

Upon numerically solving Richards PDE equation (Eq. [2.1]), both θ and Darcian flux q, from Eq. [2.18], become known values, hence the solute transport PDE can be subsequently solved (Richards 1931, Šimůnek and van Genuchten 1995, Šimůnek et al. 2022). The tortuosity factor in the liquid phase is evaluated as a function of the water content using the relationship of Millington and Quirk (1961) expressed as:

$$\tau_w = \frac{\theta^{7/3}}{{\theta_s}^2} \qquad \text{[Eq. 2.19]}$$

How the solute transport terms of these equations tie connection with hydraulic hysteresis and air entrapment are of great importance. The terms that reflect this connection are through the Darcian flux and water content from Eq. [2.17]. It has been shown in this research that hydraulic hysteresis and air entrapment affect the soil suction and water content distribution within the domain, which had an effect on the water fluxes entering the soil through the atmospheric boundary conditions. This hysteretic effect in the water fluxes would change the water flow response, or in other words, the Darcy fluid flux, q. In addition, the volumetric water content change, due to hysteresis, is also reflected in the θ from Eq. [2.17]. Furthermore, entrapment of air result in a lower water content within the pores, and as Mitchell and Mayer (1998) explained, the presence of entrapped air reduces the pore-space available for water to flow, which in return increases the rate of the advective flux of solute. In addition, the tortuosity (Eq. [2.19]) and the

dispersion coefficient (Eq. [2.18]) depend on Darcy flux and water content. So, hysteresis and air entrapment in the SWCC, reflected on the soil suction, water content, and water flux rate, can lead to both hysteretic water flow response and hysteretic solute transport response, both dependently and independently. Therefore, consideration of hysteresis and air entrapment would lead to more accurate representation of the solute fate within the variably saturated soil domains.

2.7 Slope Stability in Unsaturated Soil Framework with Consideration of Hydraulic Hysteresis

Slope stability is one of the most common engineering assessments in the geotechnical field, which ensures the quantification of the stability state of the slopes. To quantify a slope's stability, a Factor of Safety (FOS) is estimated, which can be defined as the ratio between the shear strength (i.e., resisting forces) and mobilized shear stress (i.e., driving forces) of the failing slip surface (Godt et al. 2009, Lee and Ho 2009, Tsai 2011, Ma et al. 2011, Lu et al. 2012, Cheng and Lau 2014). Slope stability using the limit equilibrium (LE) method can be used to calculate the FOS and is considered one of the oldest forms of numerical modeling techniques (SLOPE/W 2021). The aim of the LE stability analysis is to find this FOS, for which the strength of the soil is reduced to bring it to equilibrium with the shear stresses that the soil experiences (i.e., instability). The LE achieves this by presuming potential sliding masses and discretizing them into a number of vertical slices (see Figure 2.6). Then FOS is attained through finding a state or point upon where the driving force (i.e., destabilizing force) is equal to all of the stabilizing forces (i.e., resisting forces) (Cheng and Lau 2014) for all slices. Figure 2.7 shows the forces that act on a single slice of the sliding mass, within the slip surface. To achieve equilibrium between those forces and attain a factor of safety, the following static equations are satisfied (Eq.

[2.20a-c]): the summation of normal forces, tangential forces, and/or moments, at any given point, is equal to zero (GEO-SLOPE 2022).

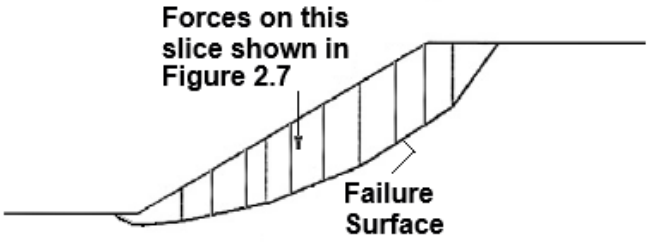

Figure 2.6 Limit equilibrium's method of slices [Modified from (Huang 2014)]

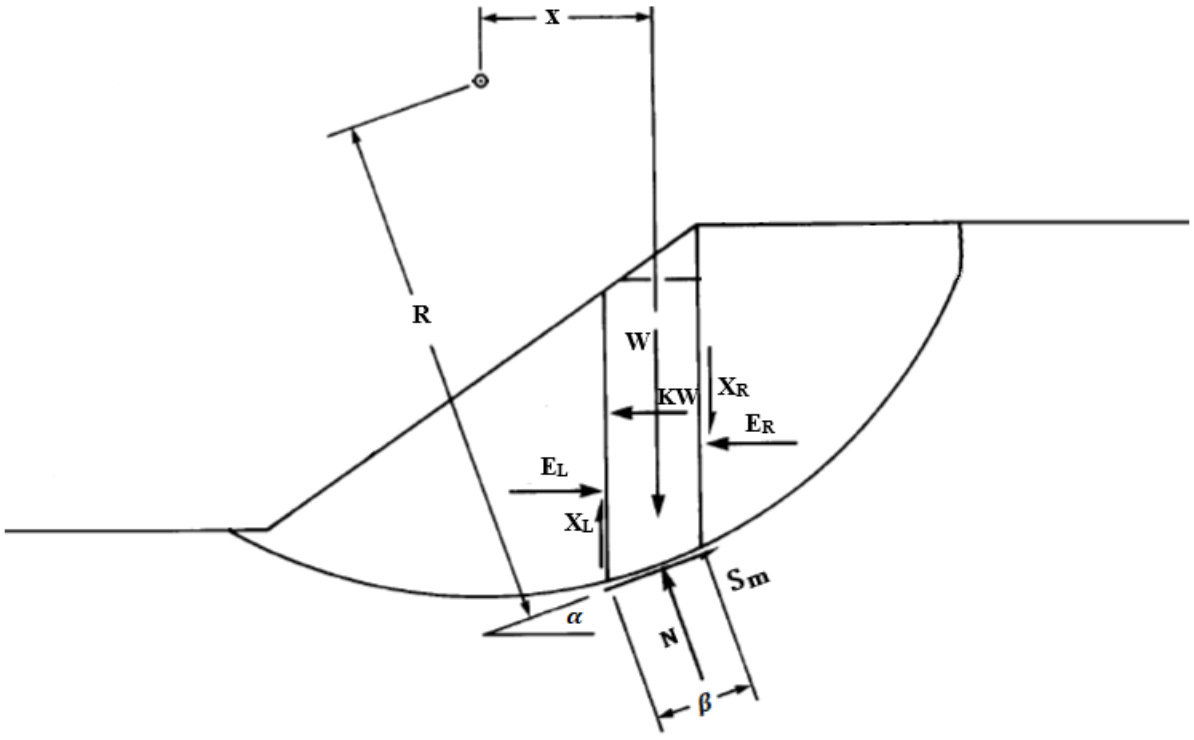

Figure 2.7 Schematic of circular sliding mass surface with forces acting on a slice [Modified from (SLOPE/W 2021)]

Equations, Eq. [2.20a] through Eq. [2.20c], satisfy the equilibrium of the moments (Eq. [2.20a]), vertical forces (Eq. [2.20b]), and horizontal forces (Eq. [2.20c]) (without consideration of point load, seismic loading, and external water forces). These equations depend on the mobilized shear force in unsaturated soil conditions (S_m), (Eq. [2.20d]), which satisfies conditions of limit equilibrium (SLOPE/W 2021):

$$F_m = \frac{\sum(C'\beta R+(N-u\beta)R\ tan\phi')}{\sum Wx-\sum Nf} \quad \text{[Eq. 2.20a]}$$

$$(X_L - X_R) - W + N\ cos\alpha + S_m\ sin\alpha = 0 \quad \text{[Eq. 2.20b]}$$

$$(E_L - E_R) - N\ sin\alpha + S_m\ cos\alpha = 0 \quad \text{[Eq. 2.20c]}$$

$$S_m = \frac{s\ \beta}{F} \quad \text{[Eq. 2.20d]}$$

where, for each slice, W is total weight, N is total normal force, E_L and E_R are left and right side's horizontal normal forces, respectively, X_L and X_R are left and right side's vertical interslice shear force, R is moment arm for the associated mobilized shear force, f is perpendicular offset of the normal force from the moments' center (with the sign changing depending on the side taken of slope with respect to the center of rotation), x is horizontal distance from the centerline to the center of moment, α is angles between tangent to slice base's center and the horizontal (with sign changing depending on its orientation in respect to the direction of the slope), S_m is mobilized shear force, s is unsaturated shear strength, β is base length of the slice, and F is factor of safety.

Equations [2.20a] through [2.20d] are indeterminate, meaning that the number of unknowns exceeds the number of equations, hence a unique FOS cannot be obtained. Therefore, assumptions must be made for simplifications purposes and to make the problem statistically

determinate by increasing the number of equations that exactly matches the number of unknowns. To solve the problem statically, one can assume the forces between two slices (Huang 2014). Morgenstern and Price (1967) proposed one of the several published methods that incorporate such an assumption. Different limit equilibrium methods for slope stability analysis vary in their treatment of rotational and translational equilibrium, consideration of forces and moments, assumptions about slip surface shape, incorporation of pore water pressure, and overall applicability. The method by Morgenstern and Price (1967) was implemented in the current research, which satisfies all static equations.

It is vital to understand the factors dictating the value of the FOS. Water content (or soil suction through SWCC) distribution within the soil slope is the main driving force to the value of FOS; any changes in this distribution is due to frequent exposure of slopes to external climatic factors such as rainfall infiltration (Chen and Zhang 2006, Rahardjo et al. 2010, Zaky and Oh 2017). This is of a critical consideration since one of the most common slope failure types is rainfall-induced failures, having been regularly reported worldwide (Haque et al. 2019). From an unsaturated soil point of view, the value of the FOS is influenced by the changes in the unsaturated shear strength, which is a function of the water content and matric suction (i.e., soil suction) of the soil. The mobilized shear of the soil (from Eq. [2.20d]) is in turn a function of the unsaturated shear strength (Eq. [2.21]) defined by method of Fredlund et al. (1996) and Vanapalli et al. (1996):

$$s = C' + (\sigma_n - u_a)\, tan\phi' + \left(\frac{\theta - \theta_r^*}{\theta_s - \theta_r^*}\right) \psi\, tan\phi' \qquad \text{[Eq. 2.21]}$$

Notice that θ_r^* is the volumetric water content at which the suction strength becomes zero and is different from the residual water content (θ_r) of the van Genuchten (1980) SWCC equation. The value of θ_r^* is usually taken as 50% of the porosity value (i.e., 50% of the saturated volumetric water content).

The equation includes two main components: the first is the effective shear strength which depends on the effective cohesion (C'), net normal stress ($\sigma_n - u_a$), and effective angle of internal friction (ϕ'), the second component is the suction strength (far right-hand side) which depends on the soil properties such as : soil suction, water content, and effective angle of internal friction. This is an important concept, since it quantifies the slope stability response under unsaturated soil conditions. In most applications, slope is regularly exposed to climate, which naturally results in saturated-unsaturated water flow through frequent rainfall and evaporation processes (i.e., wetting and drying processes). Therefore, considering the unsaturated shear strength equation (Eq. [2.21]) can lead to factor of safety that is more representative under unsaturated soil conditions. Due to regular exposure of the slope to frequent drying and wetting cycles, the soil slope's hydraulic response exhibit hysteresis, in which the drying processes are represented by the main drying and drying scanning curves, and the wetting processes are represented by the main wetting and wetting scanning curves. Thus, including hysteresis in the SWCC of the soil slope is critical. Furthermore, unsaturated shear strength (Eq. [2.21]) can also exhibit hysteresis, since it has a direct relationship with the van Genuchten (1980) hysteretic SWCC. The unsaturated shear strength' suction strength component depends on both volumetric water content and soil suction (i.e., matric suction). Should hysteresis be considered in the SWCC, therefore, the resulting suction strength becomes hysteretic. Thus, the FOS values can

also exhibit a hysteretic response, and the values can vary depending on the type of climate and the hydraulic properties of the soil slope.

One of the shortcomings of utilizing some of the common LE slope stability software, is that they only implement nonhysteretic SWCC, hence resulting in a nonhysteretic unsaturated shear strength model, hence the value of FOS becomes less representative of the site conditions. For this reason, the current thesis (in Chapter 5.4.3) proposed a correction procedure on the soil suction/water content inputs, so that hysteresis and air entrapment is accounted for in the unsaturated shear strength, specifically for implementation in software, such as SLOPE/W, that originally do not consider hysteresis.

CHAPTER 3: Effect of Hysteresis with Air Entrapment on 1-D Water Flow and Solute Transport under Varying Climatic Conditions

3.1 Abstract

Brine-produced in oilfields is a major source of saline water, leading to the contamination of soil and groundwater. The interaction of meteoric water and atmospheric evaporative energy with the unsaturated soils controls the water balance at the ground surface, hence dictating the water movement and salt/solute transport in the subsurface. Considering that unsaturated soils typically undergo frequent cyclic drying and wetting events, hydraulic hysteresis, including air entrapment consideration, plays an important role in the movement of water and solutes within the vadose zone. In most instances, hysteresis in hydraulic functions is ignored, and land-climate interaction analysis is carried out, solely by representation of soil water characteristics by either the initial or the main drainage curve, even to represent intermittent cycles of climatic drying and wetting. This research utilizes a variably saturated flow and transport model to study the impact of hydraulic hysteresis on the salt transport in the subsurface using multiyear climate data for varying climatic conditions across Alberta. The hysteretic soil water characteristic curves used for assessment also considers the air entrapment, which is usually excluded in hysteretic analysis. The results show that the inclusion of hysteresis and air entrapment in the land-climate interaction analysis results in dissimilar solute distributions in the subsurface when compared with nonhysteretic analyses. Furthermore, the relative impact scale of hysteresis on the solute transport is the function of climate type and degree of air entrapment. A larger impact of hysteresis on solute transport can be observed for fine textured soils. In addition, the results also show that excluding air entrapment in hysteretic analysis underestimates the advective flux of the

solute. In certain scenarios, the findings indicated that simulating hysteresis alone led to an approximately 2% increase in solute penetration depth compared to simulations based on nonhysteretic drying curves. Notably, a significant enhancement was observed, particularly when considering air entrapment, resulting in a deeper penetration depth with an increase of up to 40%. The study underscores the importance of accounting for hysteresis with air entrapment, as neglecting these factors may potentially lead to inaccurate assessments of concentration levels within the domain and groundwater contamination levels.

3.2 Introduction

The vadose zone, which is the subsurface area above the water table, is constantly exposed to various anthropogenic activities that can lead to surface and subsurface contamination (Mitchell and Mayer 1998). However, the vadose zone can also act as a natural filter due to its unsaturated condition, which can help attenuate the migration of solutes from the surface, preventing the contamination of groundwater (Bashir and Pastora Chevez 2018).

Assessing the flow and transport mechanisms in the vadose zone is a complex process due to various factors, such as the hydraulic properties of the soil, hydraulic variability (heterogeneity), and the interaction between the soil and the climatic conditions. For instance, a high evaporative energy climate can interact with soils that have low hydraulic conductivity and high retention properties, resulting in vertical upward water flow and solute transport (Bashir and Pastora Chevez 2018). This could pose a risk to various forms of biota, including subsurface organisms, livestock, wildlife, and humans, who may be indirectly exposed to contaminants through ingestion (Government of Alberta 2020). Also, as the vadose zone is directly linked to groundwater, any contaminants present in the vadose zone can easily move downwards, leading

to an increased risk of groundwater contamination (Pastora Chevez 2017). Groundwater contamination is a significant concern due to its negative impact on the environment and human health. This is particularly critical in countries such as Canada, where groundwater meets 30% of the population's domestic water demand (Rutherford 2004).

Numerical modeling is often used to simulate the flow and transport of contaminants in unsaturated soils. However, accurate modeling of the flow and transport processes in the unsaturated zone requires the coupling of the two processes. This coupling is important because the flow of water affects the transport of contaminants and vice versa. The coupling of flow and transport in unsaturated soils can be modeled using various approaches, including the Richards' equation and advection-dispersion equation. The Richards' equation is a partial differential equation that describes water flow in unsaturated soils, while the advection-dispersion equation is used to describe contaminant transport. To simulate the coupling of flow and transport in unsaturated soils, these equations are typically solved simultaneously using numerical methods. One common approach is to use the finite element method, which discretizes the domain into a mesh and solves the equations at discrete points. Other numerical methods, such as the finite difference method, are also commonly used.

Modeling the flow and transport in unsaturated soils also requires accurate characterization of the hydraulic properties of the soil, such as the soil-water characteristic curve (SWCC) and the unsaturated hydraulic conductivity function (HCF). These properties can be determined through laboratory experiments or estimated using pedotransfer functions. Hydraulic hysteresis refers to the phenomenon where the hydraulic properties of a porous medium, such as its hydraulic conductivity or water retention, depends on the direction of flow or the history of water content changes. In other words, the hydraulic behavior of the porous medium is not reversible and

depends on the path it takes during the wetting or drying process. Hydraulic hysteresis is particularly important in situations, where the soil water content and pressure are constantly changing due to the interactions between the soil and the atmosphere. The hysteresis effect can have significant impacts on the flow and transport of water and solutes in the vadose zone, as it can cause delays and distortions in the response of the porous medium to changes in boundary conditions (BC). Ignoring hydraulic hysteresis in the simulation of water flow and solute transport can result in significant errors in predications, and has been documented (Gillham et al. 1976, Hoa et al. 1977, Kool and Parker 1987, Kaluarachchi and Parker 1987, Parker and Lenhard 1987, Lenhard et al. 1991, Mitchell and Mayer 1998). Therefore, accurately modeling hydraulic hysteresis is crucial for predicting the fate and transport of contaminants in the vadose zone, as it can significantly affect the rates and pathways of contaminant migration.

The way water and solutes move in the vadose zone is also a function of prevailing climatic conditions. The prediction of such processes can be accomplished through land-climate interaction analysis (LCI), using numerical models. Such models require inputs of climatic data records, consisting of precipitation and potential evaporation, physical and chemical properties of the solute, and the hydraulic characteristics (i.e., SWCC and HCF) of the porous medium. The following is a brief review of the literature on the effect of hydraulic hysteresis on solute transport.

3.3 Literature Review

Pickens and Gillham (1980) conducted a study using a finite element-based model to analyze the effect of hysteresis on solute transport. The study involved vertical flow and transport of a water slug, containing a nonreactive tracer. The model simulated infiltration and redistribution events

in a soil that was highly hysteretic. The results indicated that subsurface water distribution was significantly affected by hysteresis, however hysteresis effect on solute transport was minimal. The concentration profile from the hysteretic simulations lagged behind the nonhysteretic simulation using the wetting curve. Pickens and Gillham (1980) concluded that the effect of hysteresis on solute transport would not be any more considerable than the observed examples of their study. The effect of air entrapment was not considered in their hysteretic simulations.

Russo et al. (1989) studied the impact of hysteresis and heterogeneity on bromide transport using numerical modeling. They found that consideration of these factors resulted in retardation of the solute front compared to simulations that did not consider hysteresis and heterogeneity. They used the Kool and Parker (1987) hysteresis model and compared the results with nonhysteretic-homogenous and heterogeneous cases. They did not investigate the effect of air entrapment in their hysteretic simulations or study the collective effect of hysteresis profile heterogeneity. Hysteretic simulations showed a large change in suction for smaller changes in water content, resulting in higher water content in the upper region and lower water content in the lower region compared to nonhysteretic simulations. Hysteresis was found to retard the downward migration of the solute, consistent with the findings of Jones and Watson (1987) who also studied the effect of hysteresis on solute transport under intermittent leaching conditions.

Vereecken et al. (1995) studied the combined effect of hysteresis and soil heterogeneity on water flow and transport of a conservative solute. They found that neglecting hysteresis and heterogeneity may lead to substantial errors in predicting the fate of the solute. Hysteresis was found to exhibit retardation effects on the solute migration compared to nonhysteretic simulation that only uses the wetting branch of the SWCC. Additionally, it was also noted that hysteresis hastens the solute migration when contrasted with the nonhysteretic simulation using only the

drying branch of SWCC. The effect of hysteresis was also found to be a function of the hydraulic properties, with coarser soils exhibiting smaller hysteretic effects. The authors concluded that hysteresis exhibited considerable effects in predicting the penetration depth of the solute.

Smith (1995) supported the findings of Vereecken et al. (1995) and highlighted the issue of bias in comparing results of hysteretic simulations to only the main drying or main wetting curve, which was also evident in the previous studies (e.g., Pickens and Gillham 1980, Jones and Watson 1987, Russo et al. 1989, and Vereecken et al. 1995). To address this issue, Smith recommended comparing the hysteretic results to the mean of the drying and wetting curve, which was also attempted in their earlier study (Smith 1993).

Mitchell and Mayer (1998) conducted a comprehensive study on the effects of hysteresis and air entrapment on nonreactive solute transport in different soil mediums. The study involved simulating intermittent water flow BC on a one-dimensional vertical domain by repeatedly applying a 48-hr irrigation cycle consisting of solute pulse followed by infiltration of water, then two alternating phases of redistribution (i.e., gravity drainage) and evaporation. Using one of their hysteretic materials, they compared their hysteretic results with nonhysteretic simulations using drying, wetting, and a mean (between the two main branches of the SWCC), in which they reported all three nonhysteretic curves produced similar distributions and that there would be no bias in selecting one of the nonhysteretic curves to compare against hysteretic results. Other analyses proceeded with the comparison of hysteresis against nonhysteresis which utilized wetting curve. Moreover, the study found that water content was higher near the surface and lower near the bottom boundary for the hysteretic simulations compared to nonhysteretic simulations using wetting curve, and explained that small changes in the water content exhibit with larger change in the soil suction when imposing main drying or drying scanning curve.

Mitchell and Mayer (1998) also conducted a sensitivity analysis on each of the van Genuchten (1980) parameters to assess their hysteretic effects on the solute penetration depth, and found that variations in the α^w/α^d (ratio of air entry pressure to water entry pressure) tend to have high effects on the penetration depth of the solute. They also reported that increasing the volume of trapped air exhibited larger hysteretic impacts on the solute's fate, and that the solute has penetrated deeper in comparison to simulations that neglected air entrapment. Moreover, Mitchell and Mayer (1998) argued that the deviation between hysteretic and nonhysteretic results is a function of hydraulic parameters (described in term of van Genuchten 1980 function) collectively rather than imposing individual changes. The study additionally revealed that the influence of hysteresis is more pronounced near the surface, diminishing with depth. Furthermore, it highlighted that the impact of hysteresis becomes less significant for transient problems assessed over extended periods. In coarser soils, the effect of hysteresis on solute transport is less significant due to their high n value (van Genuchten (1980) pore size distribution parameter), and lower α^w/α^d, and high hydraulic conductivity.

In a relatively more recent study by Gladnyeva and Saifadeen (2012), the authors investigated the effects of hysteresis on solute transport in one-dimensional unsaturated domain. They compared the results of hysteretic simulations to nonhysteretic simulations for twelve years of climatic data from three different geographic locations in Sweden. The study also considered the effects of different soil textures and temporal resolution of climate data (ranging from half-hourly to daily resolution). The authors reported that nonhysteretic simulations resulted in faster solute transport, but did not specify which branch type (wetting or drying) was used for reference. Interestingly, the authors found that the effect of hysteresis was more pronounced in coarse textured soils, which contradicts the findings of previous studies by Vereecken et al.

(1995) and Mitchell and Mayer (1998). The study also found that higher temporal resolution of climate data led to larger hysteretic effects. However, the authors recommended neglecting hysteresis when using daily resolution input data, as hysteresis effects were found to be negligible in such simulations.

3.4 Problem Statement

The literature review has identified several crucial areas that require further investigation. A major limitation of the current body of literature is the insufficient exploration of the impact of hydraulic hysteresis on solute transport under actual climatic conditions, particularly in relation to atmospheric boundary conditions (BCs). While Gladnyeva and Saifadeen (2012) explored this matter in a real-world context, the majority of studies in the literature have primarily depended on simulations featuring simplified infiltration boundaries and utilizing repeated flux cycles as one of the boundary conditions. As a result, these simulations may fall short in capturing the intricacies and variability present in actual field conditions, where interactions with real climates occur. This raises concerns about potential inaccuracies in interpreting the results. Therefore, more research is necessary to thoroughly investigate the effects of hydraulic hysteresis under real-world atmospheric BCs, enabling a better understanding of solute transport dynamics and the development of effective management strategies.

Moreover, there is a potential bias in the comparison of hysteretic and nonhysteretic simulations in the literature, as most studies have used the wetting curve as the hydraulic characteristic for nonhysteretic simulations. Therefore, the impact of hysteresis on solute transport when compared to the main drying curve has not been fully discussed, nor has the influence of either curve on the nonhysteretic simulations been thoroughly explored. Studies that have investigated the main

wetting curve have indicated that hysteresis tends to slow down water flow, leading to higher water content near the surface and lower near the bottom of the domain, which can ultimately impede downward solute migration within the vadose zone. Nonetheless, more research is needed to better understand the role of both the main wetting and drying curves in solute transport and the potential impacts of hysteresis on both curves.

In addition, most of the papers referenced in the literature have overlooked the impact of air entrapment, with the exception of the study by Mitchell and Mayer (1998). Their findings indicated that increasing the degree of air entrapment resulted in a greater advective flux and deeper solute penetration. The aspect of air entrapment needs to be further explored, especially in the context of soil atmospheric boundary.

3.5 Validation of the Flow and Transport Model

In order to assess the capabilities of HYDRUS-1D (H1D) to simulate water flow and solute transport using hysteretic hydraulic functions, a validation study was carried out (Šimůnek et al. 2013). A water flow and solute transport modeling study by Pickens and Gillham (1980), was chosen from the literature. Pickens and Gillham (1980) incorporated a hysteresis model, described by Gillham et al. (1976), in their one-dimensional finite element flow and transport code. They validated their hysteretic flow results against existing experimental data from Gillham et al. (1979). The effect of hysteresis on solute transport was studied by modeling infiltration of a water slug containing a non-reactive solute followed by a redistribution period.

To remodel the system reported by Pickens and Gillham (1980), a sand column of 150 cm depth was considered and simulated in H1D. At the top boundary of the domain, a variable flux of 0.17 cm/min was applied for the initial 30 minutes followed by a redistribution period. The bottom

boundary was assigned a constant head BC with a head value of 0 cm. The initial condition of the domain was assumed to be reflective of hydrostatic conditions. For the solute transport component, Cauchy BC (prescribes the solute flux) and zero concentration gradient BC (describes free drainage of solute) were assigned to the top and bottom boundaries, respectively. The simulation incorporated nonhysteretic drying and wetting characteristics along with hysteretic characteristics. The hysteresis model by Parker and Lenhard (1987) was used for the hysteretic simulations, which scales the main boundary wetting and drying curves to estimate the scanning curves. Figure 3.1 shows the distribution of suction, water content, and solute concentration with depth at three different times (30 mins, 60 mins, and 300 mins) from H1D simulations. The results are presented for hysteretic, drying, and wetting curve simulations. This figure also includes the results reported by Pickens and Gillham (1980). It can be observed that results from Hydrus simulations compare well with those reported by Pickens and Gillham (1980). Some minor differences between the two sets of results can be attributed to the different hysteresis models used in the two simulations. Overall, it can be concluded that the H1D estimated the water flow and solute transport accurately for hysteretic and nonhysteretic hydraulic functions.

3.6 Salt Transport in Variably Saturated Soil

Since the mid-20th century, the Great Plains area of Canada has been home to significant oil and gas operations. During the extraction and processing of these valuable resources, there have been instances of spills involving concentrated drilling fluids and Oil field brine that are released either on the ground surface or below it (Bashir and Pastora Chevez 2018). Oil field brine refers to the saline water that is produced along with crude oil during extraction from oil wells. It is

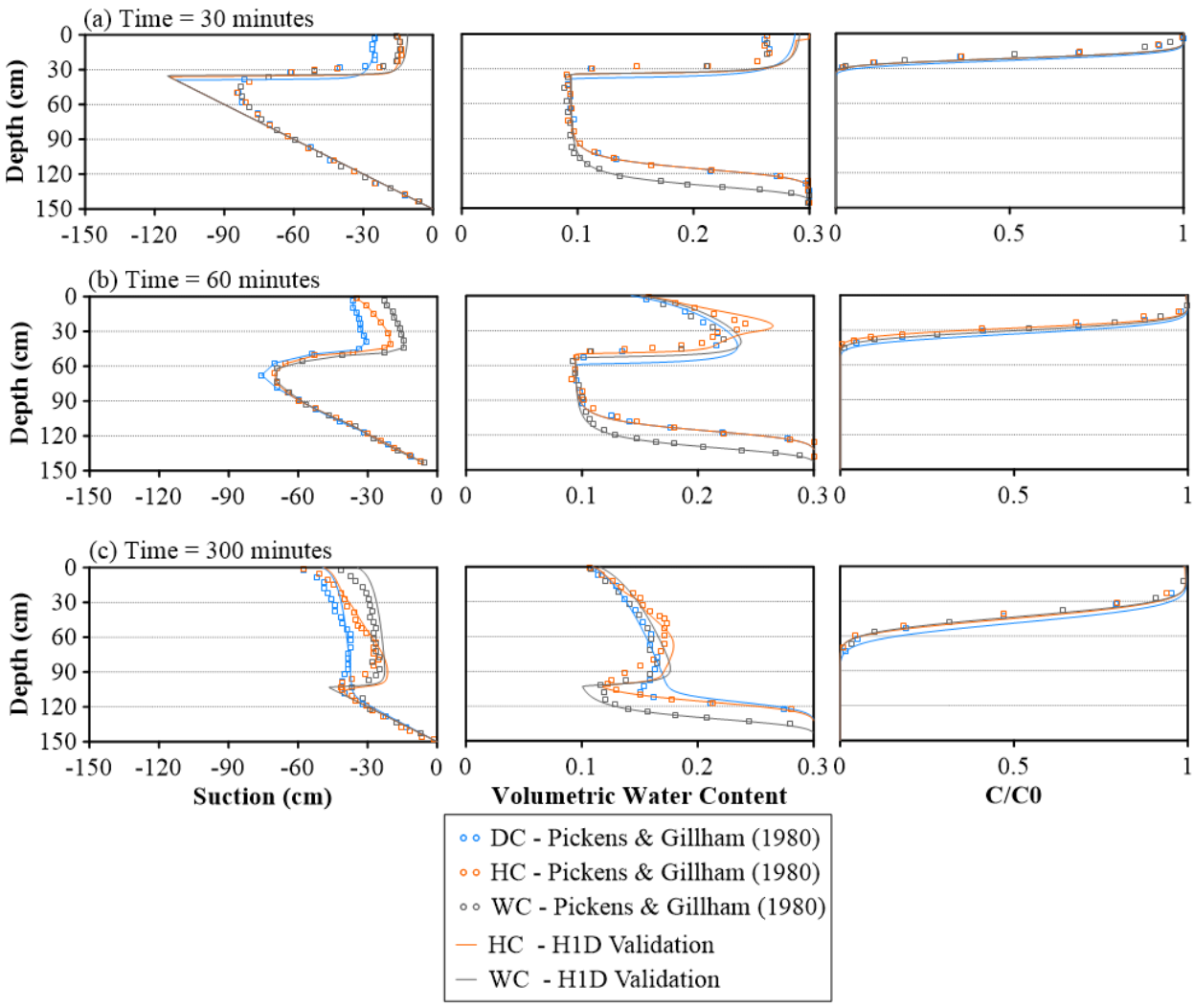

Figure 3.1 Comparison of Hydrus 1D (H1D) results with Pickens and Gillham (1980)

also known as produced water or formation water. This brine often contains high concentrations of salts, heavy metals, hydrocarbons, and other contaminants. Brine contamination in soils often occurs due to various factors such as pipeline ruptures, surface spills near wellheads or battery sites, and the movement of brine from buried reserve or disposal pits, both above and below the ground (Keiffer and Ungar 2002).

This study builds upon the research conducted by Bashir and Pastora Chevez (2018) by incorporating hysteresis into the simulations. Their previous work focused on numerically modeling one-dimensional (1-D) variably saturated water flow and salt transport within a coarse grained and fine-grained soil profile. The study utilized daily climate data from several locations in Alberta, Canada, to simulate atmospheric boundary conditions (BC). In this current research, the atmospheric BC is applied using climate data from Bighorn Dam and Calgary, Alberta. Additionally, hysteresis is considered in the soil-water characteristic curve (SWCC) by also considering air entrapment. The following sections provide a description of the Finite Element Model (FEM) employed in this study.

3.6.1 Model Details

The model consisted of a 3-meter-deep soil column consistent with the recommendation by Bashir and Pastora Chevez (2018). For all simulations, an atmospheric BC with surface runoff was applied to the top of the column. At the upper boundary, an atmospheric BC was implemented, which included surface runoff generation when the ponding height reached 10 mm. At the bottom of the column, a zero-gradient water flow BC was established to simulate free drainage, which is indicative of deep groundwater table conditions as described by Šimůnek et al. (2013).

For this study, two regions in Alberta, Canada, were selected based on their distinct climatic conditions: Bighorn Dam and Calgary. Bashir and Pastora Chevez (2018) had previously compiled nine years of daily climate records (2006-2014) for these regions, including maximum, minimum, and mean temperature, relative humidity, wind speed, net radiation, and precipitation. The data were obtained from Environment Canada (2017) and were utilized in the current land

climate interaction (LCI) analyses. Bighorn Dam represents the wetter climatic condition in Alberta, with an average annual precipitation of 409 mm and potential evaporation of 589 mm. Based on the Thornthwaite climate classification system (Thornthwaite 1948, Thornthwaite and Hare 1955), Bighorn Dam can be characterized as having a dry sub-humid climate, as depicted in Figure 3.2, with an average moisture index of -28. On the other hand, Calgary represents one of the drier climatic conditions in Alberta, with an average annual precipitation of 320 mm and potential evaporation of 981 mm. Calgary can be characterized as having an arid climate, as shown in Figure 3.2, with an average moisture index of -67.

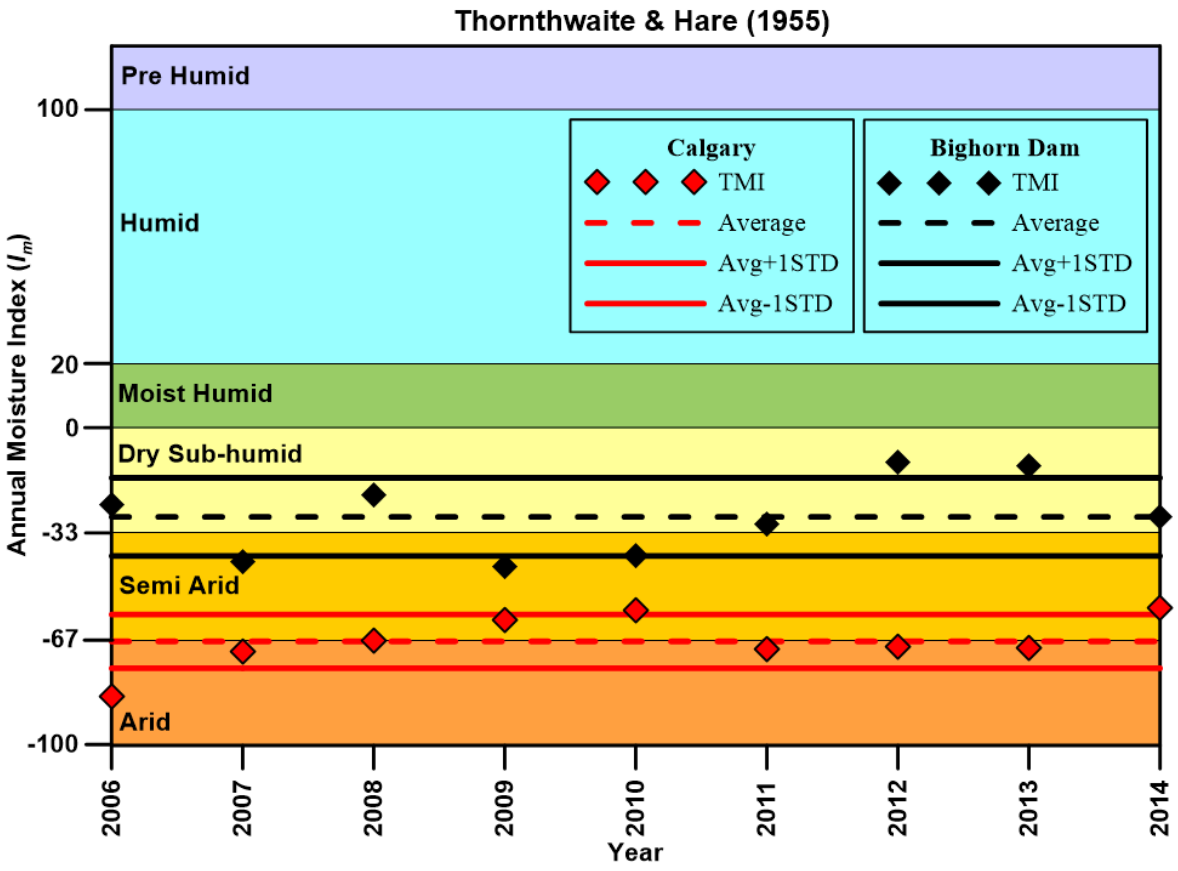

Figure 3.2 Nine years climate classification of Bighorn Dam and Calgary, Alberta, Canada, using annual Thornthwaite Moisture Index (TMI)

To streamline the modeling process and reduce computational time, the simulations were conducted solely for the active period, which corresponds to the period when the soil is in thawed conditions, as suggested by Fredlund et al. (2012) and has been used in many different studies (Bashir et al. 2015, 2020, 2022, Bashir and Pastora Chevez 2018, Pk et al. 2021, Guram and Bashir 2023). This approach is aimed at avoiding redundant computations and focus on the relevant timeframe for the analysis. The active period for each region was determined through a comprehensive statistical analysis of the daily records of maximum, minimum, and average temperatures over the course of the nine-year period. With respect to the accumulated precipitation during the inactive period in the form of snow, 50% of the melted snow was distributed over the initial 14 days of the active period. The remaining 50% was considered runoff, following a similar approach adopted by Baninajarian (2020).

For this study, to compare different textural soils, sand and clay soils were considered. The soil hydraulic properties of these selected soil types were obtained from the soil catalog available in Hydrus-1D. The soil catalog available in the Hydrus software provides a collection of soil hydraulic properties for various soil types which are approximately averages for the different USDA soil textural classes. The soil catalog is derived from extensive research and data compilation. It incorporates information from numerous sources, including field measurements, laboratory experiments, and published studies on soil properties. For this study, the parameters describing the main drying curve (DC) of the soil were obtained from the soil catalog. The soil catalogue within Hydrus provides the soil hydraulic properties in terms of the relevant (van Genuchten 1980) parameters. The van Genuchten function (1980) for SWCC is as follows:

$$S_e = \frac{1}{[1+(|\alpha\psi|^n)]^m} \quad \text{[Eq. 3.1]}$$

$$S_e = \frac{(\theta - \theta_r)}{(\theta_s - \theta_r)} \quad \text{[Eq. 3.2]}$$

where θ_r is the residual volumetric water content [$L^3\ L^{-3}$], θ_s is the saturated volumetric water content [$L^3\ L^{-3}$], S_e is the effective degree of saturation [$L^3\ L^{-3}$], α is the fitting parameter related to the inverse of air entry value (AEV) [$1/(M\ L^{-1}\ T^{-2})$], n is the fitting parameter related to the pore-size distribution [-], and m is the empirical fitting parameter [-]. Using the assumption that $m = 1 - 1/n$, van Genuchten (1980) formulated the following equation for the unsaturated hydraulic conductivity function:

$$k = k_s S_e^{\ l} \left[1 - \left(1 - S_e^{\frac{1}{m}}\right)^m\right]^2 \quad \text{[Eq. 3.3]}$$

where k is the hydraulic conductivity [$L\ T^{-1}$], k_s is the saturated hydraulic conductivity [$L\ T^{-1}$]; and l is the pore interaction t parameter, which can be assumed to be equal to 0.5 [-] for a wide range of soils.

To ensure a fair comparison, all hysteretic and nonhysteretic simulations were initialized with a similar water content condition. For the clay simulations, the water content at field capacity was obtained from the drying curve (DC) and applied consistently to all nonhysteretic and hysteretic simulations. In the case of sand simulations, a dry condition was specified as the initial water content.

For the salt transport simulations, a non-reactive and conservative solute input source was positioned between depths of 1.0 m and 1.5 m, with a relative concentration of 1.0 [consistent

with Bashir and Pastora Chevez (2018)]. A concentration flux BC was assigned to the top boundary, while a zero-concentration gradient was set at the bottom boundary. The dispersivity of salt was defined as 128 mm, as indicated by Bashir and Pastora Chevez (2018).

Hysteresis models have been extensively studied to mathematically describe the hysteretic effects on the SWCC and HCF. These models can be categorized into theoretical and empirical models, with the main focus being on describing the scanning curves based on the main boundary curves of the hysteresis loop. Earlier studies have documented theoretical models such as the domain theory of capillary hysteresis (Topp 1971, Mualem 1974, 1984), which are complex and somewhat difficult to implement in numerical models.

Empirically-based models provide a simplified approach to capture hysteresis effects and have gained widespread acceptance among engineers studying the hysteresis phenomena. These models operate on the assumption that the scanning curve in the θ-ψ-k relationship can be predicted by scaling the main boundary curves of the hysteresis loop. Kool and Parker (1987) emphasized that, for modeling hysteretic flow using empirically-based models, knowledge of at least the main drying curve, main wetting curve, and hydraulic conductivity function of the porous medium is required. Several empirical hysteresis models, based on the scaling method, have been proposed and have been used in various hysteresis studies (Scott et al. 1983, Jaynes 1984, Kool and Parker 1987, Parker and Lenhard 1987, Lenhard et al. 1991).

In this study, the model proposed by Parker and Lenhard (1987), is employed. This model suggests that the wetting and drying scanning curves of the SWCC can be derived by scaling the corresponding main curves defined by the van Genuchten (1980) equation as described above. Specifically, the residual water content and coefficient "n" of these two curves are identical

($\theta_r = \theta_r^d = \theta_r^w; n = n_d = n_w$). The disparity between the drying and wetting curves lies solely in the values of the saturated volumetric water content (θ_s^d being higher than θ_s^w) and the coefficient "α" (α^d being smaller than α^w). In contrast to other scaling-based models (Scott et al. 1983, Kool and Parker 1987), the model by Parker and Lenhard (1987) effectively avoids the artificial pumping error, which refers to the failure to close the scanning loops in simulated cyclic paths. This error is considered an abnormality rather than a characteristic of the soil (Werner and Lockington 2006). The model by Parker and Lenhard (1987) achieves this by remembering reversal points observed during the soil's wetting and drying cycles. By remembering all the reversal points for various cycles, the model enables the drawing of closed scanning loops. According to this model the wetting scanning according can be described as:

$$S(\psi) = \frac{[S_e^w(\psi) - S_e^w({}^{\Delta}\psi^{wd})]({}^{\Delta}S_e^{dw} - {}^{\Delta}S_e^{wd})}{S_e^w({}^{\Delta}\psi^{dw}) - S_e^w({}^{\Delta}\psi^{wd})} + {}^{\Delta}S_e^{wd} \qquad \text{[Eq. 3.4]}$$

where S_e is the effective saturation (estimated using Eq. [3.1] and Eq. [3.2]), and wd term describes the reversal from wetting to drying curve, also; vice versa is true for drying to wetting denoted by dw. The superscript, Δ, describes the target reversal point. In addition, drying scanning curve can be described as:

$$S(\psi) = \frac{[S_e^d(\psi) - S_e^d({}^{\Delta}\psi^{dw})]({}^{\Delta}S_e^{wd} - {}^{\Delta}S_e^{dw})}{S_e^d({}^{\Delta}\psi^{wd}) - S_e^d({}^{\Delta}\psi^{dw})} + {}^{\Delta}S_e^{dw} \qquad \text{[Eq. 3.5]}$$

The model by Parker and Lenhard (1987) is implemented in HYDRUS-1D Šimůnek et al. (2013) as mentioned earlier is used in this research. It should be noted that this model is also capable of accounting for air entrapment in SWCC using the approach described by Land (1968). In this

approach it is assumed that as the wetting/scanning path progresses from a reversal point Δ towards zero suction, there is a constant difference *R* in the reciprocal of the change in volumetric water contents between the initial and final states. Mathematically it can be expressed as following:

$$\mathrm{R} = \frac{1}{\theta_S^d - \theta_{s\Delta}} - \frac{1}{\theta_S^d - \theta_\Delta} = \frac{\theta_S^w - \theta_r}{\left(\theta_S^d - \theta_S^w\right)\left(\theta_S^d - \theta_r\right)}$$

where, the water content at the reversal point Δ is denoted as θ_Δ and $\theta_{s\Delta}$ represents the water content reached when the suction is zero, starting from Δ. The lowest value that $\theta_{s\Delta}$ can have is θ_S^w which is obtained by assuming θ_Δ is equal to θ_r.

It should be noted that for the unsaturated hydraulic conductivity function (HCF), the model by Parker and Lenhard (1987) uses the Mualem–van Genuchten equation (Eq. [3.3]). The HCF function implemented in Hydrus is not intrinsically hysteretic, however, due to varying water contents at equivalent pressure heads in the wetting and drying states the hydraulic conductivity values are equal for the same water content but different for distinct pressure heads. Therefore, the HCF, becomes implicitly hysteretic. An addition to this, Lenhard and Parker's (1987) model is implemented to account for the increase in the hydraulic conductivity upon entrapment of air.

The hysteretic SWCCs for the sand and clay are shown in Figure 3.3 and Figure 3.4. As mentioned previously the parameters for the van Genuchten (1980) function for these two soil types were taken from the soil catalogue in Hydrus 1d. For each soil type three different hysteretic SWCC were considered. The first set of SWCC corresponds to zero air entrapment. The second and third set of SWCC correspond to hysteretic SWCCs, with air entrapment values of 12 and 23% for sand and 13 and 26% for clay. The values of air entrapment for sand and clay

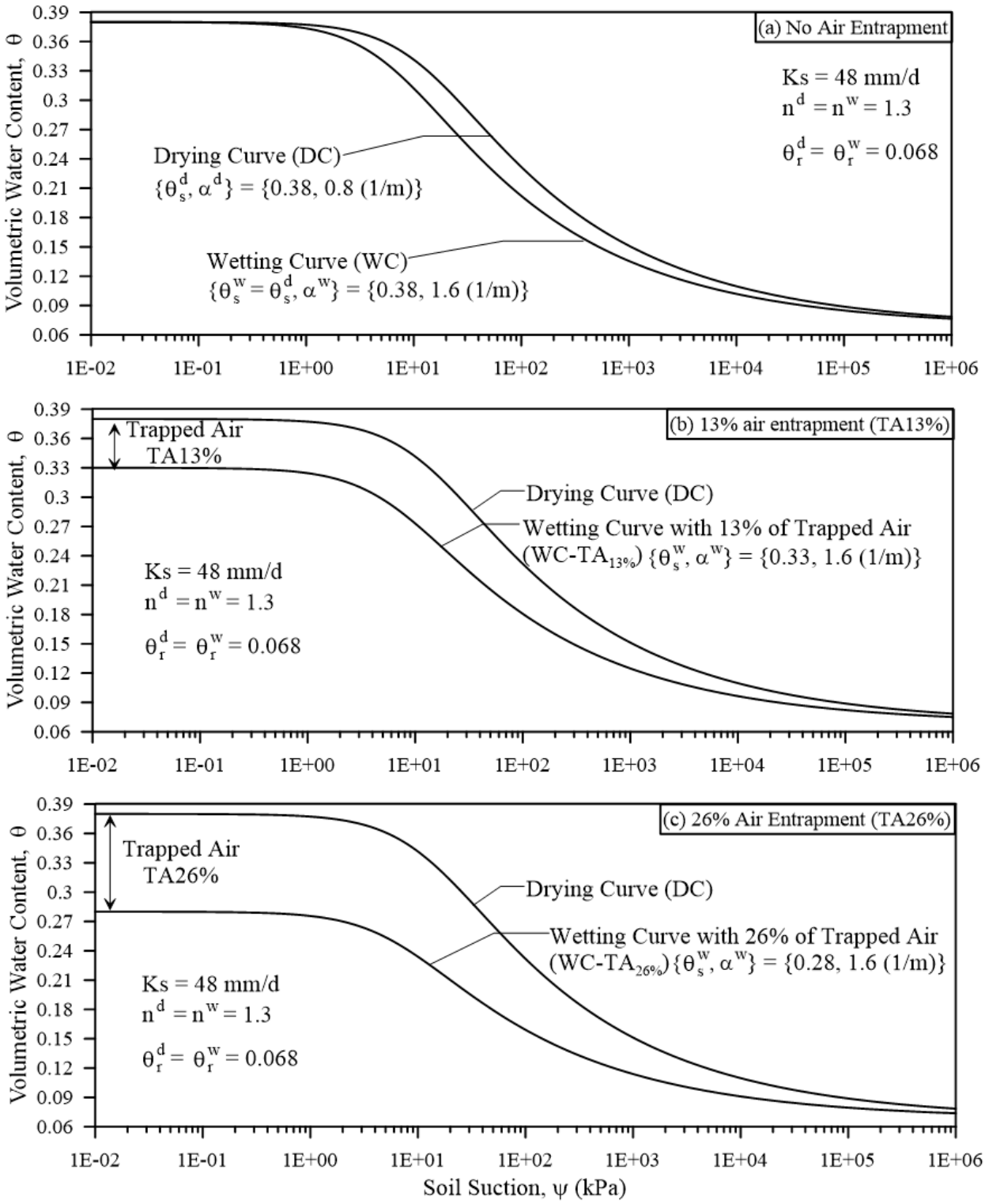

Figure 3.3 Soil water characteristic curve's hysteresis envelope for clay with three degrees of air entrapment: (a) no air entrapment, (b) 13% air entrapment, and (c) 26% air entrapment

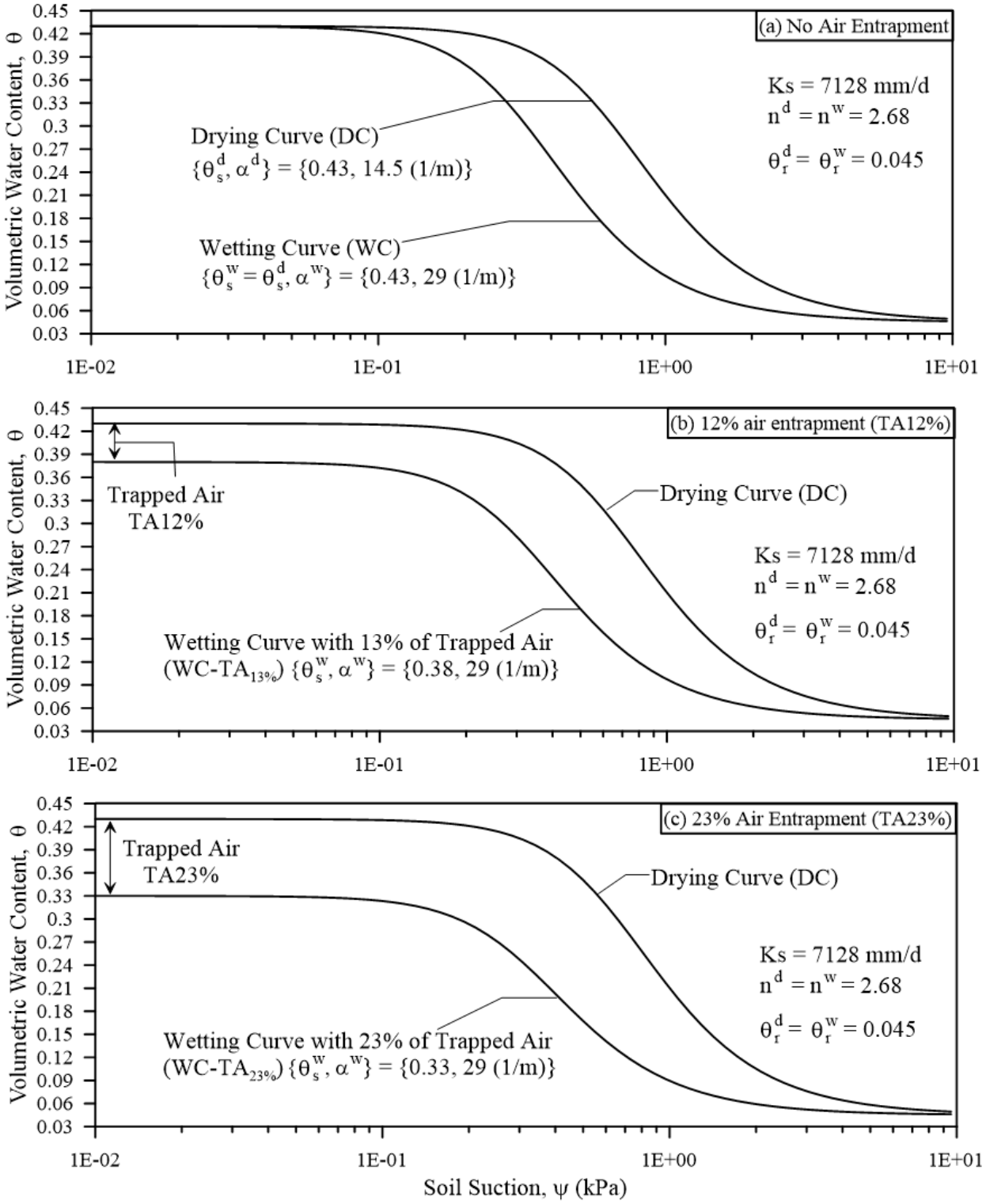

Figure 3.4 Soil water characteristic curve's hysteresis envelope for sand with three degrees of air entrapment: (a) no air entrapment, (b) 12% air entrapment, and (c) 23% air entrapment

are within the range of values reported by Lu et al. (2013) and Likos et al. (2014). For each soil, seven set of simulations were carried out for each climate type: three hysteretic (HC, HC-$TA_{13\%}$, HC-$TA_{26\%}$), one nonhysteretic drying curve (DC), and three nonhysteretic wetting curves (WC, WC-$TA_{13\%}$, WC-$TA_{26\%}$). The notation TA refers to trapped air. Multiple simulations are conducted in this study for a specific reason. It has been observed that many previous studies often compare hysteretic simulation results with either the primary drying curve or the primary wetting curve. However, in this study, the hysteretic simulation results, incorporating different levels of air entrapment, are compared with nonhysteretic simulations using both the primary drying and wetting curves. Furthermore, the hysteretic simulation results are also compared with nonhysteretic simulations utilizing the wetting curves, which reflect reduced complete saturation due to the air entrapment.

3.7 Results and Discussion

The subsequent sections present the outcomes of Land-Climate Interaction (LCI) assessments conducted on the clay domain. These assessments utilized climatic data records from Bighorn Dam (dry-sub humid) and Calgary (arid). The results for sand simulations are not presented nor discussed in this chapter, as the sand simulations demonstrated minimal differences between the hysteretic and nonhysteretic cases. The minimal hysteretic effect in sand is attributed to its coarser texture associated with the narrow SWCC or high n value (i.e., low water retention properties) as well as high hydraulic conductivity. Nevertheless, the figures of the sand results, akin to those presented for clay hereafter, are provided in Appendix A.

In this chapter, the water flow results for clay are first presented which include the water balance at the surface, bottom flux of the domain, and change in soils storage. Then, salt transport results

are presented in the form of the salt concentration distribution within the domain as a function of time; additionally, the differences are further quantified by showing the temporal distribution of the center of the salt mass. For both water flow and salt transport, the results are compared between the hysteretic and nonhysteretic simulations, while also highlighting the impact of different climates on the flow and transport mechanisms.

The accuracy of the numerical modelling results was verified by assuring the water flow and solute transport simulations achieved a relative mass balance error of less than 1%. The effectiveness of the hysteresis algorithm was verified by plotting the paired data points of water content, suction, and hydraulic conductivity on the respective SWCC and HCF. This visualization demonstrates a satisfactory performance of the hysteresis algorithm in H1D. Figure 3.5-Figure 3.7 illustrates the water content-suction, hydraulic conductivity-suction, and hydraulic conductivity-water content data pairs obtained from nodes across the entire domain (0 m, 0.01 m, 0.02 m, 0.03 m, 0.1 m, 0.3 m, 0.5 m, 1.0 m, 1.5 m, and 3.0 m) in the HC (hysteresis), DC (drying curve), and WC (wetting curve) simulations from Bighorn Dam and for clay soil. Figure 3.5, Figure 3.6, and Figure 3.7 exhibit 0%, 13%, and 26% degree of air entrapment, respectively. These data points are superimposed on the hysteretic SWCC specific to this soil. Examining Figure 3.5-Figure 3.7, it is evident that the paired data points from the DC simulation align with the drying branch of the SWCC (MDC), while those from the WC simulation correspond to the wetting branch of the SWCC (MWC). As for the HC simulation, the paired data points can fall on the MDC, MWC, or scanning curves, depending on the soil's drying and wetting history. Furthermore, the figures also reveal that the Hydrus-1D model generates scanning curves as the soil undergoes drying and wetting cycles in response to infiltration and evaporation-drainage events.

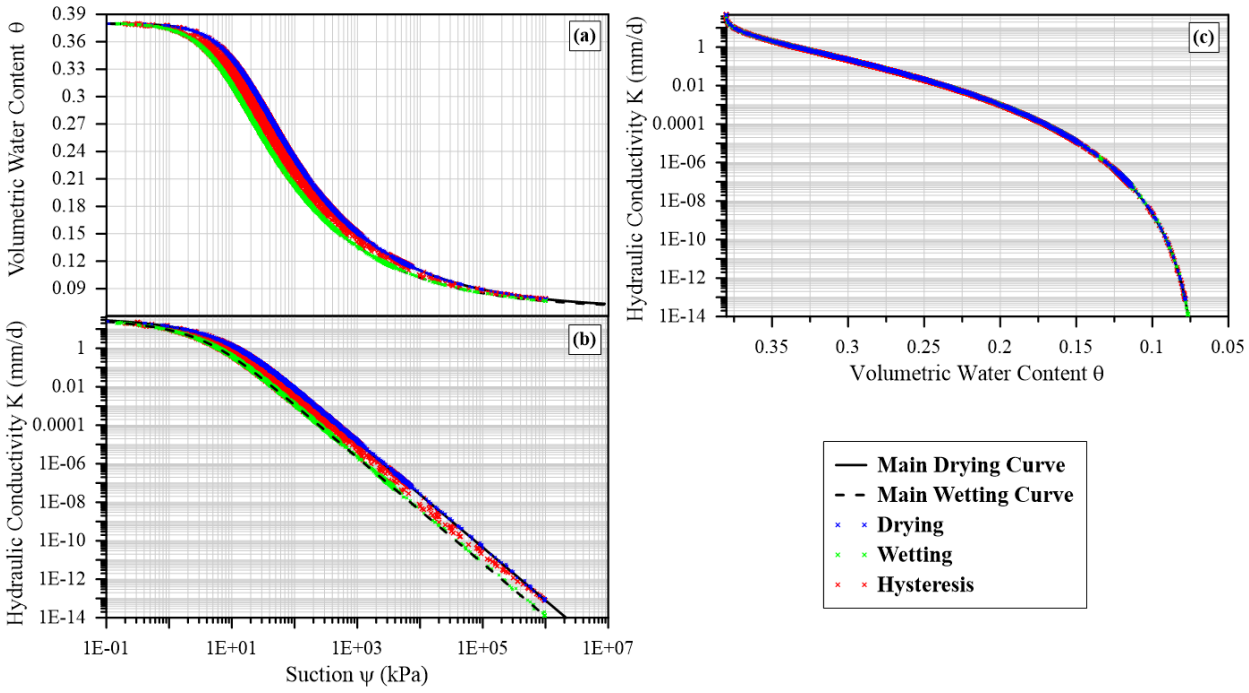

Figure 3.5 Clay's soil water characteristic curve and unsaturated hydraulic conductivity function used in simulations (data from Hydrus 1D simulations): with 0% air entrapment – Bighorn Dam

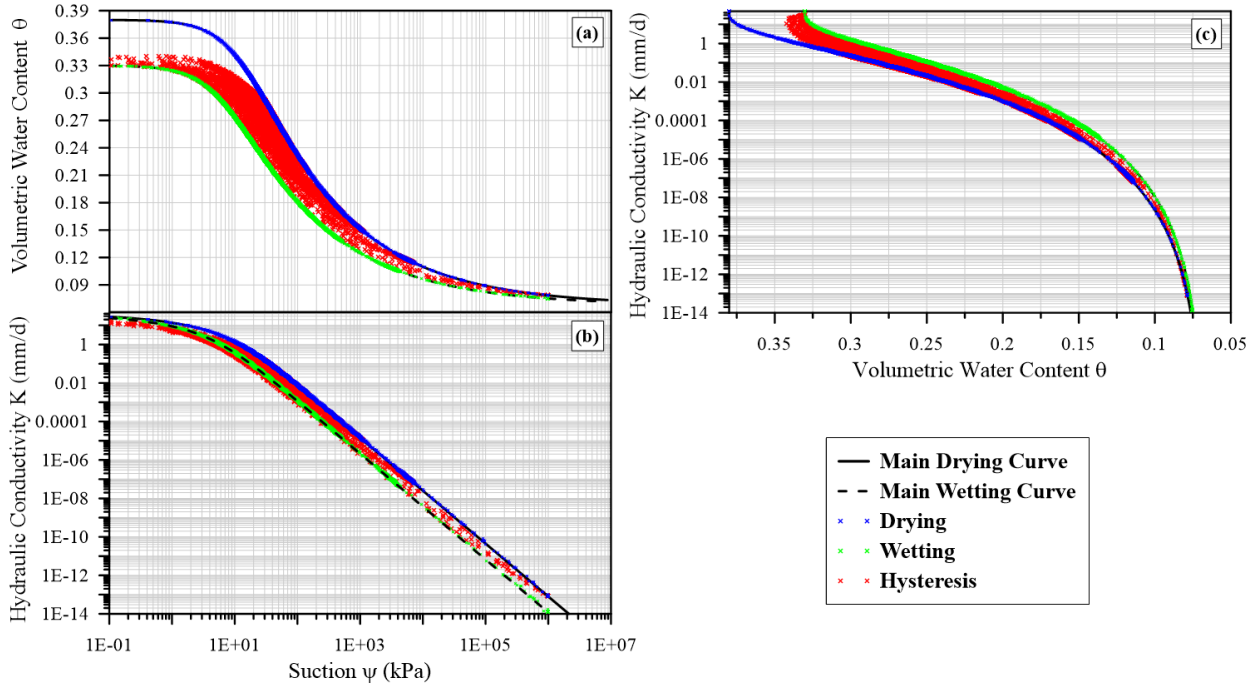

Figure 3.6 Clay's soil water characteristic curve and unsaturated hydraulic conductivity function used in simulations (data from Hydrus 1D simulations): with 13% air entrapment – Bighorn Dam

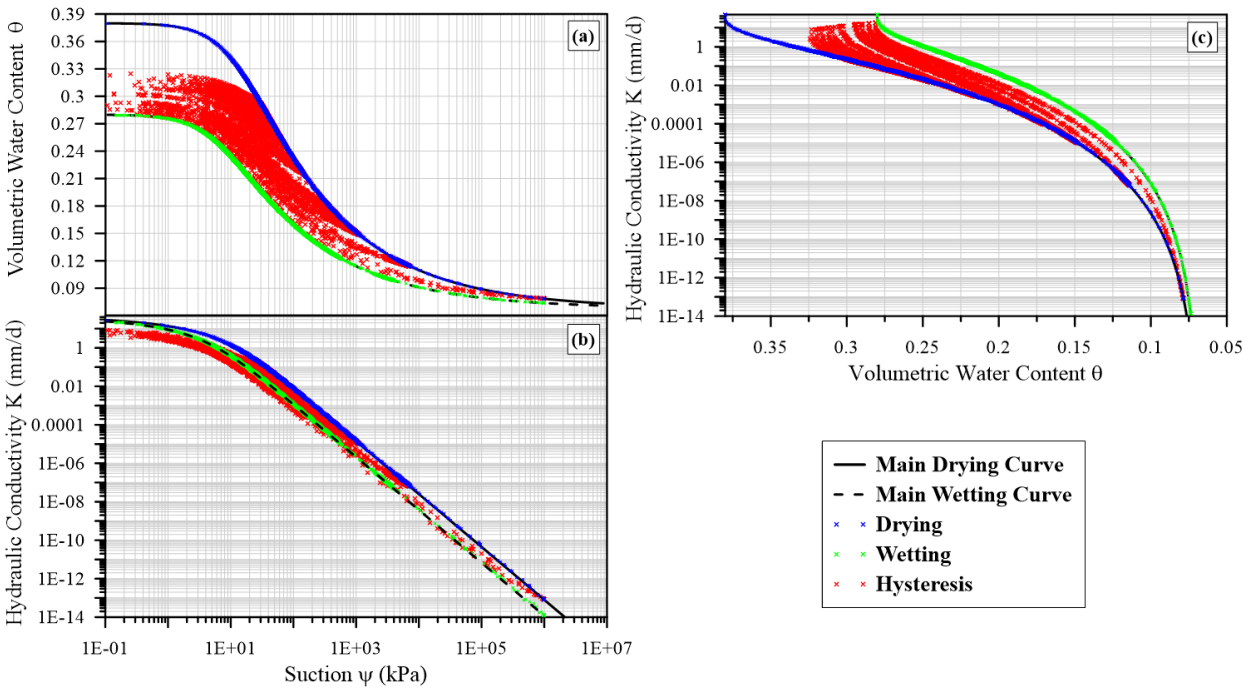

Figure 3.7 Clay's soil water characteristic curve and unsaturated hydraulic conductivity function used in simulations (data from Hydrus 1D simulations): with 26% air entrapment – Bighorn Dam

Hysteretic simulations with air entrapment (i.e., HC-TA$_{13\%}$ and HC-TA$_{26\%}$) estimated various θ values at a given suction during full saturation (i.e., zero suction to AEV), as shown in the SWCC and HCF(θ) figures. This is attributed to the entrapment of air upon rewetting, where the entrapment volume varied depending upon the path, order of the scanning curve, the history of the reversal points, and maximum degree of air entrapment (i.e., 13% or 26%). Another observation is that when simulating higher degree of air entrapment (e.g., HC-TA$_{26\%}$ as opposed to HC-TA$_{13\%}$ or HC) larger volumes air entrapment was estimated, which in return translated to lower water content. For instance, at nearly zero suction, HC simulation estimated instances of θ = 0.38, which is equivalent to the porosity value. Whereas the water content values decreased when simulating HC-TA$_{13\%}$ (θ = 0.33 - 0.34) and even lower for HC-TA$_{26\%}$ (θ = 0.28 - 0.33). In

other words, HC-$TA_{26\%}$, data points are found closer to the main wetting branch, as opposed to HC-$TA_{13\%}$ and HC where SWCC data points were found closer to DC. This means that simulating hysteretic SWCC with large degree of air entrapment (e.g., HC-$TA_{26\%}$) can more readily form wetting scanning curve leading to low water retention properties and enhancement of the downward water flow.

As mentioned previously, Hydrus 1D does not intrinsically integrate hysteresis in the HCF; however, HCF indirectly become hysteretic due to its correlation with the hysteretic SWCC, this is shown in (b) and (c) of Figure 3.5-Figure 3.7. A special case when entrapment of air is considered for which Lenhard and Parker's (1987) model is integrated. In Figure 3.5-Figure 3.7, the HCF(θ) was observed to be highly hysteretic when considering air entrapment, especially for larger air entrapment volume. It is observed that entrapment of air has led to larger hydraulic conductivity values. This is because Lenhard and Parker (1987) modified the predictive model for HCF. It is based on Parker and Lenhard's (1987) model in combination with Mualem's (1976) pore distribution model corrected to include the effect of entrapment, similar to Land's (1968) approach. Regarding Lenhard and Parker's (1987) predictive model, Parker and Lenhard (1987) explained that entrapment of nonwetting fluid (e.g., entrapment of air) obstruct the movement of the wetting fluid (i.e., water) resulting to displace the wetting fluid into larger pores, thus decreasing the flow impedance and increasing the hydraulic conductivity. Parker and Lenhard (1987) stated that the experimental investigations shown during wetting/rewetting, the wetting hydraulic conductivity were typically larger than drying hydraulic conductivity for the same actual saturation. This investigation is indicative of air entrapment increasing the hydraulic conductivity, hence justifying the correction to Mualem's model. In another observation, the HCF(θ) is nonhysteretic for HC simulations; on the other, HCF(ψ) was found to be hysteretic.

3.7.1 Water Flow Results

Figure 3.8 and Figure 3.9 illustrate the water balance at the clay's surface, showing the temporal progression of cumulative net infiltration or *NI* (where *NI* = Precipitation – Actual Evaporation - Runoff) and actual evaporation (*AE*) under two different climates: Bighorn Dam and Calgary, respectively. Cumulative bottom fluxes (*BF*) are also plotted, representing water exiting the system through the bottom boundary. When comparing hysteretic (HC) and nonhysteretic (drying curve, DC, and wetting curve, WC) simulations, the general trend of deviations is somewhat similar for both climates. However, when varying the degree of air entrapment in the hysteretic cases, the deviations are more noticeable, depending also on the simulated climate. Firstly, the general trend of hysteresis and air entrapment, in terms of atmospheric fluxes, is discussed, then the impact of climate type on the results is discussed.

For both climates, hysteretic simulations without air entrapment (HC) estimated slightly lower *AE* compared to drying curve simulations (DC) and higher *AE* than wetting curve simulations (WC). As a result, HC simulations showed slightly higher estimates of *NI* than DC and lower *NI* than WC (as shown in Figure 3.8 and Figure 3.9). To explain this, DC's SWCC is characterized by a higher air entry value (i.e., higher water retention properties) than WC, with α^w being 2 times α^d. Mitchell and Mayer (1998) explained that upon drainage, the SWCC of DC exhibits small changes in volumetric water content for a relatively larger change in suction compared to WC. This results in lower downward water flow and higher moisture retention in the pores near the surface. Consequently, in DC simulation, more moisture is held at surface and readily available for evaporation than WC simulation, leading to higher estimates of *AE* and lower *NI* values. On the other hand, when considering the SWCC properties of the WC, the pores exhibit lower water retention properties, resulting in more rapid flow and lower moisture retention near

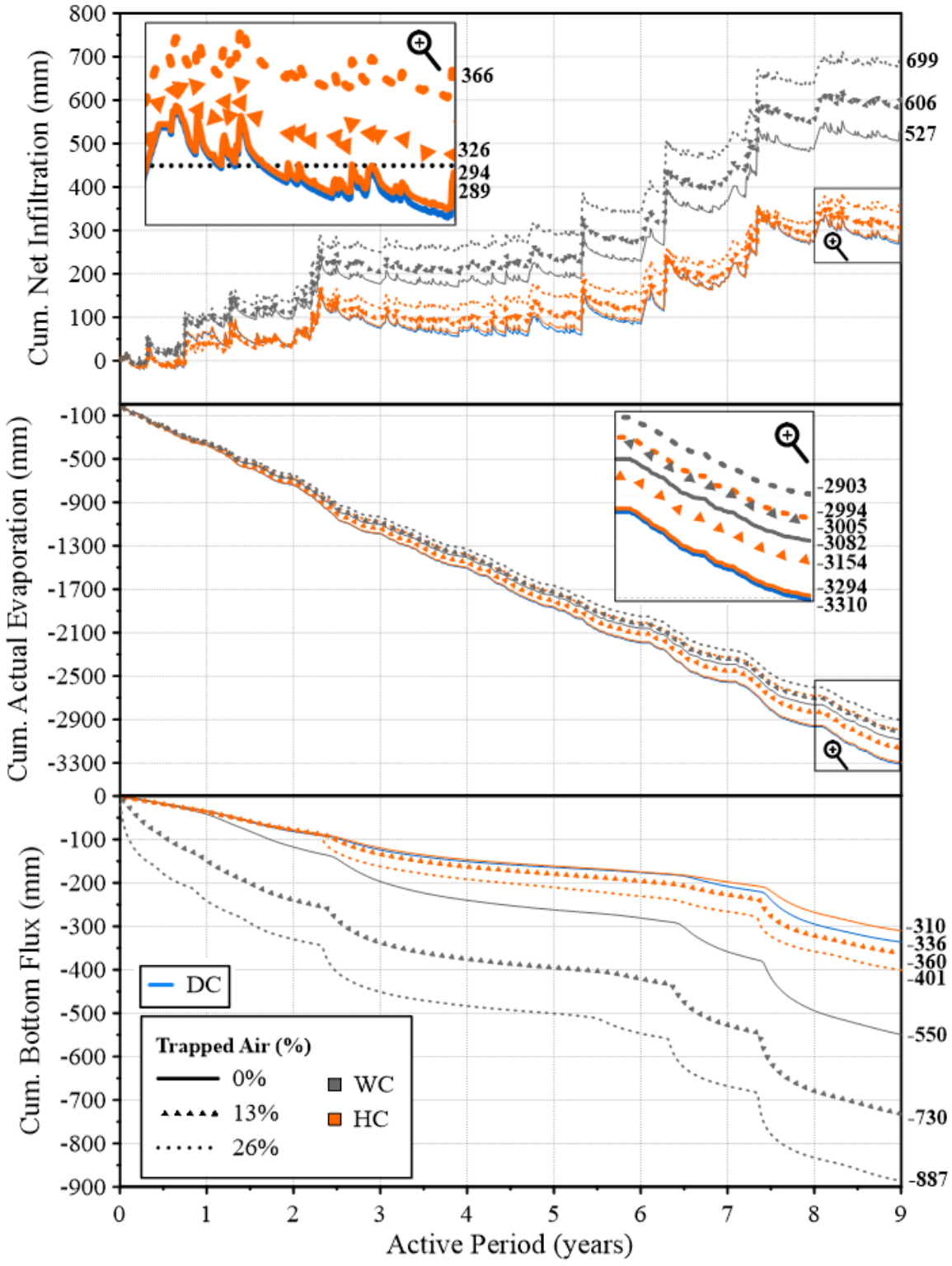

Figure 3.8 Water balance at the clay domain showing temporal distribution of cumulative fluxes: net infiltration (NI), actual evaporation (AE), and bottom flux, under Bighorn Dam climate.

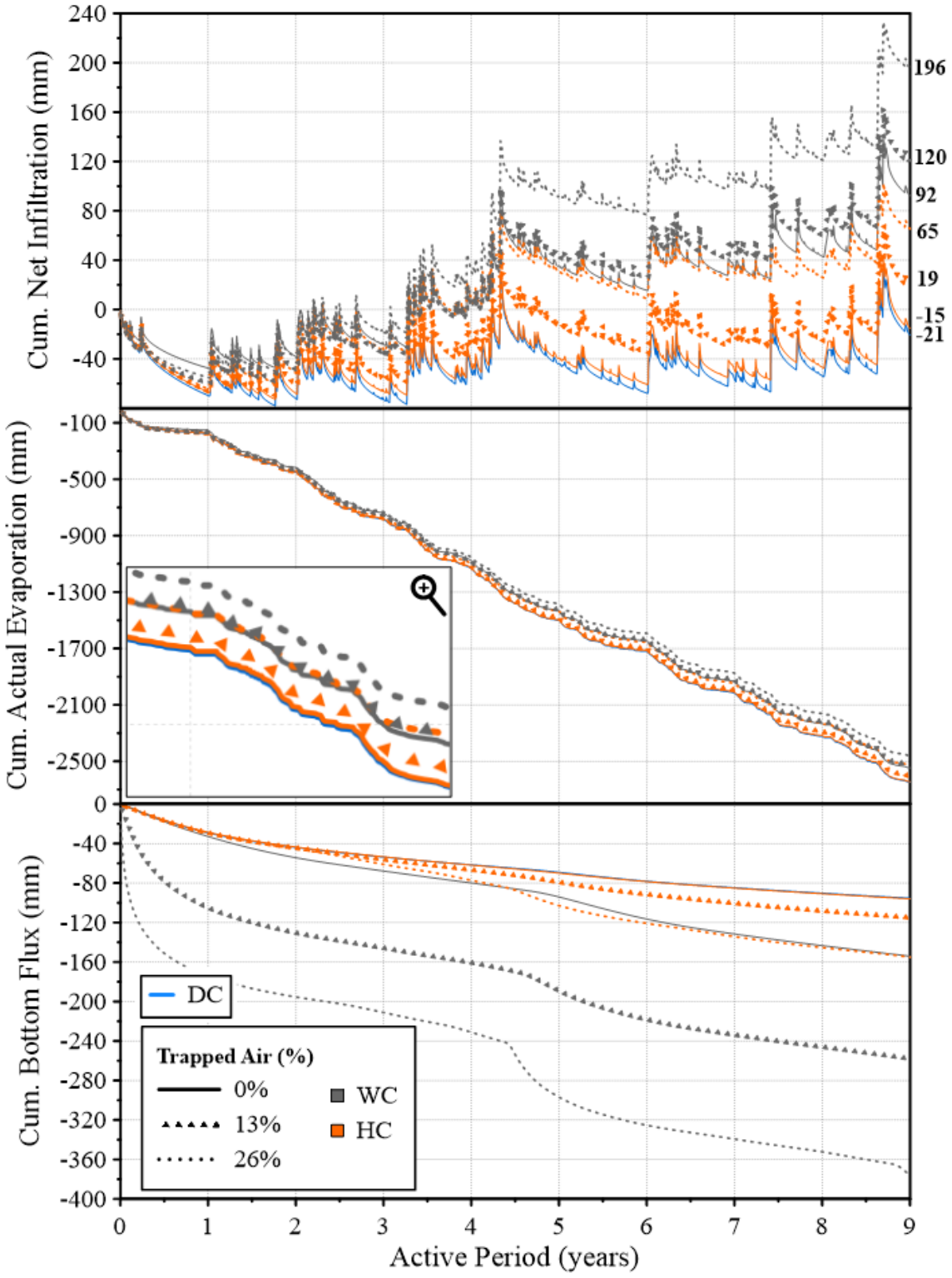

Figure 3.9 Water balance at the clay domain showing temporal distribution of cumulative fluxes: net infiltration (NI), actual evaporation (AE), and bottom flux, under Calgary climate.

the surface (i.e., lower *AE* and higher *NI*). Simulating HC tends to reduce the effect of WC and DC as the system forms scanning drying and wetting curves during drying and rewetting events (e.g., Figure 3.5-Figure 3.7). As a result, HC simulation shows higher estimates of *AE* (lower *NI*) than WC simulation and slightly lower *AE* (slightly higher *NI*) than DC simulation (as shown in Figure 3.8 and Figure 3.9).

Figure 3.8 and Figure 3.9 also show that including air entrapment in hysteretic simulations (HC-$TA_{13\%}$ and HC-$TA_{26\%}$) results in significantly lower *AE* and higher *NI* compared to HC simulations without air entrapment. Moreover, there is a clear correlation between the degree of air entrapment and the extent of this effect; HC-$TA_{26\%}$ simulation estimated higher *NI* than HC-$TA_{13\%}$ simulation. The introduction of air entrapment widens the hysteresis envelope, increasing the frequency and magnitude of wetting scanning curves. This evident in Figure 3.7 (as opposed to Figure 3.5 and Figure 3.6) in which the scanning curves formed from HC-$TA_{26\%}$ simulation covers larger area within the hysteresis loop and is closer to WC-$TA_{26\%}$ branch. In addition, those scanning curves that are closer to the WC-$TA_{26\%}$ became characterized with lower water retention properties, since greater water content change is required to achieve the same change in soil suction for WC-$TA_{26\%}$ compared to WC-$TA_{13\%}$ and WC, creating higher pressure gradient for WC-$TA_{26\%}$. In other words, larger magnitude of downward water flow according to Darcy's law, leading to lower moisture retention near the surface (hence lower *AE* and higher *NI* for HC-$TA_{26\%}$ simulation as opposed to HC-$TA_{13\%}$ and HC). Hence, it was observed that the impact of air entrapment on *AE* and *NI* becomes more significant as the degree of air entrapment increases.

Simulating wetting branches, on the other hand, led to the highest *NI* compared to their corresponding hysteretic simulations. This is particularly true when porosity values were reduced, i.e., simulating the main wetting branch only after air entrapment. As discussed earlier,

the reduction in porosity (i.e., increase in the degree of air entrapment) reduces the water retention properties, accelerating water flow and reducing evaporation, resulting in the highest *NI* values. For example, simulating WC-$TA_{26\%}$ yielded the largest *NI* estimates, followed by WC-$TA_{13\%}$, WC, HC-$TA_{26\%}$, HC-$TA_{13\%}$, HC, and DC simulations, in descending order.

The bottom flux (*BF*) trends show similarities with the *NI* trends discussed above. The exception is for HC simulation under Bighorn Dam, as can be seen in Figure 3.8. In this instance, HC's BF is slightly lower than DC's, which can be attributed to HC generating runoff (Figure 3.10). Comparing hysteretic (with and without air entrapment) relative to nonhysteretic DC simulations, higher deviations in terms of atmospheric fluxes are observed under Calgary's arid climate compared to Bighorn Dam's dry-sub humid climate. To better showcase this quantitively, Table 1 summarizes the difference in terms of total *NI* between the nonhysteretic DC simulation and other simulations. Larger differences amongst the hysteretic simulations (HC, HC-$TA_{13\%}$, and HC-$TA_{26\%}$) are observed under Calgary's climate, which is indicative of the pronounced impact of air entrapment on increasing *NI* in drier climate (i.e., Calgary). For example, after simulating hysteresis with 26% degree of air entrapment, the total *NI* value, relative to DC simulation, increased by 26.6% under Bighorn Dam climate, whereas it considerably increased

Table 1: Difference between total *NI* values for DC and other simulations.

Climate	HC	HC-$TA_{13\%}$	HC-$TA_{26\%}$	WC	WC-$TA_{13\%}$	WC-$TA_{26\%}$
Bighorn Dam	5	37	77	238	317	410
Calgary	6	40	86	113	141	217

by 409.5% under Calgary climate. To explain this behavior, the saturation reversals from-wetting-to-drying become more frequent under more dry conditions (e.g., Calgary) and the soil is found at a drier state. As a result, upon rewetting, the formation of the wetting scanning curves witnesses larger entrapment volumes of air, and as previously explained this reduces the moisture retention near the surface, minimizing the evaporation rates. Thus, higher deviations are observed amongst hysteretic simulation and nonhysteretic DC simulation under drier climate. On the other hand, the saturation reversals from-wetting-to-drying are less frequent under wetter climate (e.g., Bighorn Dam), thus reducing the effect of air entrapment and leading lower deviations. On the other hand, Bighorn Dam from Table 1 showcase larger differences for WC, WC-$TA_{13\%}$, and WC-$TA_{26\%}$, which is attributed to the wetter climatic conditions compared to Calgary. It is imperative to note that the observations from the current research in which drier climate exhibiting higher hysteretic and air entrapment effects, must not to be generalized over other set of climates or other geoclimatic locations. For example, Bashir et al. (2015) reported the importance of including hysteresis irrespective of the climate type, in which they found that for different set of climates varying from very dry (TMI < 0) to wet climates (TMI > 0), hysteresis had influenced *NI*, *AE*, *RO*, and *BF*. From the findings of the current research and research done by Bashir et al. (2015), hysteresis and air entrapment must be included as each climate is unique and can exhibit different hysteretic trends.

Figure 3.10 illustrate the temporal distribution of cumulative runoff (*RO*) for Bighorn Dam and Calgary climates, respectively. The wetter nature and lower evaporative energy in Bighorn Dam's climate resulted in larger values of *RO* at the surface compared to Calgary's climate. For the Bighorn Dam (Figure 3.10a), DC simulation did not generate any *RO*, while HC, WC, WC-$TA_{13\%}$, and WC-$TA_{26\%}$ produced a modest amount of runoff. The finding where hysteretic and

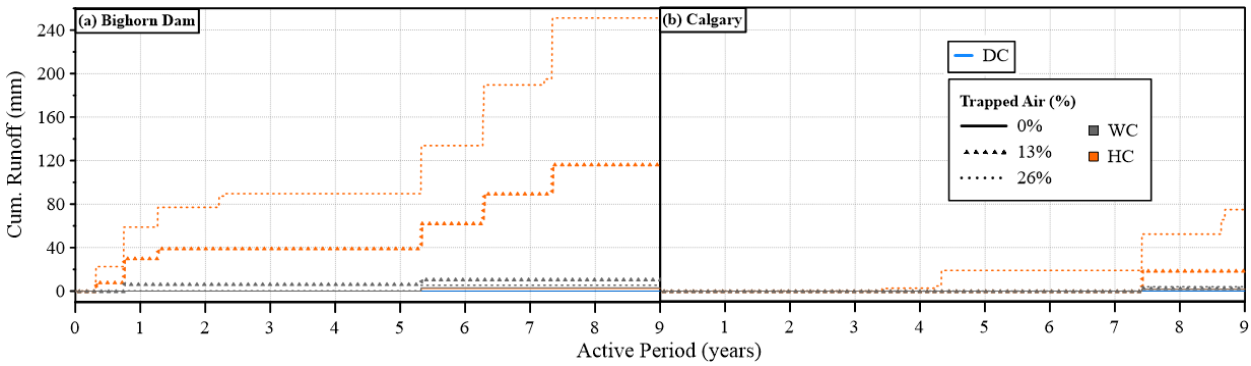

Figure 3.10 Cumulative Runoff (RO) at the surface of the clay under two different climates: (a) Bighorn Dam and (b) Calgary

wetting curve simulations generated *RO* more frequently (regardless of the modest amount) than DC was also explained by Bashir et al. (2016) who reported that simulations (HC and WC) which follows the MWC or scanning wetting curve reach saturation quickly and more frequently thereby triggering runoff when the potential surface flux intensity exceeds the saturated hydraulic conductivity. To add to their findings, the larger *AE* estimated by the DC simulation led to drier soil conditions, thus lowering the chances to generate *RO*.

Another notable observation from Figure 3.10 is the significant increase in runoff after introducing air entrapment in the hysteretic simulations (HC-$TA_{13\%}$ and HC-$TA_{26\%}$), particularly with the largest degree of air entrapment, HC-$TA_{26\%}$, which estimated 251 mm of *RO* compared to HC-$TA_{13\%}$ with 117 mm, as shown in Figure 3.10a. The increased runoff can be explained by the fact that the numerical model predicts surface *RO* when the soil near the ground surface gets saturated (i.e., $\theta = \theta_s$) and the potential surface flux intensity is greater than the saturated hydraulic conductivity of the soil (i.e., (P – PE) > K_s). With air entrapment considered, the surface pores can more readily reach full apparent saturation, meaning that the combined water

saturation and trapped air saturation equal 100%. This saturation can occur even when the measured water content values on the surface are lower than the porosity value (θ_s= 0.38) due to the presence of trapped air. In Figure 3.11, the cumulative *RO*, P-PE, water content, and pressure head for the HC-TA$_{13\%}$ simulation for the Bighorn Dam climate are presented; note that the pressure heads at the negative side were not presented since *RO* did not occur at those events.

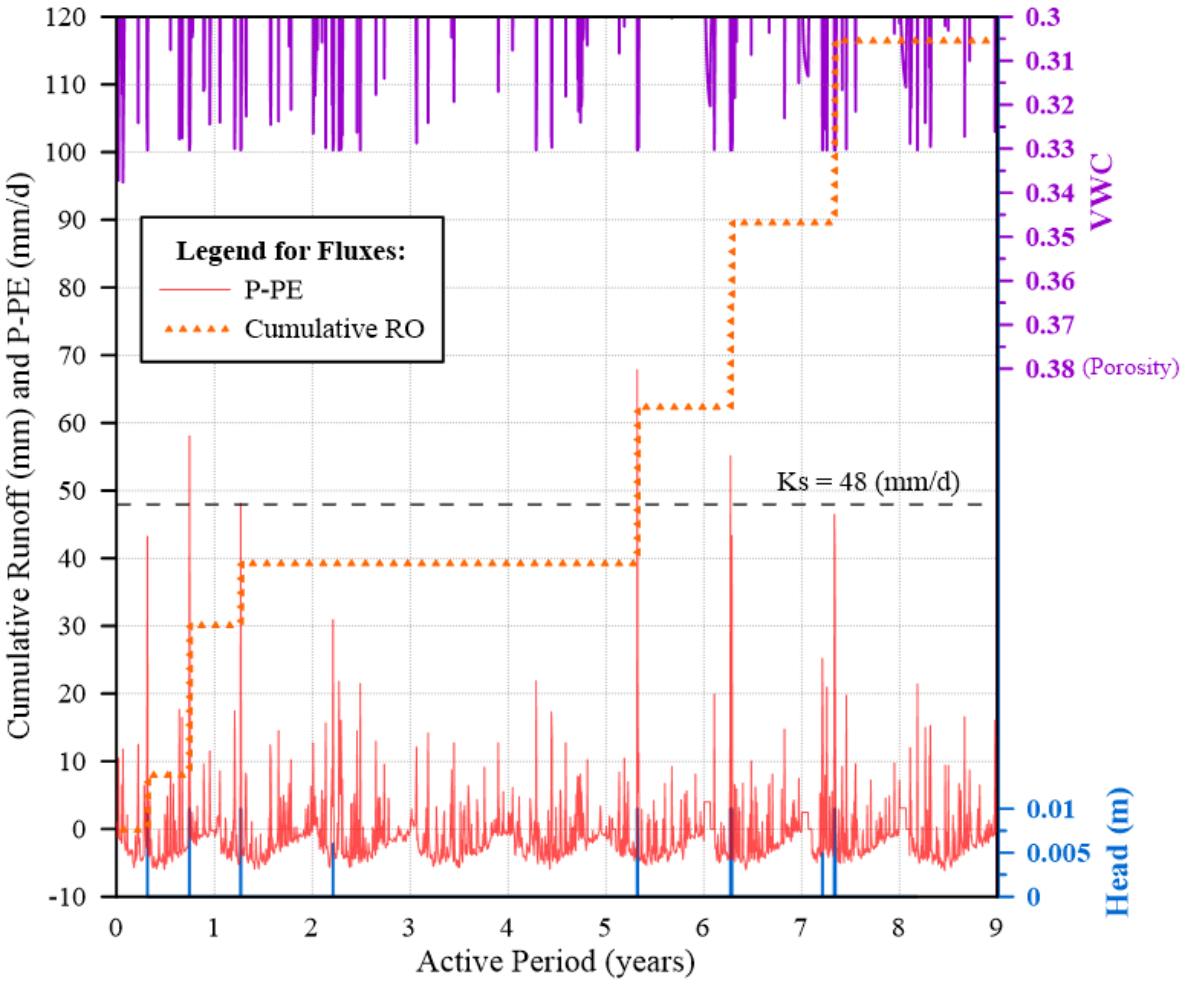

Figure 3.11 Temporal distribution of potential atmospheric flux (P-PE), cumulative runoff (RO), volumetric water content (VWC), at the ground surface for the hysteretic simulation with 13% air entrapment for Bighorn Dam

Figure 3.11 shows that *RO* events occurred at $\theta \sim 0.33$ (i.e., the saturated water content of the wetting branch) which is lower than the porosity ($\theta_s = 0.38$ or the saturated water content of the drying branch). For these events, P-PE exceeded the clay's infiltration capacity also indicated by pressure head ≥ 0 m. In contrast, neglecting air entrapment would overestimate the available pore space, creating the illusion that pores are not at full apparent saturation (of water and the neglected trapped air); thus more space to accept moisture, resulting in no *RO* to be generated for DC and HC as shown in Figure 3.10. The HC-$TA_{13\%}$ and HC-$TA_{26\%}$ simulations exhibited the largest amounts of *RO*, particularly HC-$TA_{26\%}$, due to entrapping larger volumes of air, leading to more frequent full apparent saturation thus higher *RO* fluxes (Figure 3.10) compared to HC-$TA_{13\%}$.

Numerous prior studies investigating the impact of hysteresis on solute transport, such as those conducted by Pickens and Gillham (1980), Jones and Watson (1987), Russo et al. (1989), Mitchell and Mayer (1998), and Gladnyeva and Saifadeen (2012), consistently noted that hysteresis hinders both water flow and solute transport in comparison to nonhysteretic simulations. Additionally, Russo et al. (1989) and Mitchell and Mayer (1998) provided detailed insights, revealing that in hysteretic simulations, the water content tends to be higher near the surface and lower near the bottom when contrasted with nonhysteretic scenarios. However, there are some issues with their findings that may not apply universally. Firstly, they imposed wetting curve characteristics on nonhysteretic simulations without comparing them to DC characteristics. Their analysis, secondly, utilized a simplified atmospheric boundary (except Gladnyeva and Saifadeen (2012) who employed atmospheric boundary) involving repetitive cycles of infiltration and evaporation. This approach, characterized by low evaporative energy, may be deemed unrealistic and unrepresentative of actual climatic scenarios. As an illustration, North Bay,

identified as one of the wettest climates in Ontario, Canada (humid climate), exhibited an annual average (1980-2010) potential evaporation equivalent to 68% of the annual average precipitation. In contrast, Mitchell and Mayer (1998) employed evaporative energy equal to only 5% of the water infiltration value, a notably low figure. This exceptionally low evaporative energy, employed by Mitchell and Mayer (1998), diminishes the impact of drying-wetting cycles and may yield conclusions about hysteretic behavior that might not fully capture the range of climatic conditions, especially in arid climates like Calgary. It underscores the need to consider a broader range of evaporative energy and climatic scenarios to better understand the arising behavior of hydraulic hysteresis under different real climates.

Figure 3.12 displays box whisker plots of water content data points (nodes from the domain) over a 9-year period under Bighorn Dam climate. Figure 3.12a and Figure 3.12b encompasses all nodes in the top 0.05 and 0.5 m of the clay domain respectively, while Figure 3.12c includes all nodes in the bottom 0.5 m. The plots show key features such as maximum, minimum, 25^{th} percentile, 75^{th} percentile, and median water content values. In Figure 3.12, it is evident that the water contents near the surface for DC and HC simulations are lower than those for WC simulations. This finding contradicts the results reported by Mitchell and Mayer (1998), where HC was observed to retain more moisture near the surface compared to WC simulation. In the present study, it is noted that DC and HC simulations initially do retain more moisture near the surface due to their higher retention properties. Nonetheless, the area being characterized as having a dry-sub humid climate, with evaporative energy exceeding the atmospheric water supply (i.e., precipitation) by 160%, which have led to considerable actual evaporation from the clay domain in DC and HC simulations (Figure 3.8). As a consequence, this process results in lower water content near the surface for DC and HC compared to WC simulation. In general, the

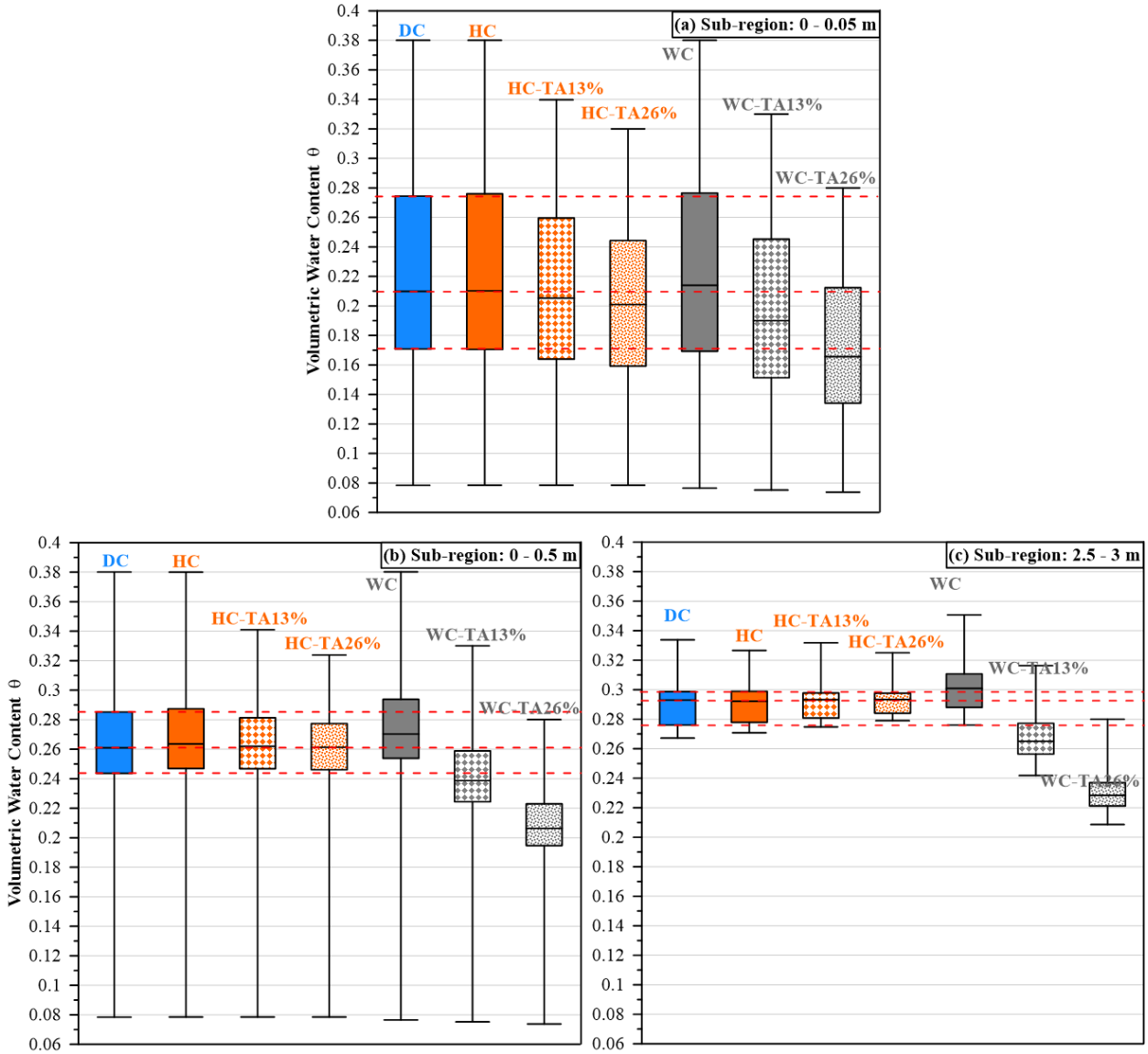

Figure 3.12 Box-whisker plot of volumetric water content from sub-regions within the clay domain: (a) 0-0.05 m, (b) 0-0.5 and (c) 2.5-3 m for Bighorn Dam climate

findings by Mitchell and Mayer (1998) may hold validity but may not apply to all cases, especially for climates with high evaporative energy, as proven in the current study. Furthermore, hysteretic simulations with air entrapment have predicted even lower water content near the surface, attributed to entrapment of air (which takes up more pore space, thus lower

water content) and rapid downward water flow. Conversely, when considering air entrapment in nonhysteretic wetting branch simulations, the water content near the surface becomes lower than their hysteretic counterparts, attributed to the reduced porosity.

3.7.2 Solute Transport Results

In Figure 3.13, the temporal distribution of salt's relative concentration is presented for the Bighorn Dam climate, encompassing various hysteretic and nonhysteretic simulations. It's important to highlight that the results were extend over 18 years rather than 9 years, as the simulations were conducted by sequentially combining two nine-year climate datasets. This approach provides a more comprehensive perspective on atmospheric boundary conditions and the fate of solutes over an extended timeframe. This is consistent with the approach used by Bashir and Pastora Chevez (2018).

During the initial 8 years, salt distribution in DC and HC simulations showed similarity. Both predicted salt discharge (through the bottom boundary) initiation at around 7 years. However, DC simulation exhibited lower concentrations near the bottom compared to HC, for example by year 14, the contour 0.3-0.4 is out of the system for DC simulation whereas HC took additional 2 years. This due to DC's slightly higher estimated *BF* compared to HC (Figure 3.8), which has resulted in increased advective flux of salt exiting the bottom boundary. However, variations between DC and HC simulations occur at low concentration levels after significant salt discharge. Both simulations retained some salt concentrations of 0.025 - 0.3 at the end of the end of the simulation time. On the other hand, simulating WC resulted in a significantly higher downward salt displacement, with salt discharge initiating after 3 years (compared to 7 years in DC and HC simulations). Unlike DC and HC, nearly all salt masses in WC simulation exited the

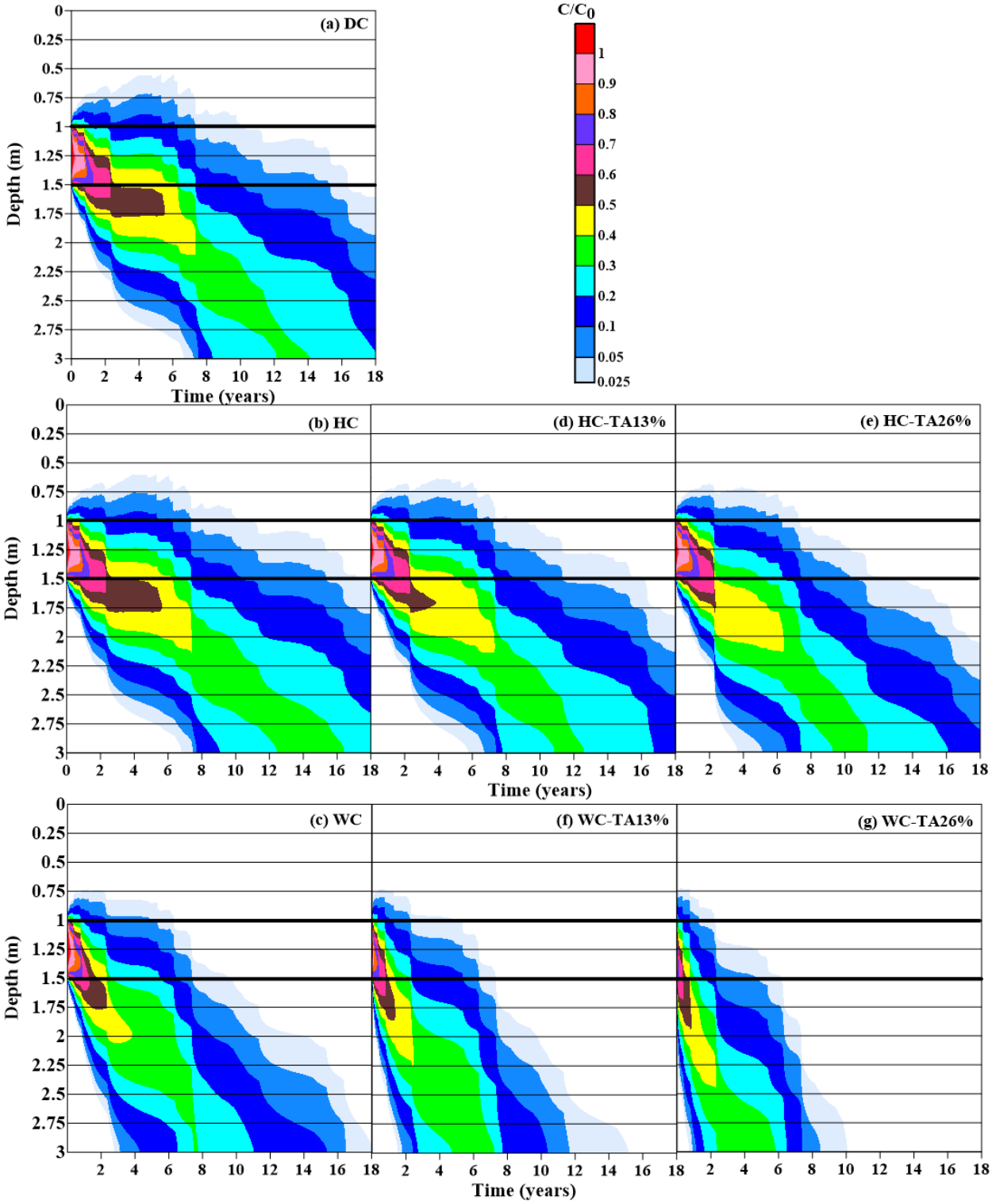

Figure 3.13 Temporal distribution of salt concentrations within the clay profile for Bighorn Dam climate.

system by the end of the 18-year period. Introducing air entrapment in wetting branches (e.g., WC-TA$_{13\%}$ and WC-TA$_{26\%}$) further increased the downward salt transport, with discharge initiation at 2 years for WC-TA$_{13\%}$ and 1.5 years for WC-TA$_{26\%}$. These wetting branch simulations required only 15 and 10 years, respectively, to completely discharge the salt. This increased downward transport was linked to the overestimation of salt advective flux influenced by the increased *NI* according to the water balance in Figure 3.8. This is especially true with higher air entrapment, i.e., WC-TA$_{26\%}$ (largest *NI* and *BF*). Hysteretic simulations with air entrapment (e.g., HC-TA$_{13\%}$ and HC-TA$_{26\%}$) resulted in a more noticeable downward displacement of salt with larger masses exiting the system compared to DC and HC simulations, however relative to WC-TA$_{13\%}$ and WC-TA$_{26\%}$, respectively, the hysteretic simulations with air entrapment have retarded the salt transport. Compared to HC (without air entrapment) and HC-TA$_{13\%}$, greater volumes of trapped air (e.g., HC-TA$_{26\%}$) led to a larger downward displacement of salt and earlier discharge of most salt masses out of the system. The first salt discharge occurred after 5.5 years for HC-TA$_{13\%}$ and 4 years for HC-TA$_{26\%}$, versus 7 years for DC and HC simulations.

After 18 years, a more notable amount of salt mass were discharged out of the system for HC-TA$_{13\%}$ and HC-TA$_{26\%}$ with 0.025-0.2 of relative concentration remaining in the bottom 1.25 m and 1.0 m respectively, compared to DC and HC with 0.025-0.3 remaining in the bottom 1.5 m. Notice how in hysteretic simulations with increasing degree of air entrapment (e.g., HC-TA$_{26\%}$), larger salt mass discharge is observed.

Air entrapment in hysteretic simulations can impact the solute advective flux (i.e., transport of salt) through two key factors: Darcian flux (q) and water content (θ) which are derived from the advective-dispersion equation. Additionally, these terms can be summarized into the pore-

velocity term ($u = q/\theta$) which controls the advective flux of the solute; this term is obtained through dividing the advective-dispersion equation by θ. Firstly, as explained earlier inclusion of air entrapment in HC-TA$_{13\%}$ and HC-TA$_{26\%}$ simulations estimated, by the end of the simulation, *NI* of 326 mm and 366 mm, respectively, which are larger than HC with 294 mm. This, in turn, increased the water flow leading to larger Darcian flux or pore-velocity, thus increasing the advective flux of salt. This trend also correlates to the larger *BF* which led to larger mass of salt exiting the system. In conclusion, increasing the degree of air entrapment in the hysteretic simulations increases the advective flux of the salt triggered by the larger estimated meteoric water entering the surface. Secondly, air entrapment can directly increase the transport processes through the arising reduction of the pore space. Mitchell and Mayer (1998) explained that trapped air reduces available pore space for water flow, leading to an increased water flow and solute downward migration. By referring to the advective-dispersion equation, Mitchell and Mayer (1998) statement holds validity since the decrease in pore-space due to entrapment of air reduces the water content (as previously illustrated in Figure 3.12). This is indicative of larger pore-velocity (through $u = q/\theta$) and larger advective flux which further amplifies the solute movement, complementing the increased meteoric water entering the system.

Regarding the salt's upward movement within the domain, some notable observations can be made. Upward salt movement occurs due to the Bighorn Dam's relatively high evaporative energy (dry sub-humid climate). Higher evaporative energy will result in less *NI*, hence less downward advective flux, this is especially the case for DC simulation (with high *AE*) more than the others. This created low moisture (high suction) in the upper layers (Figure 3.12) creating an upward gradient for water from lower layers to flow upwards. However, hysteresis and air entrapment played a crucial role in curbing the extent of this upward displacement. For instance,

DC predicted the highest upward movement (0.475 m above the source) compared to HC (0.425 m), HC-$TA_{13\%}$ (0.35 m), and HC-$TA_{26\%}$ (0.25 m). The WC, WC-$TA_{13\%}$, and WC-$TA_{26\%}$ simulations estimated an initial upward movement of 0.25 m above the source, but it dropped rapidly after 2 years. The trend of upward salt displacement height is observed to be linked by *NI*, in which hysteresis and air entrapment increases the *NI* whereas the wetting branch simulations, especially with air entrapment, overestimated the *NI*.

Figure 3.14 shows the temporal distribution of the salt concentration for Calgary's climate. Similarly, simulations were extended to 18 years by duplicating the atmospheric BC. Comparing Figure 3.13 (Bighorn Dam) to Figure 3.14 (Calgary), it become evident that there is a stronger evidence of significant upward salt displacement towards the surface for Calgary's climate. This is due to Calgary's even drier climate (arid) with higher evaporative energy resulting in larger gradient for upward water movement to seek moisture equilibrium. In both DC and HC simulations, the salt never reached the domain's bottom, with more accumulation near the surface within the top 2.4 m. The estimated negative *NI* values in DC and HC simulations (-21 and -15 mm, respectively) caused net moisture loss conditions at ground surface, consequently contributing to the upward displacement response. There are more noticeable differences between DC and HC in the arid climatic conditions (Figure 3.14) as opposed to dry sub humid climactic conditions (Figure 3.13). For arid climate, DC simulation shows more dominant upward salt displacement than the HC simulation. More accumulation of salt near the surface after 6-7 years with higher concentrations in DC aligns with the low *NI*/high *AE* which caused more readily a loss of moisture near the surface triggering more upward movement of water from lower layers. Whereas HC estimated relatively higher *NI*, resulting in more downward flow and migration and limiting saline water's upward movement in HC relative to DC. Conversely WC

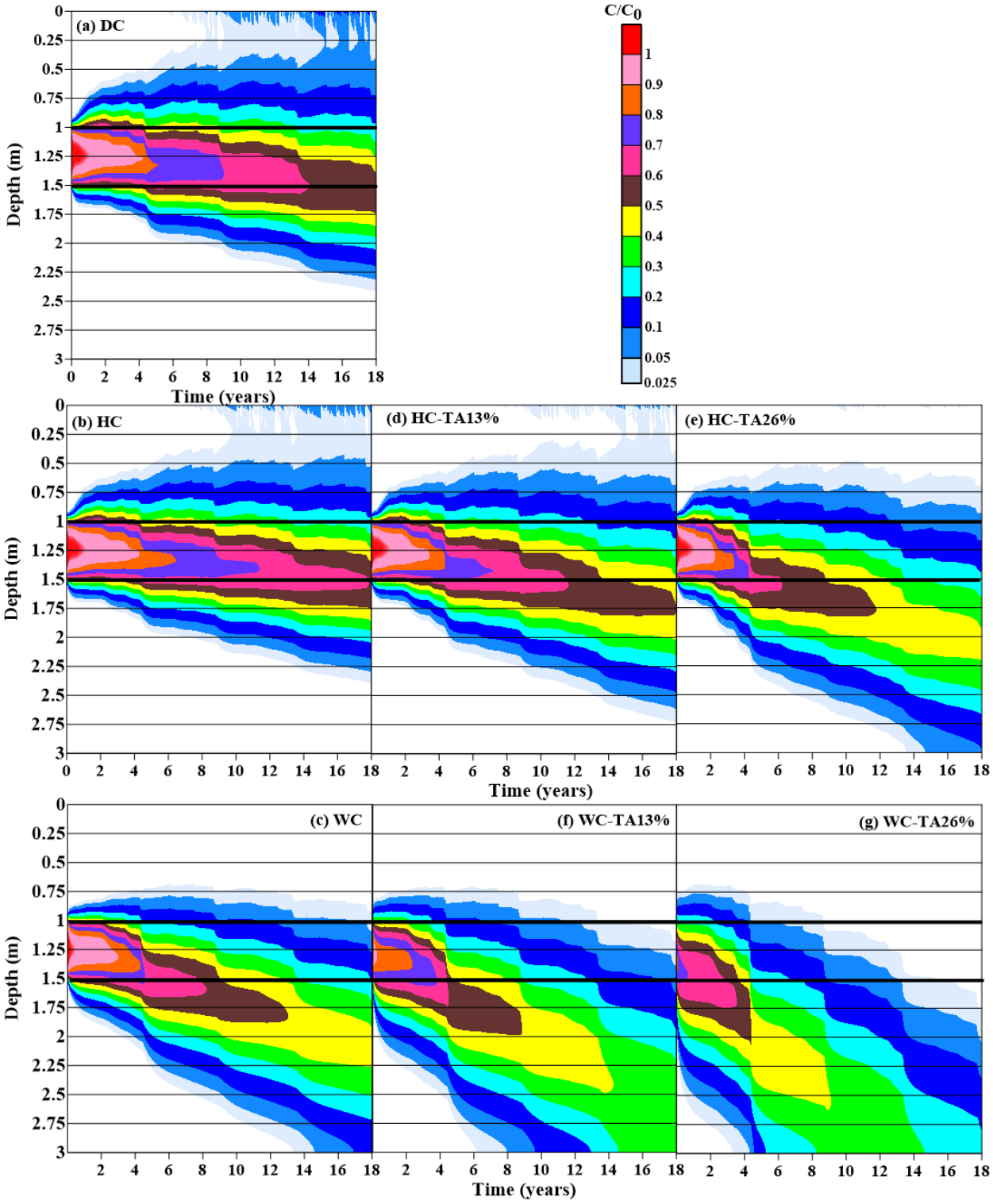

Figure 3.14 Temporal distribution of salt concentrations within the clay profile for Calgary climate

simulation exhibited predominantly downward salt migration due to higher *NI* estimates than HC. The salt in WC simulation began discharging through the bottom boundary after 13 years, while DC and HC reached only maximum depth of 2.4 m below the surface. Compared to hysteretic simulation without air entrapment (HC), introducing 13% and 26% degrees of air entrapment (HC-$TA_{13\%}$ and HC-$TA_{26\%}$) resulted in predominantly more downward migration of saline water (Figure 3.14), with larger air entrapment resulting in even more rapid and deeper salt advancement. Notably, HC-$TA_{13\%}$ showed a difference compared to DC and HC, with salt migrating 0.35 m deeper and lesser upward salt displacement (lower concentration levels near the surface). In HC-$TA_{13\%}$ (Figure 3.14), the salt migrated down to a maximum depth of 2.75 m below the surface by the end of the simulation time, without reaching the bottom boundary. In HC-$TA_{26\%}$, the advective fluxes of salt significantly increased due to its higher *NI*/lower *AE* compared to HC and HC-$TA_{13\%}$ (Figure 3.9), leading to more dominant downward water flow thus more downward salt migration. In contrast to DC, HC, and HC-$TA_{13\%}$, HC-$TA_{26\%}$witnessed salt discharge through the bottom boundary, occurring after 13 years. Also, the salt in HC-$TA_{26\%}$ simulation displaced upward only by 0.5 m above the source without reaching the surface, whereas remnants of salt managed to reach the surface in HC-$TA_{13\%}$ simulation.

For nonhysteretic wetting branch simulations (WC-$TA_{13\%}$ and WC-$TA_{26\%}$) from Figure 3.14, the introduction of air entrapment resulted in more considerable amount of salt accumulating near the bottom boundary and discharging out of the system much earlier (compared only to HC-$TA_{26\%}$). This is consistent with the wetting branch simulations overestimating the *NI* and *BF* (Figure 3.9). In WC-$TA_{13\%}$, saline water started to discharge through the bottom boundary after 6 years, while it only took 3 years for WC-$TA_{26\%}$. Remarkably, in the WC-$TA_{26\%}$, most of the saline water discharged from the system by the end of the end of the simulation time. Overall,

Calgary showed higher hysteretic and air entrapment impact on the salt transport and fate, compared to the less dry climate at Bighorn Dam.

To further quantify the salt fate and effectively compare results as a function of hydraulic properties and climate, the center of mass of (COM) was calculated as follows (Mitchell and Mayer 1998, Fetter et al. 2018):

$$COM = \frac{\int_0^\infty \theta(z,t)\, C(z,t)\, z\, dz}{\int_0^\infty (z,t)\, C(z,t)\, dz} \qquad \text{[Eq. 3.6]}$$

where θ is volumetric water content, z is vertical depth, t is time, and C is concentration.

Figure 3.15a and Figure 3.15b shows the temporal distribution of salt's COM for Bighorn Dam and Calgary climates, respectively. In Figure 3.15a (Bighorn Dam), the COM for DC and HC simulations were found to be similar, both predicting a COM of 2.82 m by the end of the

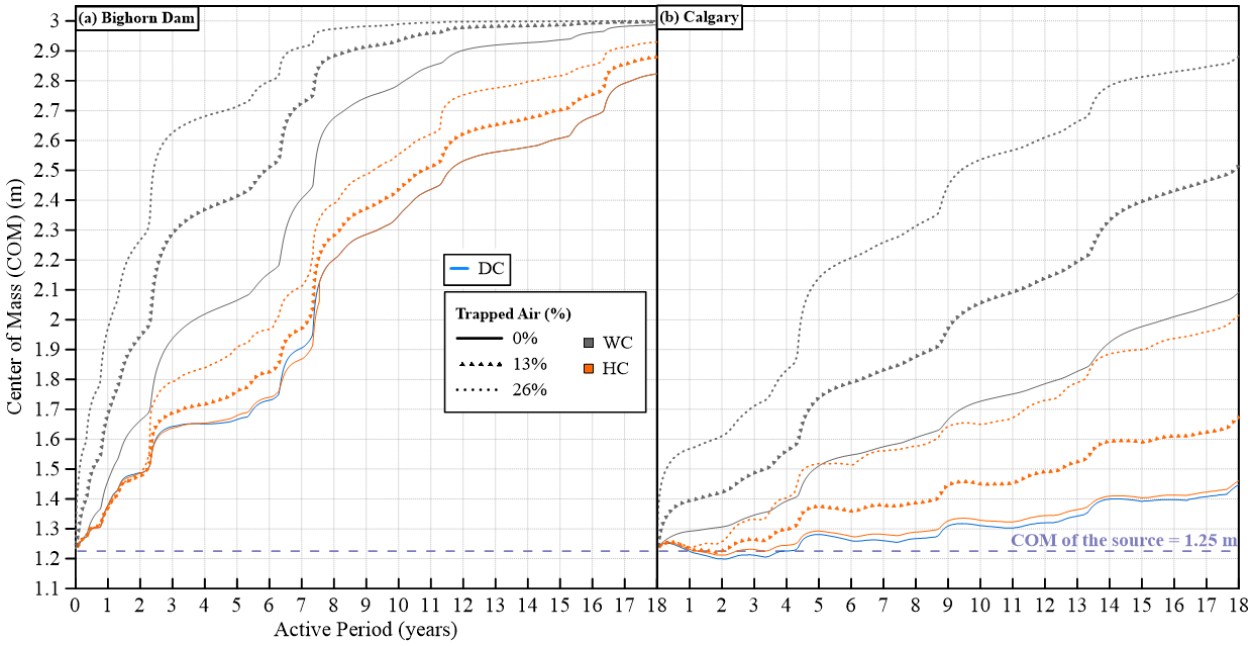

Figure 3.15 Temporal distribution of salt's Center of Mass (COM) within the clay domain under two climates: (a) Bighorn Dam and (b) Calgary

simulation, with slight variations between years 4 to 8. Hysteretic simulations with air entrapment estimated deeper COM values than HC and DC, indicating deeper penetration, with values proportional to the trapped air volume. By the end of the simulation, HC-$TA_{13\%}$ predicted that COM is at 2.88 m, while HC-$TA_{26\%}$ predicted at 2.93 m. As mentioned earlier, salt completely discharged through the bottom boundary in WC, WC-$TA_{13\%}$, and WC-$TA_{26\%}$ simulations, resulting in a COM of 3 m as shown in Figure 3.15a. Furthermore, advancing times significantly varied across the simulations. For instance, for WC, WC-$TA_{13\%}$, and WC-$TA_{26\%}$ simulations, it took 18 yrs, 15.3 yrs, and 10.1 yrs, respectively, for the COM to reach 3 m. For the COM to reach 2.82m, the estimated times for DC, HC, HC-$TA_{13\%}$, HC-$TA_{26\%}$, WC-$TA_{13\%}$, and WC-$TA_{26\%}$ were 18 yrs, 18 yrs, 16.4 yrs, 15.1 yrs, 10.5 yrs, 7.4 yrs, and 6.3 yrs, respectively. These findings indicate that DC and HC simulations (relative to hysteretic simulations with air entrapment) retarded the transport of salt, while simulating with wetting curves, especially with air entrapment, led to an overestimation of salt transport processes. Additionally, simulating hysteretic curves with a larger degree of air entrapment accelerated the downward migration of salt, highlighting that neglecting the effect of air entrapment retards the downward solute migration.

The temporal distribution of COM for Calgary (Figure 3.15b) indicates that simulating with just the drying branch of the SWCC (DC) resulted in the lowest COM values compared to other simulations. This is indicative of retarded downward solute migration as well as significant upward migration. Hysteretic simulation without air entrapment (HC) slightly accelerated the downward migration compared to DC, indicated by slightly larger COM values over time. It can also be observed that during the period of 0.8 to 4 years of the LCI, both DC and HC simulations showed predominantly upward salt movement, with COM values being lower than 1.25 m (i.e.,

initial COM value at the start of the simulation). After 4 years of the LCI and onwards, the predominant direction of salt movement became downward for DC and HC simulations, indicated by their COM values being greater than 1.25 m. The COM predicted by using only the wetting branch of SWCC without air entrapment (WC) is considerably larger than the predictions from the DC and HC simulations. By the end of the simulation, WC estimated a COM of 2.1 m, which is deeper than DC and HC with COM of 1.45 and 1.46 m, respectively. Moreover, not only did the salt travel deeper within the domain for WC simulation, but it also migrated at a much faster rate, evident from the steeper slope of the COM curve.

Hysteretic simulations with air entrapment (HC-$TA_{13\%}$ and HC-$TA_{26\%}$) estimated considerably larger COM values than HC and DC (Figure 3.15b), with predominantly downward migrations indicated by COM values greater than 1.25 m at all times. By the end of the simulation, the calculated COM for HC-$TA_{13\%}$ and HC-$TA_{26\%}$ were 1.7 m and 2 m, respectively. This suggests that considering hysteresis with a larger volume of air entrapment led to deeper and faster salt migration compared to cases neglecting air entrapment or with lower degree of air entrapment. However, relative to hysteretic simulations with air entrapment, the COM values were overestimated for simulations that utilize the characteristics of the wetting branch with air entrapment, especially for WC-$TA_{26\%}$ compared to WC-$TA_{13\%}$. The calculated COM of salt for WC-$TA_{13\%}$ and WC-$TA_{26\%}$ were 2.5 m and 2.9 m, respectively. These values were considerably larger than all other simulations.

Highlighting the differences between climates, simulating the arid climatic conditions of Calgary (i.e., the drier climate) resulted in the highest variation among different simulations (i.e., hysteretic and nonhysteretic), and this variation increased over time. This contrasts with the findings of Mitchell and Mayer (1998), who observed a constant deviation over time, and also

challenges the hypothesis of Smith (1993) suggesting that hysteresis effects are insignificant for transient problems assessed over long periods. This behavior is expected since Mitchell and Mayer (1998) simulated a single irrigation cycle repeatedly, which differs from the current study's transient simulations. In contrast, simulating a dry-subhumid or wetter climate produced lesser variations in hysteretic effects, with variations peaking at around 7 years and decreasing afterward (converging COM values of all simulations towards 2.8-3 m). This study demonstrates that hysteretic and air entrapment effects are more sensitive to arid climates compared to dry-subhumid climates. However, this behavior may not apply to other intermittent climates, where precipitation and potential evaporation distribution can vary significantly. The findings from Figure 3.15 highlight the importance of climate in quantifying hysteretic effects and show that specific behaviors cannot be generalized over a wide range of problems, as climate conditions can significantly influence the outcomes.

3.8 Summary and Concluding Remarks

In previous studies of water flow and solute transport processes in land-climate interaction (LCI) modeling, the significance of hysteresis and air entrapment has often been overlooked. This research focused on examining the impact of hysteresis combined with air entrapment on the vertical movement of saline water in a variably saturated domain. Two distinct climatic conditions were considered: the Bighorn Dam region, characterized by a dry-sub humid climate, and Calgary, which experiences arid climatic conditions. Comparisons were made between hysteresis simulations and nonhysteretic simulations based on the drying and wetting branches of the SWCC. Furthermore, the results obtained with air entrapment were contrasted with those without air entrapment, and the influence of different degrees of air entrapment was examined. The simulations conducted on the sand domain indicated negligible hysteretic effects on salt

transport. However, in the clay domain, a substantial hysteretic response was observed, prompting a more comprehensive analysis.

In clay simulations, it was observed that the predictions of solute distribution from simulations using the drying curve (DC) and hysteretic curve without air entrapment (HC) exhibited minimal variations in dry-sub humid climate. This suggests similar estimated water fluxes entering the domain. However, in arid climatic conditions, significant variations in solute transport between DC and HC were evident. The DC simulation predicted upward displacement of salt due to high actual evaporation estimates and upward moisture transfer.

In both climates, simulations employing drying curve (DC) and hysteretic curves (HC) without considering air entrapment tended to underestimate the downward migration of salt and overestimate the upward displacement, in contrast to simulations incorporating hysteresis with air entrapment. Moreover, simulations integrating hysteresis with a larger volume of air entrapment exhibited more substantial changes in water content for a marginal alteration in soil suction. This resulted in lower water retention, increased and faster downward flow, reduced actual evaporation, and consequently, larger net infiltration and larger advective fluxes of solute. Additionally, it was also found that simulations considering hysteretic soil water characteristic curve (SWCC) showed the largest runoff generation when air entrapment was considered. This occurred because the porous medium reached full apparent saturation more readily, as the pore volume was occupied by both water and air. Simulating wetting branches has been observed to consistently overestimate or accelerate the downward migration of solutes compared to hysteretic simulations, regardless of whether air entrapment is considered or ignored.

CHAPTER 4: Effect of Hysteresis with Air Entrapment on 2-D Water Flow and Solute Transport in Dry Sub-Humid Climatic Conditions

4.1 Abstract

Anthropogenic activities may lead to adverse environmental consequences such as contamination of the subsurface and the groundwater. The interaction of the vadose zone with the prevailing climate, or other types of boundary conditions, can dictate the water flow and solute transport processes in the subsurface. These processes are naturally found in unsaturated soil conditions, as well as, under intermittent climatic conditions leading to frequent drying and wetting cycles. As such, hysteresis and air entrapment effects should be considered to capture accurate hydraulic response and to accurately simulate the solute transport processes within an unsaturated soil framework. It has been a common practice to ignore hydraulic hysteresis, especially with air entrapment, when modeling water flow and solute transport processes in geotechnical engineering. This may lead to inaccurate assessment of the moisture conditions and the fate of solutes. The crux of this research is to utilize numerical modelling techniques to study the effect of hysteresis with air entrapment consideration on the transport of solutes in a two-dimensional domain. The studied problem involves solute transport from a subsurface drip irrigation system. Atmospheric boundary conditions consisting of precipitation and potential evaporation data from Bighorn Dam, Alberta, CA were applied. The hysteretic results were compared to nonhysteretic simulation that referenced both boundary curves, drying and wetting curves, to eliminate any biases in the comparison. Also, hysteretic results with air entrapment considerations were compared against results that neglected the effect of air entrapment. Additionally, the current research studied and explored the effect of varying degrees of air entrapment on the solutes' fate.

Three scenarios were investigated: subsurface irrigation with predetermined solute flux inputs (no atmospheric boundary), irrigation triggered by changes in suction influenced by climate interaction, and predetermined solute flux inputs considering climate interaction. The findings revealed that, in the triggered irrigation case, neglecting hysteresis—specifically simulating drying curve characteristics—led to an overestimation of five irrigation instances (higher concentrations within the domain) due to its elevated estimates of evaporation rates. Introducing hysteresis without air entrapment reduced the estimated irrigation instances by two, while the inclusion of air entrapment further decreased triggered irrigation to just one instance. This reduction is attributed to the mitigating effects of hysteresis and air entrapment, which lower the estimates of evaporation rates, resulting in reduced suction ranges and, consequently, fewer triggering events for irrigations. From the third examined scenario, results showed that ignoring hysteresis may underestimate or overestimate the advective fluxes of solutes if the characteristics of drying curve or wetting curve were to be used, respectively. Results also showed that ignoring air entrapment, or considering lower air entrapment volumes, can considerably underestimate the migration of solute. As an illustration, simulating hysteresis without air entrapment resulted in a 16% increase in the total flux of solute discharging through the bottom boundary compared to nonhysteretic drying curve simulation. The introduction of air entrapment at degrees of 15% and 25% led to further increases in the discharge flux by 27% and 33%, respectively. On the other hand, simulating characteristics of the nonhysteretic wetting branches, both without and with air entrapment, exhibited a notably overestimated increase ranging from 35% to 64%. Ignoring both hysteresis and air entrapment is equally detrimental, as inaccuracies related to either factor can result in improper assessments and designs for subsurface drip irrigation systems, along with potential implications for groundwater and aquifer contamination levels.

4.2 Introduction

The vadose zone refers to the region between the soil surface and the water table, characterized by unsaturated moisture conditions. Accurately estimating variably saturated flow in this zone is a complex process that depends on several factors such as hydraulic properties, interaction of prevailing climate with the variably saturated soil, hydraulic variability, and depth of the groundwater table. Contaminant transport in the vadose zone is influenced by various factors such as the physical and chemical properties of the contaminant, soil properties such as texture, structure, hydraulic conductivity, soil moisture content, and the rate of precipitation and evapotranspiration. Additionally, human activities such as industrial and agricultural practices, waste disposal, and land use changes can increase the risk of contamination in the vadose zone.

The modeling of flow and contaminant transport in the vadose zone is of paramount importance for assessing and managing contaminated sites. These sophisticated models simulate the intricate movement of water and contaminants through unsaturated soil, enabling the identification of potential sources of contamination, evaluation of exposure risks, and formulation of effective remediation strategies. Numerical models are typically employed to simulate flow and transport in the vadose zone, solve the governing equations for fluid flow and solute transport in porous media. These models consider vital data about soil hydraulic properties and contaminant characteristics. The most prevalent numerical models used for vadose zone simulations are based on the Richards' equation, which adeptly describes water flow through unsaturated porous media. Moreover, these models also incorporate the transport of contaminants through the soil matrix, using the advection-dispersion equation.

Hysteresis refers to the phenomenon where the relationship between the moisture content and pressure head of the soil is not unique, meaning that the soil will exhibit different moisture contents for the same pressure head during wetting and drying cycles. Hysteresis occurs due to various factors such as the shape and size of soil particles and pores, soil structure, contact angle, and the presence of organic matter, among other things. Hysteresis can significantly impact unsaturated flow and transport by altering the soil hydraulic properties i.e. soil water characteristic curve and unsaturated hydraulic conductivity function.

The main focus of this research is to examine how hysteresis in the soil water characteristic curve (SWCC), in combination with air entrapment, impacts solute transport and fate in the two-dimensional domain. To accomplish this, a soil atmosphere boundary was employed, integrating climatic data from the Bighorn Dam area in Alberta, Canada. The climatic data comprised of multiple years of measured daily values of precipitation and potential evaporation. Based on the Thornthwaite Climate Classification (Thornthwaite 1948, Thornthwaite and Hare 1955), the climate at Bighorn Dam falls under the dry sub-humid category. The Thornthwaite Climate Classification provides valuable information for understanding regional climates and their implications for various environmental and agricultural studies. To address the research objectives, a contaminant transport scenario related to flow and transport in subsurface drip irrigation systems is considered. Through the analysis of such a system the research aims to gain valuable insights into the influence of hysteresis and air entrapment on solute movement and distribution within the specified domains. The research also involved comparing the simulation results considering hysteresis to those from nonhysteretic simulations, wherein both wetting and drying curves were used as references. Additionally, the study delved into the effect of air entrapment and its varying volumes on flow and transport in the unsaturated domain.

4.3 Literature Review

Pickens and Gillham (1980) were among the pioneering researchers to investigate the impact of hysteresis on solute transport. They conducted simulations using a finite element model to study the transport of a non-reactive solute within a vertical domain comprising a homogeneous, yet highly hysteretic material. The problem they analyzed involved the infiltration and redistribution of a solute slug. Their results from the hysteretic simulation indicated that more water content was retained at shallower depths near the surface compared to the vicinity of the bottom boundary, as opposed to the nonhysteretic simulation. It is worth mentioning that they utilized the wetting curve characteristics for their nonhysteretic simulation. Additionally, they reported retardation effects on the solute when incorporating hysteretic characteristics, while nonhysteretic characteristics promoted downward solute migration. However, the difference in penetration depths between the two simulations was deemed insignificant. In conclusion, they noted that hysteresis had a minor effect on the solute transport component based on their findings.

Russo et al. (1989) investigated the impact of hysteresis and heterogeneity on bromide transport. The research problem involved examining transient flow and transport under intermittent boundary conditions. Their hysteretic simulation revealed significant retardation effects on the solute front, in contrast to the nonhysteretic simulation, which utilized the wetting curve and indicated accelerated solute transport processes. These findings align with the results reported by Jones and Watson (1987), who utilized infiltration and redistribution (i.e., gravity drainage) cycles as boundary conditions. Overall, Russo et al. demonstrated the influence of hysteresis on bromide transport and highlighted how it can lead to significant differences in solute movement compared to nonhysteretic scenarios.

In contrast to Russo et al. (1989), who studied hysteresis and heterogeneity on solute transport separately, Vereecken et al. (1995) conducted a comprehensive assessment, examining both effects collectively. Their study involved applying intermittent boundary conditions, comprising infiltration, redistribution, and evaporation. Additionally, they explored the impact of simulating two contrasting soil textures: coarse sandy soil and fine sandy soil. Unlike previous studies, Vereecken et al. (1995) compared the results of their hysteretic simulation not only to simulations using the drying or wetting curves but also to the mean of both curves. This approach addressed the bias observed in comparing hysteretic and nonhysteretic simulations using only one of the curves. The findings showed that considering hysteresis resulted in solute transport retardation when compared to the wetting curve simulation, while an accelerated solute displacement was observed when compared to the drying curve simulation. In support of Vereecken et al.'s approach, Smith (1995) has also emphasized the importance of comparing results using the mean curve and recommended its adoption. In their previous research (Smith 1993), they attempted to use the mean curve, further validating the significance of this approach. Contrary to Royer and Vachaud's (1975) assertion that hydraulic variability diminishes the hysteretic effects, Vereecken et al. (1995) demonstrated through their results that both hysteresis and heterogeneity significantly influence solute transport. Notably, Vereecken et al. (1995) emphasized that hysteresis had a considerable effect on predicting the penetration depths of the solute, further highlighting its importance in the solute transport prediction process.

Mitchell and Mayer (1998) conducted an extensive study to explore the combined impact of hysteresis and air entrapment on solute transport. They also performed parametric investigations on the van Genuchten (1980) SWCC model parameters to analyze the sensitivity of hysteretic effects on solute transport. To accurately capture the dynamic behavior of the system, their

models involved multiple cycles occurring over 48 hours, each cycle encompassing six stages: water infiltration with solute pulse, water infiltration, redistribution, evaporation, redistribution, then evaporation. The research encompassed five different soil types, and they compared the results of hysteretic simulations to nonhysteretic simulations. Utilizing one of their hysteretic materials, comparisons were made using the wetting, drying, and mean curves, in which they found that there would be no bias in selecting one of the nonhysteretic curves for the comparison (with hysteresis curve), since all nonhysteretic curves produced similar distributions. Subsequent analyses proceeded by comparing hysteretic to nonhysteretic simulations based on the wetting curve. Furthermore, the findings showed that the hysteretic simulation resulted in higher moisture retention near the surface and lower moisture conditions near the bottom boundary compared to simulations based on the wetting curve. Furthermore, the hysteretic simulations exhibited a retardation of solute migration, leading to lower penetration depths than the nonhysteretic curve. Their parametric study revealed that increasing the α_w/α_d (water entry pressure to air entry pressure) ratio amplified hysteretic effects, resulting in increased penetration depths. Additionally, decreasing the value of the *n* parameter led to higher penetration depths of solute. Larger hysteretic effects and deeper solute migration were observed when there were significant differences between the saturated and residual water content. The researchers also investigated the inclusion of air entrapment in the hysteretic models. The results indicated that larger volumes of trapped air led to increased advective solute fluxes and larger penetration depths compared to cases without air entrapment. They explained that air entrapment reduced the pore space, leading to increased solute flux. In their study, coarser soils exhibited considerably lower hysteretic effects compared to finer soils. Additionally, they observed that the deviation

between hysteretic and nonhysteretic simulation results diminished over time, particularly at greater depths where the effect of atmospheric boundary interaction was less pronounced.

In a relatively recent study, Gladnyeva and Saifadeen (2012) employed HYDRUS-1D to investigate the impact of hysteresis on the transport of a non-reactive solute. Their study involved a one-dimensional domain, and they utilized 12-year climate data from three different locations across Sweden. To explore the sensitivity to temporal resolution of climate data, they analyzed half-hourly, hourly, 2-hours, 4-hours, and daily climate data resolutions. Contrary to previous research (Vereecken et al. 1995, Mitchell and Mayer 1998) as well as contrary to the findings of the current thesis (Chapter 3.7), Gladnyeva and Saifadeen (2012) observed that the effect of hysteresis on solute transport was more significant for coarser grained soils. They went on to recommend that hysteresis could be disregarded in solute transport problems when using daily resolution climate data. However, it is essential to note that this recommendation is not supported by Bashir et al. (2015), particularly for problems involving only variably saturated flow.

Based on the review of the above literature the following gaps can be identified:

1. Existing studies on the impact of hysteresis on solute transport predominantly focused on one-dimensional domains. Therefore, there is a need for further research to investigate the effects of hysteresis in more complex, multi-dimensional systems;
2. With the exception of a single study (Gladnyeva and Saifadeen 2012), most of the research conducted thus far has explored soil-atmosphere interactions through cycles of infiltration, redistribution, and evaporation. It would be beneficial to expand the scope of

investigations to encompass additional aspects of these interactions using actual climate data;

3. The available studies examining the effects of hysteresis with air entrapment are notably limited. This represents a significant gap in our understanding, highlighting the necessity for more research to explore the influence of hysteresis in scenarios involving air entrapment; and
4. Comparisons between results obtained from hysteresis-inclusive models and those from nonhysteretic models have primarily focused on the wetting curve. To gain a more comprehensive understanding, it is crucial to extend these comparative analyses to include the drying curve as well.

The current research explores the effect of hysteresis with air entrapment on the solute transport within two-dimensional domains. It filled the gaps originating from previous research where air entrapment effects were commonly ignored. Also, this research applied the interaction of real climatic conditions over an extended period of time. The results of the hysteretic simulations were compared to all nonhysteretic curves; the aim was to eliminate any biases involving the comparison of the results.

4.4 Effect of Hysteresis on Water Flow and Solute Transport from Subsurface Drip Irrigation

Subsurface drip irrigation (SDI) systems are a modern and efficient method of irrigating crops. In these systems, water is delivered directly to the plant's root zone through buried drip lines or tapes. Unlike traditional surface irrigation methods, SDI reduces water loss due to evaporation and minimizes weed growth by targeting the water directly to the plant roots. This also allows

for precise control over the water supply, optimizing the moisture content in the root zone. This can also result in improved crop yield, better quality produce, and reduced incidence of diseases related to excessive moisture on plant leaves. Subsurface drip irrigation systems can also be integrated with fertigation, which is the simultaneous application of water and fertilizers through the irrigation system. By directly delivering fertilizers to the root zone, it enhances nutrient uptake efficiency and reduces fertilizer leaching, resulting in improved fertilizer use efficiency.

To maximize the benefits of drip irrigation technology, it is essential to optimize the operational variables that irrigators can control. These variables include the frequency, rate, and duration of water application, as well as the positioning of the drip tubing (Skaggs et al. 2004). Triggered drip irrigation is a specialized irrigation technique that delivers water to plants based on specific triggers or conditions. Unlike other methods that operate on a fixed schedule or time-based intervals, triggered drip irrigation systems respond to specific factors such as plant needs, soil moisture levels, or weather conditions. Numerical modeling has been identified as a swift and accurate method to optimize the operational variables of both triggered and untriggered subsurface drip irrigation systems (Skaggs et al. 2004, Dabach et al. 2013). Studying the performance of subsurface drip irrigation (SDI) systems in terms of hydraulic hysteresis and air entrapment is important due to the nature of their operation based on wetting and drying cycles.

4.4.1 Model Details

The design characteristics of the simulated subsurface drip irrigation system were based on commonly used drip systems for processing tomato crops, as described by Hanson et al. (2008). These characteristics included a drip line depth of 20 cm and an emitter spacing of 30 cm, which are typical values in practice (Figure 4.1). In the simulation setup, the drip irrigation source was

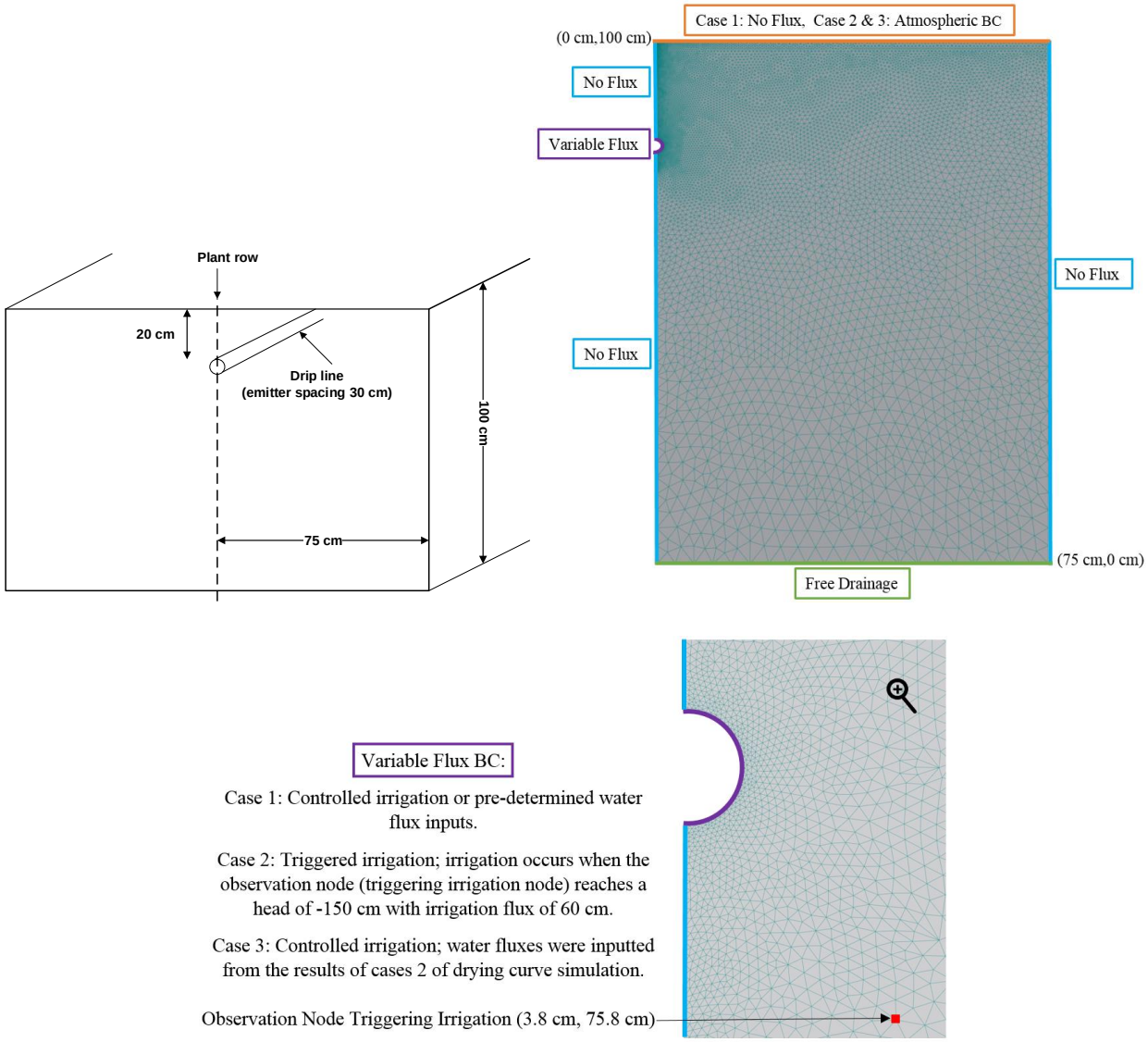

Figure 4.1 Showing domain's geometry, mesh sizes, and boundary conditions (BC) of drip the irrigation problem

positioned 20 cm below the surface and located along the left boundary of the vertical domain. This placement mimics the subsurface positioning of drip irrigation systems. Each drip irrigation input into the system contained water with a relative solute concentration of 1. Three different

cases of drip irrigation were considered in the simulation, each with its own specific details. The following are the characteristics of each individual case:

- In Case 1, a predetermined drip irrigation flux was employed without considering atmospheric boundary conditions at the top of the soil domain. The drip irrigation system was simulated using a system-independent time-variable flux boundary condition applied along the circumference of the dripper. The radius of the dripper was assumed to be 1 cm, and the irrigation discharge was set at 12 L/day. To model the drip irrigation, an infinite line source approach was utilized, which has been previously validated as an accurate representation of this specific drip irrigation system, as demonstrated by (Skaggs et al. 2004). This line-source approach has also been employed in previous studies investigating water and chemical movement in similar systems, e.g. Hanson et al. (2008). Figure 4.2 presents a schematic of the irrigation schedule, illustrating that a flux of 60 cm/day was maintained for a duration of 2.5 days. Between the two irrigation cycles, a redistribution period of 1 day was assumed to simulate the redistribution of water within the soil;

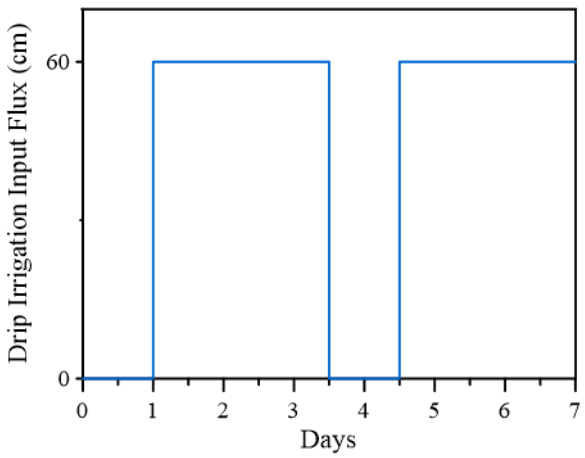

Figure 4.2 Drip irrigation inputs of the variable flux boundary - Case 1

- In Case 2, the focus was on a triggered irrigation problem with atmospheric boundary condition (BC) applied to the top boundary of the domain. In this case, irrigation events were initiated based on a specific trigger related to soil moisture levels. To accurately represent the soil moisture dynamics, the system also incorporates the interaction between land and climate (LCI) at the top soil-atmosphere boundary. Actual climate data, obtained from the Bighorn Dam in Alberta, Canada, were utilized for this purpose. These climate data encompassed a two-year period (2007-2008) and included daily measurements of precipitation and potential evaporation. The specific trigger for irrigation in this case was a pressure head of -150 cm, which was identified at a specific location within the domain, as shown in Figure 4.1. Whenever the pressure head at this location reached the specified threshold (-150 cm), a triggered irrigation event was initiated. The irrigation flux rate for these events was set at 12 L/day. By incorporating atmospheric boundary conditions and utilizing specific triggers related to soil moisture levels, Case 2 provided a realistic representation of triggered irrigation events and their impact on the soil-water and associated solute dynamics within the system. The application of actual climate data further enhanced the accuracy and applicability of the simulation; and
- Case 3 also incorporates atmospheric BC at the top boundary, similar to Case 2. However, in this case, the variable flux BC is controlled instead of being triggered by pressure head conditions. The objective of Case 3 stems from the findings of Case 2, where different simulations with varying hydraulic characteristics resulted in dissimilar timing of triggered irrigation events. Consequently, the fate of solutes was significantly influenced by the variation in irrigation inputs. The primary goal of Case 3 is to

investigate the influence of hysteresis and air entrapment exclusively on the solute transport processes, rather than their impact on the occurrence of triggered irrigation events and subsequent solute fate. To achieve this, the input source was controlled using a predetermined flux. This was accomplished by applying the flux inputs obtained from nonhysteretic drying curve simulation conducted in Case 2. By controlling the input source with a predetermined flux derived from the nonhysteretic drying curve simulations, Case 3 allows for a focused examination of the impact of hysteresis and air entrapment on solute transport processes. This approach provides valuable insights into the specific mechanisms at play, enabling a more detailed understanding of how these factors influence solute movement in the system.

In all three cases, the remaining left and right boundary was characterized by a no flux boundary. Also, a free drainage BC was applied at the bottom boundary, which is also known as “zero-gradient” water flow BC. This type of BC simulates water tables that are far below the domain of interest. A water content initial condition was applied to all simulations for case 1, and it is similar to the initial conditions from PC-Progress's (2022) Example A. This was done for better comparability of the results between wetting curve simulations and other simulations. In case 2, the initial condition obtained from PC-Progress's (2022) Example B and was accordingly applied in the form of pressure head initial condition to all simulations. It is worth noting that a consistent initial pressure head distribution across different simulations is to ensure that the triggering node is sensitive to pressure head conditions (SDI designed for) rather than water content change. The initial pressure head of case 3 was like case 2.

For the solute transport, a non-reactive and conservative solute with relative concentration of 1 is discharged whenever irrigation is initiated. Longitudinal and transverse dispersivity for loam

were assumed to be 2 cm and 0.2 cm, respectively (PC-Progress 2022). A Third-type Cauchy BC, also known as “mixed or flux type BC”, was applied at the source, bottom boundary, and at top boundary (only when atmospheric BC was applicable). A no flux solute BC was accordingly applied at the remaining boundaries (Figure 4.1). It was also assumed that initially there was no solute in the soil domain.

In each of the three cases described above, various simulations were carried out using hysteretic and nonhysteretic soil water characteristic curve (SWCC), while also considering the presence or absence of air entrapment. The van Genuchten (1980) model was used to parameterize the SWCC. The van Genuchten (1980) function for SWCC is as follows:

$$S_e = \frac{1}{[1+(|\alpha\psi|^n)]^m} \quad \text{[Eq. 4.1]}$$

$$S_e = \frac{(\theta - \theta_r)}{(\theta_s - \theta_r)} \quad \text{[Eq. 4.2]}$$

where θ_r is the residual volumetric water content [L^3/L^3], θ_s is the saturated volumetric water content [L^3/L^3], S_e is the effective degree of saturation [L^3/L^3], α is a fitting parameter related to the inverse of air entry value (AEV) [1/(M/L/T^2)], n is fitting parameter related to the pore-size distribution [-], and m is an empirical fitting parameter [-] and can be assumed as $m = 1 - 1/n$.

The vector describing the van Genuchten parameters for the hysteresis loop includes the following: $\{\theta_s^d, \theta_s^w, \theta_r^d, \theta_r^w, \alpha^d, \alpha^w, n^d, n^w\}$, where the superscript "*d*" represents the drying curve and "*w*" represents the wetting curve. To simplify the hysteretic characteristics and reduce the number of parameters, Kool and Parker (1987), Pham et al. (2005), and Likos et al. (2014) suggested that the "*n*" parameter, related to pore-size distribution, can be considered equal for

both the drying and wetting curves (i.e., $n^d = n^w$). Likos et al. (2014) have reported that the parameter α^w can be approximated as $\alpha^w \approx 2\alpha^d$, and $\theta_r^d = \theta_r^w$. Consequently, the number of parameters to describe hysteretic SWCC reduce from 8 to 5, resulting in the following set of parameters: $\{\theta_s^d , \theta_s^w, \theta_r , \alpha^d, \alpha^w = 2\alpha^d, n\}$.

In the simplest form, the assumption of zero air entrapment can be made, where $\theta_s^w = \theta_s^d$. This simplification results in the following parameter vector: $\{\theta_s^d , \theta_r , \alpha^d, \alpha^w = 2\alpha^d, n \}$, where α^w becomes the sole driving parameter for the hysteretic effects. This assumption has been commonly used by researchers studying hysteresis. However, disregarding air entrapment is not entirely accurate, as air can naturally become trapped during rewetting events; Hopmans and Dane (1986) expressed that the relationship, $\theta_s^w < \theta_s^d$, is mostly true during rewetting of the pores, indicating that the volume of trapped air is larger than zero. Additionally, Likos et al. (2014) conducted experiments on a range of coarse- and fine-grained soils to study the hysteretic effects on the SWCC. Their analysis suggests that the degree of air entrapment can vary from 5% to 25% with an average value of 15%. In adopting the findings of Likos et al. (2014), the current study simulated different scenarios of air entrapment: 15 and 25%. Additionally, the 0% of air entrapment was adopted to simulate a case that neglects the effect of air entrapment. The aim was to examine the influence of varying degrees of air entrapment on solute transport within the system. By considering different levels of air entrapment, the study aimed to gain insights into the impact of air entrapment on solute movement and better understand its role in the overall transport processes.

In this study, the hysteresis model proposed by Parker and Lenhard (1987) is used to describe the wetting and drying scanning curves of the SWCC. This model scales the corresponding main

curves defined by the van Genuchten (1980) equation. The key assumptions of this model are that the residual water content (θ_r) and the coefficient "n" are the same for both the wetting and drying curves, while the saturated volumetric water content (θ_s) and the coefficient "α" differs between the two curves. The Parker and Lenhard (1987) model effectively avoids the artificial pumping error that occurs in other scaling-based models, ensuring closed scanning loops during simulated cyclic paths. This is achieved by remembering all the reversal points observed during wetting and drying cycles, allowing for the drawing of closed scanning loops. The model also considers air entrapment in the SWCC, following the approach proposed by Land (1968). The model accounts for a constant difference (R) in the reciprocal of the change in volumetric water contents between the initial and final states as the wetting/scanning path progresses towards zero suction.

The model by Parker and Lenhard (1987), is impended HYDRUS-2D/3D, and is capable of considering hysteresis in the SWCC with air entrapment. The SWCC can be utilized to estimate the Hydraulic Conductivity Function (HCF). van Genuchten (1980) derived a predictive equation for the HCF by combining empirical fitting parameters from the SWCC with the Mualem (1976) model. Mualem's model employs a statistical pore-size distribution to describe the hydraulic conductivity function. The resulting equation for the HCF in terms of the van Genuchten (1980) parameters as implemented in Hydrus can be expressed as follows:

$$k = k_s S_e^{\,l} \left[1 - \left(1 - S_e^{\frac{1}{m}}\right)^m\right]^2 \qquad \text{[Eq. 4.3]}$$

where k is the hydraulic conductivity [L/T], k_s is the saturated hydraulic conductivity [L/T], S_e is effective degree of saturation [L^3/L^3], and l is the pore interaction constant parameter, which can

be assumed to be equal to 0.5 [-] for a wide range of soils. It is important to note that the implementation of the HCF in Hydrus is inherently nonhysteretic. Nonetheless, due to the variation in water contents at equivalent pressure heads between the wetting and drying states, the hydraulic conductivity values become equal for the same water content but different for distinct pressure heads, resulting in implicit hysteresis in the HCF. On the other hand, when entrapment of air is considered, Hydrus integrates Lenhard and Parker (1987) predictive model for HCF, in which entrapment of air increases the hydraulic conductivity values. Parker and Lenhard (1987) shown that during wetting or rewetting, the hydraulic conductivity was typically larger than during drying for the same actual saturation.

For each of the three cases (Case 1, Case 2, and Case 3) described above, a total of seven simulations were conducted. These simulations comprised three hysteretic scenarios: HC (hysteretic characteristics without trapped air), HC-$TA_{15\%}$ (hysteretic characteristics with 15% trapped air), and HC-$TA_{25\%}$ (hysteretic characteristics with 25% trapped air). Additionally, one nonhysteretic simulation was performed using the initial drying curve (DC), and three other nonhysteretic simulations using the main wetting curve with and without entrapment (WC, WC-$TA_{15\%}$, and WC-$TA_{25\%}$). The notation "TA" refers to trapped air, indicating the percentage of air entrapment in the hysteretic and nonhysteretic wetting curve simulations. Figure 4.3 shows the hysteretic SWCC for loam with different air entrapment percentages: 0% [Figure 4.3a], 15% [Figure 4.3b], and 25% [Figure 4.3c]. The parameters for the van Genuchten (1980) function for loam were taken from the soil catalogue in Hydrus 2D/3D and are also presented in Figure 4.3.

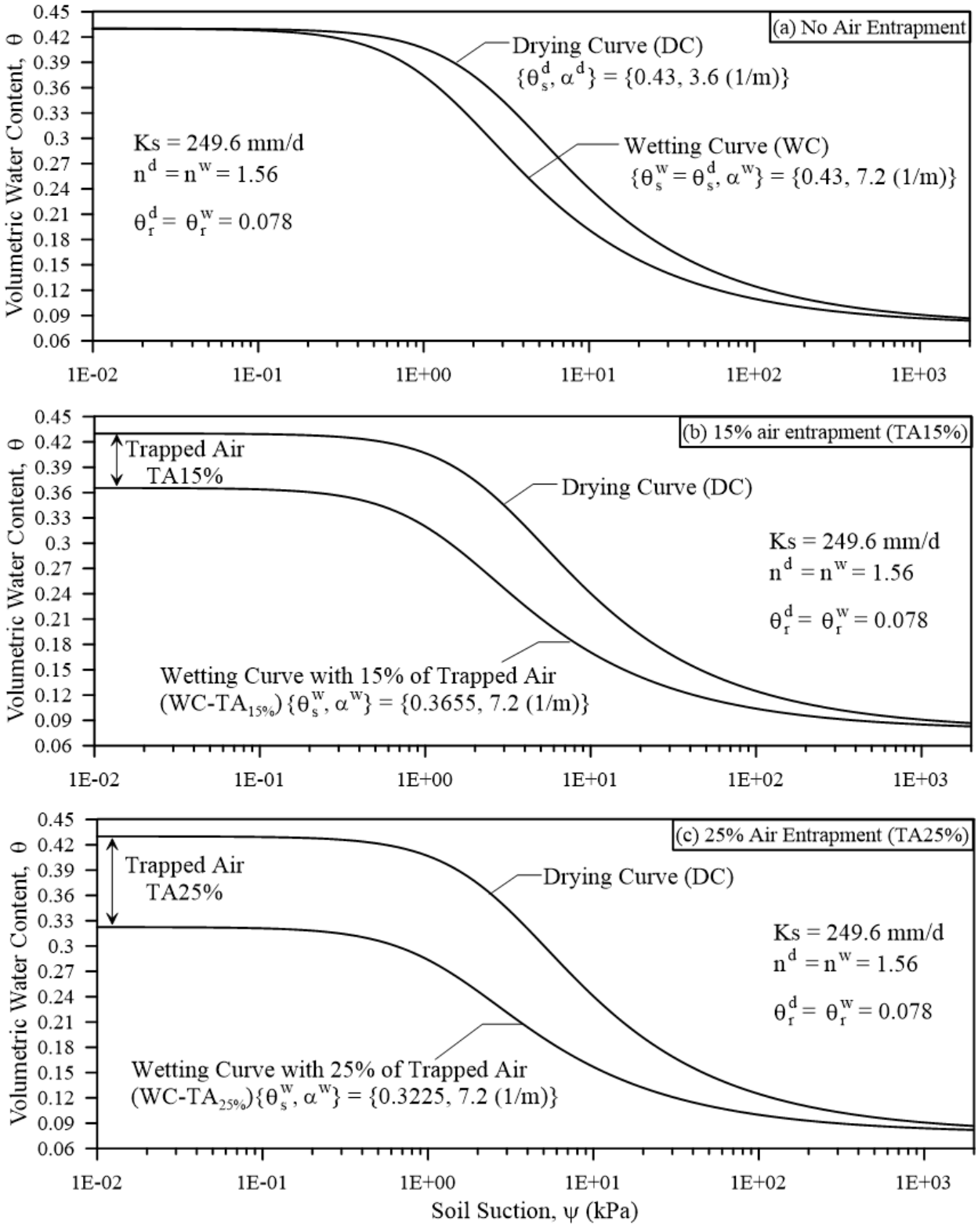

Figure 4.3 Hysteretic envelopes of SWCC of loam with three air entrapment considered (a) no air entrapment, (b) 15% air entrapment, and (c) 25% air entrapment

4.4.2 Results and Discussion

4.4.2.1 Case 1

In Case 1, the study focused on drip irrigation with predefined flux inputs (refer to Figure 4.2 for specific values). Each irrigation input carried a solute's relative concentration of 1. It's important to remind that, in this first case, atmospheric boundary conditions were not taken into consideration.

Figure 4.4 present the theoretical hysteretic envelopes represented by solid and dashed lines, respectively, along with the paired water content and pressure head data from HYDRUS-2D simulations (H2D). The simulations include DC (Drying Curve), HC (Hysteretic Curves without air entrapment), HC-$TA_{15\%}$, HC-$TA_{25\%}$, WC (Wetting Curve without air entrapment), WC-

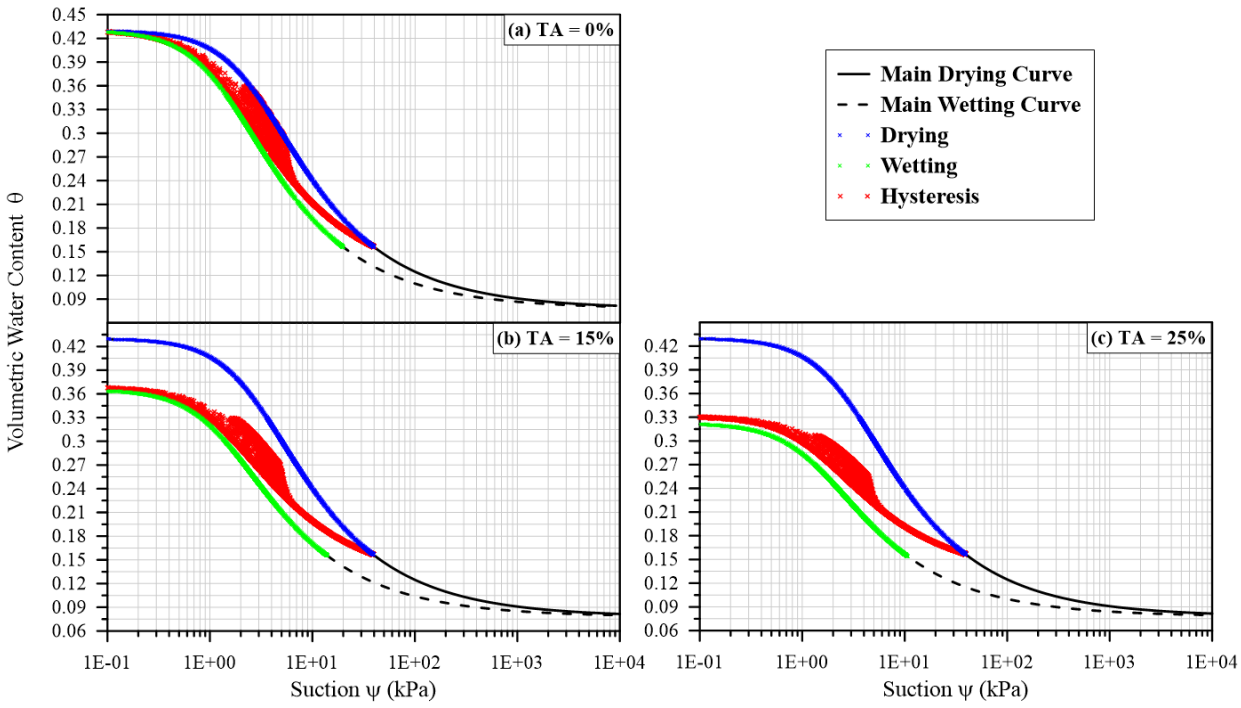

Figure 4.4 Paired water content and pressure head data from different simulations superimposed on SWCC

$TA_{15\%}$, and WC-$TA_{25\%}$. Notably, the data points follow distinct paths within the SWCC, depending on the chosen hydraulic characteristics and the volume of trapped air. A noteworthy observation is that when air entrapment is considered in the hysteretic characteristics, the data points tend to closely align within the vicinity of the wetting branch. This phenomenon occurs because the domain primarily experiences rewetting rather than drying, which leads to a more pronounced impact of wetting characteristics. Due to the lower capillary forces associated with scanning and main wetting branches, this implies that the downward water flow is expected to be more rapid for HC-$TA_{15\%}$ and HC-$TA_{25\%}$, especially for WC-$TA_{15\%}$ and WC-$TA_{25\%}$ simulations compared to DC and HC simulations.

Figure 4.5 shows the solute distribution within the loam domain after 7 days for different hysteretic (HC, HC-$TA_{15\%}$, and HC-$TA_{25\%}$) and nonhysteretic (DC, WC, WC-$TA_{15\%}$, and WC-$TA_{25\%}$) simulations. Simulation using DC has resulted in a retardation effect on the solute compared to simulation using WC, indicated by the higher solute concentrations near the source and the surface for DC simulation. The advective flux of the solute is directly linked to the water flux because the solute is transported within the flowing water. In mathematical terms, the advective flux of the solute (J_s) is given by the product of the water flux (q) and the solute concentration (C) at a specific location in the porous medium:

$$J_s = q\ C \qquad \text{[Eq. 4.4]}$$

This relationship shows that as the water flux increases, the advective flux of the solute also increases, leading to a faster transport of solutes within the medium. To elucidate the implications of this relationship, it is important to consider that the drying curve (DC) is

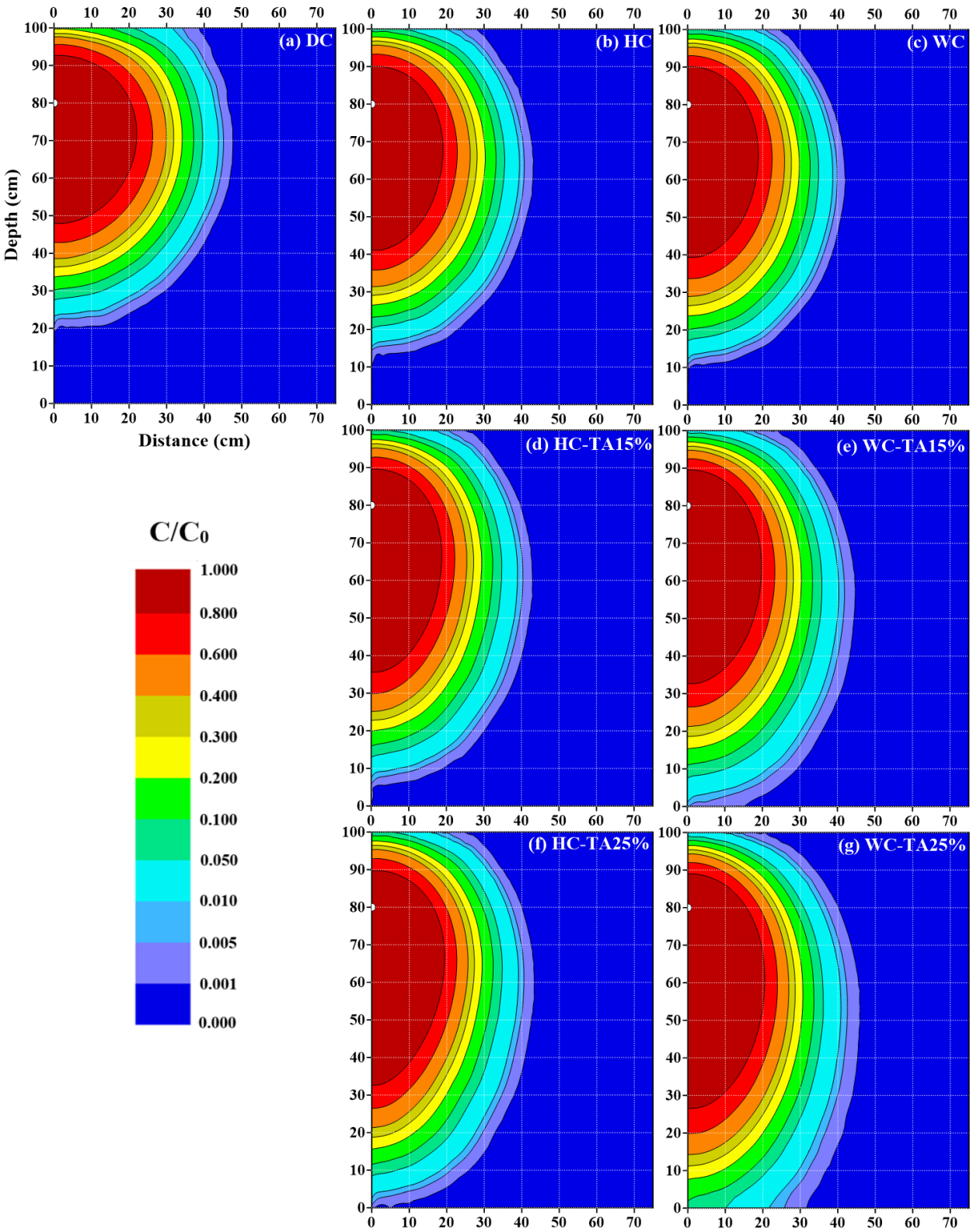

Figure 4.5 Distribution of solute after 7 days using different hysteretic and nonhysteretic characteristics - Case 1

characterized by a lower α^d value (where $\alpha^w = 2\alpha^d$), indicating a higher entry value. In terms of the SWCC, DC is also distinguished by a larger change in suction for a relatively small change in water content compared to the wetting curve (WC). As a result, the drying curve exhibits higher water retention properties than the wetting curve, leading to a greater retention of water in the upper layers during simulations that use the drying curve, as seen in Figure 4.5. The increased water retention in the upper layers implies reduced downward water flow, which, in turn, affects the advective solute flux. Since the advective solute flux is directly linked to the water flow through the term "q" in the advective-dispersion equation, we can expect lower downward advective flux in simulations using the drying curve (DC) compared to simulations using the wetting curve (WC). This can be observed in the concentration profiles for simulations DC, where the concentration is lower in deeper layers as compared to simulation WC. It should also be noted that the hysteretic simulation without air entrapment (HC) produced solute distribution relatively similar to WC simulation, with some slight retardation effects. Since the domain has experienced, mostly, wetting events, the HC simulation had a higher tendency to follow the wetting scanning paths as well as main wetting branch (Figure 4.4). The slight vertical retardation in HC simulation, compared to the WC simulation, is caused due to the formation of some scanning drying curves during redistribution phases. Another important observation from this figure is that for the case of DC simulation there is more horizontal spreading of solute when compared to the HC and WC simulations. This is also not surprising, as it is well known that a decrease in capillary forces (lower retention as in the case of WC) for similar gravitational forces, one can expect an infiltration pattern with an increase in vertical seepage and a decrease in horizontal spreading (Boduroglu and Bashir 2023).

It is worth noting that considering air entrapment in the hysteretic simulations, as seen in Figure 4.5, resulted in deeper penetration depths of the solute, compared to HC (i.e., without air entrapment). The penetration depths of the solute were found proportional to increases in the air entrapment volume being considered. For example, in HC-$TA_{25\%}$ simulation, the solute has reached, and even, started to discharge out of the bottom boundary, as opposed to HC- $TA_{15\%}$, in which the solute has migrated to maximum depths that are a few centimeters above the bottom boundary. This indicates that increasing the volume of air entrapment has increased the advective flux and the penetration depths of the solute. To understand the connection, there are two processes in which air entrapment can affect the solute transport. The first is through the term, q from the advective-dispersion equation. For an arbitrary water content, the porous medium could reach lower suction values when air becomes entrapped. For example, for the same water content, hysteretic simulations after entrapment of air recorded lower suctions than simulations of lower degree, even more than with no air entrapment (Figure 4.4). The lower suction has reduced the water retention thus enhanced the water flow and advective flux of solute, and in return, accelerated the migration of solute and estimated deeper penetrations (e.g., HC-$TA_{25\%}$ as opposed to HC-$TA_{15\%}$ and HC). The second way is through the water content component of the pore-velocity term, $u = q/\theta$, of the advective dispersion equation. The water content became lower when air was entrapped, resulting in larger pore-velocity value and deeper solute transport. This explained why HC-$TA_{25\%}$ estimated deeper solute migration compared to HC-$TA_{15\%}$, and more considerably, to HC.

When simulating the wetting branches of the hysteretic SWCC with air entrapment (WC-$TA_{15\%}$ and WC-$TA_{25\%}$), there was a noticeable overestimation of the solute concentration near the bottom boundary, relative to hysteretic simulations with air entrapment. In other words, the

downward solute migration was overestimated. The inclusion of air entrapment and the imposition of ($\alpha^w = 2\alpha^d$) resulted in a reduction of water retention properties and larger advective flux as result of air entrapment. As a consequence, there is greater downward solute migrations, especially for WC-$TA_{25\%}$, where a largest degree of air entrapment was considered. It is essential to highlight that only the simulations HC-$TA_{25\%}$, WC-$TA_{15\%}$, and WC-$TA_{25\%}$ reported the discharge of solute through the bottom boundary. This suggests that these specific scenarios led to the solute being transported and exiting the domain through the bottom boundary. The other simulations did not exhibit this behavior. These findings indicate the importance of considering air entrapment and the associated changes in water retention behavior when simulating the wetting branches of the hysteretic envelope. The presence of air entrapment can significantly influence solute transport and migration patterns, particularly in simulations with higher degrees of air entrapment.

To better assess how hysteresis and air entrapment play a role in dictating the horizonal and vertical movement of the solute, two horizontal cross-sections were specified as shown in Figure 4.6. Cross-section 1 (CS1) is located 10 cm below the surface (i.e., 10 cm above the source), and it will help in interpreting the upward and lateral movement of water and solute. Cross-section 2 (CS2) is located 70 cm below the surface (i.e., 50 cm below the source). The volumetric water content and concentration levels from the CS1 and CS2 are presented in Figure 4.7 and Figure 4.8, respectively, and are further discussed below.

Figure 4.7 shows the distribution of water content and solute vs. horizontal distance at CS1 at three time instances (related to the BC at the emitter): 2 days, 4 days, and 7 days (i.e., end of simulation). Considering that CS1 is located 10 cm above the source, it provides insight into any

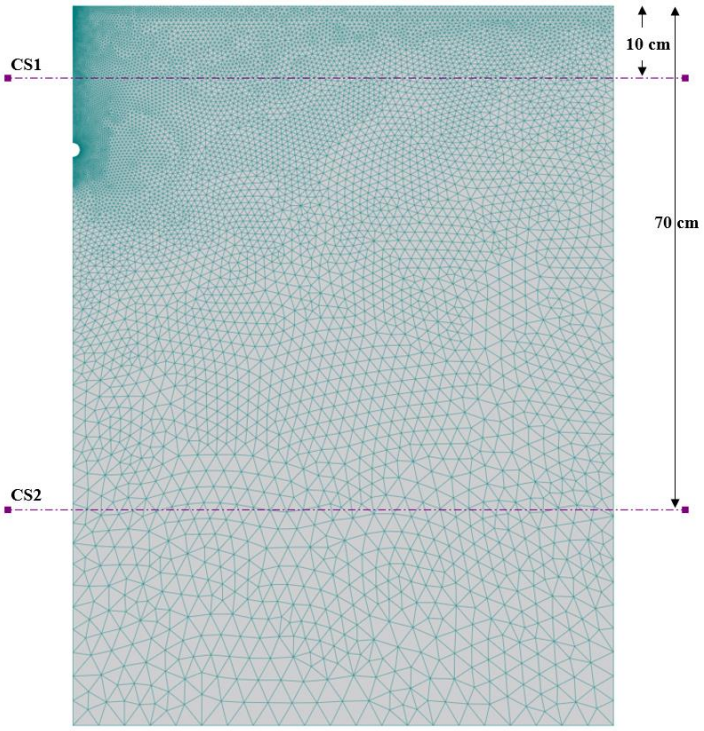

Figure 4.6 Two horizontal cross-sections for water content and concentration results: Cross-section 1 (CS1) and Cross-section 2 (CS2)

upward water and solute movement as well as lateral displacement relative to distance to the emitter. The figure implies that DC simulation tends to retain more moisture near the surface compared to other simulations, explained by their larger water content. Similarly, in DC simulation, the relative concentration of solute near the surface has increased with time, reaching a maximum value of 0.9 by the end of the simulation. This indicates that DC, which is characterized by higher air entry value and larger water retention properties, resulted in larger upward solute displacements. Whereas, for hysteretic simulations and wetting curve simulations the concentrations were found to be below 0.8, due to higher effects of downward water and solute migrations. Simulating hysteric effects resulted in slightly larger effects of upward solute movement compared to WC simulation; however, the differences appear to be minimal.

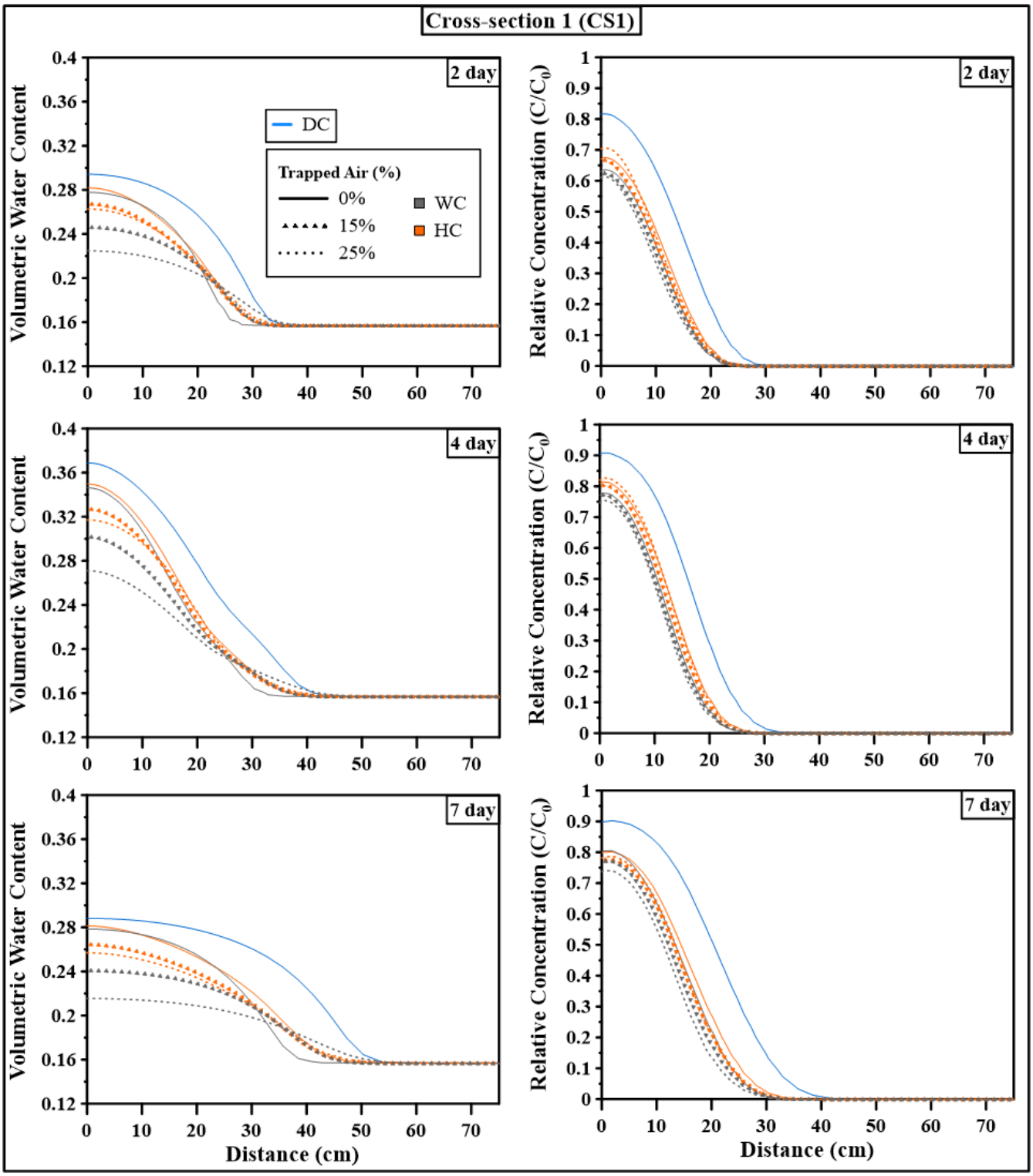

Figure 4.7 Distribution of volumetric water content (left) and solute's relative concentration (right) at CS1 (10 cm below surface) at 3-time instances: 2 day (top), 4 day (middle), and 7 day (bottom)

From Figure 4.7, simulating HC with air entrapment (i.e., HC-$TA_{15\%}$ and HC-$TA_{25\%}$) resulted in lower water content near the surface compared to HC; this is due to entrapment of air. However, the inclusion of air entrapment in hysteretic simulations has not impacted concentration profiles near the surface (CS1), relative to the case without air entrapment. The water content profiles appear to exhibit higher hysteretic effects than solute profiles near surface for this case. Simulating the wetting branches of the hysteretic envelope with air entrapment (i.e., WC-$TA_{15\%}$ and WC-$TA_{25\%}$) produced less, but insignificant, effects of upward water movement and solute displacement compared to HC-$TA_{15\%}$ and HC-$TA_{25\%}$.

The difference in extent of solute's lateral displacement can also be observed in CS1. This is most pronounced for DC simulation, where the lateral spreading of solute has reached a greater distance compared to other simulations. After 7 days, the solute in DC simulation travelled to a maximum distance of approximately 42 cm away from the source. Whereas for the remaining simulations, the solute spread laterally to a shorter distance of approximately equal to 33 cm. Larger horizontal displacement in DC simulation at CS1 is due to the higher capillary forces in the DC simulation for similar gravitational forces as explained above.

Overall, regarding the upward and lateral solute displacement, only the DC simulation has shown considerable deviations from the other simulations. Hysteretic and nonhysteretic wetting curve simulations showed noticeable similarities in their solute transport results at that area. This was attributed to the system being mostly experiencing wetting events, in which the pores followed the wetting scanning and main wetting curves within the SWCC envelope.

Figure 4.8 shows the distribution of water content and solute vs. horizontal distance at CS2. The implication CS2 being located 50 cm below the source, of downward water and solute

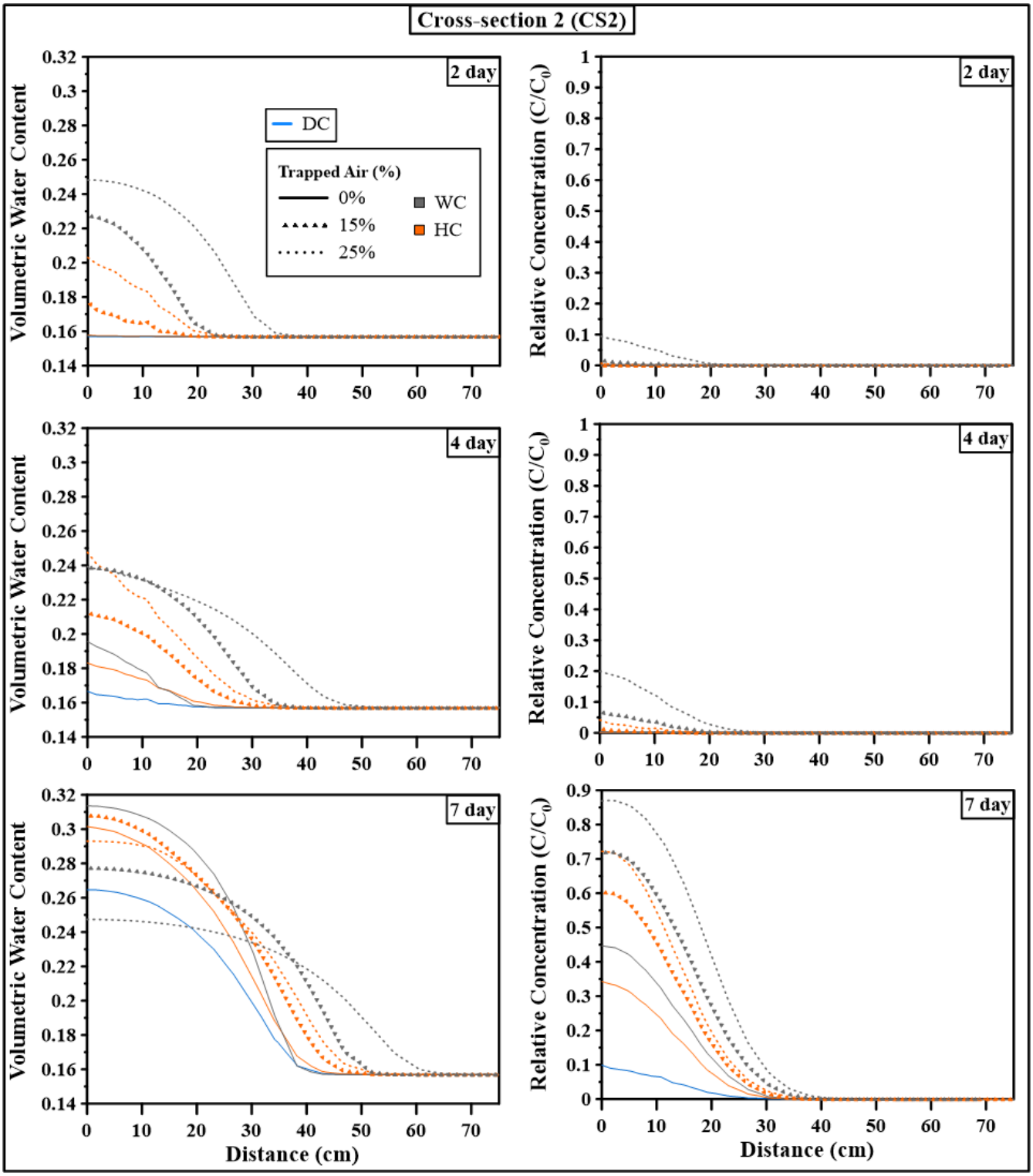

Figure 4.8 Distribution of volumetric water content (left) and solute's relative concentration (right) at CS2 (70 cm below surface) at 3-time instances: 2 day (top), 4 day (middle), and 7 day (bottom)

displacement below the source zone as well as lateral displacement relative to distance to the left boundary. The results in this figure indicate that after 2 days, the water front from the first drip irrigation reached this depth for simulations: WC-$TA_{25\%}$, WC-$TA_{15\%}$, HC-$TA_{25\%}$, and HC-$TA_{15\%}$, as indicated by the increase in the water content. Whereas the water front for DC, HC, and WC simulations, has been retarded and has not yet arrived at this depth. It can also be observed that after 2 days, only WC-$TA_{25\%}$ simulation reports the arrival of the solute front.

From Figure 4.8, it can be observed that the water content and solute concentrations increased as time progressed. The highest deviations between the different simulations can be observed after 7 days. It can be observed that for DC simulation, the solute's downward migration relative to other simulations was delayed considerably as evidenced by the lowest concentration levels ($<$ 0.1). On the other hand, considering hysteretic SWCC with no air entrapment (HC simulation) accelerated the downward migration of the solute with concentration levels at CS2 reaching $\leq$ 0.34. Considering only the wetting curve of SWCC (WC simulation) further accelerated the transport processes as the concentration levels increased to values $\leq$ 0.45. Additionally, simulating hysteretic characteristics with air entrapment further accelerated the downward migration of the solute, compared to HC and DC, as the concentration levels were $\leq$ 0.6 and 0.72 for HC-$TA_{15\%}$, and HC-$TA_{25\%}$, respectively. This trend clearly shows that there is a direct relation between the solute transport and degree of air entrapment with higher degree of entrapment results in increased solute movement. The results presented in Figure 4.8 also clearly show that simulations using the wetting branch of SWCC with air entrapment (i.e., WC-$TA_{25\%}$ and WC-$TA_{15\%}$), show the highest levels of concentration at CS2. These concentration levels were found to be $\leq$ 0.72 and 0.87 for WC-$TA_{15\%}$, and WC-$TA_{25\%}$, respectively.

Observations on solute's lateral spreading from Figure 4.8, show that there are higher deviations at CS2 between different simulations. In addition, there are correlational trends between higher concentration levels and the distance to which the solute can laterally spread. For example, after day 7, WC-$TA_{25\%}$ simulation reported the farthest solute lateral displacement to approximately 40 cm, which also coincides with its highest estimated concentration levels. Whereas DC estimated the lowest concentrations and the shortest lateral travelling distance of solute (<25 cm). To better compare between different simulations, at a relative concentration of 0.3, the lateral travelled distance is N/A, 6 cm, 11.7 cm, 15.4 cm, 16.9 cm, 19.2 cm, 22.8 cm, for DC, HC, WC, HC-$TA_{15\%}$, HC-$TA_{25\%}$, WC-$TA_{15\%}$, and WC-$TA_{25\%}$, respectively. So, simulating hysteretic characteristics have increased the lateral spreading of solute near the bottom boundary. In addition, the influence lateral displacement of solute increased after including air entrapment, with a proportional increase with the volume of air entrapment being considered. On the other hand, simulating the drying curve underestimated the lateral solute displacement near the bottom boundary, whereas, the wetting branches overestimated it, especially for branches with air entrapment. So far, simulating different characteristics have shown deviations in both vertical and horizontal (i.e., lateral) penetration depths of solute, in which vertical downward migrations were largely influenced by hysteresis and air entrapment.

4.4.2.2 Case 2

In case 2, triggering of drip irrigation was enabled while imposing an atmospheric boundary condition at the top boundary. As mentioned earlier, irrigation was triggered whenever the specified triggering node (positioned 24 cm below the surface and 4 cm horizontally from the emitter) has reached a head of -150 cm. The irrigation flux was 60 cm/day and has been

distributed over the circumference of the source. Furthermore, the relative concentration of each irrigation input was set to 1.

Figure 4.9 shows the timing of the irrigation events for DC, HC, HC-$TA_{15\%}$, and HC-$TA_{25\%}$ simulations. For wetting curve simulations (i.e., WC, WC-$TA_{15\%}$, and WC-$TA_{25\%}$), the triggering node never reached a head of -150 cm, hence irrigation was never triggered. The DC simulation [in Figure 4.9 (a)] predicted five irrigation instances. Whereas HC simulation [in Figure 4.9 (b)] predicted only two instances of irrigation. Introducing air entrapment in HC-$TA_{15\%}$ and HC-$TA_{25\%}$, predicted only one triggered irrigation event. It is also worth noting that irrigation events have not occurred at a similar time, specifically for DC simulation. This can be attributed to the unique characteristics of each simulation, resulting in different water content distribution, hence different irrigation time instances. One way to explain why the DC simulation has predicted

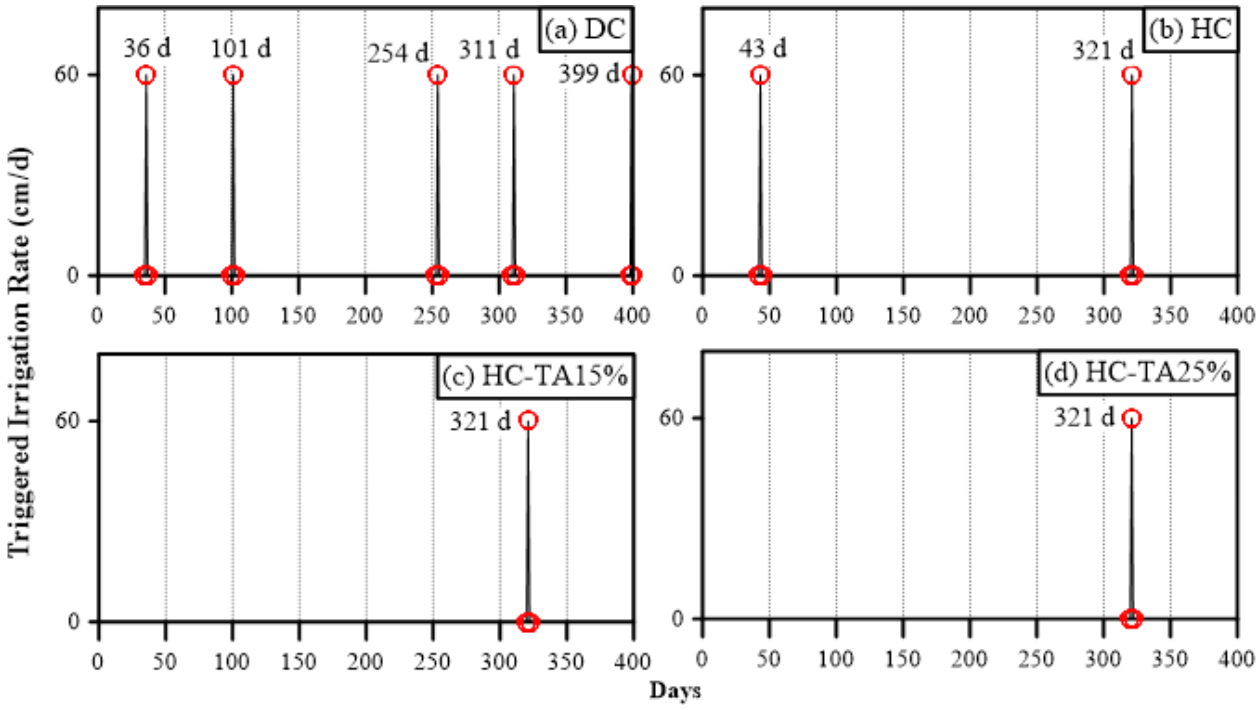

Figure 4.9 Instances of triggered irrigation (Note: simulations where irrigation did not trigger are not plotted)

more irrigation instances is through the water balance at the ground surface as presented in Figure 4.10. As discussed earlier in the previous section, DC simulation tends to retain more moisture near the ground surface as well as enhance the upward water movement, which is attributed to DC's higher water retention properties ($\alpha^w = 2\alpha^d$). This results in moisture becoming more readily available for evaporation in the upper layers of the system. For these

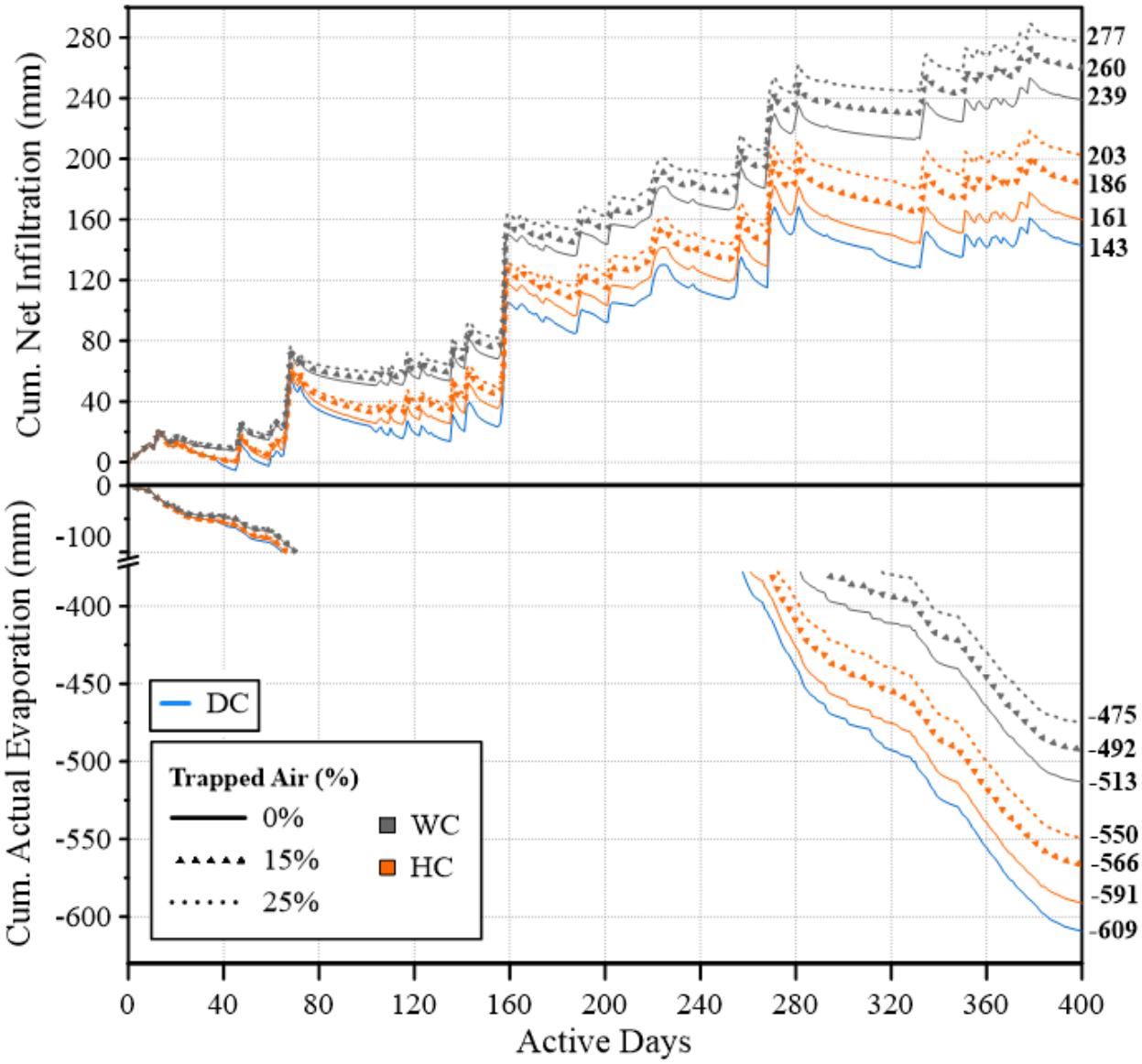

Figure 4.10 Estimated water balance at the surface and bottom flux of the loam's profile – Case 2

reasons, DC simulation estimated the largest actual evaporation (*AE*) rate, and accordingly, the lowest net infiltration (*NI*) rate. The higher evaporation rates have made the triggering node more susceptible to drier conditions and larger suction ranges nearby. On the other hand, the wetting simulations are characterized by lower water retention properties. To showcase this, Figure 4.11 is presented which plots the paired water content-suction at the triggering node throughout the entire simulation time. The figure shows that the triggering node never reached the triggering suction, explaining why irrigation never triggered. It is because WC (relative to DC) is characterized by lower suction for the same water content. Additionally, for a small change in the water content, WC's SWCC is characterized by a relatively smaller change in suction. These mechanisms enhanced the water flow in wetting curve simulations, resulting in less moisture retained in the upper layer, hence lower *AE* and higher *NI* (Figure 4.10). Whereas HC simulation resulted in the formation of scanning wetting curves (Figure 4.11), which in return reduced water

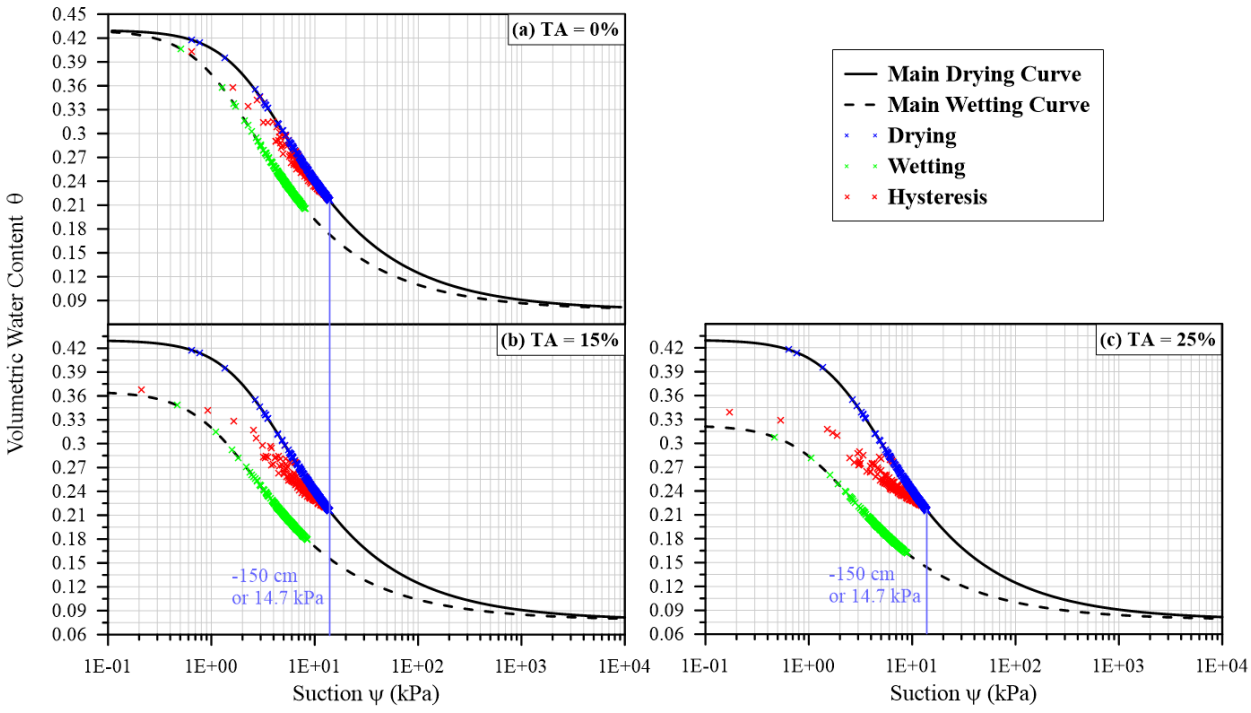

Figure 4.11 Loam's SWCC and paired water content and suction data at the triggering node

retention relative to DC and accelerated water flow. This resulted in lower moisture retention at the surface, lower *AE*, and higher *NI*. Consequently, this has lowered the suction ranges, or in other words, minimized the chances for HC to reaching -150 cm head, hence less occurrences of triggered irrigation. Compared to WC, the formation of scanning drying curve in HC caused the water retention properties to relatively increase explaining why *NI* is lower and why a few triggered irrigation instances occurred in HC simulation.

The introduction of air entrapment in the hysteretic simulations (HC-$TA_{15\%}$ and HC-$TA_{25\%}$) has further reduced the instances of triggered irrigation (Figure 4.9) to one as opposed to two for HC simulation without air entrapment. That is because air entrapment's contribution in widening the hysteresis envelope, in which the scanning curve is formed closer to the wetting branches (Figure 4.11). These types of scanning curves, after air entrapment, are characterized with an even smaller change in suction for the same water content change. This correlation is true for larger degree of air entrapment (i.e., HC-$TA_{25\%}$). So, simulating hysteresis with larger degree of air entrapment translated to enhancement of water flow, lower *AE*, higher *NI* (Figure 4.10), thus less occurrences of triggered irrigation than DC and HC.

In support to this, Figure 4.12 plots the temporal progression of water content and suction at the triggering node, presented from day 280 to 334. It shows that, since day 283, the triggering node in the drying and hysteretic (with and without air entrapment) simulations are progressively losing moisture with water content converging to the same values. However, suction varied across those simulations. Only DC triggered irrigation earlier (at day 311); this is because suctions in DC were greater beforehand, therefore reached -150 cm sooner. This is supported by DC's SWCC being characterized by larger suction for the same water content. Whereas since the

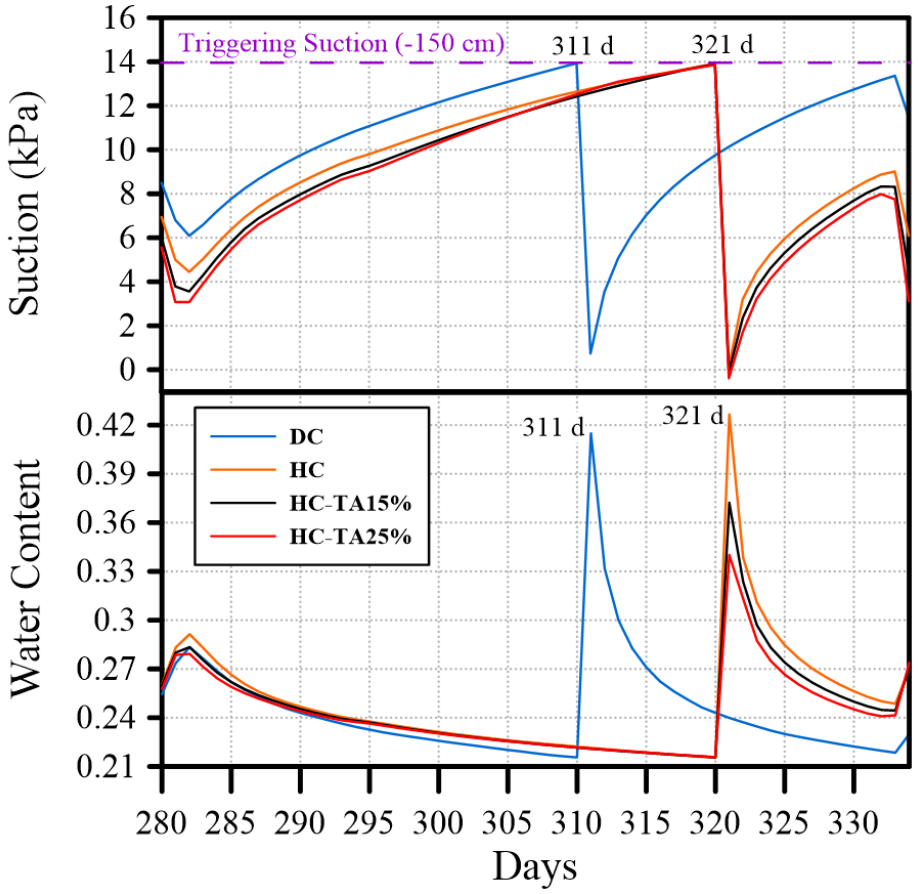

Figure 4.12 Suction and volumetric water content at the triggering node vs. days (day 280 to 334)

SWCC of the hysteretic simulations, especially with air entrapment, is characterized by smaller suctions for the same water content, they witnessed a delay which required further drying of water and buildup of suction to cause triggered irrigation (day 321). Upon irrigation on day 321, the suctions are the same across HC, HC-$TA_{15\%}$, and HC-$TA_{25\%}$, however, the water content lowered down in that same order, which is attributed to the increasing degree of air entrapment and the resulting enhancement of flow. These observations clearly show that simulating DC can more readily trigger irrigation, whereas simulating hysteresis, especially with air entrapment, can less readily trigger irrigation.

The discrepancies between the occurrences of irrigation events, resulted in a completely dissimilar solute distributions for different simulations; as shown in Figure 4.13 after 400 days of land-climate interaction. The DC simulation predicted a substantially higher concentration levels within the profile compared to other simulations. This is due to DC's five instances of triggered irrigation events, as opposed to only two instances for HC simulation. The HC-$TA_{15\%}$ and HC-$TA_{25\%}$ simulations reported only one irrigation instance, which resulted in much lower concentration levels. The zero concentration levels profiles for WC, WC-$TA_{15\%}$, and WC-$TA_{25\%}$ simulations are result of no triggered irrigation events.

4.4.2.3 Case 3

Case 3 considers a case in which the irrigation inputs were prescribed while considering an atmospheric BC at the top of the domain. The irrigation inputs are from the results of DC simulation of case 2, as presented in Figure 4.9a. It was accordingly applied to all simulations. The objective of case 3 is to compare the impact of simulating different hydraulic characteristics on solute transport processes under a soil-atmosphere boundary and prescribed irrigation inputs.

Figure 4.14 through Figure 4.17 show the solute distribution within the soil profile after 100, 260, 300, and 400 days, respectively. The days were selected arbitrarily (every after 100 days), except for day 260 which was deliberately selected to compare solute profiles shortly after an irrigation event. It is important to note that relative concentrations near the surface can reach values higher than 1, as occurred in Figure 4.14, Figure 4.16, and Figure 4.17. This is attributed to the nature of the top solute boundary condition, where moisture leaves across the evaporative boundary, then solute must remain behind causing relative concentrations to increase > 1 (Šimůnek 2013). Overall, the figures showed dissimilar distributions of solute when simulating

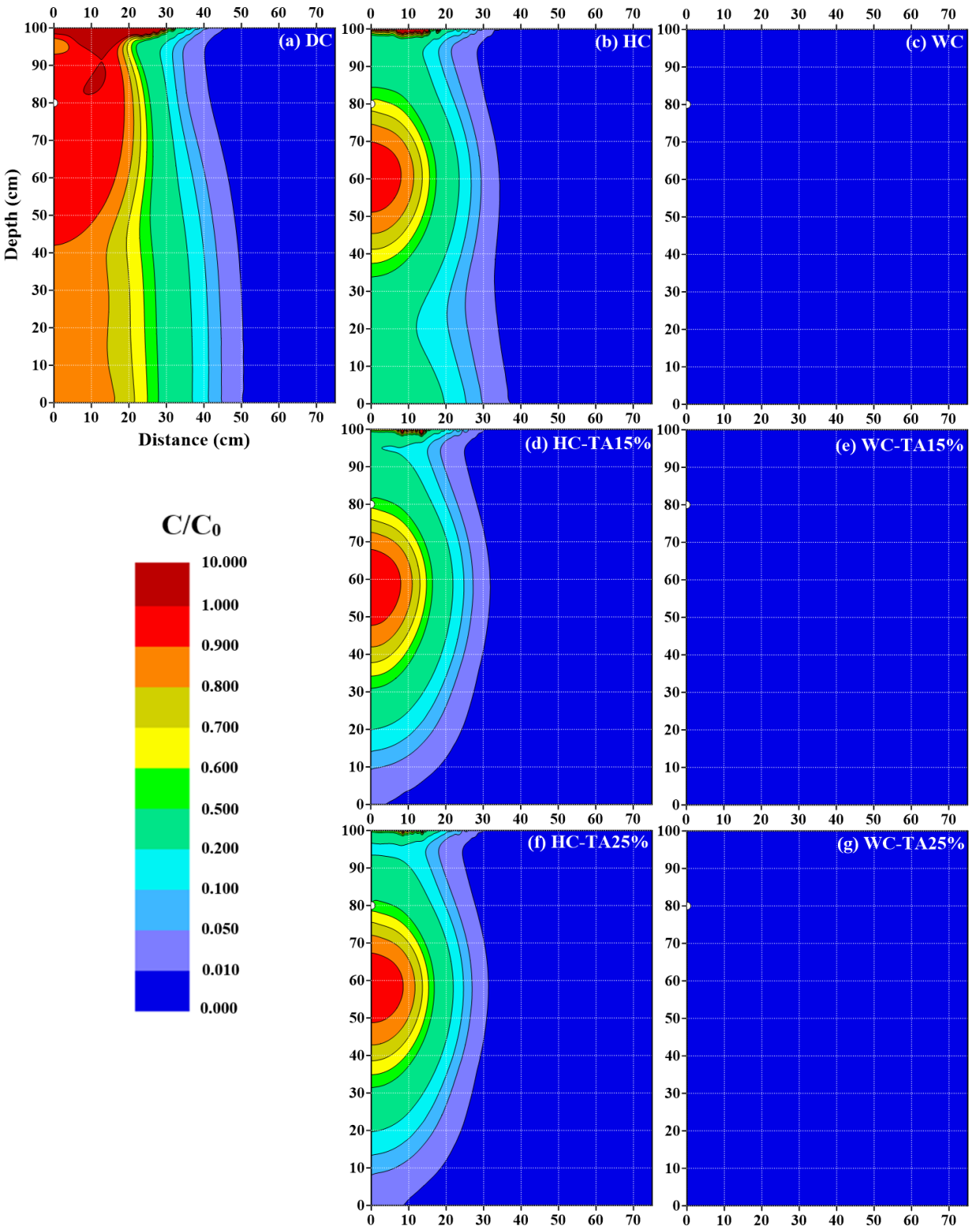

Figure 4.13 Distribution of solute after LCI of 400 days using different hysteretic and nonhysteretic characteristics - Case 2

different hysteretic and nonhysteretic hydraulic characteristics. The most prominent observations are attributed to the retardation effects caused by simulating nonhysteretic drying curve characteristics (DC). In which, the results for the DC simulation showed larger accumulation of solute in the vicinity of the ground surface. This is indicative of upward movement of water and solute due to higher capillarity in the system and more moisture loss at the ground surface due to atmospheric interaction (high *AE* and low *NI;* refer to the water balance at the surface, Figure B4, from Appendix B). Moreover, substantial acceleration of solute downward advancement was observed when simulating wetting branches (WC), especially with air entrapment (WC-$TA_{15\%}$ and WC-$TA_{25\%}$). Hysteresis is found to increase the downward advancement of solute relative to DC and retard relative to wetting curve simulations. Additionally, there is also a clear correlation of greater solute penetration depths with the increase in the degree of air entrapment.

Figure 4.14 shows the solute distribution after 100 days following the first irrigation input at the day 36. From this figure it is evident that the solute has reached the bottom boundary for all simulations except for the DC simulation.

Special attention must be paid, the concentration levels near the bottom boundary were the highest for DC simulation after 300 days (Figure 4.16). This is due to DC's exhibited retardation effects, in which preceding the solute inputs have lagged behind. The opposite is observed in hysteretic and nonhysteretic wetting curve simulations, with and without air entrapment, where more solute masses have discharged out of the system leaving behind concentration levels lower than that in DC simulation. To illustrate, there are two zones of high concentrations in DC simulations that remained within the domain. Whereas in HC, HC-$TA_{15\%}$, HC-$TA_{25\%}$, WC-$TA_{15\%}$, and HC-$TA_{25\%}$ simulations, the second zone has moved past the bottom domain boundary with only one zone of high concentrations remaining behind. Compare Figure 4.16

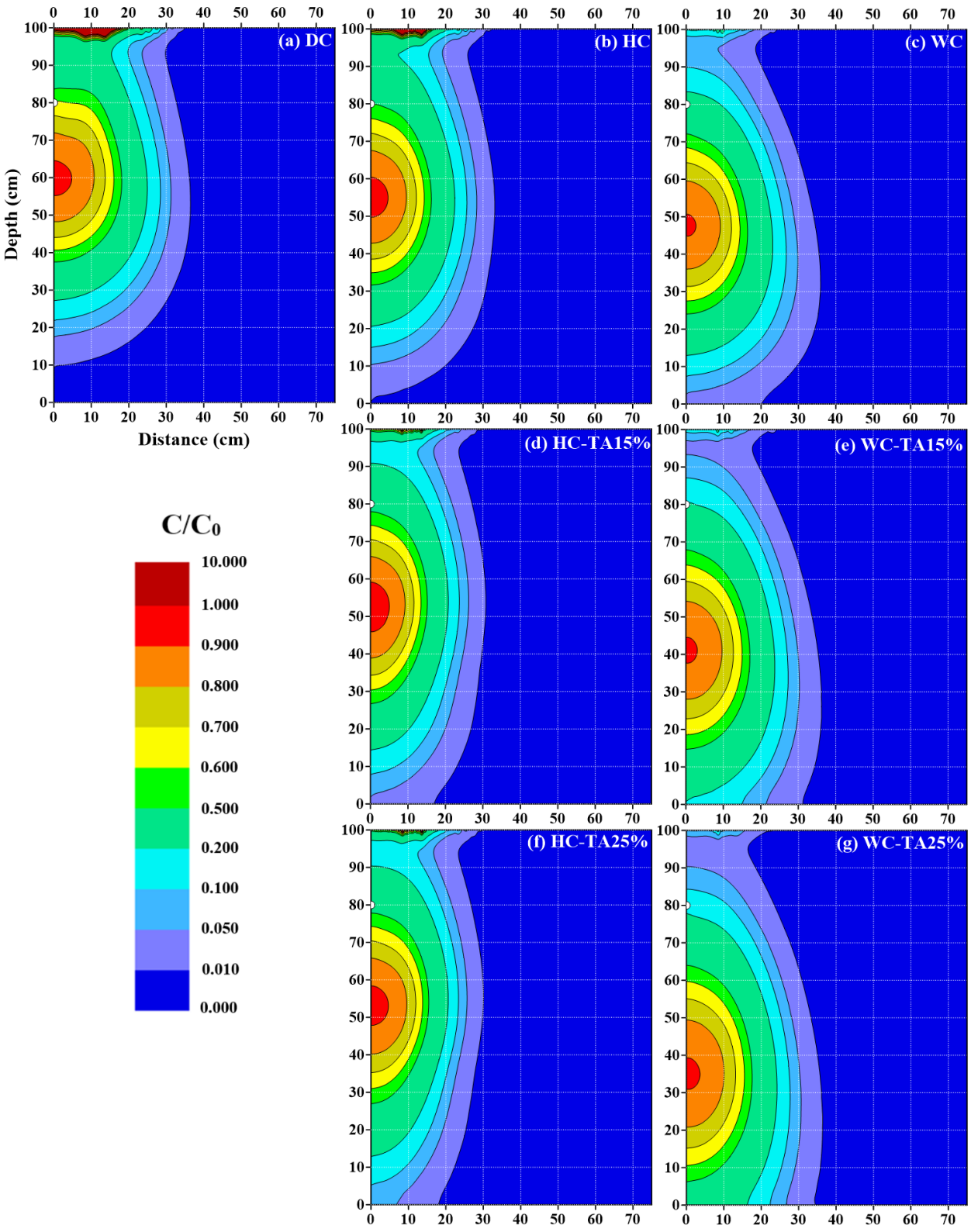

Figure 4.14 Distribution of solute after LCI of 100 days using different hysteretic and nonhysteretic characteristics - Case 3

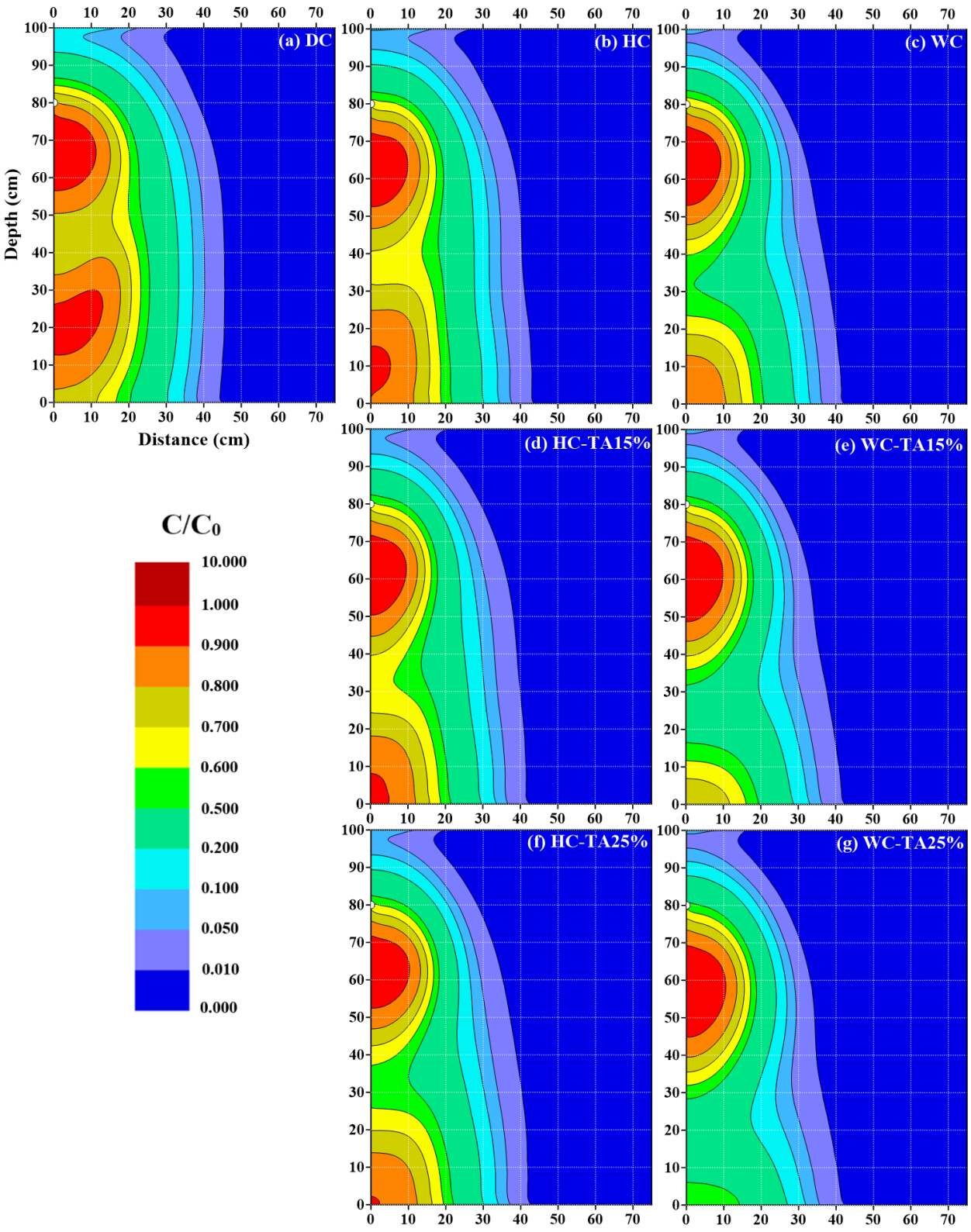

Figure 4.15 Distribution of solute after LCI of 260 days using different hysteretic and nonhysteretic characteristics - Case 3

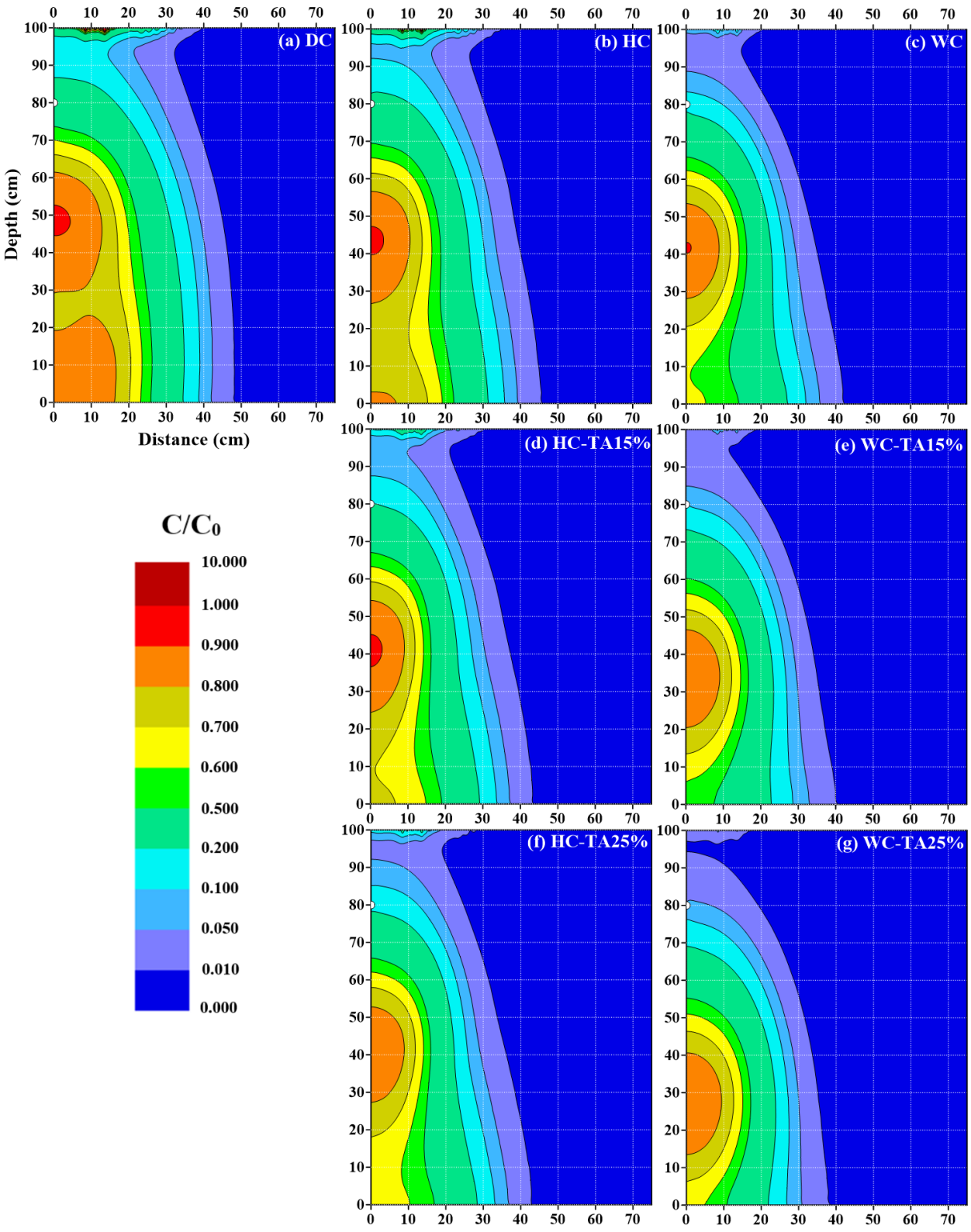

Figure 4.16 Distribution of solute after LCI of 300 days using different hysteretic and nonhysteretic characteristics - Case 3

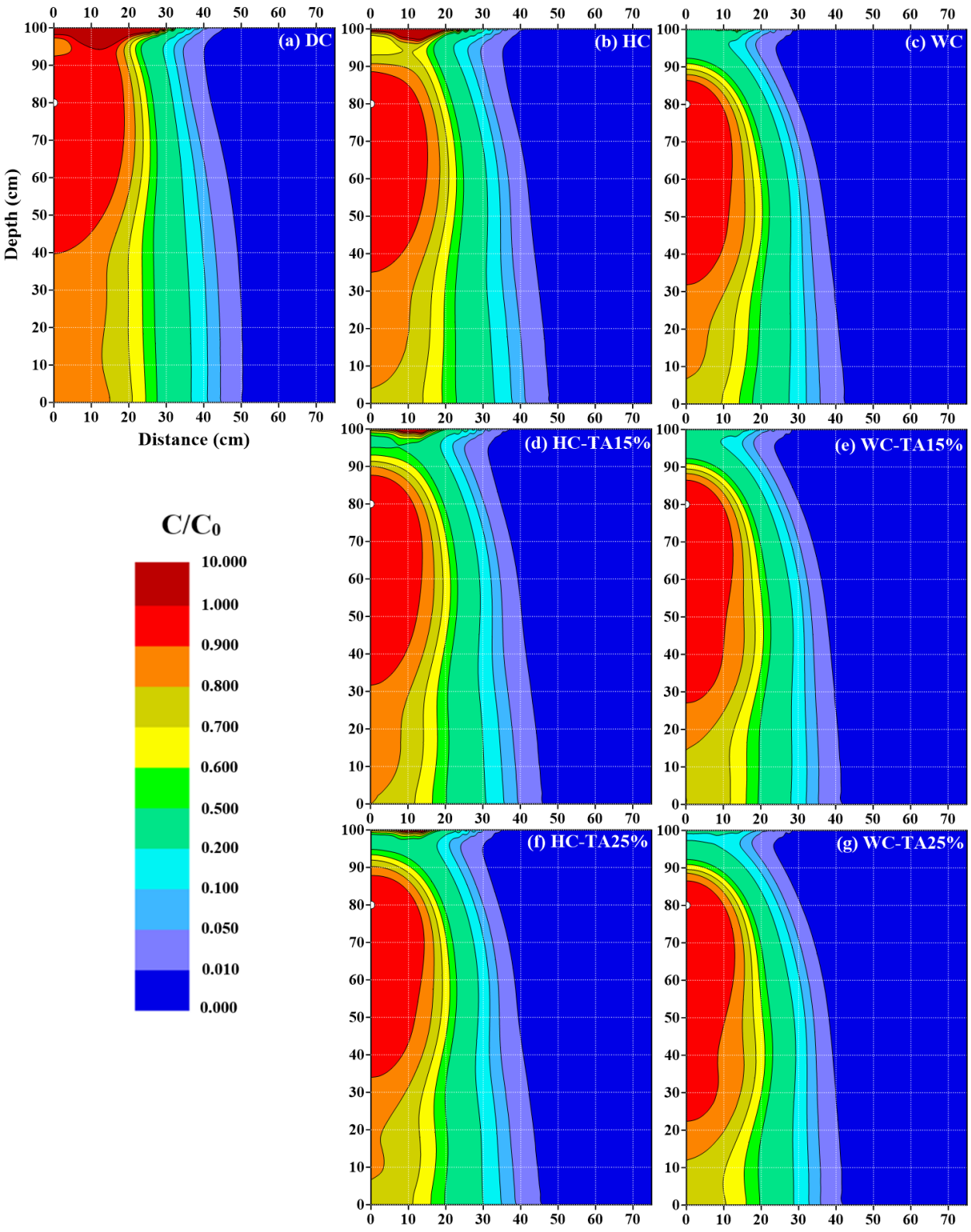

Figure 4.17 Distribution of solute after LCI of 400 days using different hysteretic and nonhysteretic characteristics - Case 3

(day 300) against Figure 4.15 (day 260) to witness the advancements of these zones. This can be attributed to prediction of lower *NI* and lower advective flux of the solute by the DC simulation.

Figure 4.17 shows the distribution of solute after 400 days. The largest accumulation of solute at surface is observed for DC simulation, whereas lesser accumulation is for HC. In addition, a larger lateral spreading of solute observed for DC, which is attributed to DC's tendency to retain/retard solute thus larger lateral spreading. Another notable observation is for higher concentrations found with depth for DC (orange contour), these concentrations are deemed leftover explained by DC's retardation effects.

Figure 4.18 and Figure 4.19 shows solute's relative concentration vs. horizontal distance at two horizontal cross-sections: CS1 and CS2, located at the depths of 10 and 98 cm below the surface, respectively. These plots present concentration values at these cross-sections at 100, 260, 300, and 400 days.

Since CS1 is located 10 cm above the source, Figure 4.18 presents the upward and lateral migration of the solute. It can be observed that the DC simulation estimated the highest concentration levels compared to simulations run with other hydraulic characteristics. This is indicative of DC's more dominant upward solute displacement response. Again, this is consistent with DC being characterized with higher water retention properties and associated higher actual evaporative fluxes, which tends to displace the moisture and solute in the upward direction and limits the downward displacement due to reduced net infiltration. For the HC simulation, the upward displacements are less prominent than DC simulation, as indicated by the lower concentration levels. This can be attributed to the fact parts of the domain experiencing wetting

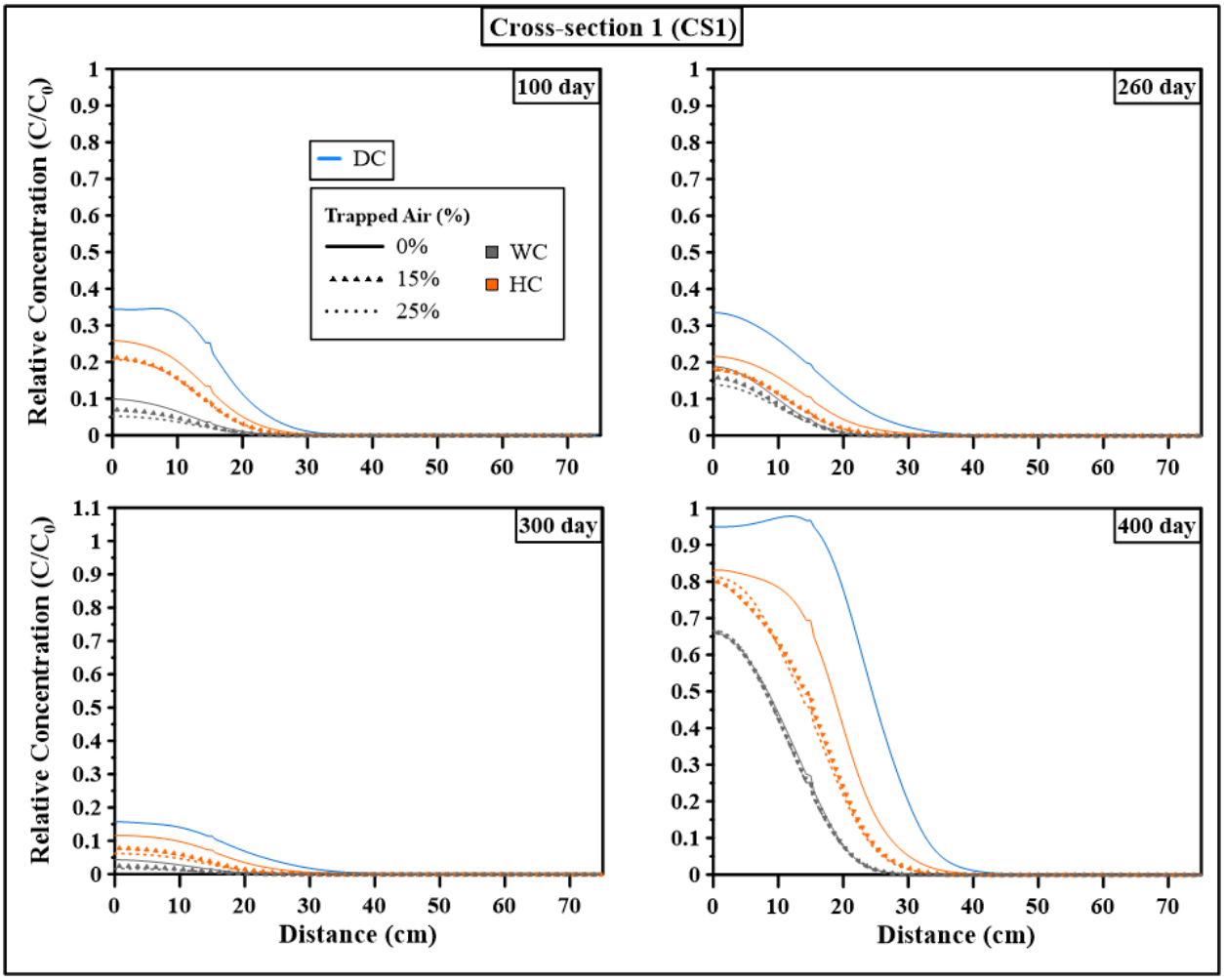

Figure 4.18 Distribution of solute's relative concentration at CS1 (10 cm below surface) at 4-time instances: 100 day, 260 day, 300 day, and 400 day – Case 3

will follow either the main wetting curve or scanning wetting curves, reducing the effect of the capillary forces, and resulting in amplified downward movement of water and solute.

Introducing air entrapment in the hysteretic characteristics has increased the magnitude of the wetting curve and scanning wetting curves. In return, this enhanced more rapid and larger downward advective fluxes; hence, it reduced the upward flow and transport response. In Figure

4.18, HC-$TA_{15\%}$ and HC-$TA_{25\%}$ simulation estimated a notably lower effects of upward solute displacements, depicted by their lower concentrations at CS1 compared to HC. However, the increase in air entrapment of 10% (from 15% to 25%) had minimal effect on the upward solute displacement. On the other hand, simulations carried out using the wettings characteristics of the SWCC resulted in the lowest upward displacement response of the solute. However, this response appears to be not sensitive to variations in the air entrapment.

Similar to Case 1, DC simulation in case 3 estimated the farthest lateral migration of solute near the surface (i.e., CS1). There is a clear correlation between the accumulation of solute and lateral spreading of solute, as evidenced by DC's response. Again, this is anticipated since the downward advective fluxes in DC simulation were smaller, allowing for higher chances of lateral solute movements. Furthermore, as the downward advective fluxes increased, the distance upon which the solute travelled laterally decreased. This trend is consistent with considerations of hysteresis and air entrapment in the hydraulic characteristics. For example, after 400 days and at the relative concentration of 0.5, the lateral travelled distances are 25 cm, 19 cm, 15 cm, 13 cm for DC, HC, HC-$TA_{15\%}$, and HC-$TA_{25\%}$, respectively. Whereas the lateral travelled distance was considerably underestimated by WC, WC-$TA_{15\%}$, and WC-$TA_{25\%}$ simulations, with a value of only 8 cm for all three.

Figure 4.19 shows the distribution of solute at CS2 which is 78 cm below the source and is representative of lateral migration of solute near the bottom domain. At day 100, the lateral spreading of solute in WC-$TA_{15\%}$, and WC-$TA_{25\%}$ were the highest, whereas in other simulations the solute still lagged behind, hence showing no signs of lateral spreading. The lateral spreading of solute in all simulations are relatively the same with minor differences after 260 days. This was anticipated since at day 260, the domain followed the third irrigation input shortly after (day

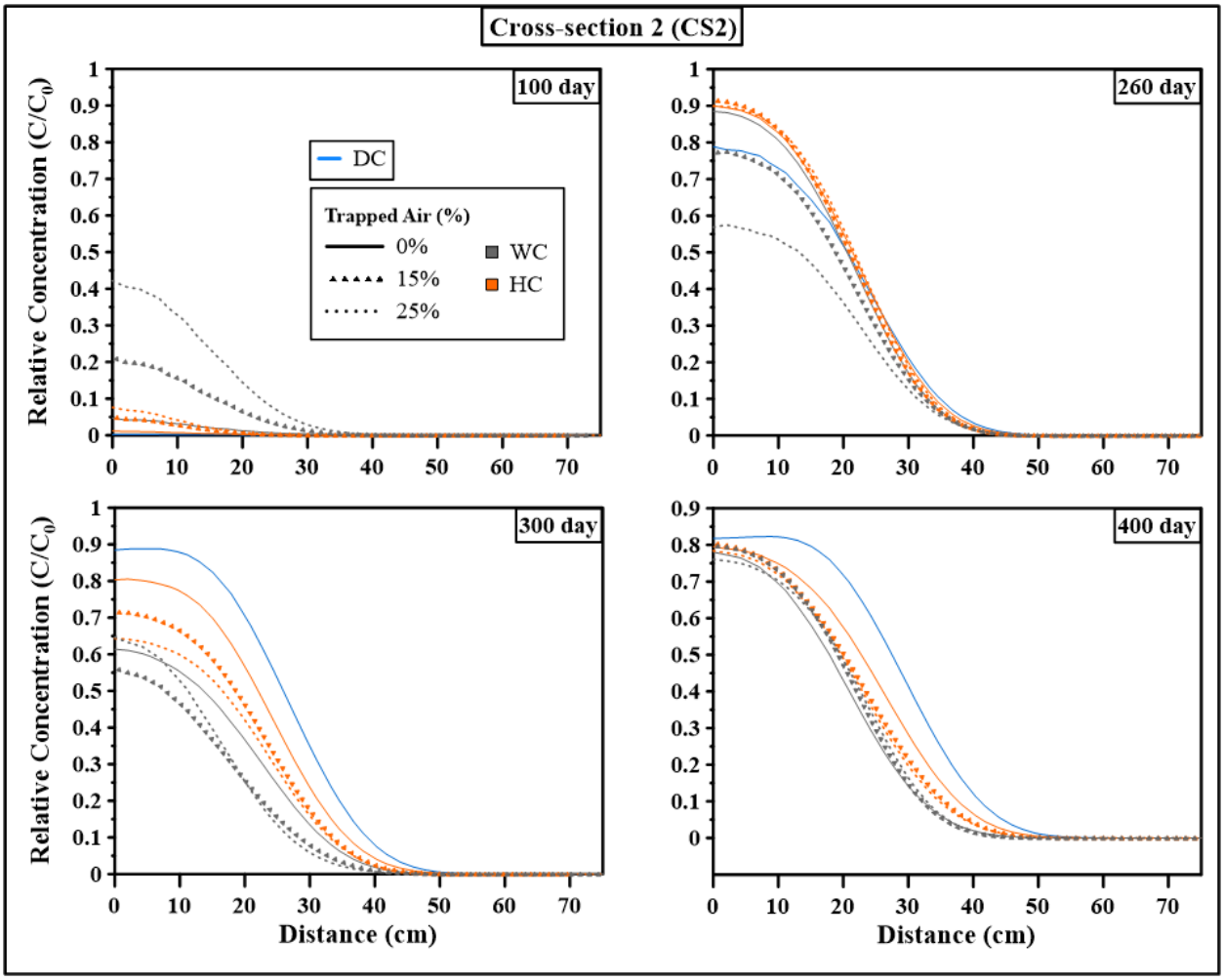

Figure 4.19 Distribution of solute's relative concentration at CS2 (98 cm below surface) at 4-time instances: 100 day, 260 day, 300 day, and 400 day – Case 3

254). However, deviations are observed the highest after 300 days. Higher deviations at this time was anticipated since it followed the latest irrigation input (day 254) by 46 days, allowing more time to exhibit different migration response for different hydraulic characteristics. At this time, DC reported the highest concentrations compared to other simulations, due to DC's tendency to retard and accumulate concentrations. This translated to higher lateral spreading of solute for DC. On the other hand, the tendency for hysteresis and air entrapment to trigger larger solute

advective flux, resulted in faster discharge (through bottom boundary) leaving lower concentrations within the domain, thus explaining the lesser lateral spreading compared to DC and HC (without air entrapment). Simulating wetting branches, especially after air entrapment, underestimated the lateral spreading of solute due to their overestimation of faster discharge.

After 400 days, DC reported the highest lateral spreading, whereas other results showed comparable response with lesser spreading than DC. Notice, that the day 400 followed the last irrigation input by 1 day. Similar to what has been observed at day 300, it is anticipated that deviation between simulations, in terms of lateral spreading, will overtake should the simulation proceed with time.

Figure 4.20(a) and Figure 4.20(b) shows the discharge rates of water and solute, respectively, through the free draining bottom boundary. From Figure 4.20(a), the discharge flux rate of water is consistent with the water balance trends (refer to the water balance at the surface, Figure B4, from Appendix B). The bottom water flux values from DC and HC simulations are relatively

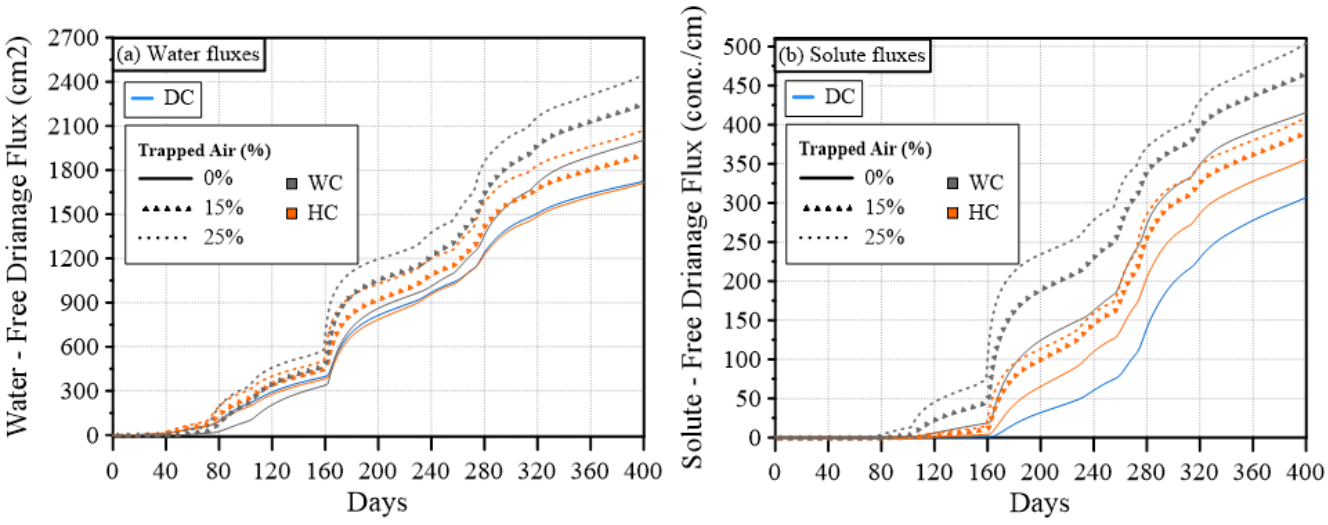

Figure 4.20 Cumulative free drainage fluxes of (a) water and (b) Solute - Case 3

similar due to their similar *NI* values. Simulating characteristics of nonhysteretic DC have underestimated the discharge flux, which is consistent with their lower *NI* value. On the other hand, considering both hysteresis and air entrapment have increased the value of the bottom water fluxes, in which the value was also proportional to increases in the volume of air entrapment being considered. Also, simulating characteristics of the nonhysteretic wetting branches, especially with air entrapment, have overestimated the *NI*, this has also led to overestimating the bottom water fluxes as shown in Figure 4.20(a).

In most cases, the trends of solute discharge fluxes or rates [from Figure 4.20(b)] are consistent with the water fluxes trends [from Figure 4.20(a)]. An exception was observed where deviations between different simulations were more noticeable for solute discharge than water discharge. Additionally, higher deviations between DC and HC simulation, where total solute fluxes in the HC simulation increased by 16.0% relative to the total solute flux in DC simulation. This increase of the solute flux, due to incorporation of hysteretic characteristics, was evident even though the cumulative water fluxes [Figure 4.20(a)] are relatively equal for both simulations. This evidence demonstrates that the impact of hysteresis on solute transport can manifest independently, thereby contributing to the hysteresis effect on water fluxes. As previously explained, changes in the volumetric water content due to hysteresis can independently influence the pore-velocity term from the advective-dispersion equation.

Furthermore, from Figure 4.20, simulating hysteresis with air entrapment have increased the bottom fluxes of both water and solute, and the rates were proportional for larger the volume of trapped air. Simulating HC-$TA_{15\%}$ and HC-$TA_{25\%}$ estimated increase of the total solute flux (relative to DC) by 27.3% and 33.1%, respectively. On the other hand, simulating WC, WC-

$TA_{15\%}$, and WC-$TA_{25\%}$ have led to considerable increase by 35.5%, 52.0%, and 64.4%, respectively.

4.5 Summary and Concluding Remarks

In the scope of this research, a focused investigation was conducted on a subsurface drip irrigation system. The intention was to thoroughly investigate the effects of hysteresis and air entrapment of SWCC on the complex intricacies of solute transport dynamics. Three different cases were considered. Case 1 involved subsurface drip irrigation with predetermined flux inputs; Case 2 considered a subsurface drip irrigation system where triggering of water and solute flux was influenced by the interaction of the imposed atmospheric boundary condition (BC). The atmospheric BC used precipitation and potential evaporation data from Bighorn Dam, Alberta, Canada. The climate of Bighorn Dam can be classified as sub-humid climate. Case 3 involved a predetermined drip irrigation flux inputs with the consideration of an atmospheric BC. For each case seven different simulations were carried out. These simulations encompassed three distinct scenarios involving hysteresis: without air entrapment (HC) as well as with 15% and 25% degrees of air entrapment (HC-$TA_{15\%}$ and HC-$TA_{25\%}$). Furthermore, four nonhysteretic simulations were executed including the initial drying curve (DC), alongside three additional nonhysteretic simulations utilizing the primary wetting curve, both with air entrapment (WC-$TA_{15\%}$ and WC-$TA_{25\%}$) and without air entrapment (WC).

The results of case 1 showed that the DC simulation predicted retardation in the downward solute migration, where most of the solute was concentrated near the surface and around the source. On the other hand, the WC simulation predicted accelerated downward migration of solute owing to lower water retention properties. The HC simulation indicated accelerated solute

transport in comparison to DC simulation, whereas it slightly retarded behind the WC simulation with relatively small differences. The similarity between the HC and WC simulation can be attributed to the fact that the system was mostly rewetting, and the slight retardation of HC is indicative of the formation of drying scanning curves during the redistribution periods (i.e., during gravity drainage). Considering larger volume of air entrapment in the hysteretic simulations resulted in greater flow rates and thus deeper solute migration. The hysteretic simulations with air entrapment have also slightly retarded behind their counterparts of wetting curve simulations. As reported in the literature, hysteretic simulations had higher similarities to WC simulations. This aligns with the findings from case 1 in the current study, however, it was only because the system's tendency for wetting events was a contributing factor, leading mostly to the formation of main wetting and scanning wetting curves. However, it's essential to note that this observation may not hold true when intermittent flow plays a significant role, especially under dry climatic conditions where the imposition of drying curve and formation drying scanning curves take over. Generalizing a specific hysteretic effect across diverse problems is cautioned against, as its manifestation is profoundly influenced by the unique characteristics of each problem.

The results of case 2 showed that simulating different hydraulic characteristics altered the water balance at the surface contributing to varying occurrences of triggered irrigation. Relative to hysteretic simulations (especially with air entrapment), simulating DC resulted in an overestimation of the occurrence of triggered irrigation events, stemming from an increased projection of surface evaporation rates and drier, higher suction ranges. This overestimation had adverse effects, causing increased irrigation triggers, higher relative concentration profiles, and larger solute fluxes exiting through the bottom domain. Simulating hysteretic characteristics,

especially when considering larger volumes of trapped air, resulted in reduced occurrences of triggered irrigation events, stemming from its lower water retention properties and lower estimates of evaporation rates. This diminished the solute concentration in the profile and solute discharge fluxes at bottom of the domain. Simulating nonhysteretic wetting curves did not result in any triggered irrigation events. This studied case highlights that employing various simulations (hysteretic vs. nonhysteretic/air entrapment vs. without air entrapment) yields entirely distinct irrigation instances and water content/concentration profiles.

The intent of case 3 was to study differences between simulations based on their solute transport processes rather than their influence on triggering events. The deviations between water and concentration profiles and their trends for case 3 are somewhat similar to case 1. However, the application of atmospheric BC amplified the differences between the various simulations. This is owed to dissimilar water balances at the ground surface for different simulations. For the DC simulation, higher capillary forces resulted in larger estimates of actual evaporation indicating larger upward solute displacement response and substantial retardation of downward solute migration. Also, the DC predicted more lateral solute movement when compared to other simulations, attributed to its influence for solute retardation and the resulting accumulation of solute throughout the domain. Reduction in solute concentrations near the surface was predicted when hysteretic characteristics of SWCC were taken into consideration. This is the result of the lower actual evaporation resulting in larger net infiltration and associated downward advective flux and discharge. An increase in the net infiltration was proportional to volume of trapped air hence resulting in larger the advective fluxes of solute. In other words, when considering lower air entrapment volumes, or more importantly when ignoring air entrapment, the hysteretic simulations underestimate the downward solute migration. Simulating water flow and transport

in which only wetting branch(s) of SWCC is used, especially for larger volume of trapped air, predicts largest estimates of advective flux. Furthermore, it was observed that the impact of hysteresis and air entrapment on solute transport can manifest independently, in addition to being influenced by the interplay of water fluxes with hysteresis and air entrapment. In conclusion, the findings underscore the equally detrimental effects of neglecting both hysteresis and air entrapment. Inaccuracies associated with these factors can result in improper assessments and designs of subsurface drip irrigation systems, misestimations in trigger timing and irrigation occurrences, inaccurate numerical estimates of plant water and solute intakes, and miscalculations in potential contamination levels in groundwater and aquifers.

CHAPTER 5: Effect of Hydraulic Hysteresis with Air Entrapment on Slope Stability Assessments Under Varying Climatic Conditions

5.1 Abstract

Slopes are exposed to the atmosphere and undergo frequent drying and wetting cycles due to the atmospheric conditions. In unsaturated soil slopes, soil hydraulic hysteresis significantly influences the water balance at the ground surface, soil suction distribution within the slope, shear strength of the slope material, and consequently, the resulting factor of safety (FOS) of the slope. In most cases, hydraulic hysteresis is ignored in slope stability analyses considering soil-atmosphere interaction, and instead, the drying branch of the soil water characteristic curve (SWCC) is used to describe water flow during intermittent and variable wetting and drying. This research examines the effect of soil hydraulic hysteresis with air entrapment on the stability of a typical highway embankment slope in the province of Ontario, Canada. Multiyear measured climate data is used in a variably saturated hysteretic flow model to assess the water balance at the ground surface and soil suction distribution within the embankment. The numerical model is capable of simulating the soil-atmosphere boundary and taking into consideration the hysteresis and air entrapment in the soil hydraulic functions. The slope stability assessments were carried out using the Limit Equilibrium Method (LEM). A correction equation is proposed in this thesis for soil suctions, allowing existing commercial LE software to consider hysteresis and air entrapment in the unsaturated shear strength model of Vanapalli et al. (1996). The results indicate that ignoring both hysteresis and air entrapment effects in soil hydraulic functions, could potentially result in overestimation of the FOS. The results showed that accounting for hysteresis

and air entrapment have led to cases with reductions in the FOS (relative to DC) of 15.8% under Toronto's climate and 21.3% under North Bay's climate. Some of the slopes have even failed to meet the stability criteria after introducing hysteresis and air entrapment. This research addressed the necessity to include hysteresis and air entrapment in a coupled hydrological-stability model, as ignoring both effects could lead to inaccurate assessment of the slope stability, where the slope can be deemed overly stable.

5.2 Introduction

Slope failures can result from various phenomena and combinations of factors, such as geological and topographical characteristics (e.g., slope surface cover, loss of vegetation, earthquakes, and volcanic eruptions), hydrological characteristics (e.g., climatic factors such as snowmelt, rainfall, and evaporation), and human activities (Kang et al. 2020). In recent years, there has been increasing attention given to numerical modeling studies that assess the stability of slopes while considering climate variables. These studies are crucial because slopes are exposed to climate fluctuations and rainfall infiltration (Zaky and Oh, 2017). Rainfall-induced slope failures are common and have been regularly reported worldwide (Haque et al. 2019). Such failures can be highly destructive, leading to property damage and posing a potential risk to human life (Lee and Ho 2009). This is especially evident in regions subjected to high rainfall seasons (Huat et al. 2004, Ebel et al. 2010, Ma et al. 2011). Historical incidents consistently demonstrate that slope failures tend to occur during or shortly after rainfall events (Gavin and Xue 2008).

The Factor of Safety (FOS) is a commonly used parameter to assess the stability of a slope. It is defined as the ratio of the ultimate shear strength to the mobilized shear stress at a presumed failure surface (Godt et al. 2009, Lee and Ho 2009, Tsai 2011, Ma et al. 2011, Lu et al. 2012,

Cheng and Lau 2014). Infiltration and variably saturated flow in slopes plays a crucial role in influencing the value of the Factor of Safety (Chen and Zhang 2006, Rahardjo et al. 2010). This influence occurs through various mechanisms, including changes in porewater pressure and unsaturated shear strength, due to water exchange at the soil-atmosphere boundary (Ma et al. 2011, Baninajarian 2020). The water retention properties of the soil also contribute to these changes (Gui et al. 2000, Le et al. 2011, Zhu et al. 2013, Zhang et al. 2015, Liu et al. 2017) in conjunction with the prevailing climatic conditions. Climate and hydrological processes, including precipitation, evaporation, infiltration, and groundwater flow, possess the capability to modify water storage within a slope. Notably, the infiltration process initiates a wetting front, leading to alterations in the volumetric water content (VWC) and the potential reduction of soil suction. As a consequence, the decrease in soil suction diminishes the tension force at the air-water interface, resulting in a decline in shear strength (Krahn et al. 1989, Rahardjo et al. 1995, 2004, Kim et al. 2004, Travis et al. 2010, Ma et al. 2011, Fredlund et al. 2012, Kristo et al. 2019). Noteworthy studies conducted by Rahardjo et al. (1995), Fourie et al. (1999), Likos and Lu (2004), Godt et al. (2009), Tsai and Chen (2010), and Fredlund et al. (2012) have documented that these alterations have the potential to initiate slope instabilities. Consequently, a comprehensive understanding of the processes influencing soil suction and shear strength in slopes is imperative for identifying and mitigating potential instabilities.

Matric suction (or soil suction or negative pore-water pressure) and normal stress are two commonly used stress state variables within the unsaturated soil mechanics framework (Fredlund and Morgenstern 1977, Fredlund et al. 1978, Fredlund and Rahardjo 1993). Soil suction holds significance as a key parameter in the soil-water characteristic curve (SWCC). This curve represents a nonunique functional relationship between volumetric water content (VWC) and soil

suction, serving as the cornerstone for understanding water flow processes in unsaturated soils. As previously discussed, soil water content undergoes continuous fluctuations under the influence of prevailing climatic conditions, impacting soil suction (via the soil-water characteristic curve), material mass, stress state, and the suction component of shear strength (Liu et al. 2017). From a slope stability perspective, the unsaturated shear strength exhibits a non-linear and direct correlation with the SWCC (Fredlund et al. 1996, Vanapalli et al. 1996). Consequently, the SWCC serves as the nexus that links unsaturated seepage processes with slope stability analyses.

In most slope stability studies, it is a common practice to assume a nonhysteretic SWCC, even though, the SWCC is observed to be naturally hysteretic (Tami et al. 2004, Liu et al. 2015, 2017). For example, assuming that the drying branch of the hysteretic SWCC is representative of both wetting and drying processes (i.e., sorption and desorption) is unreasonable, since most of the rainfall induced slope failures occur during the wetting events (Kristo et al. 2019). The propagation of a wetting front during or after a rainfall event, results in water content and suction distribution that is reflective of either the main wetting curve or any of the scanning wetting curves of the SWCC (Ran et al. 2018). For such instances, assuming a nonhysteretic SWCC comprising of the main drying branch of the SWCC may lead to incorrect estimation of water content and suction distribution within the slopes. Conversely, the same holds true when one assumes a wetting curve without hysteresis during a drying process. Assuming a nonhysteretic SWCC may lead to errors; moreover, errors may especially become significant when slopes are exposed to fluctuating climatic conditions. For example, the unsaturated shear strength is directly related to the SWCC (Vanapalli et al. 1996). Accordingly, differences in VWC and soil suction induced by the hysteretic SWCC can bring about a hysteretic shear strength response (Bishop 1959, cited from Liu et al.

2017), and the hysteretic shear strength response can be further amplified by frequent drying and wetting cycles due to intermittent climate interaction . So, assuming nonhysteretic SWCC could result in an inaccurate seepage flow results, hence affecting the distribution of unsaturated shear strength (Ma et al. 2011), leading to errors in the FOS values and an improper slope stability assessment. Incorporating hysteresis into seepage analysis yields a more realistic and notably impactful influence on the distribution of pore water pressure (Dye et al. 2011, Mavara and Bashir 2018), leading to potentially more efficient and accurate assessment of the slope stability.

Additionally, air entrapment is an inherent phenomenon that contributes to the hysteresis in SWCC. Air entrapment occurs when air is trapped within the soil pores during wetting/rewetting. As the soil starts to saturate, the air is pushed out, but some air remains trapped within smaller or isolated pores. The drying branch is typically above the wetting branch due to the presence of air entrapment in the wetting branch. Larger volume of air entrapment further increases the difference between the wetting and drying branches of the SWCC, indicating that a higher suction is required from the drying branch to achieve a particular water content from the wetting branch. The inclusion of hysteresis and air entrapment can alter the prediction of the unsaturated slope behavior, as they are capable of dictating the soil's hydraulic response (through hysteretic SWCC) as well as the mechanical behavior of the slope (through hysteretic shear strength response).

The present study seeks to explore the interplay between atmospheric boundary conditions and slopes, with a specific emphasis on slope stability. This investigation takes into account the influences of hysteresis and air entrapment in the analysis. The analyses that include hysteresis will be compared to cases that only use one branch of the SWCC. Additionally, the influence of different degrees of air entrapment will be examined and compared with scenarios without air entrapment. By conducting these comparisons, the study aims to highlight and contribute to a

better understanding of how real atmospheric conditions, hysteresis, and air entrapment collectively affect slope behavior, emphasizing the significance of including these factors in hydrological simulations and slope stability assessments.

5.3 Literature Review

Tami et al. (2004) conducted a study examining the impact of hysteresis on a laboratory slope model. The research involved steady-state infiltration of artificial precipitation with varying intensities and for different initial saturation conditions. Subsequent to the experimental phase, numerical analyses were implemented utilizing drying and wetting hydraulic characteristics to scrutinize disparities in the resultant matric suction compared to the experimental findings. The outcomes of both laboratory and numerical experiments conducted by Tami et al. (2004) revealed that hysteresis, even in conditions of steady-state infiltration, significantly influenced the distribution of soil suction within the slope model. They argued that assigning the appropriate hydraulic properties (i.e., drying curve or wetting curve) should depend upon the processes that the soil is experiencing (i.e., adsorption or desorption processes). This is even true for slopes undergoing steady-state infiltration conditions, according to their reported results. The experiments overlooked the impact of evaporation, and the study did not delve into correlating the findings with the Factor of Safety (FOS).

Ebel et al. (2010) conducted a study on the effects of hysteresis on hydrological response and slope stability in an unsaturated slope. They employed a 3D variably saturated subsurface flow model and an infinite slope model to evaluate both hydrological aspects and slope stability. The research was motivated by a slope failure event in Coos Bay 1, USA, triggered by intense rainfall in 1996. They conducted a comparison between simulations with hysteretic SWCC and

nonhysteretic SWCC simulations, including drying, wetting, and mean curves. The simulation of the drying curve indicated the most stable slope conditions, potentially leading to an underestimation of the onset of slope failure. Conversely, the wetting curve simulation portrayed the least stable conditions. The hysteretic simulation exhibited similarities to the wetting curve, while the mean curve simulation demonstrated an intermediate slope failure response. Initially, the hysteretic simulations aligned with the drying curve values, influenced by the initial conditions, but they rapidly converged with the values of the wetting curve. In scenarios of intense rainfall, the results of the hysteretic curve consistently mirrored those of the wetting curve.

Ma et al. (2011) studied the wetting front movement within unsaturated slopes influenced by hydraulic hysteresis, under an infiltration boundary. The results of the numerical model were compared against a laboratory experiment involving infiltration in a sand box. The authors established a method to assess the stability analysis of unsaturated infinite soil slopes by combining the impact of infiltration and hysteresis in the water retention curve. Their stability assessment involved coupled hydrological infiltration model and advanced Mohr-Coulomb criterion to assess the FOS variations. In their study, they observed the significant hysteretic influence on the water content, shear strengths, and FOS values, as well as how they affect shallow landslides. Experimental study of water content and suction distribution was also carried out to validate the accuracy of hysteretic hydrological simulations. Their results showed that simulating the traditional slope stability analysis which uses single nonhysteretic curve (i.e., wetting curve) underestimated the shear strength. The authors stated that incorporating an infiltration model in combination with hysteresis and unsaturated shear strength theory appear to considerably influence the predicted time of shallow slope failure. The authors also suggested the use of appropriate

SWCC branch (i.e., drying or wetting curve) in accordance with the drying or wetting processes that the slope is actually experiencing.

Likos et al. (2014) investigated the uncertainty associated with estimating the hysteretic van Genuchten (1980) parameters for the wetting curve based on the initial drying curve. This estimation was conducted using scalar multipliers derived from experimental work. This approach was compared with direct laboratory measurements of the van Genuchten (1980) parameters for both the initial drying curve and the primary wetting curve. The latter was determined using the transient release and imbibition method (TRIM) as outlined by Wayllace and Lu (2012) and Lu and Godt (2013). The study encompassed 25 natural soil suites, representing diverse soil types. They implemented the concept of suction stress characteristic curve (SSCC) which defines the relationship among effective stress, matric suction, and degree of saturation (Lu and Likos 2004, 2006). They observed that uncertainties in estimating wetting SWCC parameters through the scalar multiplier approach translated into uncertainties in the resulting SSCC values. Furthermore, their findings also highlighted the development of hysteresis in suction stress, attributed to its direct correlation with the hysteretic SWCC. In the same study, Likos et al. (2014) extended their investigation to assess the impact of uncertainty and hysteresis in the SWCC on rainfall-induced landslides. They employed an infinite slope analysis method outlined by Lu and Godt (2008). The equation derived for the infinite slope and the corresponding suction stress values were then used to compute the Factor of Safety (FOS) for the slope. Notably, the FOS exhibited variation along different drying and wetting paths. Similar to the lower suction stress values for the main wetting curve for SWCC and SSCC, the FOS was also lower compared to that of the initial drying curve. This observation indicated hysteresis effects in the FOS values, where values along the wetting

path were lower than those along the drying path. Moreover, the FOS exhibited a rapid decline for a slight increase in saturation when solving for the wetting path as opposed to the drying path.

Liu et al. (2015) assessed the effect of hysteresis on the stability of an unsaturated slope under fluctuating water level and transient seepage. Sinusoidal curves were imposed to imitate cyclic water level fluctuation at the upstream face of the embankment. A water flow analysis had been first conducted, after then, results of suction stress and water content were imported to slope stability analysis, in which they implemented the extended Mohr-Coulomb failure criterion combined with Bishop's effective stress to calculate the shear strength. They utilized a FEM slope stability code and employed a strength reduction method to obtain the FOS. To consider hysteretic effects in the water flow analysis, the authors assumed that the n parameter (of van Genuchten (1980) SWCC), related to the pore-size distribution, were identical for both drying and wetting curves. Whereas the α^w parameter (of van Genuchten (1980) SWCC), which is inversely related to air entry value, of the wetting curve was taken two times the α^d of the drying curve. Also, the authors assumed a linear transitioning between main curves when forming scanning curves. Their study showed that the water contents and soil suctions varied significantly between hysteretic and nonhysteretic simulations. In the wetting processes, the SWCC in the hysteretic simulations closely followed the scanning curves, leading to a rapid reduction in matric suction with a small increase in VWC. This resulted in a significant decrease in shear strength and effective stress for the hysteretic simulation compared to the nonhysteretic simulation. Consequently, the hysteretic simulation estimated a lower FOS. The study also revealed that the effect of hysteresis diminished when simulating water level fluctuations over a short period but became more noticeable when the simulation period exceeded a specific threshold.

Liu et al. (2017) studied the slope stability response of heterogeneous earth embankment under transient seepage, specifically experiencing external cyclic fluctuations of the water level, as well as under the effect of hysteresis. The method of Bishop's effective stress with extended Mohr-Coulomb failure criterion was used to simulate the shear strength parameter of the slope stability model. The hydrological model was first simulated to obtain variation of VWC and suction, after which the distributions were imported into a FEM slope stability model. The author used the method by Yang et al. (2011) to describe the scanning curve of the SWCC hysteresis loop. They assumed $\alpha^w = 2\alpha^d$ to describe the hysteretic effects in the SWCC. For comparison purposes, the author employed the hydraulic properties of the drying curve to describe the nonhysteretic SWCC. Similar to Liu et al. (2015), the author illustrated considerable influence of hysteresis on the distribution of soil suction and water content within the embankment, hence affecting the slope stability results. The authors found that VWC of the hysteretic simulation were larger than or equal to the values from the nonhysteretic simulation; this resulted in smaller soil suction values when simulating hysteresis. The authors explained that higher VWC in hysteretic simulations has led to increases in the soil weight, hence, the overturning moment. Therefore, the FOS of the hysteretic simulation resulted in a lower FOS than the nonhysteretic simulation (using drying curve). The authors hypothesized, should the wetting curve be taken to describe the nonhysteretic SWCC, it would underestimate the FOS values, relative to simulation with hysteresis. Furthermore, the authors noted a rapid change of the soil suction in the hysteretic simulation; the author attributed this behavior due to the formation of scanning curves. The authors also conducted a sensitivity analysis on the soil hydraulic parameters to study their influence on slope stability. They found that the FOS increased with saturated hydraulic conductivity; however, FOS decreased with

increases in the α, n, and θ_s. Variations in θ_r was found to have less significant effects, since the soil did experience a response near the residual water content.

Chen et al. (2017) studied the effect of hysteresis and air entrapment. Their study focused on two hypothetical hillslope scenarios subjected to simplified steady-state infiltration of varying intensities and unsaturated seepage conditions. They extended the suction stress concept, and infinite slope stability analysis by Lu and Godt (2008) to include the effect of air entrapment. Through experimental investigation (e.g., Faybishenko 1995, Lu et al. 2013), they adopted the effect of air entrapment on the hydraulic conductivity by reducing the saturated hydraulic conductivity of the wetting branch (after entrapment of air) by factor of ten of that the initial drying curve ($k_s^w = k_s^d/10$). Their results suggested that both effects, hysteresis and air entrapment, have decreased the suction stress values within the slope. This in return decreased the FOS values. They reported that hysteresis has decreased the FOS marginally compared to the more stable nonhysteretic case, which uses the drying curve. They also reported that slope failures were triggered when air entrapment was introduced in the SWCC. Discrepancies between the hysteretic and nonhysteretic cases were more pronounced for the finer soil slope as opposed to coarser soil one. Additionally, the slopes were more readily susceptible to slope instability when air entrapment was introduced to both SWCC and hydraulic conductivity, as opposed to the case with only air entrapment in the SWCC. It was also reported that these slope failures have taken place during unsaturated conditions. The argument posited is that slope failures are not exclusive to saturated conditions alone.

Mavara and Bashir (2018) assessed the influence of hysteresis on slope stability using Toronto's multi-year climate data. They simulated a sandy clay loam soil embankment by employing a soil-atmosphere model with hysteresis considerations, using the Kool and Parker (1987) hysteresis

model. For stability assessment, the researchers utilized the limit equilibrium method and the empirical unsaturated soil shear strength model proposed by Vanapalli et al. (1996). Comparative analysis of nonhysteretic simulations (employing both drying and wetting curves) with a hysteretic case demonstrated that simulations using the wetting curve resulted in a lower Factor of Safety (FOS) due to increased net infiltration. Conversely, the drying curve simulation estimated the highest FOS. The FOS value from the hysteretic simulation fell between the two nonhysteretic curves. The study emphasized the importance of considering hysteresis in unsaturated slope stability assessments, cautioning against potential overestimation of slope stability with non-hysteretic drying curve simulations and overestimation of slope failure with wetting curve simulations. The researchers also highlighted the impact of storm intensity and the temporal frequency of rainfall events on stability assessments, ultimately emphasizing the necessity of incorporating multi-year climate datasets with hysteretic considerations for realistic unsaturated slope stability assessments. Their research did not delve into the effect of air entrapment on slope stability.

In addressing the gaps of the previous research, the literature study indicates that the effect of hysteresis on the seepage analyses and slope stability is not well studied and is yet unclear, a point also underscored by Liu et al. (2017) and Kristo et al. (2019). This knowledge gap is particularly pronounced considering intermittent climatic conditions. Additionally, some of those papers considered hysteresis in a way that drying curve was used during drainage and wetting curve during wetting process. The study of the effect of scanning curves in hysteresis loop was not reported in a number of papers in the literature. Furthermore, for some research that did study hysteresis in slope stability, the role of air entrapment has been excluded. Moreover, none of the papers have explored the impact of hysteresis and air entrapment on unsaturated shear strength.

The interaction of the real climatic conditions with the slope within the context of hysteresis and air entrapment remains unexplored. These are gaps in knowledge that the current thesis is seeking to address.

5.4 Materials and Methods

Consideration of hydraulic hysteresis in unsaturated soil slope stability assessment requires the development of a coupled hydrogeological-slope-stability model. To obtain a more realistic Factor of Safety (FOS) reflective of the site's conditions, the slope stability model necessitates data on soil suction and the water content distribution across the slope. Consequently, the methodology employed in this study involves the initial construction and simulation of a hydrological model, accounting for atmospheric boundary conditions and hysteresis. Subsequently, the obtained water content and soil suction distributions were incorporated into a slope stability model to calculate the Factor of Safety (FOS) for the critical slip surface. The stability assessment utilized an unsaturated shear strength model coupled with the hydrological evaluation, incorporating the hysteretic SWCC. The times chosen for the slope stability analyses corresponded to two hydrological events: maximum average saturation of the slope (*Max Sat*) and daily maximum net infiltration (*Max NI*) at ground surface. Additional information is elaborated in the subsequent sections.

5.4.1 Model Setup

The embankment's profile considered in this study is shown in Figure 5.1, which displays a typical highway embankment in Ontario (Baninajarian 2020).

A 2H:1V ratio describes the angle of the slope; the embankment is 14.0 m high and 66.0 m wide,

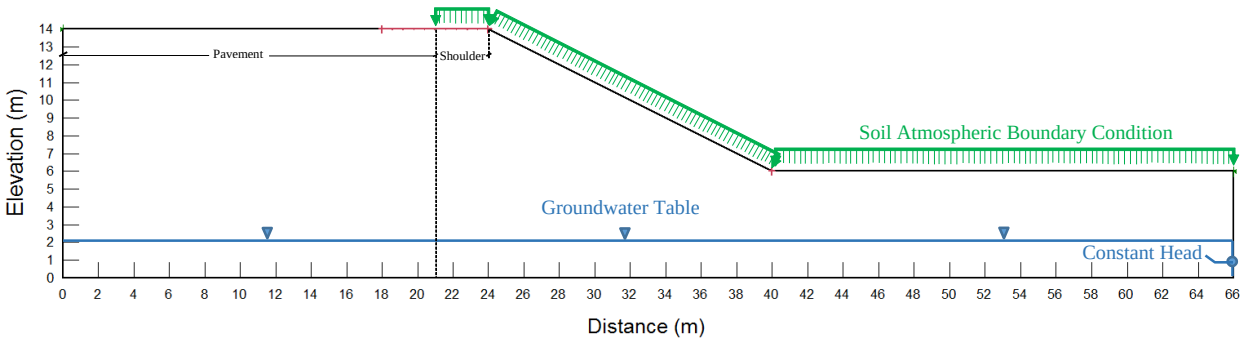

Figure 5.1 Model setup including geometry, boundary condition, and entry and exit points of the slope stability model's slip surface [Modified from (Baninajarian 2020)]

with 3.0 m wide unpaved shoulder. Similar to Baninajarian (2020), two different textural soils were studied: silty sand and sandy silt, which are referred to as sand and silt, respectively. An atmospheric boundary condition was assigned on the unpaved areas of the slope. A no-flow boundary condition was assigned to the paved road area. The groundwater table is assumed to be 4.0 m below the toe of the slope, with a constant head boundary condition assigned to the right-hand boundary. The initial condition of the slope was kept at hydrostatic condition. Above the water table, moisture equilibrium of the drying curve was applied to all hysteretic and nonhysteretic simulations. The minimum slip surface depths considered in this study are 0.3 m and 1.0 m. This research focuses on investigating two modes of slope failures: surficial failures (occurring at minimum depths of 0.3 meters) and general failures (occurring at minimum depths of 1.0 meter), akin to the approach taken by Baninajarian (2020). As a stability criterion, a minimum acceptable Factor of Safety (FOS) of 1.3 is employed to characterize a slope state deemed both acceptable and stable. This threshold aligns with the guidelines set forth by the

Ministry of Transportation Ontario (MTO) for the design of earth embankment slopes, as outlined by Baninajarian (2020).

Figure 5.2 displays the 30-year (1981-2010) climate classification of 10 cities across Ontario, Canada, using the Annual Moisture Index (I_m) as the climate classification index, as introduced by Thornthwaite (1948) and further developed by Thornthwaite and Hare (1955). As one of the primary objectives of this research is to investigate the coupled effects of climate interaction and hysteresis, two cities with divergent climatic conditions have been selected for analysis: North Bay and Toronto. North Bay, characterized by an average I_m of 47, falls under the humid climate category. Among the chosen cities in Ontario, North Bay experiences the wettest climate, with an annual average precipitation and potential evaporation of 1036 mm and 705 mm, respectively. On the other hand, Toronto, with an average I_m of -3, is classified as dry subhumid. Toronto exhibits one of the driest climates among the chosen cities in Ontario, with an annual average precipitation and potential evaporation of 775 mm and 815 mm, respectively. The rationale behind selecting cities with distinct climates is to discern and comprehend the impact of varying climate conditions on the hysteresis observed in slope stability assessments. In accordance with the recommendation by Fredlund et al. (2012), the land-climate interaction (LCI) analysis exclusively incorporates the active period, characterized by the thawed condition of the soil.

Initially, a hydrological model was constructed employing the HYDRUS (2D/3D) software package (Šimůnek et al. 2022) to conduct land-climate interaction (LCI) analyses. The analyses were carried out separately for the climates of North Bay and Toronto. Climate data records spanning two years (2009-2010) were incorporated into the model to simulate the interaction between the atmosphere and the soil on the slope. The HYDRUS (2D/3D) software incorporates the hysteresis model developed by Lenhard et al. (1991), which has the capability to estimate

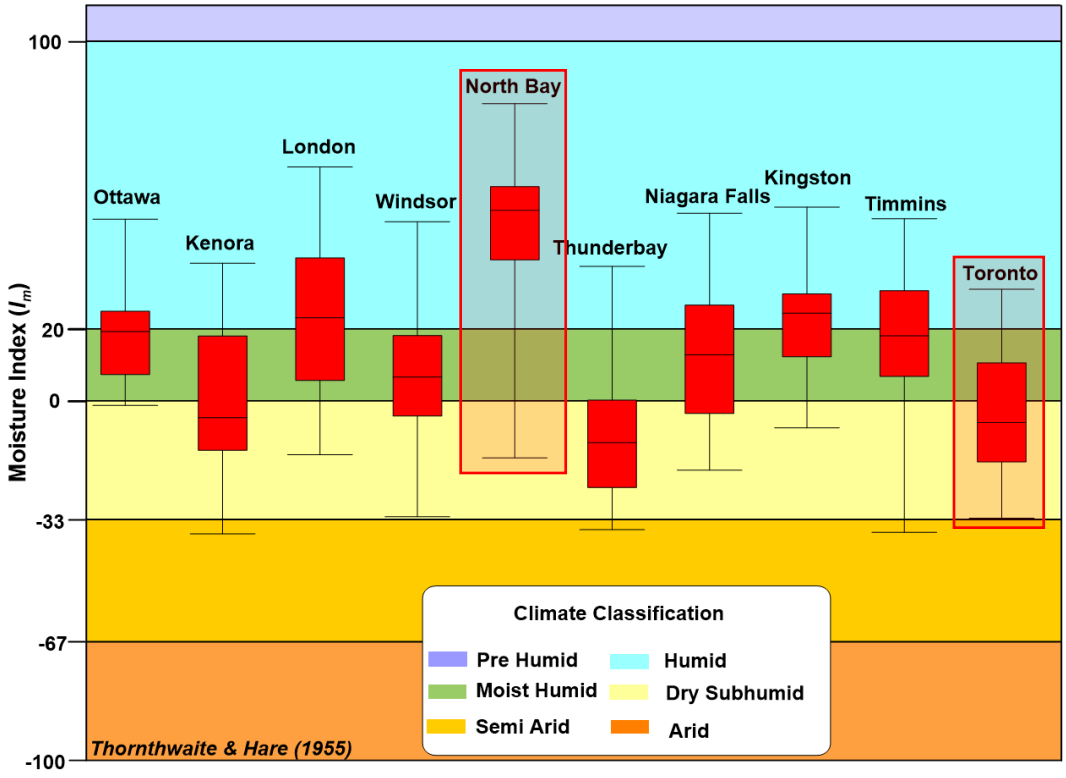

Figure 5.2 Climate classification of cities across Ontario, CA over period of 1981-2010

drying and wetting scanning curves by rescaling the main boundary curves while accounting for air entrapment. In this research, the hysteresis model by Lenhard et al. (1991) was employed within the HYDRUS (2D/3D) framework to simulate the hysteretic impact on water balance at the ground surface, as well as the distribution of water content and soil suction in the slope.

5.4.2 Hydraulic Properties

The hysteretic and nonhysteretic Soil Water Characteristic Curves (SWCC) were parameterized using the van Genuchten's model (van Genuchten 1980). The vector $\{\theta_s^d , \theta_s^w, \theta_r^d , \theta_r^w , \alpha^d, \alpha^w, n^d, n^w\}$ describes any arbitrary hysteresis loop, where 'd' denotes the drying curve and 'w'

denotes the wetting curve. Studies by Kool and Parker (1987), Pham et al. (2005), and Likos et al. (2014) suggested imposing $n^d = n^w$, where 'n' is related to the soil pore-size distribution. Additionally, Kool and Parker (1987) and Likos et al. (2014) reported that $\alpha^w \approx 2\alpha^d$, where '$\alpha$' is inversely related to the air entry value. It has also been noted that hysteresis has a negligible effect on residual water content, leading to $\theta_r^d = \theta_r^w$. Consequently, the reduced parameter vector is $\{\theta_s^d , \theta_s^w, \theta_r , \alpha^d, \alpha^w = 2\alpha^d, n\}$. Further simplification, neglecting the effect of air entrapment, led to $\{\theta_s^d , \theta_r , \alpha^d, \alpha^w = 2\alpha^d, n\}$. Although assuming equal saturated water content during wetting and drying ($\theta_s^w = \theta_s^d$) is a common practice in research on hysteretic effects, it may not accurately represent field conditions, especially during rewetting events, as demonstrated by Hopmans and Dane (1986). This oversight could result in inaccurate estimations of water content and soil suction values.

In the present study, hydraulic properties for sand and silt, sourced from Baninajarian (2020), were assumed to characterize the drying curve. The hydraulic properties for the wetting curve were derived using the relationship $\alpha^w \approx 2\alpha^d$ and by incorporating assumptions about the degree of air entrapment. Degrees of 0%, 15%, and 25% air entrapment were selected, serving as input parameters for the numerical simulations. The selection of the degree of air entrapments, 15% and 25%, were based on experimental study conducted by Likos et al. (2014), where they investigated 25 sets of cohesive and cohesionless soils. Their results, reflected in their regression statistics, revealed varying degrees of air entrapment. Their study found that the extent of air entrapment ranged from 5% to 25%, with an average value of 15%. Additionally, a 0% degree of air entrapment was considered in the current research to simulate a scenario where the effect of air entrapment is neglected. Consequently, for each soil type, three hysteretic SWCC were generated: HC (hysteretic curve with 0% air entrapment), HC-$TA_{15\%}$ (hysteretic curve with 15%

air entrapment), and HC-$TA_{25\%}$ (hysteretic curve with 25% air entrapment). Here, the notation 'TA' signifies trapped air phenomena, and the subscript denotes the degree of air entrapment as a percentage (i.e., the ratio between trapped air volume and the total volume of the pores). Figure 5.3(a), Figure 5.3(b), and Figure 5.3(c), illustrate the SWCC hysteresis envelope for sand with 0%, 15%, and 25% air entrapment, respectively. Similarly, Figure 5.4(a), Figure 5.4(b), and Figure 5.4(c), showcase the SWCC hysteresis envelope for silt with 0%, 15%, and 25% air entrapment, respectively. The figures also display the set of van Genuchten (1980) parameters describing the curves. For comparative analysis, four nonhysteretic simulations were conducted, each derived from specific segments of the hysteresis envelope. These simulations were based on: the initial drying curve (DC), the wetting branch of the hysteretic curve (HC) denoted as WC, the wetting branch of HC with 15% air entrapment (WC-$TA_{15\%}$), and the wetting branch of HC with 25% air entrapment (WC-$TA_{25\%}$). Therefore, a total of seven simulations were carried out for each soil type.

It is important to highlight that the unsaturated hydraulic conductivity function (HCF) employed in HYDRUS 2D/3D, utilizing the Mualem–van Genuchten equation, is inherently nonhysteretic. Nevertheless, owing to variations in water content at different suctions within the hysteretic SWCC, the hydraulic conductivity values appear identical for the same water content but diverge for equivalent suctions. Therefore, the HCF, becomes implicitly hysteretic. In a special case, HYDRUS 2D/3D employs Lenhard and Parker's (1987) model to account for the effect of air entrapment on HCF, in which the entrapment of air increases the hydraulic conductivity values. Parker and Lenhard (1987) described that nonwetting fluid entrapment, like air, obstructs the wetting fluid movement, like water, resulting to displace the water towards larger pores, leading to a decrease in the flow impedance and increase in the hydraulic conductivity values.

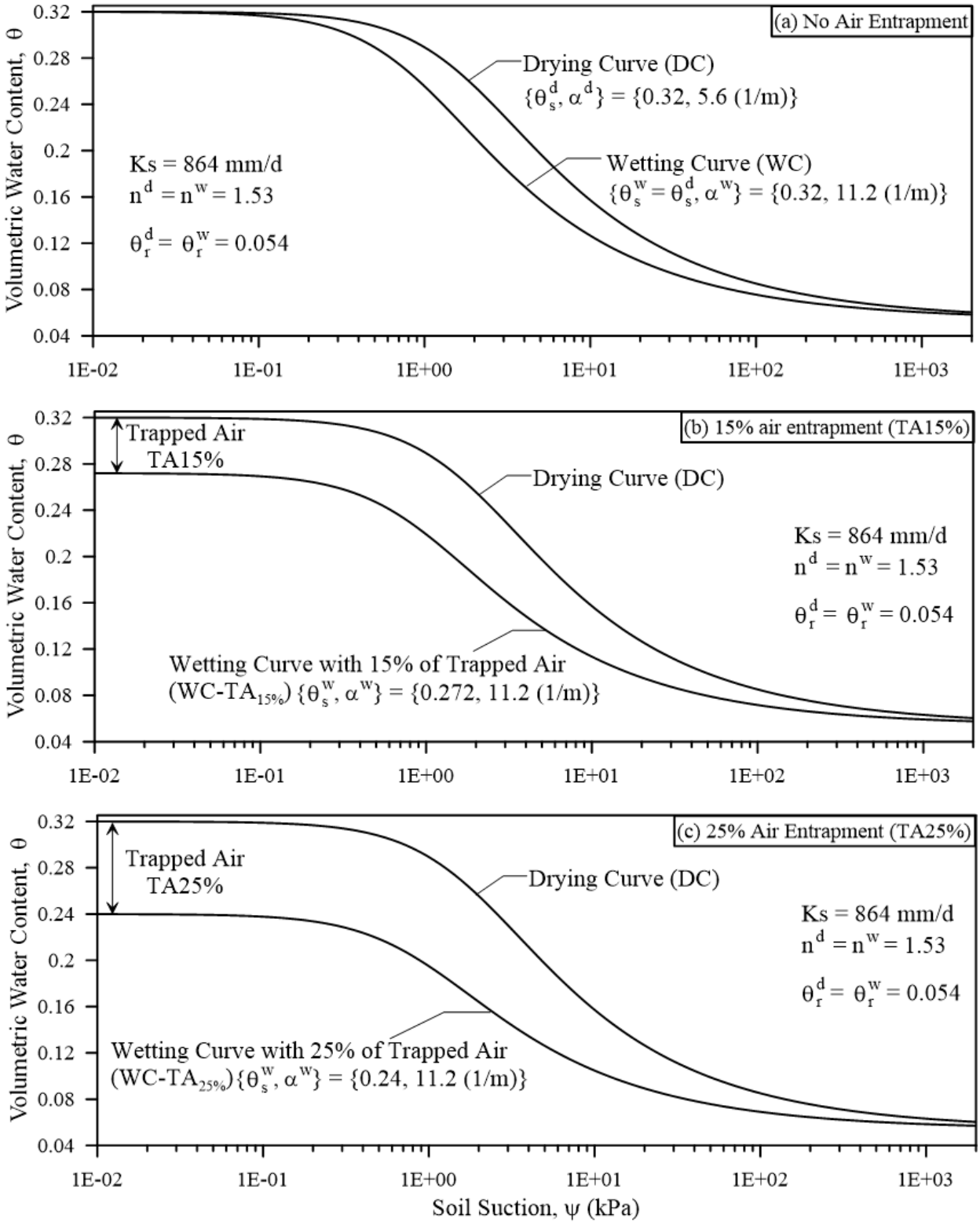

Figure 5.3 SWCC hysteresis loop for sand soil with three air entrapment volumes considered (a) no air entrapment, (b) 15% air entrapment, and (c) 25% air entrapment

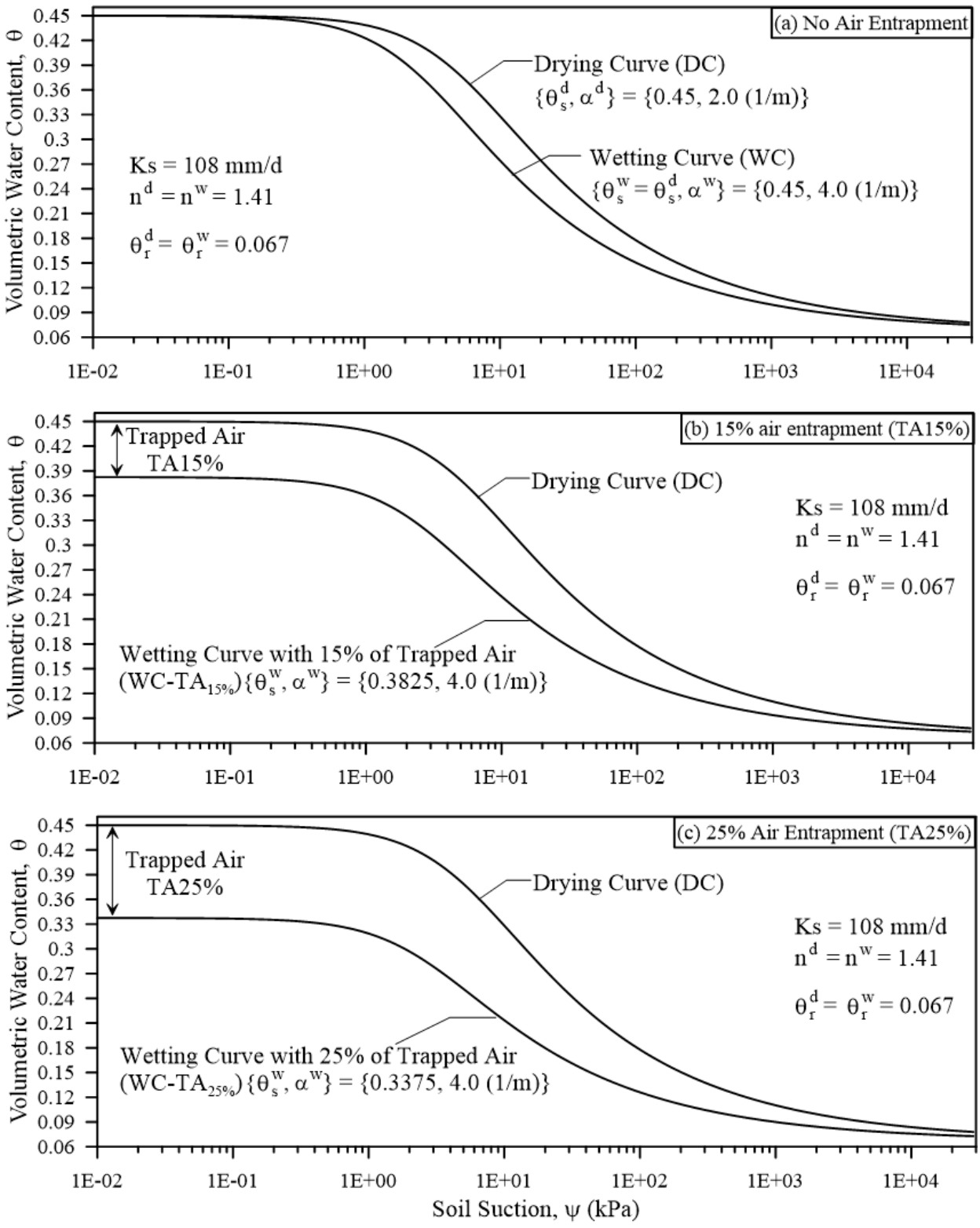

Figure 5.4 SWCC hysteresis loop for silt soil with three air entrapment volumes considered (a) no air entrapment, (b) 15% air entrapment, and (c) 25% air entrapment

5.4.3 Development of Hysteretic Soil Slope Stability Framework

After conducting the hydrological simulations, the resulting soil suction distributions were imported into the slope stability model developed in SLOPE/W (version 2021). The Factor of Safety (FOS) was determined using the Morgenstern-Price method (Morgenstern and Price 1967). Analysis of soil suction distribution, detailed in the subsequent section, indicated that the slope of the embankment was in an unsaturated condition. Recognizing the significance of soil suction on slope strength, the unsaturated shear strength was computed using Eq. [5.1], formulated by Fredlund et al. (1996) and Vanapalli et al. (1996). This equation, incorporated into SLOPE/W, played a pivotal role in the present study. It calculates the unsaturated shear strength based on effective shear strength parameters (C' and and ϕ') and the van Genuchten (1980) parameters of the SWCC within SLOPE/W. The unsaturated shear strength equation is expressed as follows:

$$s = C' + (\sigma_n - u_a)\, tan\phi' + \left(\frac{\theta - \theta_r^*}{\theta_s - \theta_r^*}\right) \psi\, tan\phi' \qquad \text{[Eq. 5.1]}$$

where C' is the effective cohesion [M/L/T^2], $(\sigma_n - u_a)$ is net normal stress [M/L/T^2], ψ is soil suction or matric suction [M/L/T^2], ϕ' is effective angle of internal friction [-], θ_s is saturated volumetric water content, and θ_r^* is volumetric water content at which the suction strength becomes zero [-]. It should be noted that SLOPE/W uses the van Genuchten (1980)'s equation and the input soil suction data to calculate θ. The third term of Eq. [5.1] represents the suction strength (SS) of the unsaturated soil, written as:

$$Suction\ Strength = \left(\frac{\theta - \theta_r^*}{\theta_s - \theta_r^*}\right) \psi\, tan\phi' \qquad \text{[Eq. 5.2]}$$

It is important to note that the parameter, θ_r^*, from the suction strength equation, Eq. [5.2], is different from the van Genuchten (1980) parameter, θ_r . The parameter, θ_r^*, is the water content at which the suction strength becomes zero. Specifically, it is when the soil is drained to the point that the available water is insufficient to maintain any suction strength (GeoStudio 2021). As suggested by GeoStudio (2021), the current study assumes θ_r^* to be equal to 50% of the porosity (i.e., 50% the saturated water content of the initial drying branch); the same value was used in all simulations.

Equation [5.2] establishes a direct correlation between suction strength and SWCC, as it factors in both volumetric water content and soil suction. As the SWCC inherently exhibits hysteresis, the suction strength follows suit. Illustrated in Figure 5.5 is the suction strength plotted against water saturation for both sand and silt, showcasing evident hysteretic effects. Mirroring the hysteresis in the SWCC profile, the suction strength of the wetting branch consistently remains below that of the drying curve. The imposition of $\theta_s^w < \theta_s^d$ and $\alpha^w \approx 2\alpha^d$ (indicating hysteresis with air entrapment) diminishes the suction strength. A heightened degree of air entrapment further diminishes suction strength values. Therefore, accounting for hysteresis and air entrapment is crucial in slope stability assessments. These factors not only influence soil suction distribution during seepage analyses but also directly correlate with the distribution of suction strength within the slope. Neglecting these effects may result in inaccuracies in estimating suction strength and, consequently, Factor of Safety values.

Incorporating hysteretic suction strength into slope stability modeling presents a significant challenge, especially since widely used software like SLOPE/W does not inherently consider hysteresis in its algorithms. The dilemma arises from the software's limitation in allowing the

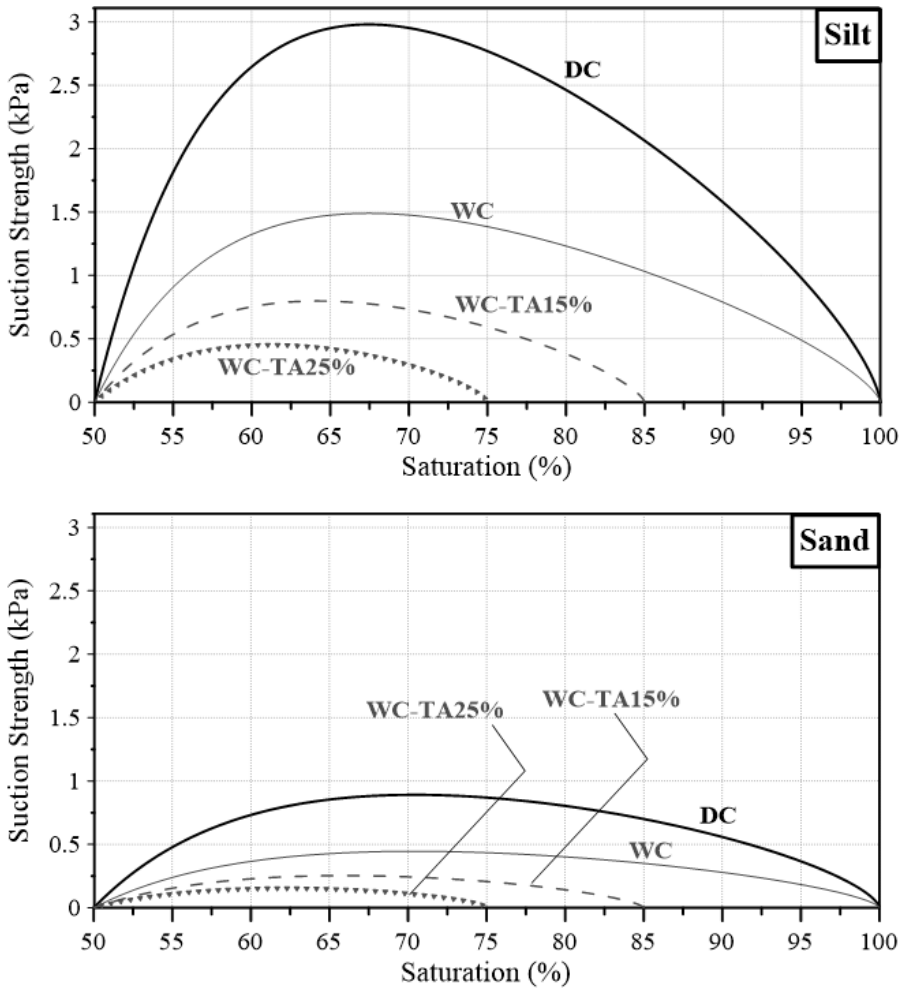

Figure 5.5 Hysteretic suction strength profile of silt and sand with and without air entrapment

input of the spatial distribution of only soil suction, neglecting water content. Consequently, the suction strength profile generated by SLOPE/W remains nonhysteretic. This limitation stems from the software's process of internally calculating volumetric water content when importing hysteretic soil suction data. SLOPE/W utilizes the SWCC equation and parameters of a single nonhysteretic curve to derive water content, but this results in an inaccurate representation. Specifically, the calculated water content aligns with either the drying or wetting curve, depending on whether SWCC parameters for drying or wetting are provided. This discrepancy

leads to inaccurate estimations of suction strength values and, subsequently, the Factor of Safety (FOS). To address this shortfall, the current research introduced a correction to the soil suction inputs. This modification ensures that SLOPE/W calculates water content values corresponding to the drying and/or wetting history. By adopting this approach, SLOPE/W accurately computes hysteretic suction strength values, aligning with the profile depicted in Figure 5.5. As a result, the FOS estimates become more consistent with the hysteretic suction profile. The subsequent steps outline how this correction was implemented in SLOPE/W and can be applied to other software with similar algorithms:

1- Input the van Genuchten (1980)'s SWCC parameters of the initial drying curve in SLOPE/W model:

2- The correction can be achieved when the actual suction strength (using the actual data from the hydrological model) is equal to the calculated suction strength using the corrected soil suction and volumetric water content. This can be accomplished by the following equation:

$$\frac{(\theta^{actual\ data} - \theta_r^*)}{(\theta_s - \theta_r^*)}\ \psi^{actual\ data}\ tan\phi' = \frac{(\theta^{d,corrected} - \theta_r^*)}{(\theta_s - \theta_r^*)}\ \psi^{d,corrected}\ tan\phi'; \qquad \text{[Eq. 5.3]}$$

where $\theta^{actual\ data}$ and $\psi^{actual\ data}$ is, respectively, the water content and soil suction data obtained from the hysteretic hydrological model; $\theta^{d,corrected}$ and $\psi^{d,corrected}$ is, respectively, the water content and soil suction aimed for correction; the superscript, d, indicates the hydraulic properties of the initial drying curve used in the slope model. Equation [5.3] can be further simplified by eliminating $tan\phi'$ and $(\theta_s - \theta_r^*)$ from both sides, yielding the following:

$$\left(\theta^{actual\ data} - \theta_r^*\right)\psi^{actual\ data} = \left(\theta^{d,corrected} - \theta_r^*\right)\psi^{d,corrected} \qquad \text{[Eq. 5.4]}$$

Based on van Genuchten (1980)'s equation, $\theta^{d,corrected}$ can be considered as a function of $\psi^{d,corrected}$ using Eq. [5.5] as follows:

$$\theta^{d,corrected} = \theta_r + \frac{\theta_s - \theta_r}{\left[1+\left(|\alpha^d \psi^{d,corrected}|^n\right)\right]^m}; \quad m = 1 - \frac{1}{n}; \qquad \text{[Eq. 5.5]}$$

By combining Eq. [5.4] and Eq. [5.5], the equation required to correct the soil suction is as follows:

$$\left(\theta^{actual\ data} - \theta_r^*\right)\psi^{actual\ data} = \left[\left(\theta_r + \frac{\theta_s - \theta_r}{\left[1+\left(|\alpha^d \psi^{d,corrected}|^n\right)\right]^m}\right) - \theta_r^*\right]\psi^{d,corrected}$$

[Eq. 5.6]

3- Since the relationship of Eq. [5.6] is highly non-linear, an iterative solution scheme is required to achieve the condition of the equation and to solve for $\psi^{d,corrected}$; and
4- Input the corrected soil suction, $\psi^{d,corrected}$, into the SLOPE/W model and run the slope stability simulations.

Based on the aforementioned steps 1 through 4, SLOPE/W employs the parameters of the initial drying curve alongside the corrected soil suction to determine the corrected (hysteretic) water content. Subsequently, SLOPE/W utilizes this corrected water content and the adjusted soil suction in Eq. [5.1] and Eq. [5.2] to compute actual (hysteretic) suction strength and associated unsaturated shear strength. The suction strength values now considered by SLOPE/W adheres to the hysteretic suction strength profile illustrated in Figure 5.5, comprehensively considering air entrapment. It is also important to note that the same correction procedure must be applied to the nonhysteretic WC-TA$_{15\%}$ and WC-TA$_{25\%}$ while keeping the θ_s^d an input in SLOPE/W, since

SLOPE/W will not exhibit the effect of air entrapment in case the θ_s^w was inputted and correction was not made.

5.5 Results and Discussion

In this section, the detailed results of the interaction between Toronto's climate and the silt slope are discussed (the figures, akin to those presented here, are provided in Appendix C for sand and North Bay). Furthermore, a comparative analysis was carried out to emphasize the effects of soil texture and climate type on the hysteretic impact and its implications on the FOS results.

Figure 5.6 illustrates the water balance for the silt slope surface, showcasing temporal cumulative net infiltration (*NI*), actual evaporation (*AE*), and surface runoff (*RO*) values under Toronto's climate. The figure provides a comparative analysis of simulations employing hysteretic and nonhysteretic hydraulic characteristics (DC, HC, and WC) and various degrees of air entrapment (0%, 15%, 25%). Numerical simulations employing nonhysteretic drying SWCC properties (DC) yield the lowest *NI* values. Conversely, simulations with hysteretic properties (HC) but without air entrapment show a modest 0.7% increase in *NI* values. Simulating wetting curve properties without air entrapment (WC) results in a more substantial 12% increase in *NI* values. This trend is inversely reflected in the *AE* values, where DC estimates the highest *AE*, given its higher water retention properties compared to WC. This distinction arises from the assumption $\alpha^w = 2\alpha^d$, meaning the air entry value of DC is approximately twice that of WC, allowing DC to retain more moisture near the surface. Consequently, DC simulations exhibit higher *AE* and lower *NI* values as moisture is readily available for surface evaporation. Conversely, WC simulations trigger a faster and larger water flow, leading to less moisture

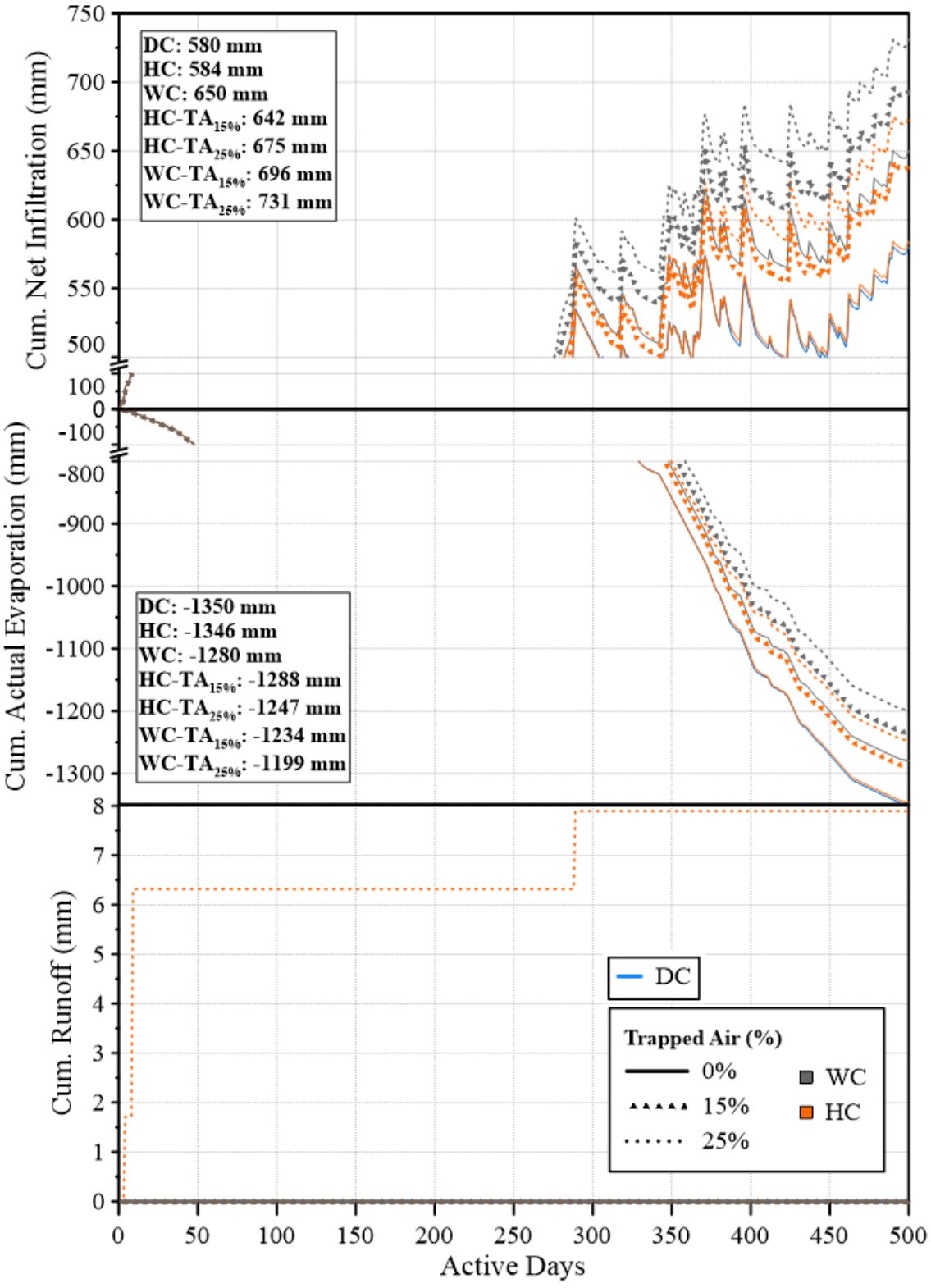

Figure 5.6 Estimated water balance at the surface of the silt profile – Toronto

available near the surface for evaporation. Consequently, WC simulations result in lower *AE* and higher *NI* values. Simulating HC facilitates the formation of scanning drying and wetting curves, contributing to slightly lower *AE* and larger *NI* values compared to DC simulations.

Another noteworthy observation is depicted in Figure 5.6, where the inclusion of air entrapment has significantly increased the amount of water entering the system. More precisely, higher degrees of air entrapment have led to lower *AE* and higher *NI* values, irrespective of using hysteretic curves or just the wetting branch. When accounting for air entrapment, notable distinctions emerge between the primary drying and wetting branches. In this context, the primary wetting and scanning curves corresponding to a specific water content exhibit relatively diminished soil suction compared to scenarios devoid of air entrapment. As such, the water retention properties of the soil are significantly reduced (especially for larger volume of air entrapment), triggering much larger and rapid changes in water content, leaving behind less moisture near the surface for evaporation. This explains the lower *AE* and higher *NI* trends (Figure 5.6) when increasing the volume of air entrapment. For example, simulation using nonhysteretic wetting branch with 25% of air entrapment, WC-$TA_{25\%}$, estimated the largest *NI* value (731 mm) compared to WC-$TA_{15\%}$ (696 mm), and WC (650 mm). Similarly, simulating hysteretic simulations with air entrapment produced the same trend, where the estimated cumulative *NI* values of HC-$TA_{25\%}$, HC-$TA_{15\%}$, and HC were 675 mm, 642 mm, and 584 mm. Hysteretic simulations consistently yield lower *NI* values than their wetting curve counterparts. This discrepancy arises from the formation of scanning curves, particularly the drying scanning curves, characterized by enhanced water retention properties. As previously elucidated, this results in higher *AE* and lower *NI* values compared to simulations based on wetting curves.

Figure 5.6 also reveals that only the hysteretic curve simulation with 25% air entrapment (HC-$TA_{25\%}$) was evident to show instances of runoff generation. This phenomenon is attributed to the larger air entrapment volumes in the hysteretic characteristics, causing pores to reach a full apparent saturation state (water saturation + trapped air saturation = 100%). Put simply, the pores become saturated with both water and entrapped air to a degree where pores can no longer accommodate additional water. This saturation, attributed to restricted pore space, reduces the infiltration capacity resulting in the initiation of runoff. For example, on day 289 (i.e., third runoff instance), the values of the soil suction near the surface were found to be equal to zero (refer to Figure C17 and Figure C18, from Appendix C, for the water content and pressure head distributions at day 289). However, the estimated volumetric water contents (0.34-0.38) on day 289 were found to be lower than the porosity value (0.45). This is indicative of air entrapment and that the pores near the surface have reached full apparent saturation (i.e., trapped air saturation + water saturation = 100% @ soil suction = 0). Therefore, runoff was generated as shown in Figure 5.6 for HC-$TA_{25\%}$.

Using the soil suction and volumetric water content data obtained from the hydrological simulations, the suction strength (SS) was calculated using Eq. [5.2] and were plotted accordingly in Figure 5.7 (SS vs. degree of saturation); where $C' = 0$ (for both silt and sand) and ϕ' for silt and sand are 32 and 34, respectively. Similar to the behavior of a hysteretic SWCC (Figure 5.7), there is not a single SS value at a single saturation value, indicating that SS is also hysteretic. The hydraulic properties of DC estimated the largest overall SS values, in which the maximum value reached is approximately 3 kPa; in contrast, WC estimated a lower maximum SS value, 1.5 kPa. Furthermore, it is observed that air entrapment plays a notable role in reducing the suction strength values, where WC-$TA_{15\%}$ and WC-$TA_{25\%}$ estimated a maximum SS value of

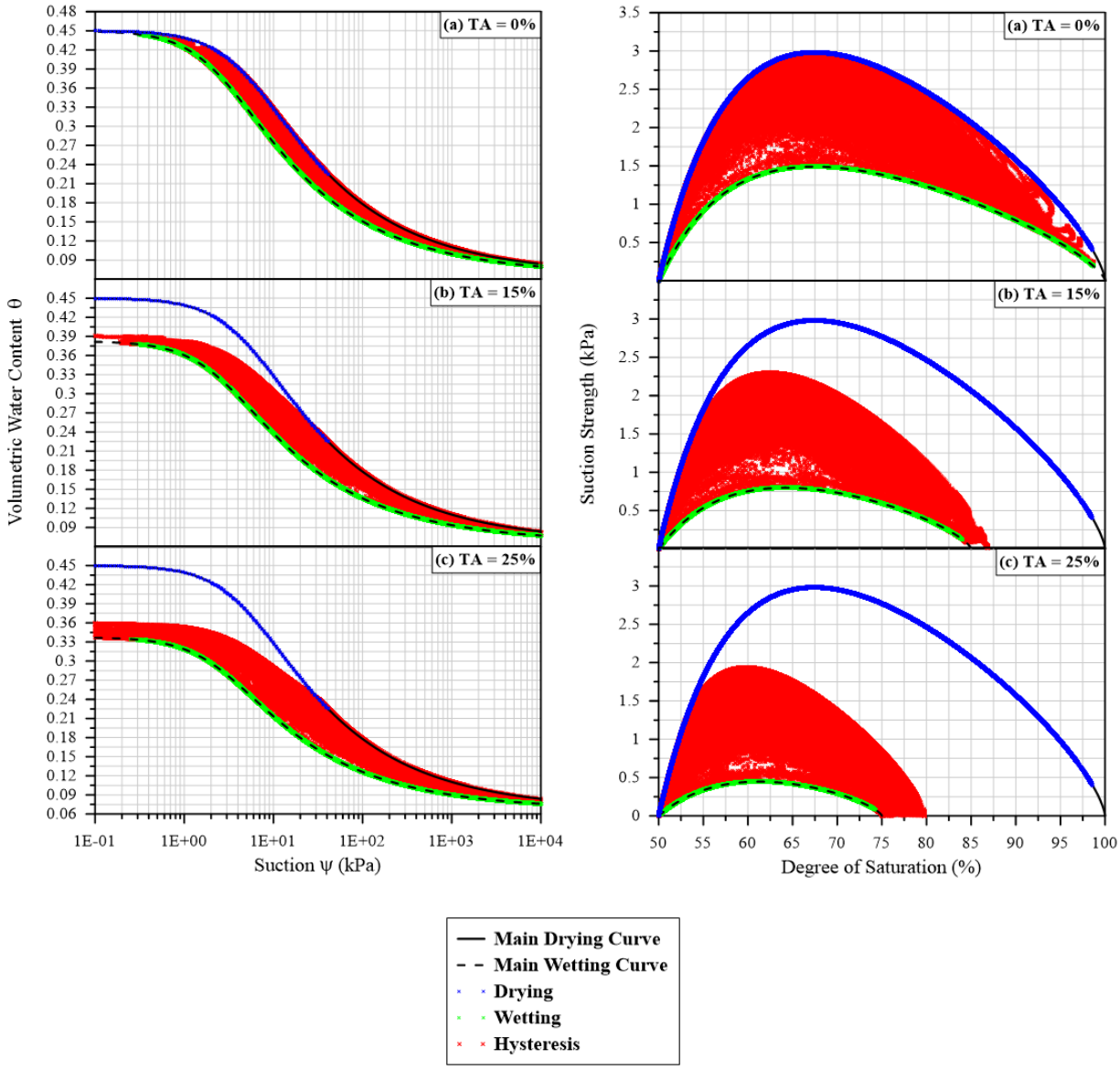

Figure 5.7 Hysteresis profiles of SWCC (left) and suction strength (right) for silt, including data points (blue, red, and green) from the hysteretic and nonhysteretic simulations with and without air entrapment– Toronto

0.8 kPa and 0.4 kPa, respectively. As can be seen on Figure 5.7, SS data points of the HC simulation covers almost the entire area of the SS envelope. However, when introducing air entrapment, especially when simulating HC-$TA_{25\%}$, the area covered is reduced and becomes

more skewed towards SS profile of the wetting branch. The suction strength affinity towards the wetting branch can be attributed to the noticeable entrapment of air during the rewetting process from a relatively dry soil condition, influenced by the drier climate of Toronto. This behavior is closely linked to the SWCC depicted in Figure 5.7. Notably, wetting scanning curves in the SWCC mostly initiated at high suction and low water content. Upon reaching full apparent saturation (at zero suction), the observed water content is notably lower than the porosity value (from initial drying curve) or closer to saturated water content of the wetting branch, signifying the entrapment of air in the soil. The entrapment of air has led to a significant reduction in the overall value of the SS, where SS is inversely proportional to the degree of air entrapment. This further indicates the notable influence of air entrapment in reducing the SS or the overall soil resistance against slope failure. Figure 5.7 also indicates that SS could drastically vary for the same saturation, depending on which curve and degree of air entrapment being simulated. Hysteresis and air entrapment have not only influenced the water balance and the distribution of the soil suction or volumetric water content, but also has a direct impact on the SS values, hence the unsaturated soil shear strength.

The slope stability assessments were attempted based on two hydrological events: maximum average saturation of the slope (*Max Sat*) and daily maximum net infiltration (*Max NI*). The reason behind selecting both events is because *Max Sat* does not necessarily coincide with *Max NI* event, where the occurrence of the *Max Sat* may be caused by the frequency of several smaller infiltration events rather than a single larger infiltration event. Table 2 shows the selected time occurrences for both climates (Toronto and North Bay) as well as for the two soil types (silt and sand); note that the time occurrences of *Max Sat* and *Max NI* were selected based on the results from DC simulations. Following the hydrological modelling, the soil suction distributions

Table 2: Selected time for slope stability assessment based on maximum net infiltration and maximum saturation.

	Time of Occurrence (day), Saturation (%) and quantity (mm)			
	Silt		Sand	
Climate	*Max Sat*	*Max NI*	*Max Sat*	*Max NI*
Toronto	289 d (91.4%)	120 d (36.4 mm)	9 d (79.8%)	369 d (65.4 mm)
North Bay	14 d (91.5%)	50 d (43.3 mm)	396 d (79.1%)	50 d (63.3 mm)

were extracted from the HYDRUS 2D/3D simulations at those times, corrected according to the procedure described above and then imported into SLOPE/W for stability assessment.

Figure 5.8 shows the distributions of the suction strength (SS) within the silt slope for each of the 7 hysteretic and nonhysteretic simulations following the *Max NI* event. The DC simulation estimated the largest overall SS values compared to the hysteretic and nonhysteretic (i.e., wetting characteristics) simulations. Furthermore, the SS values reduced when HC was simulated, especially at areas near the surface where the climatic interactions took place. There is a noticeable SS differences between HC and DC (Figure 5.8), even though the water balance showed similarities in the *NI* values between the two (Figure 5.6). This is attributed to the hysteretic nature of soil suction (i.e., hysteretic SWCC) and hysteretic suction strength (SS). Considering these values are after the day with largest *NI*, the system is representative of wetting state, this would imply that for similar water contents, DC will have higher suction values as the simulation follows drying curve while the HC will follow the main and scanning wetting curves

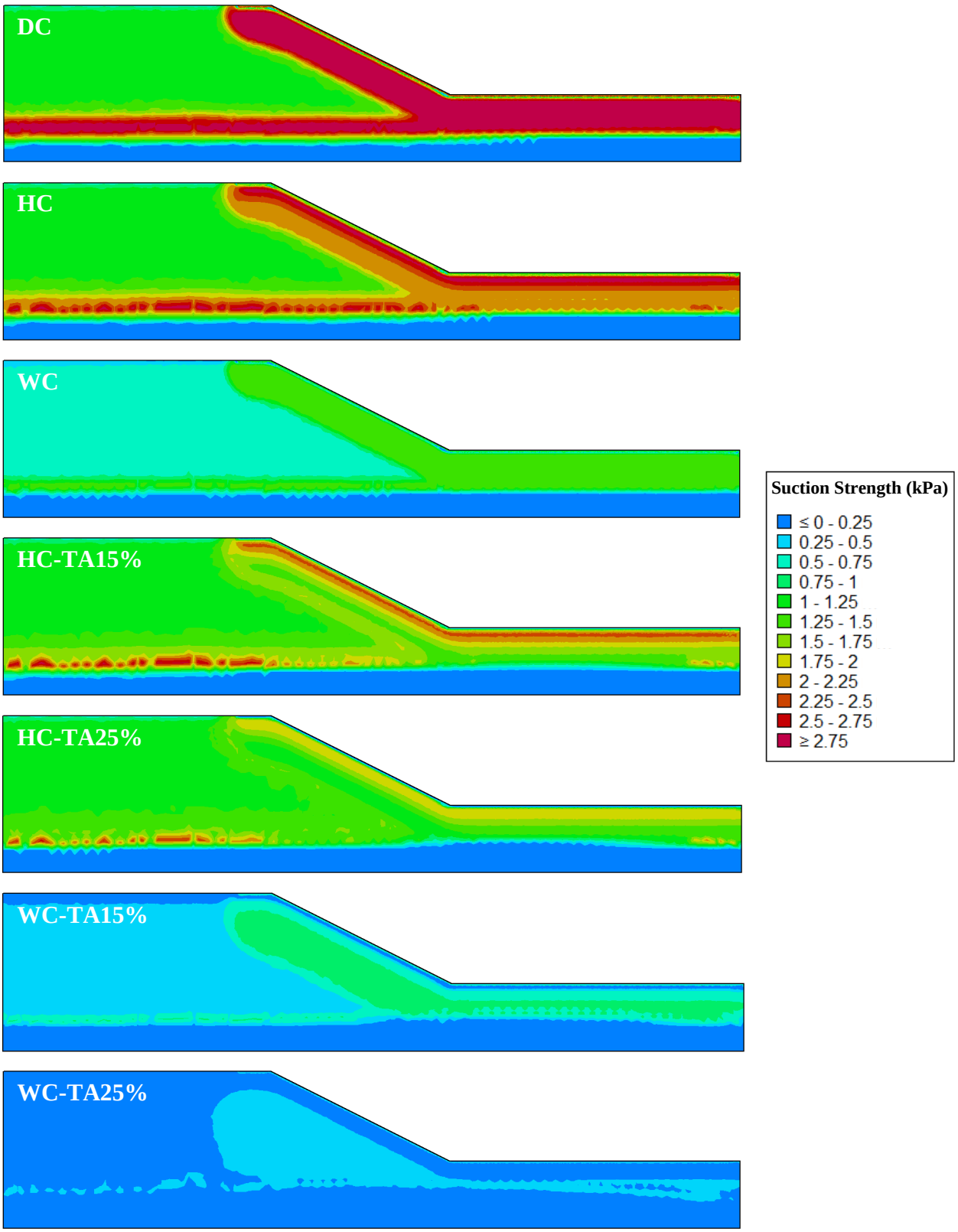

Figure 5.8 Suction strength distribution within silt slope at 120 d (*Max NI*) – Toronto

have lower suction and lower suction strength as shown in Figure 5.8. The condition becomes more pronounced with air entrapment. The introduction of air entrapment, particularly with an increase in volume, in the hysteretic characteristics has significantly diminished the suction strength (SS) values for simulations HC-$TA_{15\%}$ and HC-$TA_{25\%}$, in contrast to the simulations HC and DC. The maximum SS value that the slope sustained in HC simulation, was equal to 3 kPa. Whereas the maximum SS values reduced to values $\leq$ 2.5 kPa and $\leq$ 2 kPa when simulating HC-$TA_{15\%}$ and HC-$TA_{25\%}$, respectively. The decrease in suction strength (SS) observed in the slopes for HC-$TA_{15\%}$ and HC-$TA_{25\%}$ simulations is attributed to the influence of air entrapment. This is evident in the noticeable reduction of suction for the same water content, as depicted by the hysteretic Soil- SWCC in Figure 5.7. Consequently, more water flows through the system, resulting in larger estimates of *NI*. Additionally, the direct reduction of SS, as seen in the hysteretic SS profile in Figure 5.7, contributes to this effect. Simulations that incorporated the characteristics of the wetting branches in their analyses exhibited the most significant reduction in SS values within the slope, as illustrated in Figure 5.8. This is because the wetting branches follow the lowest values of soil suction and SS, accentuated by the larger estimates of *NI*.

Figure 5.9 shows a bar chart of the FOS for each of the 7 hysteretic and nonhysteretic simulations, at the *Max NI* event. It also includes two sets of FOS, which differ by the minimum slip surface depths: 0.3 m (i.e., surficial slope failure) and 1.0 m (i.e., general slope failure). The red dashed line is indictive of the minimum FOS (1.3), below which the stability state of the slope is considered unacceptable, according to the stability criterion of the Ministry of Transportation Ontario (MTO) guidelines.

Given the elevated SS estimated by the DC simulation (Figure 5.8), it yielded the highest Factor of Safety (FOS) value. This implies that simulating the hydraulic characteristics with a

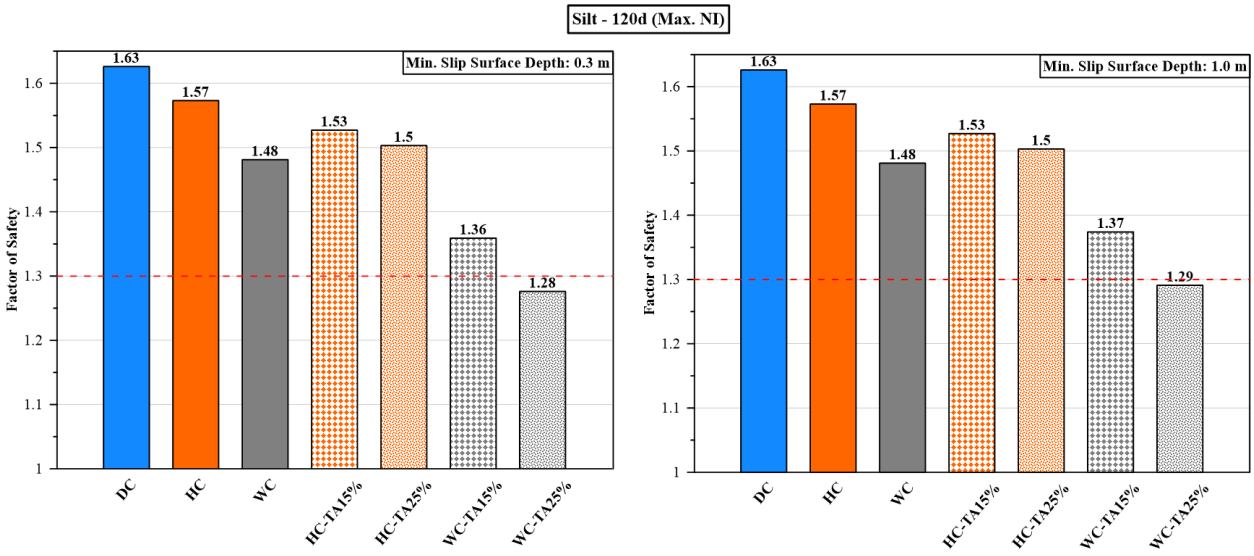

Figure 5.9 FOS of silt slope during *Max NI* occurrence (120 d) using different hydraulic characteristics, with two considered minimum slip surface depths: 0.3 m (left) and 1.0 m (right) – Toronto

nonhysteretic drying curve overestimated the FOS or underestimated the slope's failure likelihood.

The FOS values decreased when hysteresis was considered, aligning with the trends in suction strength (SS) reduction as presented in Figure 5.8. Additionally, as air entrapment was found to diminish SS, FOS results reflected a reduction in their values due to a higher degree of air entrapment considered (i.e., the lowest FOS among hysteretic simulations for HC-$TA_{25\%}$; the second lowest FOS for HC-$TA_{15\%}$). In Figure 5.9, none of the hysteretic simulations approached near-slope-unacceptable conditions (i.e. FOS < 1.3), but their influence on reducing the FOS is considerably noticeable. Simulating wetting branches significantly underestimated the Factor of Safety (FOS), with the most substantial FOS reduction observed in simulations incorporating air entrapment. The FOS was notably underestimated when simulating wetting branches with 25%

air entrapment, to the extent that WC-$TA_{25\%}$ even indicated potential unacceptable slope stability conditions (FOS < 1.3).

Both minimum slip surface depths (0.3 m and 1.0 m) have exhibited similar FOS results in Figure 5.9. This attributed to the selection of *Max NI*, where the front of high water content (refer to Figure C13, from Appendix C, for water content distribution at day 120) and low suction strength values (Figure 5.8) propagated deeper than 0.3 m, plus they both yielded spatial distributions of low variability (of water content, pressure head, and SS) near the slope. Hence, for the case of 0.3 m and 1.0 m minimum slip surface depths, they produced similar slip surface shapes (refer to Figure C15 and Figure C16 of Appendix C, for the slip surface shapes at day 120 under 0.3 m and 1.0 m minimum depths, respectively) thus producing comparable FOS values.

In the second phase of the slope stability assessment, simulations were conducted, focusing on the maximum saturation (*Max Sat*) event, representing the peak water storage condition. Figure 5.10 provides a visual representation of the suction strength (SS) profiles throughout this specific scenario. Notably distinct from the *Max NI* case depicted in Figure 5.8, the *Max Sat* event in Figure 5.10 exhibits a higher spatial variability in suction strengths (SS). This is characterized by more pronounced changes in SS values along the sloped area of the embankment, particularly when comparing various simulations.

In Figure 5.10, the SS trends for DC, HC, and WC are similar to Figure 5.8, where higher values are predicted by the DC simulation and lower values by WC simulation. The inclusion of air entrapment in the hysteretic simulation led to considerable SS reduction, where the reduction appears to be proportional to increases in the air entrapment volume. For example, in HC

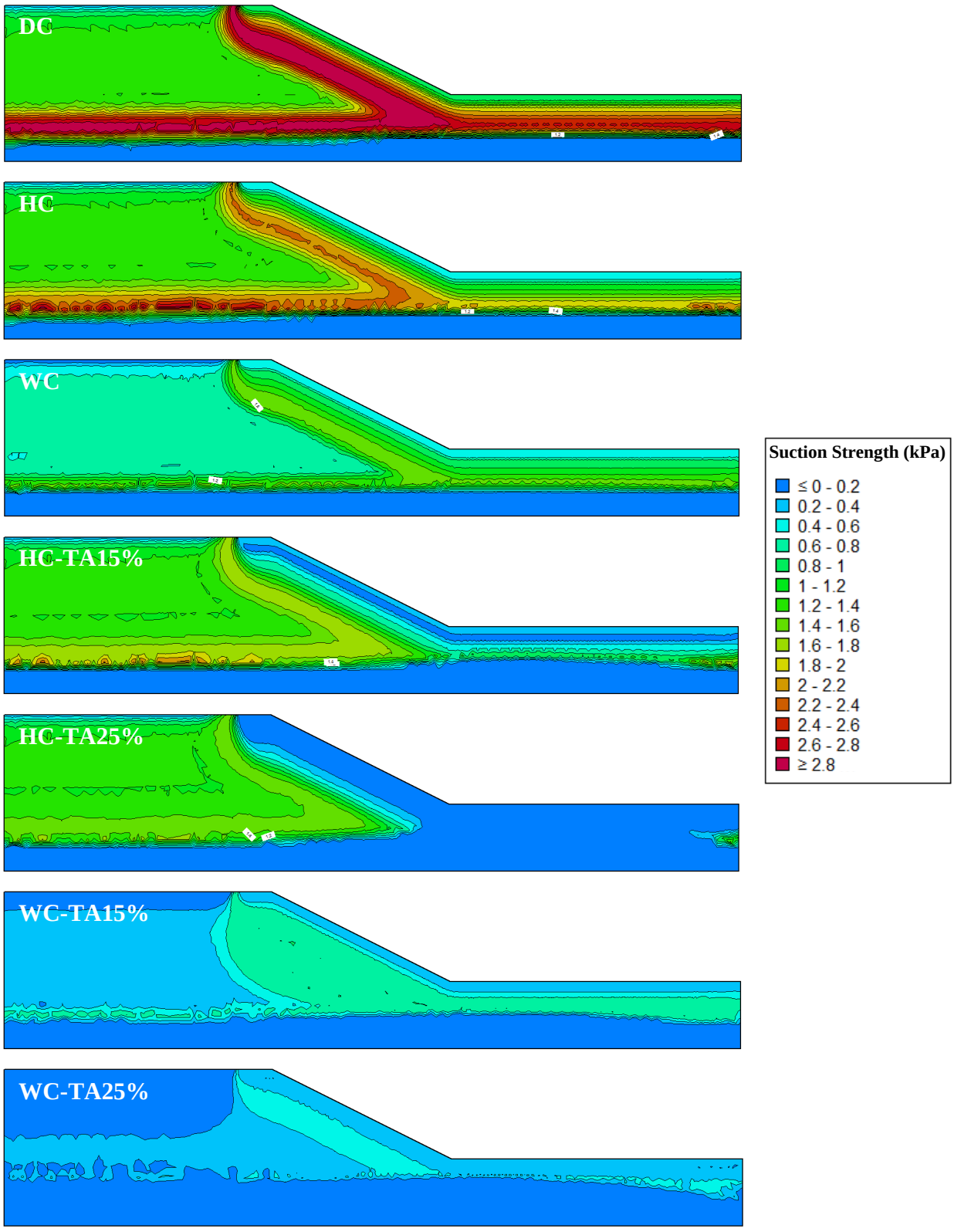

Figure 5.10 Suction strength distribution within silt slope at 289 d (Max. Sat.) – Toronto

simulation, there is a front with high SS values underneath the slope surface, shown in dark orange contour. Nevertheless, for the simulation of hysteresis with air entrapment, it becomes apparent that the leading edge of high suction strength (SS) occurs at considerably lower values and at slightly deeper levels compared to cases with lower entrapment volume, and even more prominently when contrasted with scenarios without air entrapment. As previously explained, entrapment of air has a correlation with increasing the *NI* values which reduces the soil suction and SS values, in addition to this, air entrapment has a direct correlation with reducing the SS values (Figure 5.7). Unlike all other simulations from Figure 5.10, HC-$TA_{25\%}$ simulation reported the largest area of low SS values (~ 0 kPa) at the slope surface.

A crucial observation from Figure 5.10, the WC-$TA_{15\%}$ and WC-$TA_{25\%}$ estimated higher SS values near the slope surface compared to HC-$TA_{15\%}$ and HC-$TA_{25\%}$, respectively. This trend is different from Figure 5.8 (*Max NI*) where WC-$TA_{15\%}$ and WC-$TA_{25\%}$ estimated the lowest SS values. However, unlike the previous case where slope stability was assessed based on a single infiltration event (*Max NI*), *Max Sat* event occurred following a number of lower infiltration events, rather than a single large infiltration, which resulted in more moisture availability within the slope. To further explain this difference, the HC-TA simulations tend to lag the downward water flow behind (compared to WC-TA simulations) due to their higher water retention properties (due to formation of scanning and drying scanning curves). However, for *Max Sat* event, the sloped portion of the embankment has higher saturation than the *Max NI* event. More water is retained near the surface for hysteretic simulations than the WC simulations as WC simulations tend to expedite the downward water flow, hence higher suction values. To put this into perspective, at *Max Sat* event, the formation of the scanning curves in HC-$TA_{25\%}$ delayed the downward water flow, and exacerbated by *Max Sat* event and high availability of moisture,

the sloped portion of the embankment achieved average saturation of 77.5%. This saturation was high enough to cause considerable reduction of suction strength as can be seen in both Figure 5.10 and Figure 5.7. Whereas the much faster downward flow response by WC-$TA_{25\%}$ during *Max Sat* achieved lower water content near the slope surface (sloped area achieving average saturation of 70.6%), however the saturation is relatively lower enough to cause increase in soil suction and suction strength compared to HC-$TA_{25\%}$. On the other hand, looking at *Max NI* case, the sloped portion of the embankment in HC-$TA_{25\%}$ simulation achieved average saturation of 66.9%, whereas, WC-$TA_{25\%}$ achieved average saturation of 58.5%. The trend remains the same, with the former, HC-$TA_{25\%}$, retaining more moisture than latter, WC-$TA_{25\%}$. However, for this case (*Max NI*), the saturation in HC-$TA_{25\%}$ has reached a more moderate value, allowing the slope to retain some of its strength. Whereas, the lower saturation of 58.5% in WC-$TA_{25\%}$ is excessively low and is attributable to causing a significant reduction of soil suction and suction strength, with values even nearing zero. This is also indicated in Figure 5.7, where saturation converging towards 50% translate to zero suction strength. These findings underscore that *Max NI* may not always be the worst-case scenario; instead, the interplay between moisture availability (i.e., *Max Sat*) and the responses of hysteresis and air entrapment determines the strength distribution within the slope. Another important point to add, although DC is attributed with highest water retention properties, it has estimated largest SS value; this is due to the high estimates of actual evaporation value leading to less wet conditions and added strength, as well as to high soil suction for the same water content.

The above discussion illustrates the complexity involving the land-climate interaction. Thus, proving the importance of conducting such analyses to better understand the coupled response

between water balance, moisture/suction distributions, and mechanical response through unsaturated suction strength; the response is transient and highly dynamic in nature.

Figure 5.11 shows a bar chart of the FOS of the silt slope during *Max Sat* event, for two minimum slip surface depths: 0.3 m (left) and 1.0 (right), and for each of the 7 hysteretic and nonhysteretic simulations. The simulation, DC, estimated in the highest FOS values. Whereas, HC and WC simulations, noticeably, lowered the FOS values, for which WC simulation estimated a slightly lower value. The relative similarities between HC and WC simulations, in terms of FOS, is attributed to the more frequent formation of wetting scanning curve (Figure 5.7) during maximum saturation event.

Similar to the SS trend from Figure 5.10, introducing air entrapment in the hysteretic hydraulic characteristics results in lowering of the FOS. For example, the HC-$TA_{15\%}$ simulation predicted

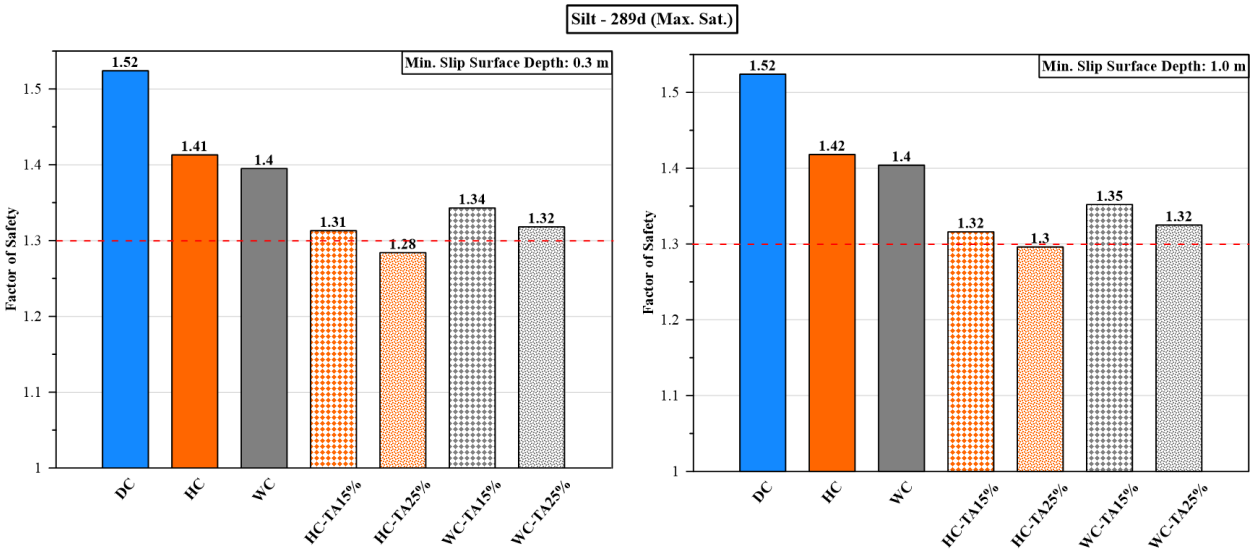

Figure 5.11 FOS of silt slope during maximum saturation occurrence (289 d) using different hydraulic characteristics, with two considered minimum slip surface depths: 0.3 m (left) and 1.0 m (right) – Toronto

an almost unacceptable slope stability condition (FOS = 1.31). Further increase in the volume of air entrapment (HC-$TA_{25\%}$) results in unacceptable slope stability conditions (i.e., FOS < 1.3). Since WC-$TA_{15\%}$ and WC-$TA_{25\%}$ estimated higher SS near the slope surface compared to HC-$TA_{15\%}$ and HC-$TA_{25\%}$, respectively (as seen in Figure 5.10), this translated into higher FOS values as shown in Figure 5.11. This demonstrates that implementing the characteristics of main wetting branches in slope stability assessment is not always an overly conservative approach.

The FOS under both minimum slip surface depths, 0.3 m and 1.0 m, shown comparable results amongst all simulations, which is due to the formation general failure mode under both cases, attributed to the low suction strength fronts located near the slope surface.

In order to investigate the influence of diverse climate types and textural soils on the hysteresis and air entrapment effects influencing slope stability, the comparative findings between North Bay and Toronto are discussed in this section. This analysis is presented in Figure 5.12 (*Max NI*) and Figure 5.13 (*Max Sat*), encompassing slopes composed of both sand and silt. The figures illustrate the difference between the computed Factor of Safety (FOS) and the prescribed minimum acceptable FOS value of 1.3. The red dashed line, positioned at zero, signifies the minimum acceptable limit. A positive value on the graph indicates that the slope is deemed acceptably stable. Conversely, negative values denote that the slope stability is considered unacceptable. This analysis provides insights into how distinct climate and soil characteristics influence the stability of slopes, with a focus on the hysteresis and air entrapment phenomena.

The results for sand embankment in Figure 5.12 and Figure 5.13, indicate that simulation considering hysteretic SWCC (HC) predicts a lower FOS in comparison to nonhysteretic

simulation using the drying curve (DC). Moreover, the incorporation of air entrapment has demonstrated a discernible impact on diminishing the FOS value, with the reduction being

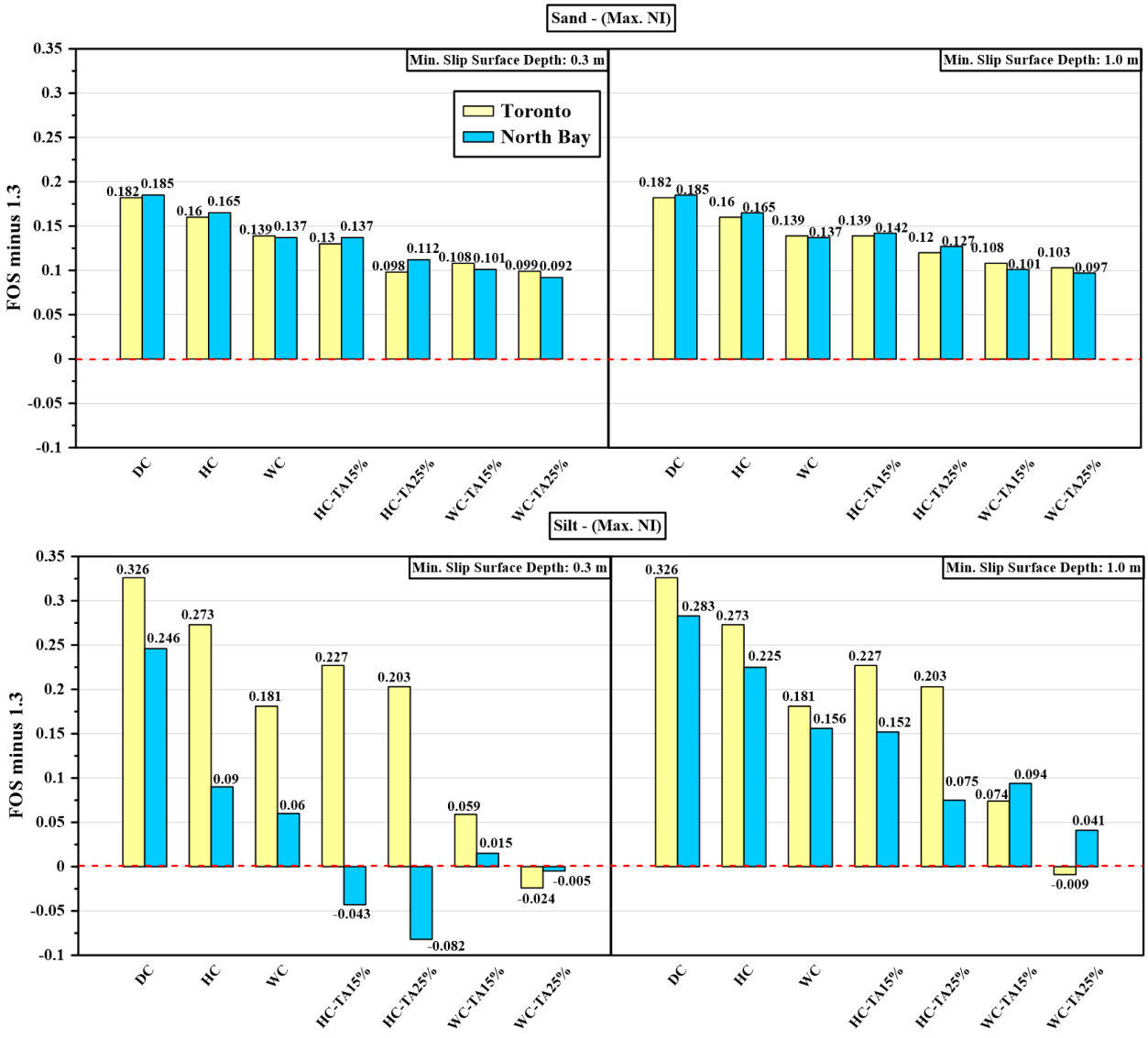

Figure 5.12 Showing the difference between the FOS and the minimum acceptable FOS (1.3) occurring at maximum net infiltration, for sand slope (top) and silt slope (bottom), with two considered minimum slip surface depths: 0.3 m (left) and 1.0 m (right)

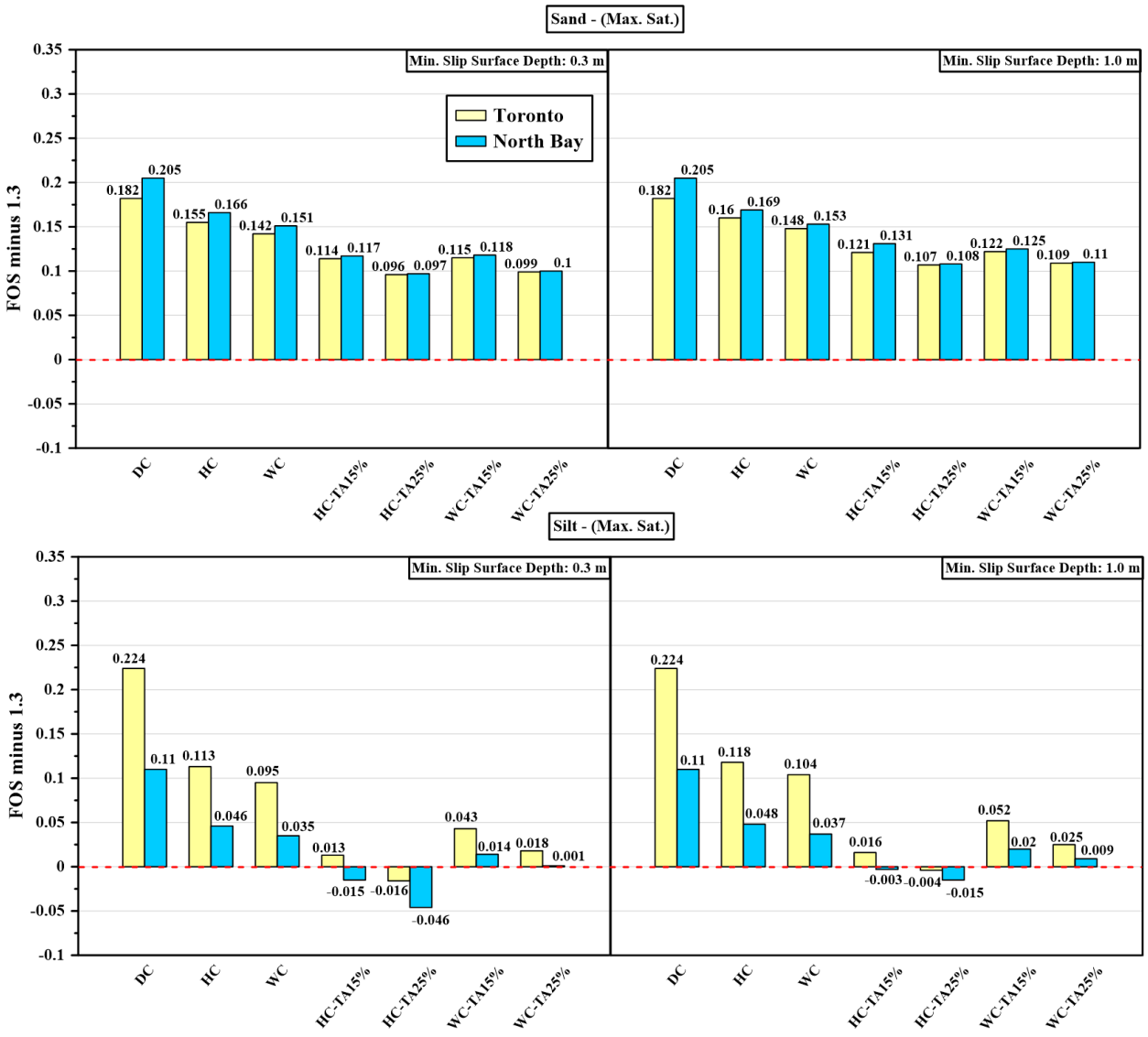

Figure 5.13 Showing the difference between the FOS and the minimum acceptable FOS (1.3) occurring at maximum saturation, for sand slope (top) and silt slope (bottom), with two considered minimum slip surface depths: 0.3 m (left) and 1.0 m (right)

proportional to the escalation in the volume of air entrapment. Nevertheless, the influence of hysteresis and air entrapment on the FOS for the sand slope appears to be less pronounced compared to the impact on the silt slope. This discrepancy can be attributed to the lower water

retention properties and a reduced degree of hysteresis (maximum deviation between effective saturations of the primary drying and wetting curves) associated with sand. Despite these mitigating factors, the perceptible distinctions highlight the significance of considering hysteresis and air entrapment in the assessment of slope stability, even for slopes comprising of coarse materials.

Relative to the sand embankment, the silt embankment showcased more pronounced hysteretic effects on the Factor of Safety (FOS) values. Moreover, the silt slope consistently demonstrated a higher susceptibility to instability in the North Bay climate compared to Toronto, particularly when accounting for hysteresis coupled with air entrapment. One of the important observations is that during the *Max NI* event, surficial slope failures were more likely than the general slope failure mode, particularly when simulating wetter climates (e.g., North Bay) rather than drier climates (such as Toronto). This is attributed to the silt's high water retention properties, leading to a significant accumulation of water near the slope surface. This, in turn, enhances the susceptibility to surficial slope failures, especially pronounced during wetter climatic conditions, such as those experienced in North Bay. In summarizing the potential for silt slope failures, it's noteworthy that only the WC-$TA_{25\%}$ and HC-$TA_{25\%}$ simulations in Toronto indicated potential instability under *Max NI* and *Max Sat* conditions, respectively. This observation held true for both surficial and general slope failure modes. In the case of North Bay, simulations for HC-$TA_{15\%}$, HC-$TA_{25\%}$, and WC-$TA_{25\%}$ indicated surficial slope failure under *Max NI*, while HC-$TA_{15\%}$ and HC-$TA_{25\%}$ reported both surficial and general slope failure under *Max Sat* conditions.

In the majority of simulations conducted for Toronto's climate, the silt slope consistently displayed markedly lower Factor of Safety (FOS) values under *Max Sat* conditions in comparison to *Max NI*, a trend observed across both failure modes. For *Max NI*, none of the

hysteretic simulations, with or without air entrapment, resulted in slope failures for Toronto, except in the case of simulating nonhysteretic WC-$TA_{25\%}$. It was only under *Max Sat* conditions in Toronto that the HC-$TA_{25\%}$ simulation triggered a slope failure. Overall, simulating *Max Sat* events in Toronto's climate revealed a heightened potential for slope failure compared to *Max NI*, particularly when incorporating hysteresis with 25% air entrapment. In North Bay, the trend closely resembles that of Toronto. Generally, FOS values in North Bay tend to be lower during *Max Sat* compared to *Max NI*. However, the *Max NI* conditions resulted in significantly lower FOS values than *Max Sat* only in simulations where the slope is near or at failure, such as HC-$TA_{15\%}$, HC-$TA_{25\%}$, and WC-$TA_{25\%}$. This is particularly true for surficial failure modes, where higher intensities raise greater concern. When considering general failure, *Max Sat* events consistently exhibited much lower FOS values across all simulations. Therefore, caution is advised against drawing a definitive conclusion that large rainfall intensities invariably lead to the most unstable slope conditions. Instead, it is essential to recognize that lower-intensity rainfalls with higher frequency could pose a greater concern, as demonstrated in cases analogous to the present research.

In the comprehensive analysis of hysteretic and air entrapment effects on the silt embankment, simulations with consideration of hysteresis significantly reduces the FOS compared to the DC simulations, which tend to notably estimate a more stable slope. The slope edges perilously closer to unstable conditions and even experiences failure when air entrapment is taken into account in hysteretic simulations, especially with larger volumes of air entrapment, as seen in HC-$TA_{25\%}$ in contrast to HC-$TA_{15\%}$ and especially HC (without air entrapment). The impact of hysteresis and air entrapment on silt slope failures is more pronounced in North Bay, owing to its wetter climate, compared to Toronto. Moreover, for both Toronto and North Bay under both

failure modes, the findings suggest that simulating main wetting branches after air entrapment (WC-$TA_{15\%}$ and WC-$TA_{25\%}$) can result in an overestimation of the FOS relative to their corresponding hysteretic simulations (HC-$TA_{15\%}$ and HC-$TA_{25\%}$). This highlights the potential inaccuracies in slope stability assessments if hysteresis and air entrapment are neglected. The study unequivocally demonstrates the critical importance of considering hysteresis and air entrapment in slope stability assessments, especially for slopes comprising of finer materials. Simulating the hydraulic characteristics ignoring both hysteresis and air entrapment, or especially using the commonly used nonhysteretic drying curve has been shown to overly estimate the slope's stability state.

5.6 Summary and Concluding Remarks

The impact of hysteresis and air entrapment on the stability of a standard MTO highway road embankment was evaluated through the application of the land-climate interactive (LCI) modeling technique. The analyses focused on homogeneous sand and silt slopes, simulating scenarios under two distinct climatic conditions: North Bay (representing wetter climate conditions) and Toronto (representing drier climate conditions). To conduct the Land-Climate Interactive (LCI) modeling, a finite element-based hydrological model was employed. Various hydraulic characteristics, encompassing both hysteretic and nonhysteretic behaviors, were simulated for comparative analysis. These characteristics included nonhysteretic drying and wetting branches as well as hysteresis which entails both branches. Also, three different degrees of air entrapment were considered: 0% (neglecting the effect of air entrapment), 15%, and 25%. The hysteresis model developed by Lenhard et al. (1991) was employed to estimate scanning drying and scanning wetting curves, with the added capability of accounting for the impact of air entrapment.

The soil suction profile generated by the hydrological model was extracted, corrected (using the thesis's proposed correction equation), and then incorporated into the limit equilibrium (LE) model for the slope stability assessment. This correction is crucial for incorporating hysteresis effects into software like SLOPE/W, where unsaturated shear strength calculations typically do not consider hysteresis in suction strength as a function of hysteresis in SWCC. Ignoring the hysteretic nature of suction strength could result in inaccuracies when estimating unsaturated shear strength values and, consequently, the Factor of Safety (FOS).

Results of the different hysteretic and nonhysteretic simulations were compared in terms of water balance at the ground surface, suction strength, and factor of safety (FOS). The results revealed that the simulation using the drying curve, characterized by its heightened water retention properties, retained more water near the surface. Consequently, this translated into a higher estimated actual evaporation (*AE*) and a lower net infiltration (*NI*) value at the ground surface. Conversely, the simulation using hysteretic SWCC resulted in reduced water retention capacity, leading to a larger *NI*. When air entrapment was included in the hysteretic simulations, an amplified hysteretic effect was observed, further increasing the *NI*. Notably, the increments in *NI* were found to be proportional to increases in air entrapment volumes. Simulating the characteristics of the main wetting curve in simulations resulted in an overestimation of *NI*, exhibiting an increasing trend that was also proportional to the air entrapment volume.

In the context of the unsaturated strength component of the slope, simulation using the drying curve of the SWCC led to an overestimation of suction strength within the slope. On the contrary, simulations employing hysteretic SWCC significantly reduced suction strength compared to the DC scenario. The impact of air entrapment was particularly noteworthy, resulting in a considerable reduction in suction strength, especially with a higher volume of air

entrapment (i.e., 25% degree of air entrapment as opposed to 15%). However, simulations involving the main wetting branches, in conjunction with air entrapment, did not consistently estimate the lowest suction strength values. This was especially evident during major wetting events when the use of wetting branches of SWCC results in accelerated water flow, leading to higher suction near the slope surface. In contrast, the wetting front lagged behind in hysteretic curve simulations with air entrapment, resulting in lower suction strength near the surface. The current research researched the dynamic and complex nature of water movement processes, particularly under the influence of different climates, underscoring the crucial importance of employing Land-Climate Interactive (LCI) models to capture these intricate interactions.

After conducting the slope stability assessment, it was established that the influence of hysteresis and air entrapment was relatively minor when considering slopes composed of coarser soils, such as sands. While there were discernible variations in the Factor of Safety (FOS) trends attributable to hysteresis and air entrapment on sand slopes, these variations did not give rise to any failure risks or significant concerns. As a result, they were not further discussed. Conversely, the effects of hysteresis and air entrapment were more pronounced and noteworthy when examining silt slopes.

For silt slopes, simulations based on the drying curve (DC) of the hysteretic SWCC significantly overestimated the stability conditions, resulting in the highest calculated FOS values. The introduction of hysteresis contributed to a notable decrease in FOS, indicating an elevated vulnerability to slope instability. Furthermore, when air entrapment was factored into the hysteretic simulations, especially with larger volumes, the FOS experienced a significant and precipitous drop, leading to instances of potential slope instabilities. Under wetter climatic conditions, such as for the city of North Bay, simulations exhibited heightened occurrences of

potential slope instabilities, further magnified by the combined influences of hysteresis and air entrapment. During maximum *NI* event, it was found that consideration for hysteresis and air entrapment in the analyses led to maximum reductions in the FOS (relative to DC) of 8.0 % under Toronto's climate and 21.3% under North Bay's climate. Whereas, during maximum saturation event the reduction reached 15.8% under Toronto's climate and 11.3% under North Bay's climate. In contrast to water balance trends, hysteretic simulations with air entrapment consistently yielded FOS values lower than the corresponding simulations using the main wetting curves. This divergence was particularly evident during sequences of frequent rainfalls, as opposed to single higher-intensity rainfall events. The current research underscores the suggestion that simulating the main wetting branches after the entrapment of air may not always offer the most conservative approach from a slope stability design perspective.

The present study highlights the pivotal role of both hysteresis and air entrapment in assessing the stability of slopes amid the complexities of intermittent climatic conditions. Neglecting to account for hysteresis and air entrapment can lead to significant inaccuracies in assessing slope stability. The stability condition of the slope may be excessively estimated, particularly when relying on hydraulic characteristics of the drying curve and/or overlooking the influence of air entrapment in hysteretic characteristics.

CHAPTER 6: Conclusions and Recommendations for Future Studies

6.1 Summary

This research was aimed at exploring the impact of hysteresis, taking into account air entrainment, on variably saturated flow, solute transport, and slope stability under interaction of intermittent atmospheric boundary, utilizing numerical modelling.

In identification of the gaps in previous research, the current research's focal objective is to shed light on the importance of considering hysteresis and air entrapment, as both phenomena are commonly neglected in numerical modelling and frequently omitted when measuring soil hydraulic functions. The drying curve of the Soil-Water Characteristic Curve (SWCC) is typically employed to simulate nonmonotonic water flow in unsaturated domains, overlooking the fact that this curve is not reflective of both drying and wetting behaviors. This omission is not rooted in the belief that the effects of hysteresis are negligible; rather, it stems from the practical considerations of expediency, scarcity of data required for calibrating hysteresis models, and impracticality of the additional labor and expenses associated with obtaining such data. In addition, historically, the complex nature of variably saturated water flow in the vadose zone, led to the belief that incorporating hysteresis would further complicate the problem and extend computational times. However, it's no longer a significant challenge given the current capabilities of powerful processors and computers. Moreover, disregarding hysteresis has been demonstrated in previous studies to result in considerably erroneous moisture distributions. Nevertheless, many studies incorporating hysteresis into hydraulic characteristics have often overlooked the impact of air entrapment. Furthermore, a significant gap in many of prior

research on hysteresis lies in the analysis conducted with simplified atmospheric boundaries, primarily emphasizing monotonic water infiltration at the surface.

Consequently, the present research fills in those gaps, and the primary objective of this research, as detailed in this thesis, is to explore the combined effects of hysteresis and air entrapment on solute transport and slope stability assessments. Furthermore, this research uniquely probes into the underexplored realm of studying hysteresis under multi-year intermittent climatic conditions. Given the inherent intermittency of climate, characterized by frequent drying and wetting cycles, understanding the interaction between climate, hysteresis, and air entrapment becomes vital. In addition to examining hysteresis, another focal point of this study is to evaluate the impact of varying degrees of air entrapment.

The current research investigated the influence of hysteresis and air entrapment on three different geotechnical studies selected from the literature: one-dimensional salt transport at an oilfield brine site, two-dimensional flow and solute transport in subsurface drip irrigation (DSI) systems, and slope stability assessment of a typical MTO highway embankment.

The research was divided into different distinct steps. First was to present procedures for calibrating and obtaining the set of the hysteresis van Genuchten (1980) parameters. This was done by obtaining the van Genuchten (1980) parameter of the initial drying curve, then by utilizing experimentally-driven constraints from the literature (e.g., $\alpha^w \approx 2\alpha^d$, $\theta_r^d = \theta_r^w$, and $n^d = n^w$ reported from Kool and Parker (1987), Pham et al. (2005), and Likos et al. (2014)) to obtain the van Genuchten (1980) parameters representing the hysteretic soil-water characteristic curve (SWCC). Also, air entrapment was accounted for by considering different degrees of air entrapment ranging from 5% to 25% as experimentally investigated by Likos et al. (2014) over

wide range of soils; also 0% of air entrapment was accounted for to represent the case neglecting the effect of air entrapment. The second step was to develop hydrological models which account for atmospheric boundary conditions, hysteretic hydraulic characteristics, variably saturated modelling technique, and hysteresis model that can simulate formation of scanning curves in hysteretic SWCC. Hydrus software packages was utilized to perform the hydrological modelling while utilizing the integrated hysteresis model by Lenhard et al. (1991). The third step entailed performing the nonhysteretic and hysteretic hydrological simulations, with and without the air entrapment consideration. The volumetric water content and soil suction resulting from the hydrological simulations were imported into solute transport/slope stability models. The final step involved comparing and contrasting the results between hysteretic and nonhysteretic simulations based on the water balance at the ground surface, water storage, solute transport and fate, and slope stability (in the form of factor of safety). The reported findings are systematically compared with nonhysteretic drying and wetting curves to ensure an unbiased assessment. Unlike previous studies that predominantly compared hysteretic results with the nonhysteretic wetting curve, our intentional inclusion of both nonhysteretic curves aims to eliminate biases in the comparison and assessment process. This approach counters the common practice that has led to potentially misleading conclusions in prior research. In addition to examining hysteresis, results of varying degrees of air entrapment were compared, and amongst them is the case neglecting air entrapment.

6.2 Overall Conclusions

In the broader context, the inclusion of hysteresis with air entrapment in simulating flow in variably saturated porous media has shown importance, particularly under intermittent atmospheric boundary conditions where water saturation reversals were frequent. This

phenomenon led to disparate hydraulic responses in simulations utilizing hysteretic and nonhysteretic hydraulic functions, as well as between scenarios considering air entrapment versus those neglecting it. This disparity had significant implications for assessing solute fate and transport and slope stability conditions when both effects (i.e., hysteresis and air entrapment) were overlooked.

In evaluation of the water balance at the ground surface for all scenarios explored in this thesis, simulations with consideration of hysteresis demonstrated their tendency to augment water flow within the system when compared to simulations utilizing nonhysteretic drying curve (DC) properties. During drainage or drying phases, the DC displayed a smaller change in water content for a relatively significant shift in soil suction, indicating heightened water retention properties. Conversely, hysteretic curves without air entrapment (HC) exhibited the development of scanning drying and, notably, scanning wetting curves, resulting in a more pronounced alteration in water content for a similar change in soil suction. Under atmospheric boundary conditions, this manifested as increased water retention near the surface in DC simulations, providing more moisture for evaporation. Consequently, this led to an overestimation of actual evaporation (*AE*) and an underestimation of net infiltration (*NI*) at the ground surface in DC simulations. The simulations incorporating hysteresis in hydraulic functions displayed relatively diminished water retention properties, yielding lower *AE* and higher *NI* compared to DC simulations. The introduction of air entrapment into hysteretic characteristics was observed to amplify the hysteretic effects, particularly with larger volumes of air entrapment. Consequently, air entrapment further expedited water flow within the system, resulting in reduced moisture retention near the surface, significantly decreased *AE*, and markedly increased *NI* compared to hysteretic cases without air entrapment. This trend exhibited proportionality to the volume of the

entrapped air. Simulations solely employing the wetting curve, both with and without air entrapment, consistently showcased an overestimation of water flow within the soil domain and actual water fluxes at the ground surface. The overall conclusions specific to solute transport processes and slope stability are summarized in the following sections.

6.2.1 1-D Salt Transport at an Oilfield Brine Site

The initial challenge addressed in this study involves the transport of salt in a 1-D domain, portraying the movement of saline water from oilfield brine. Two distinct soil mediums, sand and clay, were investigated in conjunction with the influence of two contrasting climatic conditions in Alberta, Canada: Bighorn Dam, representing relatively wetter conditions, and Calgary, embodying much drier conditions. It was observed that coarser soil (sand), displayed lower hysteretic effects on the salt movement due to its low water retention properties and increased conductivity (i.e., large saturated hydraulic conductivity) for water infiltration and percolation. Due to these characteristics, the results for sand were not discussed in detail. In contrast, finer soils exhibited pronounced hysteresis effects, with clay showcasing a substantial impact on the salt distribution in the soil domain. The study revealed that consideration of hysteresis without air entrapment slightly increased penetration depth compared to the nonhysteretic simulation considering only the drying curve. However, a considerable retardation effect on salt was observed when hysteretic simulations compared with the simulation using the wetting curve. For example, after 18 years of land-climate interaction under Calgary’s climate, the saline water in the drying curve (DC) simulation and hysteretic simulations without air entrapment (HC), the center of mass (COM) reached 1.45 and 1.46 m, respectively, whereas for simulation using the wetting curve without air entrapment (WC) COM reached at a deeper depth of 2.1 m. The inclusion of air entrapment in hysteretic simulations significantly increased salt's

advective fluxes and penetration depth, particularly for larger volumes of air entrapment. For example, compared to HC simulation with COM at 1.5 m after 18 years (under Calgary's climate), hysteretic simulations with 13% and 26% degrees of air entrapment estimated deeper depths of 1.7 m and 2.0 m, respectively. Simulating wetting branches, on the other hand, especially with the consideration of air entrapment, consistently overestimated penetration depths compared to their counterparts' hysteretic simulations. The wetting curve simulations with 13% and 26% air entrapment estimated the COM to be at 2.5 m and 2.9 m, respectively, after 18 years under Calgary's climate. Climate type played a pivotal role in dictating hysteretic effects on the salt fate and transport. Calgary, with the drier climate, exhibited the highest deviation (compared to Bighorn Dam) in terms of salt movement across various hysteretic and nonhysteretic simulations. Notably, simulating the drying curve and hysteretic curve without air entrapment for Calgary resulted in a more noticeable upward displacement of salt, attributed to the drier climate and higher estimates of actual evaporation (*AE*) for the two simulations. Conversely, the predominant mechanism for downward migration of salt was observed with the introduction of air entrapment in the hysteretic simulations. On the other hand, the solute movements were predominantly downward under Bighorn Dam's wetter climate for all hysteretic and nonhysteretic simulations. This study underscores the significance of considering hysteresis and air entrapment in hydraulic characteristics to accurately predict salt transport and fate under contrasting climatic conditions.

6.2.2 2-D Flow and Solute transport in Subsurface Drip Irrigation (SDI) Systems

The second challenge addressed in this study involves flow and solute transport within a 2-D domain, considering the influences of hysteresis with and without air entrapment. Specifically, the investigation focuses on solute transport under the influence of a subsurface irrigation

system. Even in a simplified irrigation scenario without intermittent atmospheric boundary conditions, it was observed that solute pulses exhibited both hysteretic and air entrapment effects, consistently leading to deeper penetration of solute. To further examine the impact, a triggered irrigation problem was studied, wherein irrigation was initiated whenever a specified region reached a prescribed soil suction value. Notably, nonhysteretic simulation using the drying curve (DC) overestimated irrigation occurrences (i.e., five occurrences) due to higher estimates of actual evaporation (*AE*), resulting in increased release of solute pulses and higher concentrations within the domain. In contrast, simulations incorporating hysteresis, especially with air entrapment, demonstrated fewer occurrences of irrigation (i.e., two occurrences in the hysteretic simulation without air entrapment, and only one occurrence when air entrapment was introduced). This is attributed to their lower water retention properties and higher estimates of net infiltration (*NI*), leading to wetter conditions in the domain with few triggered events for hysteretic curve simulations with air entrapment. This finding emphasizes that using DC characteristics in triggered irrigation problems may overirrigate the system with unrealistically high concentration levels. Whereas simulation based on characteristics of the wetting branches did not trigger any irrigation, posing concerns over their inaccuracies. To isolate the effects of hysteresis and air entrapment on solute fate, the irrigation inputs were controlled, and the problem was simulated under intermittent boundary conditions. Results showed that hysteresis accelerated the downward migration of solute, contrasting with DC simulations that retarded solute migration, holding it near its source and surface. Air entrapment significantly accelerated solute migration and increased solute discharge through the bottom boundary, raising concerns about groundwater contamination. Hysteretic simulations without air entrapment retarded solute migration compared to cases with air entrapment, especially with larger volumes of air

entrapment considered. To quantify these earlier conclusions, the estimated cumulative solute flux that discharged out of the bottom boundary increased by 16.0% when simulating hysteresis without air entrapment, relative to the result from the nonhysteretic DC. However, the discharge (relative to DC) considerably increased by 27.3% and 33.1% with the introduction of 15% and 25% air entrapment, in the hysteretic simulations. Simulating nonhysteretic wetting curves resulted in an overestimation of downward solute migration and discharge rates, especially when increasing the degree of air entrapment. To illustrate, the cumulative solute discharge through the bottom boundary, concerning DC, experienced substantial increments. Specifically, there was a surge of 35.5%, 52.0%, and 64.4% when simulating the wetting curve without air entrapment, the wetting curve with 15% air entrapment, and the wetting curve with 25% air entrapment, respectively. Regarding lateral solute migration, nonhysteretic simulations with DC showed more lateral migration near the surface, where solute mainly accumulated due to its retardation of the wetting front. In contrast, simulations considering hysteresis and air entrapment exhibited higher lateral solute displacement near the bottom boundary due to more rapid transport and larger accumulation of solute in that area. This study underscores the importance of hysteresis and air entrapment in 2-D solute transport problems, specifically in the context of subsurface drip irrigation systems.

6.2.3 Slope Stability of a Typical MTO Highway Embankment

In the last phase of this research, the influence of hysteresis with air entrapment on the stability of a typical Ontario highway road embankment slope was studied under intermittent boundary conditions. The study incorporated two soil types, sand and silt, and simulated the interaction under divergent climatic conditions in North Bay (wetter climate) and Toronto (drier climate).

This part of the thesis illustrates how hysteresis manifests its impact on slope stability through two primary avenues: the water balance and the unsaturated shear strength component. A crucial element of the unsaturated shear strength equation, as proposed by Fredlund et al. (1996) and Vanapalli et al. (1996), is the suction strength. Suction strength is directly related to SWCC, parametrized by van Genuchten (1980) equation. Given the inherent hysteresis in the SWCC, suction strength naturally exhibits hysteresis. However, most limit equilibrium-based slope stability software, such as SLOPE/W (version 2021), do not incorporate hysteresis into their algorithms, resulting in the calculation of nonhysteretic suction strength. To address this, the thesis proposes an equation to correct soil suction data, ensuring that software like SLOPE/W, which adopts the unsaturated shear strength framework, can calculate and obtain a hysteretic suction strength profile.

A hydrological model was simulated under intermittent climate conditions, and the resulting soil suctions were extracted at maximum slope saturation and maximum infiltration events. The data was then corrected to take into account the hysteretic and air entrapment effects and were then imported into SLOPE/W for slope stability assessment. Results indicated that the coarser sand slope exhibited less hysteretic effects compared to the finer silt slope; however, differences due to hysteresis and air entrapment were still observed. For the silt slope, the simulation using the nonhysteretic drying curve (DC) of the SWCC overestimated the factor of safety (FOS), raising concerns about potential overestimation of slope stability conditions. The inclusion of hysteresis significantly reduced the FOS, and the incorporation of air entrapment, especially for larger volumes, substantially decreased FOS values. In some instances, the synergistic impact of hysteresis with air entrapment resulted in computed values falling below the threshold for the minimum acceptable Factor of Safety (FOS), indicating a potential vulnerability to slope failures.

For the maximum infiltration event, the FOS outcomes indicated that simulations accounting for both hysteresis and air entrapment resulted in the value reductions, relative to the base condition (DC), reaching up to 8.0% for Toronto's climate and 21.3% for North Bay's climate. Conversely, during the maximum saturation event, the reductions in FOS were observed to be up to 15.8% in Toronto's climate and 11.3% in North Bay's climate.

In the analysis, it was also noted that simulations using the wetting curve without air entrapment consistently led to an underestimation of Factor of Safety (FOS) values compared to hysteretic simulations without air entrapment. However, this trend was not the same for wetting curve simulations with air entrapment. In specific cases, simulations run with wetting curve with air entrapment resulted in an overestimation of FOS relative to hysteretic simulations with air entrapment. This disparity can be attributed to the distinct characteristics of the wetting curve, particularly when air entrapment is involved. The more rapid flow for simulations with wetting curve with air entrapment causes higher suction near the surface, while simulations using the hysteretic curve with air entrapment exhibit a less rapid flow, resulting in greater water retention near the surface exacerbated by the moisture availability especially in wetter climates. This nuanced distinction in flow dynamics contributes to variations in the stability assessment, emphasizing the intricate interplay between hysteretic characteristics and air entrapment effects on slope stability.

6.3 Contributions of This Research

The current research quantified the impacts of hysteresis and air entrapment on hydraulic response (manifested through surface water balance and changes in moisture/suction), solute transport and fate, and slope stability. Unlike previous studies focusing solely on the influence of

hysteresis on solute transport and slope stability without considering air entrapment while only considering a simplified atmospheric boundary, this research delved into the intricate interplay of hysteresis, air entrapment, and hydraulic response, accounting for interactions of real and intermittent multi-year climate. Furthermore, the study employed hysteretic unsaturated shear strength framework to assess slope stability while considering air entrapment. To enhance practical applicability, an equation was proposed to adjust the as-built soil suction, enabling software like SLOPE/W, which relies on nonhysteretic unsaturated shear strength concept, to incorporate the effects of hysteresis and air entrapment in the suction strength and overall slope stability assessments. Notably, the research avoided biases associated with the comparison to a single branch of the hysteresis envelope, as seen in earlier studies, by simulating all nonhysteretic branches (with and without air entrapment), allowing for a comprehensive comparison across different hysteretic analyses.

6.4 Recommendations for Future Studies

This thesis explores the implications of overlooking both hysteresis and hysteresis with air entrapment in solute transport and slope stability assessments, which can lead to inaccuracies in the design and consideration of geotechnical and geoenvironmental studies. Hence, this study underscores the significance of incorporating accurate measurements of hysteretic and air entrapment soil hydraulic characteristics into numerical modeling. Additionally, it emphasizes the need to integrate these characteristics for a more comprehensive and accurate understanding of the environmental and geotechnical dynamics involved in such studies.

Considering some limitations of the current thesis, it is recommended to extend this research by incorporating the following studies to enhance understanding of the effects of hysteresis and air entrapment:

While investigating the impact of hysteresis and air entrapment in relation to climate, this study focused on two contrasting climates within a specific geographic location, ranging from the driest to wettest extremes. To broaden the scope, it is recommended to explore the influence of hysteresis and air entrapment under diverse sets of climatic conditions. This is particularly important considering that precipitation and potential evaporation can vary in intensity, frequency, and duration across different locations. Thus, it would be beneficial to examine these factors beyond just wet and dry climates.

The domains of the studies under investigation were limited to homogeneous soils. Given that real site conditions often involve heterogeneous soils, further research is recommended to explore the interactions between heterogeneity, hysteresis, and air entrapment. This understanding would enhance insights into the influence of these factors on solute transport and slope stability, particularly under the influence of intermittent climatic conditions.

Given that the present research entailed the calibration of hydraulic characteristics to integrate hysteresis and air entrapment, relying on experimentally-driven relationships from prior studies, there is a potential for uncertainty in the results. Therefore, it is recommended for future research to conduct sensitivity analyses on these hydraulic characteristics, supported by experimental investigations, to comprehend the implication of such uncertainties. This approach would provide valuable insights, especially in the context of solute transport and slope stability results.

Additionally, analyzing soils with varying degrees of hysteresis indices would contribute to a more comprehensive understanding.

This study operated under the assumption that hysteretic simulations would initiate at predetermined water content/suction values derived from the primary drying branch of the hysteretic SWCC. Further research is essential to investigate the potential impact on solute fate and slope stability when initiation occurs at scanning curves of different orders. Additionally, exploring whether hysteresis and air entrapment exert distinct influences under varying initial conditions would contribute valuable insights.

References

Aziz, K., and Settari, A. 1979. Petroleum Reservoir Simulation. London: Applied Science Publishers.

Baninajarian, L. 2020. Effect of Future Extreme Precipitation Events on the Stability of Soil Embankments Across Ontario. York University, Toronto, Canada.

Bashir, R., Ahmad, F., and Beddoe, R. 2020. Effect of Climate Change on a Monolithic Desulphurized Tailings Cover. Water, **12**(9): 2645. doi:10.3390/w12092645.

Bashir, R., and Pastora Chevez, E. 2018. Spatial and Seasonal Variations of Water and Salt Movement in the Vadose Zone at Salt-Impacted Sites. Water, **10**(12): 1833. doi:https://doi.org/10.3390/w10121833.

Bashir, R., Sahi, M.A.N., and Sharma, J. 2022. Using Synthetic Climate Datasets for Geotechnical and Geoenvironmental Design Problems. Canadian Geotechnical Journal, **59**(8): 1305–1320. doi:10.1139/cgj-2021-0408.

Bashir, R., Sharma, J., and Stefaniak, H. 2015. Effect of Hysteresis of Soil-Water Characteristic Curves on Infiltration Under Different Climatic Conditions. Canadian Geotechnical Journal, **53**(2): 273–284. doi:10.1139/cgj-2015-0004.

Bear, J. 1972. Dynamics of Fluid in Porous Media. American Elsevier Publishing Company, New York, USA.

Beese, F., and van der Ploeg, R.R. 1976. Influences of Hysteresis on Moisture Flow in an Undisturbed Soil Monolith. Soil Science Society of America Journal, **40**(4): 480–484.

Bishop, A.W. 1959. The Principle of Effective Stress. **39**: 859–863.

Boduroglu, S., and Bashir, R. 2023. Numerical Experiments for Surfactant Infiltration in the Vadose Zone to Demonstrate Concentration-Dependent Capillarity, Viscosity, and Sorption Characteristics. Geosciences, **13**(4): 104. doi:10.3390/geosciences13040104.

Chen, P., Mirus, B., Lu, N., and Godt, J.W. 2017. Effect of Hydraulic Hysteresis on Stability of Infinite Slopes under Steady Infiltration. Journal of Geotechnical and Geoenvironmental Engineering, **143**(9): 04017041. doi:10.1061/(ASCE)GT.1943-5606.0001724.

Chen, Q., and Zhang, L.M. 2006. Three-Dimensional Analysis of Water Infiltration into the Gouhou Rockfill Dam using Saturated-Unsaturated Seepage Theory. Canadian Geotechnical Journal, **43**(5): 449–461.

Cheng, Y.M., and Lau, C.K. 2014. Slope Stability Analysis and Stabilization: New Methods and Insight. *In* Second Edition (2nd ed.). CRC Press, Taylor & Francis Group, Boca Raton.

Dabach, S., Lazarovitch, N., Šimůnek, J., and Shani, U. 2013. Numerical investigation of irrigation scheduling based on soil water status. Irrigation Science, **31**(1): 27–36. doi:10.1007/s00271-011-0289-x.

Dye, H.B., Houston, S.L., and Welfert, B.D. 2011. Influence of Unsaturated Soil Properties Uncertainty on Moisture Flow Modeling. Geotechnical and Geological Engineering, **29**(2): 161–169. doi:10.1007/s10706-009-9281-0.

Ebel, B.A., Loague, K., and Borja, R.I. 2010. The Impacts of Hysteresis on Variably Saturated Hydrologic Response and Slope Failure. Environmental Earth Sciences, **61**(6): 1215–1225. doi:10.1007/s12665-009-0445-2.

Environment Canada. 2017. Historical Data. Available from https://climate.weather.gc.ca/historical_data/search_historic_data_e.html.

Faybishenko, B.A. 1995. Hydraulic Behavior of Quasi-Saturated Soils in the Presence of Entrapped Air: Laboratory Experiments. Water Resources Research, **31**(10): 2421–2435. doi:https://doi.org/10.1029/95WR01654.

Fayer, M.J., and Hillel, D. 1986a. Air Encapsulation: I. Measurement in a Field Soil. Soil Science Society of America Journal, **50**(3): 568–572. doi:https://doi.org/10.2136/sssaj1986.03615995005000030005x.

Fayer, M.J., and Hillel, D. 1986b. Air Encapsulation: II. Profile Water Storage and Shallow Water Table Fluctuations. Soil Science Society of America Journal, **50**(3): 572–577. doi:https://doi.org/10.2136/sssaj1986.03615995005000030006x.

Feddes, R.A., Bresler, E., and Neuman, S.P. 1974. Field Test of a Modified Numerical Model for Water Uptake by Root Systems. Water Resources Research, **10**(6): 1199–1206. doi:10.1029/WR010i006p01199.

Fetter, C.W., Boving, T., and Kreamer, D. 2018. Contaminant Hydrogeology. *In* Third edition. Waveland Press, Inc, Long Grove, Illinois.

Fourie, A.B., Rowe, D., and Blight, G.E. 1999. The Effect of inÆltration on the Stability of the Slopes of a Dry Ash Dump. Géotechnique, **49**(1): 1–13. doi:10.1680/geot.1999.49.1.1.

Fredlund, D.G., and Morgenstern, N.R. 1977. Stress State Variables for Unsaturated Soil. Journal of the Geotechnical Engineering Division, **103**(5): 447–466. doi:https://doi.org/10.1061/AJGEB6.0000423.

Fredlund, D.G., Morgenstern, N.R., and Widger, R.A. 1978. The Shear Strength of Unsaturated Soils. Canadian Geotechnical Journal, **15**(3): 313–321. doi:10.1139/t78-029.

Fredlund, D.G., and Rahardjo, H. 1993. Soil Mechanics for Unsaturated Soils. John Wiley & Sons, Inc, New York.

Fredlund, D.G., Rahardjo, H., and Fredlund, M.D. 2012. Unsaturated Soil Mechanics in Engineering Practice. John Wiley & Sons, Inc.

Fredlund, D.G., Xing, A., Fredlund, M.D., and Barbour, S.L. 1996. The Relationship of the Unsaturated Soil Shear Strength to the Soil-Water Characteristic Curve. Canadian Geotechnical Journal, **33**(3): 440–448. doi:https://doi.org/10.1139/t96-065.

Gavin, K., and Xue, J. 2008. A Simple Method to Analyze Infiltration into Unsaturated Soil Slopes. Computers and Geotechnics, **35**(2): 223–230. doi:10.1016/j.compgeo.2007.04.002.

van Genuchten, M.Th. 1980. A Closed-Form Equation for Predicting the Hydraulic Conductivity of Unsaturated Soils. Soil Science Society of America Journal, **44**(5): 892–898. doi:https://doi.org/10.2136/sssaj1980.03615995004400050002x.

GEO-SLOPE. 2022. Limit Equilibrium Formulation. GEO-SLOPE International Ltd., Calgary, AB, Canada,.

Gillham, R.W., Klute, A., and Heermann, D.F. 1976. Hydraulic Properties of a Porous Medium: Measurement and Empirical Representation. Soil Science Society of America Journal, **40**(2): 203–207. doi:https://doi.org/10.2136/sssaj1976.03615995004000020008x.

Gillham, R.W., Klute, A., and Heermann, D.F. 1979. Measurement and Numerical Simulation of Hysteretic Flow in a Heterogeneous Porous Medium. Soil Science Society of America Journal, **43**(6): 1061–1067. doi:https://doi.org/10.2136/sssaj1979.03615995004300060001x.

Gladnyeva, R., and Saifadeen, A. 2012. Effects of Hysteresis and Temporal Variability in Meteorological Input Data in Modeling of Solute Transport in Unsaturated Soil Using HYDRUS-1D. Journal of Water Management and Research, **68**: 285–293.

Godt, J.W., Baum, R.L., and Lu, N. 2009. Landsliding in Partially Saturated Materials. Geophysical Research Letters, **36**(2). doi:10.1029/2008GL035996.

Government of Alberta. 2020. Subsoil Salinity Tool Version 3.0 User Manual. : 184.

Gui, S., Zhang, R., Turner, J.P., and Xue, X. 2000. Probabilistic Slope Stability Analysis with Stochastic Soil Hydraulic Conductivity. Journal of Geotechnical and Geoenvironmental Engineering, **126**(1): 1–9. doi:https://doi.org/10.1061/(ASCE)1090-0241(2000)126:1(1).

Guram, S., and Bashir, R. 2023. Examination of Measured to Predicted Hydraulic Properties for Low Impact Development Substrates. Hydrology, **10**(5): 105. doi:10.3390/hydrology10050105.

Haines, W.B. 1930. Studies in the Physical Properties of Soil. V. The Hysteresis Effect in Capillary Properties, and the Modes of Moisture Distribution Associated Therewith. The Journal of Agricultural Science, **20**(1): 97–116. doi:10.1017/S002185960008864X.

Hanson, B., Hopmans, J.W., and Šimůnek, J. 2008. Leaching with Subsurface Drip Irrigation under Saline, Shallow Groundwater Conditions. Vadose Zone Journal, **7**(2): 810–818. doi:10.2136/vzj2007.0053.

Haque, U., da Silva, P.F., Devoli, G., Pilz, J., Zhao, B., Khaloua, A., Wilopo, W., Andersen, P., Lu, P., Lee, J., Yamamoto, T., Keellings, D., Wu, J.-H., and Glass, G.E. 2019. The Human Cost of Global Warming: Deadly Landslides and Their Triggers (1995–2014). Science of The Total Environment, **682**: 673–684. doi:10.1016/j.scitotenv.2019.03.415.

Hoa, N.T., Gaudu, R., and Thirriot, C. 1977. Influence of the Hysteresis Effect on Transient Flows in Saturated-Unsaturated Porous Media. Water Resources Research, **13**(6): 992–996. doi:10.1029/WR013i006p00992.

Hopmans, J.W., and Dane, J.H. 1986. Combined Effect of Hysteresis and Temperature on Soil-Water Movement. Journal of Hydrology, **83**(1–2): 161–171. doi:10.1016/0022-1694(86)90190-3.

Huang, Y.H. 2014. Slope Stability Analysis by the Limit Equilibrium Method: Fundamentals and Methods. *In* ASCE Press. American Society of Civil Engineers, Reston, VA.

Huat, B.B.K., Gue, S.S., and Haji Ali, F. (*Editors*). 2004. Tropical Residual Soils Engineering. *In* 1st ed. A.A.Balkema Publishers, Taylor & Francis Group plc, London, UK.

Jaynes, D.B. 1984. Comparison of Soil-Water Hysteresis Models. Journal of Hydrology, **75**(1–4): 287–299. doi:10.1016/0022-1694(84)90054-4.

Jones, M.J., and Watson, K.K. 1987. Effect of Soil Water Hysteresis on Solute Movement During Intermittent Leaching. Water Resources Research, **23**(7): 1251–1256. doi:10.1029/WR023i007p01251.

Kaluarachchi, J.J., and Parker, J.C. 1987. Effects of Hysteresis with Air Entrapment on Water Flow in the Unsaturated Zone. Water Resources Research, **23**(10): 1967–1976. doi:10.1029/WR023i010p01967.

Kang, S., Lee, S.-R., and Cho, S.-E. 2020. Slope Stability Analysis of Unsaturated Soil Slopes Based on the Site-Specific Characteristics: A Case Study of Hwangryeong Mountain, Busan, Korea. Sustainability, **12**(7): 2839. doi:10.3390/su12072839.

Keiffer, C.H., and Ungar, I.A. 2002. Germination and Establishment of Halophytes on Brine-affected Soils. Journal of Applied Ecology, **39**(3): 402–415. doi:10.1046/j.1365-2664.2002.00720.x.

Kim, J., Jeong, S., Park, S., and Sharma, J. 2004. Influence of Rainfall-Induced Wetting on the Stability of Slopes in Weathered Soils. Engineering Geology, **75**(3–4): 251–262. doi:10.1016/j.enggeo.2004.06.017.

Klausner, Y. 1991. Fundamentals of Continuum Mechanics of Soils. London : Springer-Verlag.

Klute, A., and Heermann, D.F. 1974. Soil Water Profile Development Under a Periodic Boundary Condition. Soil Science, **117**(5): 265–271.

Kool, J.B., and Parker, J.C. 1987. Development and Evaluation of Closed-Form Expressions for Hysteretic Soil Hydraulic Properties. Water Resources Research, **23**(1): 105–114. doi:10.1029/WR023i001p00105.

Krahn, J., Fredlund, D.G., and Klassen, M.J. 1989. Effect of Soil Suction on Slope Stability at Notch Hill. Canadian Geotechnical Journal, **26**(2): 269–278. doi:https://doi.org/10.1139/t89-036.

Kristo, C., Rahardjo, H., and Satyanaga, A. 2019. Effect of Hysteresis on the Stability of Residual Soil Slope. International Soil and Water Conservation Research, **7**(3): 226–238. doi:10.1016/j.iswcr.2019.05.003.

Land, C.S. 1968. Calculation of Imbibition Relative Permeability for Two- and Three-Phase Flow From Rock Properties. Society of Petroleum Engineers Journal, **8**(02): 149–156. doi:10.2118/1942-PA.

Le, T.M.H., Gallipoli, D., Sanchez, M., and Wheeler, S.J. 2011. Stochastic Analysis of Unsaturated Seepage through Randomly Heterogeneous Earth Embankments. International Journal for Numerical and Analytical Methods in Geomechanics, **36**(8): 1056–1076. doi:10.1002/nag.1047.

Lee, K.T., and Ho, J.-Y. 2009. Prediction of Landslide Occurrence Based on Slope-Instability Analysis and Hydrological Model Simulation. Journal of Hydrology, **375**(3–4): 489–497. doi:10.1016/j.jhydrol.2009.06.053.

Lenhard, R.J., and Parker, J.C. 1987. A Model for Hysteretic Constitutive Relations Governing Multiphase Flow: 2. Permeability-Saturation Relations. Water Resources Research, **23**(12): 2197–2206. doi:10.1029/WR023i012p02197.

Lenhard, R.J., Parker, J.C., and Kaluarachchi, J.J. 1991. Comparing Simulated and Experimental Hysteretic Two-Phase Transient Fluid Flow Phenomena. Water Resources Research, **27**(8): 2113–2124. doi:10.1029/91WR01272.

Likos, W.J., and Lu, N. 2004. Hysteresis of Capillary Stress in Unsaturated Granular Soil. Journal of Engineering Mechanics, **130**(6): 646–655. doi:https://doi.org/10.1061/(ASCE)0733-9399(2004)130:6(646).

Likos, W.J., Lu, N., and Godt, J.W. 2014. Hysteresis and Uncertainty in Soil Water-Retention Curve Parameters. Journal of Geotechnical and Geoenvironmental Engineering, **140**(4): 04013050. doi:10.1061/(ASCE)GT.1943-5606.0001071.

Liu, K., Vardon, P.J., Arnold, P., and Hicks, M.A. 2015. Effect of Hysteresis on the Stability of an Embankment Under Transient Seepage. IOP Conference Series: Earth and Environmental Science, **26**(1): 12013–12021. doi:10.1088/1755-1315/26/1/012013.

Liu, K., Vardon, P.J., Hicks, M.A., and Arnold, P. 2017. Combined Effect of Hysteresis and Heterogeneity on the Stability of an Embankment Under Transient Seepage. Engineering Geology, **219**: 140–150. doi:10.1016/j.enggeo.2016.11.011.

Lu, N., and Godt, J. 2008. Infinite Slope Stability Under Steady Unsaturated Seepage Conditions. Water Resources Research, **44**(11). doi:10.1029/2008WR006976.

Lu, N., and Godt, J.W. 2013. Hillslope Hydrology and Stability. Cambridge University Press, Cambridge, UK.

Lu, N., Kaya, M., Collins, B.D., and Godt, J.W. 2013. Hysteresis of Unsaturated Hydromechanical Properties of a Silty Soil. Journal of Geotechnical and Geoenvironmental Engineering, **139**(3): 507–510. doi:10.1061/(ASCE)GT.1943-5606.0000786.

Lu, N., and Likos, W.J. 2004. Unsaturated Soil Mechanics. Wiley, Hoboken, NJ.

Lu, N., and Likos, W.J. 2006. Suction Stress Characteristic Curve for Unsaturated Soil. Journal of Geotechnical and Geoenvironmental Engineering, **132**(2): 131–142. doi:10.1061/(ASCE)1090-0241(2006)132:2(131).

Lu, N., Şener-Kaya, B., Wayllace, A., and Godt, J.W. 2012. Analysis of rainfall-induced slope instability using a field of local factor of safety. Water Resources Research, **48**(9): 2012WR011830. doi:10.1029/2012WR011830.

Ma, K.-C., Tan, Y.-C., and Chen, C.-H. 2011. The Influence of Water Retention Curve Hysteresis on the Stability of Unsaturated Soil Slopes. Hydrological Processes, **25**(23): 3563–3574. doi:10.1002/hyp.8081.

Mavara, T., and Bashir, R. 2018. Hysteresis in Soil Water Characteristic Curve of Unsaturated Soil and its Influence on Slope Stability. Canadian Geotechnical Society,: 1–7.

Millington, R.J., and Quirk, J.P. 1961. Permeability of Porous Solids. Transactions of the Faraday Society, **57**: 1200–1207. doi:10.1039/tf9615701200.

Mitchell, R.J., and Mayer, A.S. 1998. The Significance of Hysteresis in Modeling Solute Transport in Unsaturated Porous Media. Soil Science Society of America Journal, **62**(6): 1506–1512. doi:10.2136/sssaj1998.03615995006200060005x.

Morgenstern, N.R., and Price, V.E. 1967. A Numerical Method for Solving the Equations of Stability of General Slip Surfaces. The Computer Journal, **9**(4): 388–393. doi:10.1093/comjnl/9.4.388.

Mualem, Y. 1974. A Conceptual Model of Hysteresis. Water Resources Research, **10**(3): 514–520. doi:10.1029/WR010i003p00514.

Mualem, Y. 1976. A New Model for Predicting the Hydraulic Conductivity of Unsaturated Porous Media. Water Resources Research, **12**(3): 513–522. doi:10.1029/WR012i003p00513.

Mualem, Y. 1984. A Modified Dependent-Domain Theory of Hysteresis. Soil Science, **137**(5): 283–291.

Neuman, S.P., Feddes, R.A., and Bresler, E. 1974. Finite Element Simulation of Flow in Saturated-Unsaturated Soils Considering Water Uptake by Plants. Hydraulic Engineering Lab.

Parker, J.C., and Lenhard, R.J. 1987. A Model for Hysteretic Constitutive Relations Governing Multiphase Flow: 1. Saturation-Pressure Relations. Water Resources Research, **23**(12): 2187–2196. doi:10.1029/WR023i012p02187.

Pastora Chevez, E.M. 2017. Effect of Climate Type and Temporal Variability in Meteorological Input Data in Modeling of Salt Transport in Unsaturated Soils. York University, Toronto, Ontario, Canada.

PC-Progress. 2022. Subsurface Line Source. Available from https://www.pc-progress.com/en/Default.aspx?h3d2-tut-22.

Pham, H.Q., Fredlund, D.G., and Barbour, S.L. 2005. A Study of Hysteresis Models for Soil-Water Characteristic Curves. Canadian Geotechnical Journal, **42**(6): 1548–1568. doi:10.1139/t05-071.

Pickens, J.F., and Gillham, R.W. 1980. Finite Element Analysis of Solute Transport Under Hysteretic Unsaturated Flow Conditions. Water Resources Research, **16**(6): 1071–1078. doi:10.1029/WR016i006p01071.

Pk, S., Bashir, R., and Beddoe, R. 2021. Effect of Climate Change on Earthen Embankments in Southern Ontario, Canada. Environmental Geotechnics, **8**(2): 148–169. doi:10.1680/jenge.18.00068.

Rahardjo, H., Heng, O.B., and Choon, L.E. 2004. Shear Strength of a Compacted Residual Soil from Consolidated Drained and Constant Water Content Triaxial Tests. Canadian Geotechnical Journal, **41**(3): 421–436. doi:10.1139/t03-093.

Rahardjo, H., Lim, T.T., Chang, M.F., and Fredlund, D.G. 1995. Shear-Strength Characteristics of a Residual Soil. Canadian Geotechnical Journal, **32**(1): 60–77.

Rahardjo, H., Nio, A.S., Leong, E.C., and Song, N.Y. 2010. Effects of Groundwater Table Position and Soil Properties on Stability of Slope during Rainfall. Journal of Geotechnical and Geoenvironmental Engineering, **136**(11): 1555–1564. doi:10.1061/(ASCE)GT.1943-5606.0000385.

Ran, H., Jia-Min, H., Yi-Feng, C., and Chuang-Bing, Z. 2018. Hydraulic Hysteresis Effects on the Coupled Flow–Deformation Processes in Unsaturated Soils: Numerical Formulation and

Slope Stability Analysis. Applied Mathematical Modelling, **54**: 221–245. doi:10.1016/j.apm.2017.09.023.

Richards, L.A. 1931. Capillary Conduction of Liquids Through Porous Mediums. Physics, **1**(5): 318–333. doi:10.1063/1.1745010.

Royer, J.M., and Vachaud, G. 1975. Field Determination of Hysteresis in Soil-Water Characteristics. Soil Science Society of America Journal, **39**(2): 221–223. doi:10.2136/sssaj1975.03615995003900020006x.

Russo, D., Jury, W.A., and Butters, G.L. 1989. Numerical Analysis of Solute Transport during Transient Irrigation: 1. The Effect of Hysteresis and Profile Heterogeneity. Water Resources Research, **25**(10): 2109–2118. doi:10.1029/WR025i010p02109.

Rutherford, S. 2004. Groundwater Use in Canada. West Coast Environmental Law, Vancouver, BC.

Scott, P.S., Farquhar, G.J., and Kouwen, N. 1983. Hysteresis effects on net infiltration, Advances in Infiltration. American Society of Agricultural Engineers Publication 11-83,: 163–170.

Šimůnek, J. 2013. PC-Progress Discussion Forums. Available from https://www.pc-progress.com/forum/viewtopic.php?f=3&t=2274&p=8110&hilit=Evaporation#p8110.

Šimůnek, J. 2022. System-Dependent Boundary Conditions – Atmospheric Boundary Condition. PC-Progress.

Šimůnek, J., and van Genuchten, M.Th. 1995. Numerical Model For Simulating Multiple Solute Transport In Variably-Saturated Media. U.S. Salinity Laboratory, USDA, ARS, 4.50 Big Springs Road, Riverside, CA, 92507, USA,: 21–30.

Šimůnek, J., van Genuchten, T., and Šejna, J. 2022. The HYDRUS Software Package for Simulating One-, Two-, and Three-Dimensional Movement of Water, Heat, and Multiple Solutes in Variably-Saturated Porous Media, Technical Manual II, Hydrus 2D/3D. Version 5.0. PC Progress, Prague, Czech Republic.

Šimůnek, J., Kodešová, R., Gribb, M.M., and van Genuchten, M.T. 1999. Estimating Hysteresis in the Soil Water Retention Function from Cone Permeameter Experiments. Water Resources Research, **35**(5): 1329–1345. doi:10.1029/1998WR900110.

Šimůnek, J., Šejna, M., Saito, H., Sakai, M., and van Genuchten, M.Th. 2013. HYDRUS1D-4.17.pdf. Department of Environmental Sciences, University of California.

Skaggs, T.H., Trout, T.J., Šimůnek, J., and Shouse, P.J. 2004. Comparison of HYDRUS-2D Simulations of Drip Irrigation with Experimental Observations. Journal of Irrigation and Drainage Engineering, **130**(4): 304–310. doi:10.1061/(ASCE)0733-9437(2004)130:4(304).

SLOPE/W. 2021. Stability Modeling with SLOPE/W. GEO-SLOPE International Ltd, Calgary, AB, Canada.

Smith, R.E. 1993. Simulation Experiments on the Role of Soil Hydraulic Characteristics in Argo-Ecosystems. Modelling Geo-Biosphere Processes 2:1-14,.

Smith, R.E. 1995. Unbias the Evaluation of Soil Hysteresis Effects on Transport. Ecological Modelling, **82**(2): 205–206. doi:10.1016/0304-3800(95)00133-G.

Stauffer, F., and Dracos, T. 1984. Local Infiltration into Layered Soil and Response of the Water Table, Experiment and Simulation. Frontiers in hydrology,: 228–242.

Tami, D., Rahardjo, H., and Leong, E.-C. 2004. Effects of Hysteresis on Steady-State Infiltration in Unsaturated Slopes. Journal of Geotechnical and Geoenvironmental Engineering, **130**(9): 956–967. doi:10.1061/(ASCE)1090-0241(2004)130:9(956).

Thornthwaite, C.W. 1948. An Approach Toward a Rational Classification of Climate. Taylor & Francis, Ltd, **38**(1): 55–94. doi:10.2307/210739.

Thornthwaite, C.W., and Hare, F.K. 1955. Climatic Classification in Forestry.

Topp, G.C. 1971. Soil-Water Hysteresis: the Domain Theory Extended to Pore Interaction Conditions. Soil Science Society of America Journal, **35**(2): 219–225. doi:10.2136/sssaj1971.03615995003500020017x.

Travis, Q.B., Houston, S.L., Marinho, F.A.M., and Schmeeckle, M. 2010. Unsaturated Infinite Slope Stability Considering Surface Flux Conditions. Journal of Geotechnical and Geoenvironmental Engineering, **136**(7): 963–974. doi:10.1061/(ASCE)GT.1943-5606.0000301.

Tsai, T.-L. 2011. Influences of soil water characteristic curve on rainfall-induced shallow landslides. Environmental Earth Sciences, **64**(2): 449–459. doi:10.1007/s12665-010-0868-9.

Tsai, T.-L., and Chen, H.-F. 2010. Effects of Degree of Saturation on Shallow Landslides Triggered by Rainfall. Environmental Earth Sciences, **59**(6): 1285–1295. doi:10.1007/s12665-009-0116-3.

Vanapalli, S.K., Fredlund, D.G., Pufahl, D.E., and Clifton, A.W. 1996. Model for the Prediction of Shear Strength with Respect to Soil Suction. Canadian Geotechnical Journal, **33**(3): 379–392. doi:10.1139/t96-060.

Vereecken, H., Diels, J., and Viaene, P. 1995. The Effect of Soil Heterogeneity and Hysteresis on Solute Transport: a Numerical Experiment. Ecological Modelling, **77**(2–3): 273–288. doi:10.1016/0304-3800(94)00183-I.

Viaene, P., Vereecken, H., Diels, J., and Feyen, J. 1994. A Statistical Analysis of Six Hysteresis Models For the Moisture Retention Characteristic. Soil Science, **157**(6): 345–355.

Wayllace, A., and Lu, N. 2012. A Transient Water Release and Imbibitions Method for Rapidly Measuring Wetting and Drying Soil Water Retention and Hydraulic Conductivity Functions. J. ASTM Geotech Test, **35**(1): 1–15.

Werner, A.D., and Lockington, D.A. 2006. Artificial Pumping Errors in the Kool–Parker Scaling Model of Soil Moisture Hysteresis. Journal of Hydrology, **325**(1–4): 118–133. doi:10.1016/j.jhydrol.2005.10.012.

Yang, C., Sheng, D., and Carter, J.P. 2011. Hysteretic Seepage analysis in Unsaturated Soil Covers. Proceedings of the 5th Asia-Pacific Conference on Unsaturated Soils,: 541–546.

Zaky, F.A., and Oh, S. 2017. Transient Analysis on Infiltration and Stability for Unsaturated Soils in Busan Landslide Area. International Journal of Environmental Science, **2**: 5.

Zhang, L.L., Fredlund, M.D., Fredlund, D.G., Lu, H., and Wilson, G.W. 2015. The Influence of the Unsaturated Soil Zone on 2-D and 3-D Slope Stability Analyses. Engineering Geology, **193**: 374–383. doi:10.1016/j.enggeo.2015.05.011.

Zhu, H., Zhang, L.M., Zhang, L.L., and Zhou, C.B. 2013. Two-Dimensional Probabilistic Infiltration Analysis with a Spatially Varying Permeability Function. Computers and Geotechnics, **48**: 249–259. doi:10.1016/j.compgeo.2012.07.010.

Appendix – A

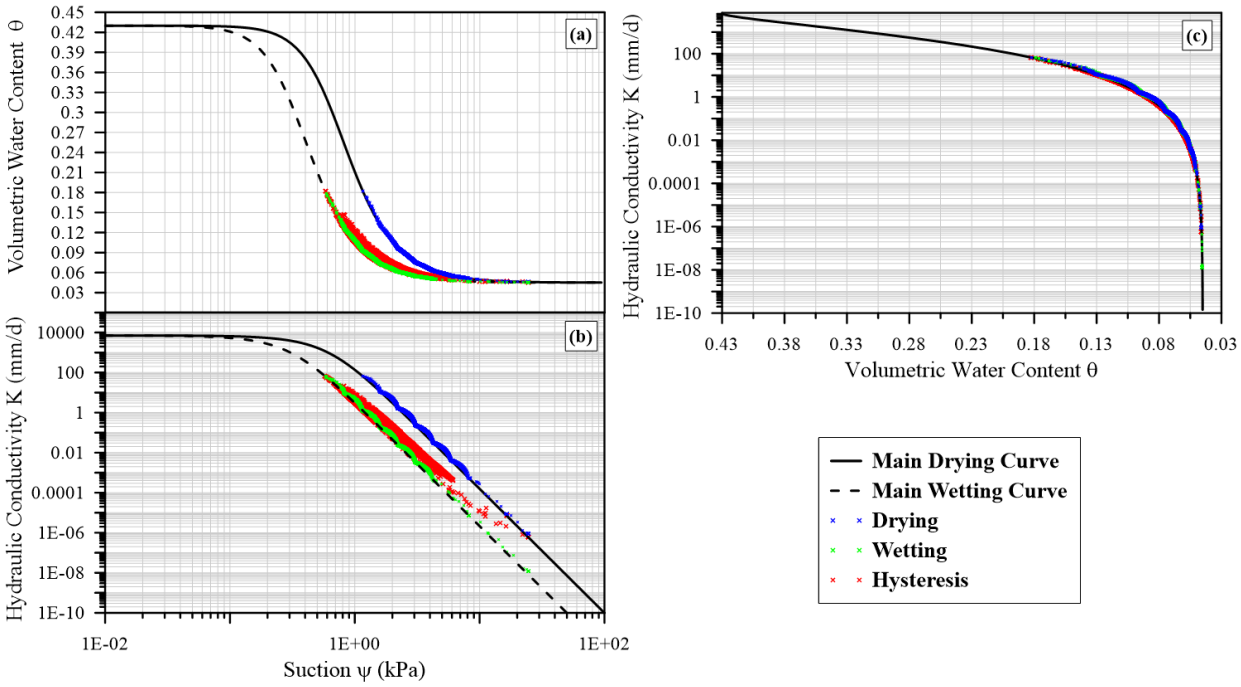

Figure A1 Soil water characteristic curve and unsaturated hydraulic conductivity function for sand used in simulations (data from Hydrus 1D simulations at nodes: 0 m, 0.01 m, 0.02 m, 0.03 m, 0.1 m, 0.3 m, 0.5 m, 1.0 m, 1.5 m, 3.0 m): with 0% air entrapment – Bighorn Dam

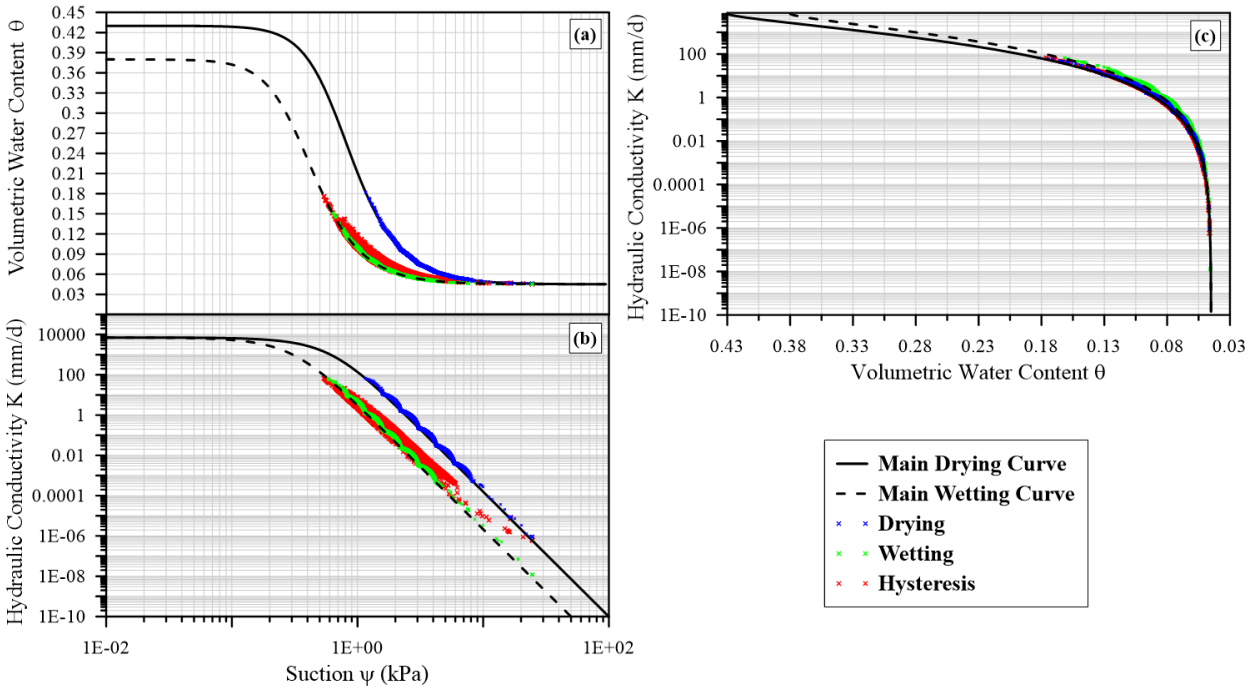

Figure A2 Soil water characteristic curve and unsaturated hydraulic conductivity function for sand used in simulations (data from Hydrus 1D simulations at nodes: 0 m, 0.01 m, 0.02 m, 0.03 m, 0.1 m, 0.3 m, 0.5 m, 1.0 m, 1.5 m, 3.0 m): with 12% air entrapment – Bighorn Dam

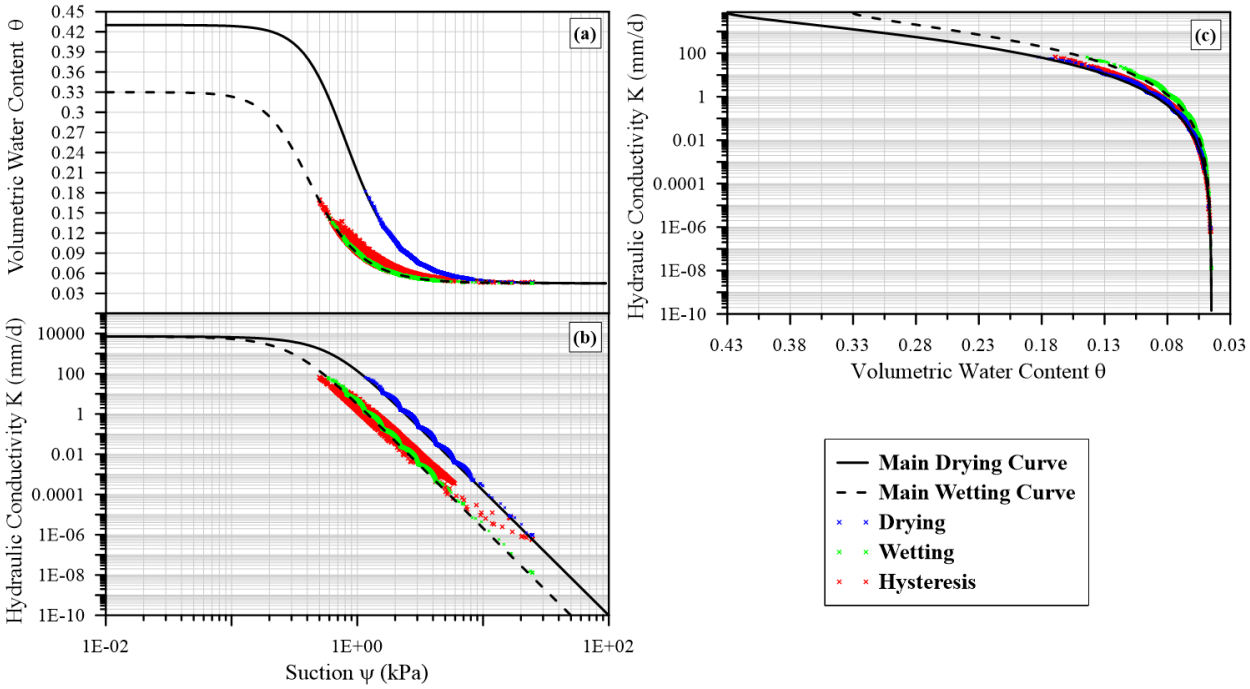

Figure A3 Soil water characteristic curve and unsaturated hydraulic conductivity function for sand used in simulations (data from Hydrus 1D simulations at nodes: 0 m, 0.01 m, 0.02 m, 0.03 m, 0.1 m, 0.3 m, 0.5 m, 1.0 m, 1.5 m, 3.0 m): with 23% air entrapment – Bighorn Dam

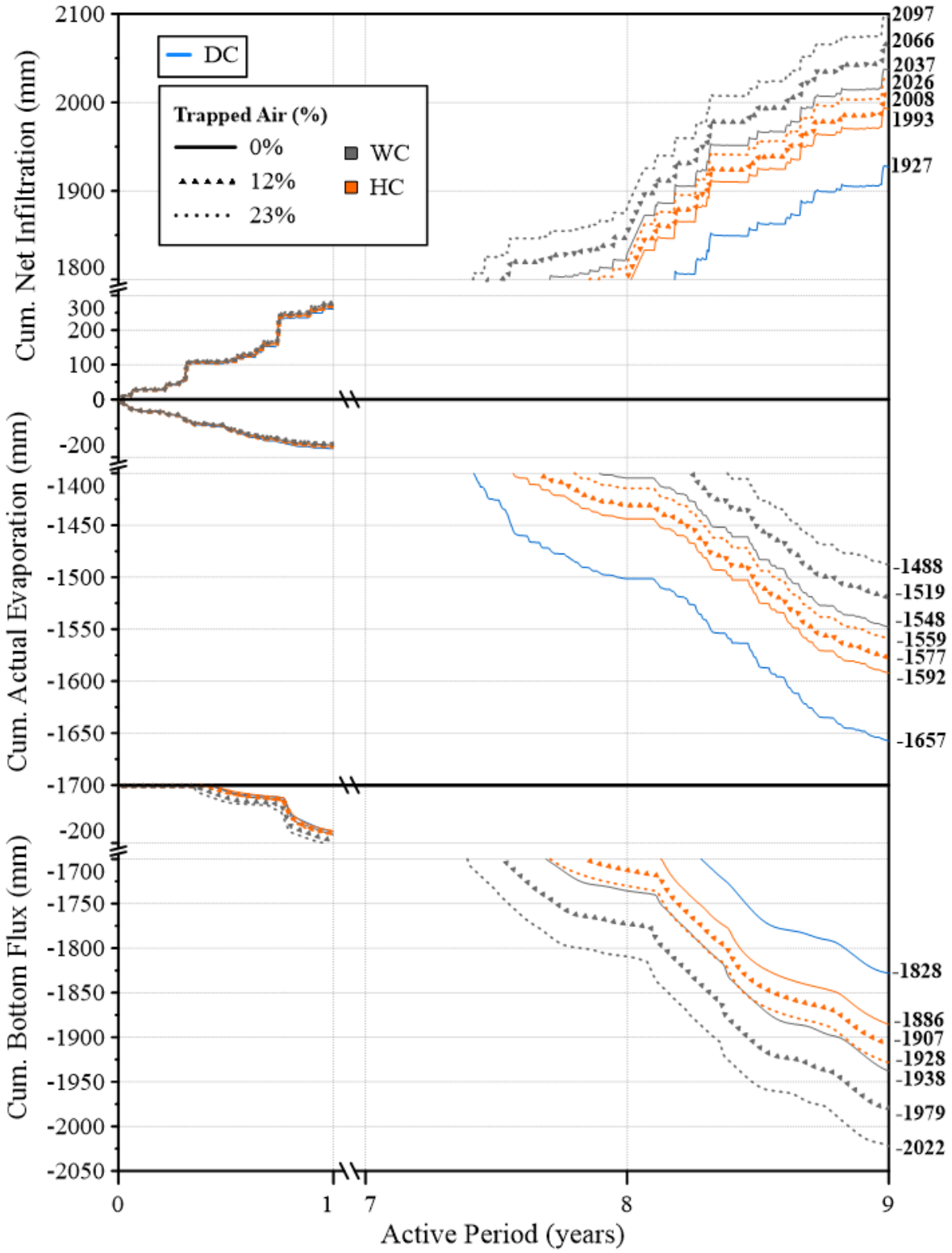

Figure A4 Estimated water balance at the surface of the sand profile – Bighorn Dam

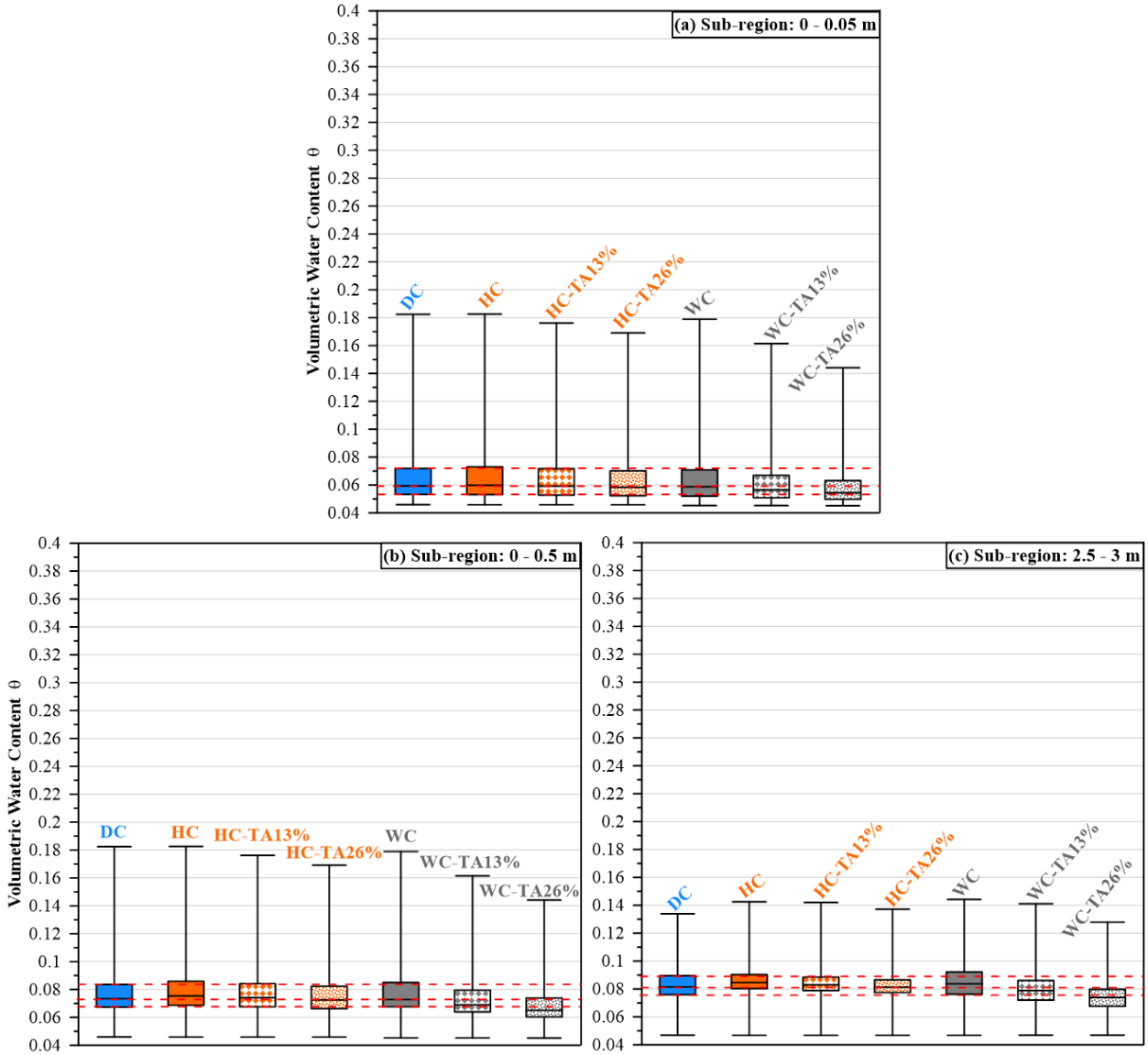

Figure A5 Box-whisker plot of volumetric water content from sub-regions within the sand domain: (a) 0-0.05 m, (b) 0-0.5 and (c) 2.5-3.0 m for Bighorn Dam climate

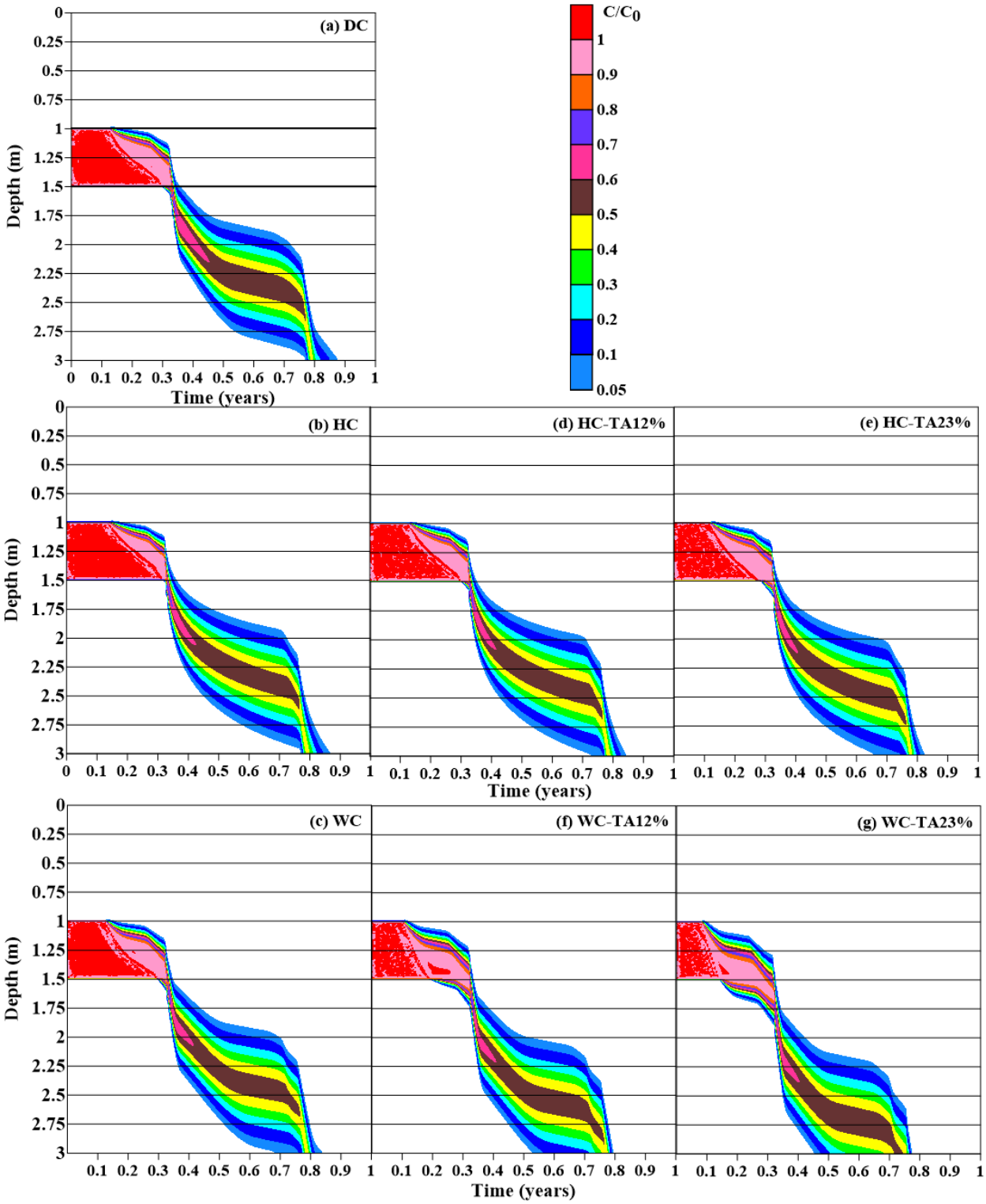

Figure A6 Temporal distribution of salt concentrations within the sand profile – Bighorn Dam

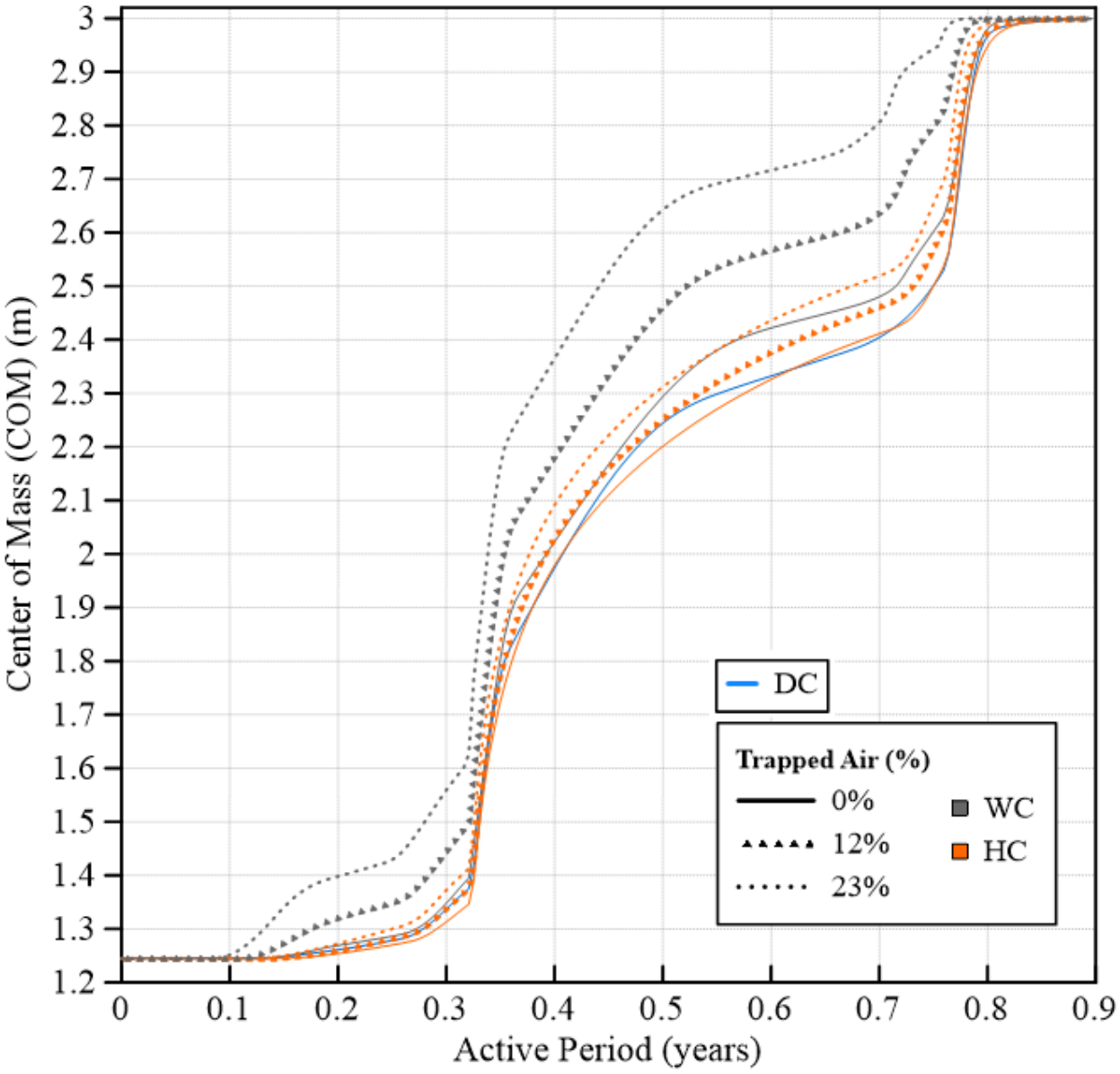

Figure A7 Temporal distribution of salt's Center of Mass (COM) within the sand profile – Bighorn Dam

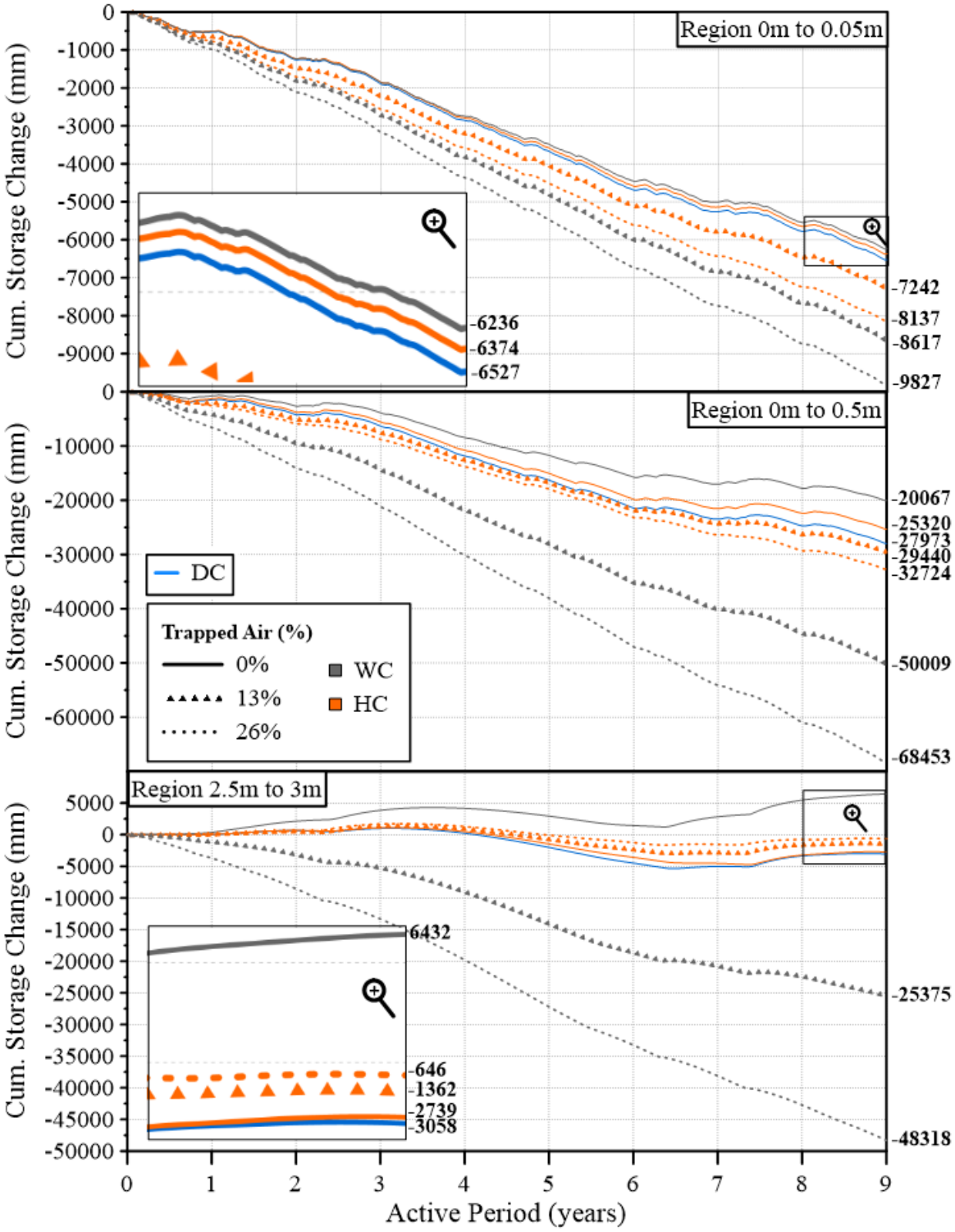

Figure A8 Cumulative storage change within three sub-regions of clay profile: 0-0.05 m, 0-0.5 m, and 2.5-3.0 m, using different hysteretic and nonhysteretic characteristics for Bighorn Dam climate

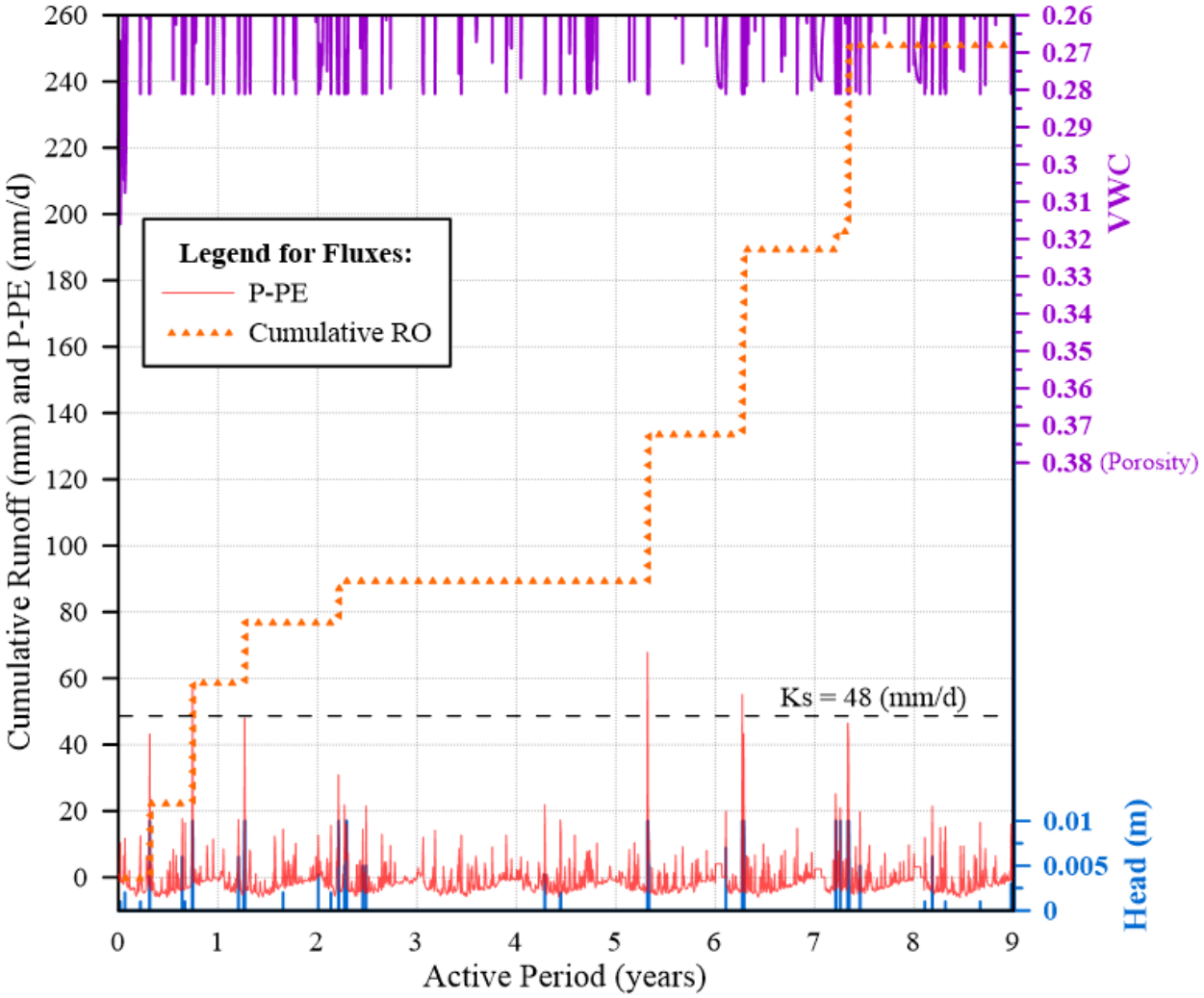

Figure A9 Temporal distribution of potential atmospheric flux (P-PE), cumulative runoff (RO), volumetric water content (VWC), at the ground surface of clay for the hysteretic simulation with 26% air entrapment for Bighorn Dam

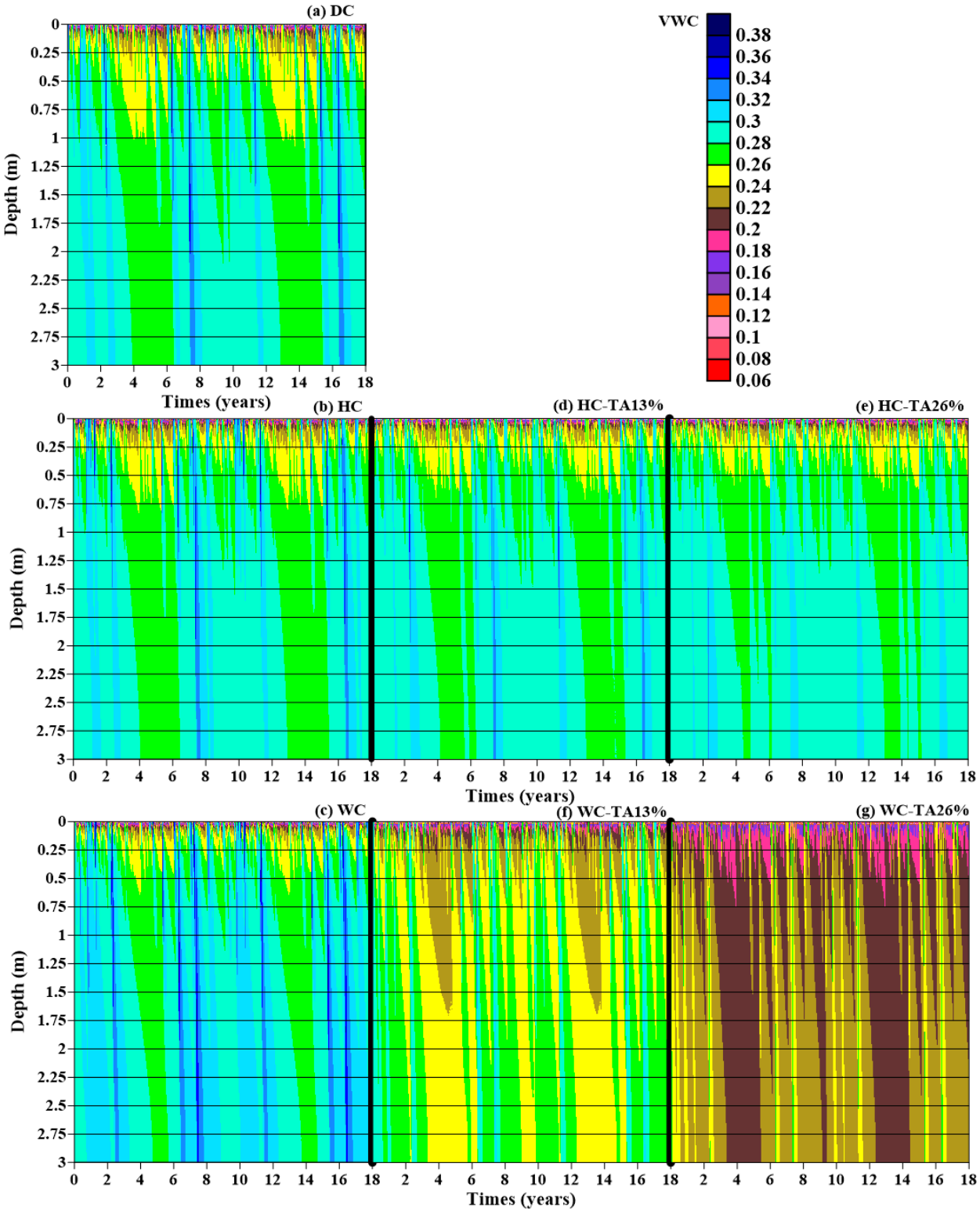

Figure A10 Temporal and spatial distribution of water within the clay profile using different hysteretic and nonhysteretic characteristics for Bighorn Dam climate

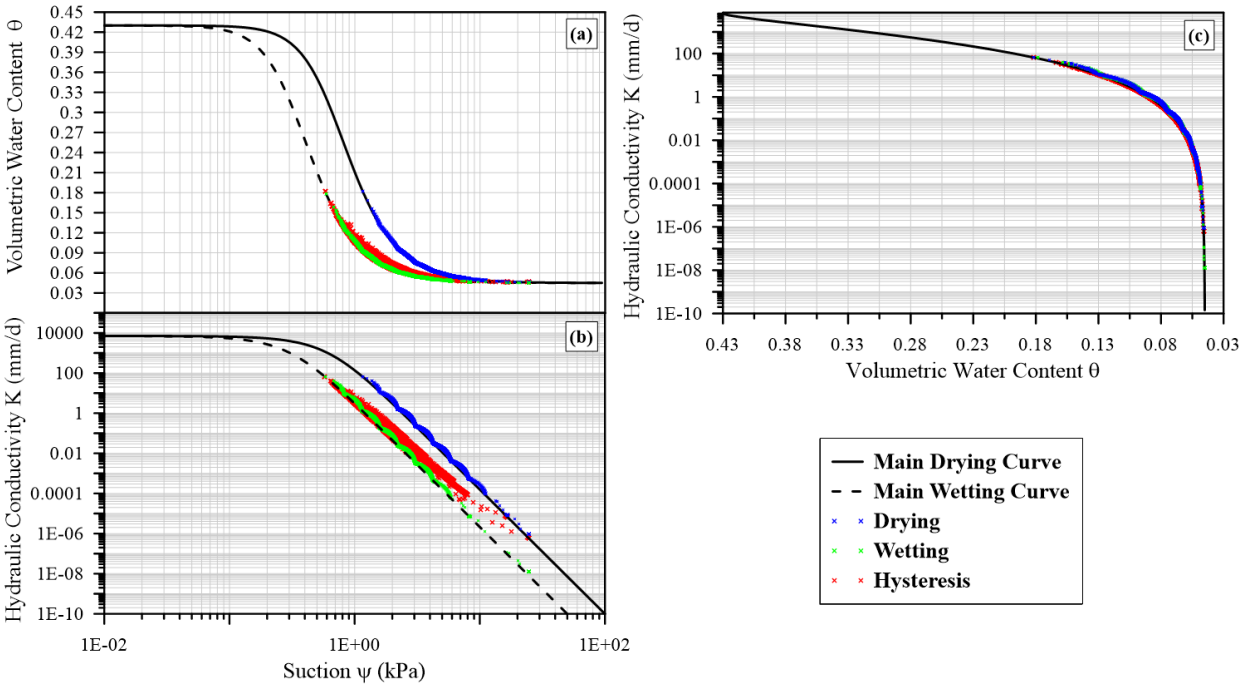

Figure A11 Soil water characteristic curve and unsaturated hydraulic conductivity function for sand used in simulations (data from Hydrus 1D simulations at nodes: 0 m, 0.01 m, 0.02 m, 0.03 m, 0.1 m, 0.3 m, 0.5 m, 1.0 m, 1.5 m, 3.0 m): with 0% air entrapment – Calgary

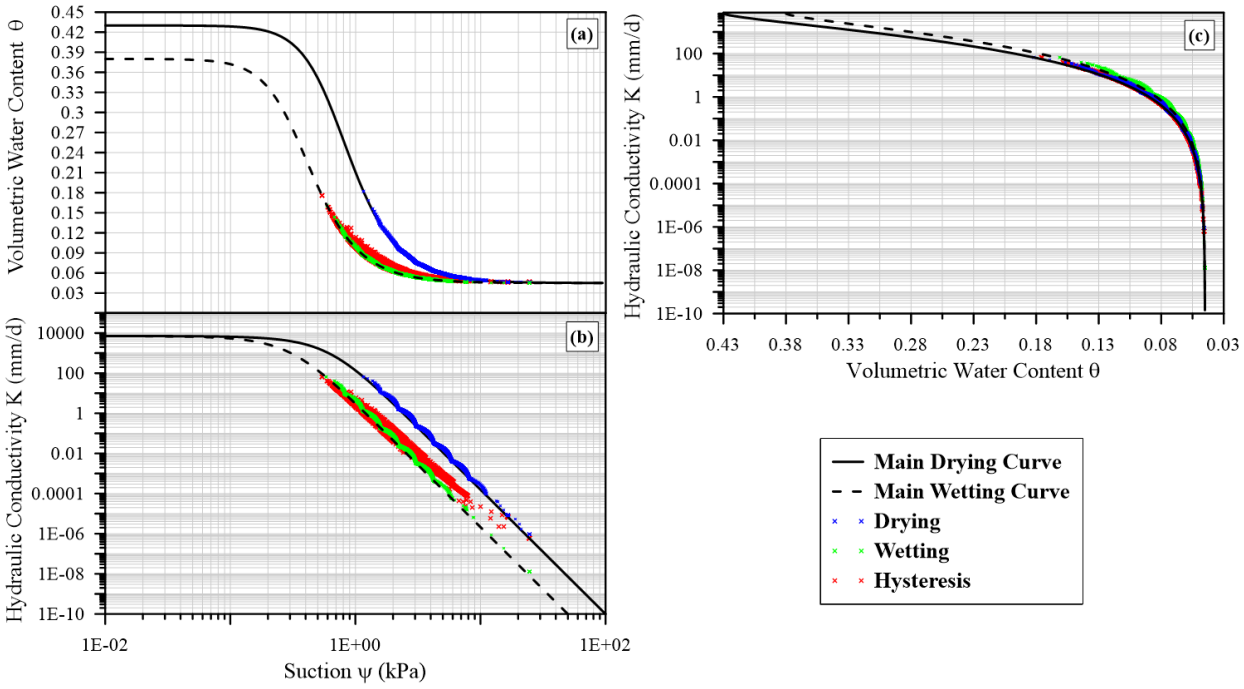

Figure A12 Soil water characteristic curve and unsaturated hydraulic conductivity function for sand used in simulations (data from Hydrus 1D simulations at nodes: 0 m, 0.01 m, 0.02 m, 0.03 m, 0.1 m, 0.3 m, 0.5 m, 1.0 m, 1.5 m, 3.0 m): with 12% air entrapment – Calgary

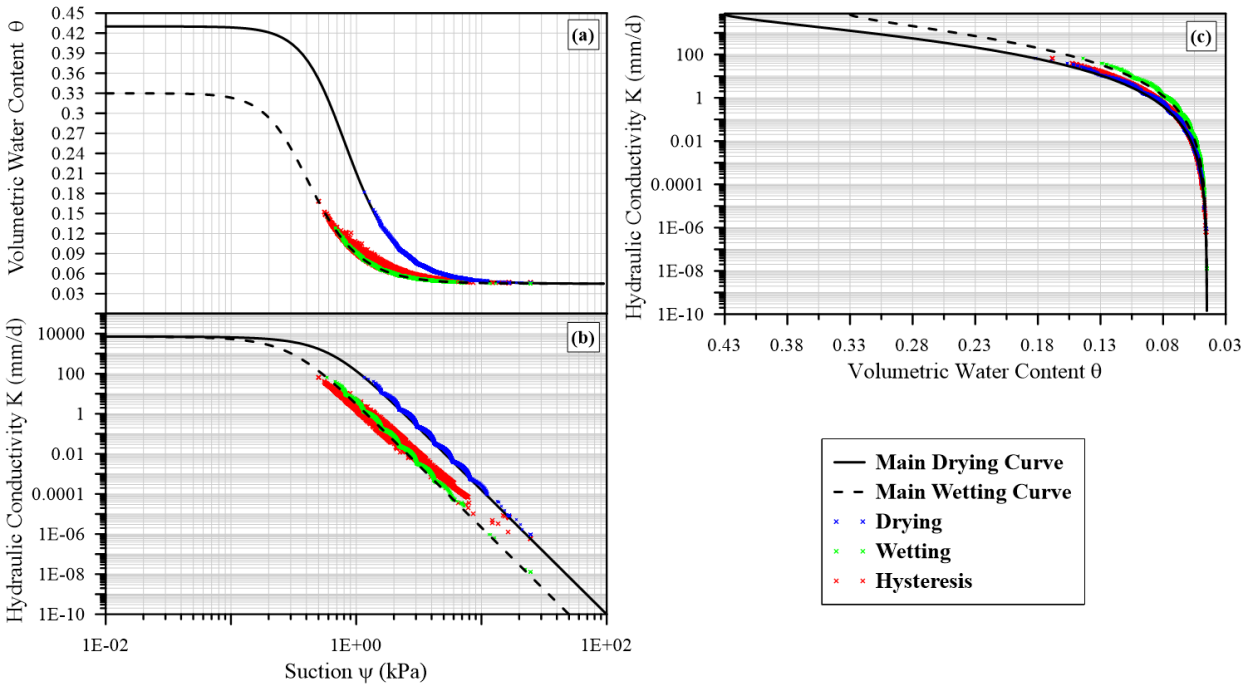

Figure A13 Soil water characteristic curve and unsaturated hydraulic conductivity function for sand used in simulations (data from Hydrus 1D simulations at nodes: 0 m, 0.01 m, 0.02 m, 0.03 m, 0.1 m, 0.3 m, 0.5 m, 1.0 m, 1.5 m, 3.0 m): with 23% air entrapment – Calgary

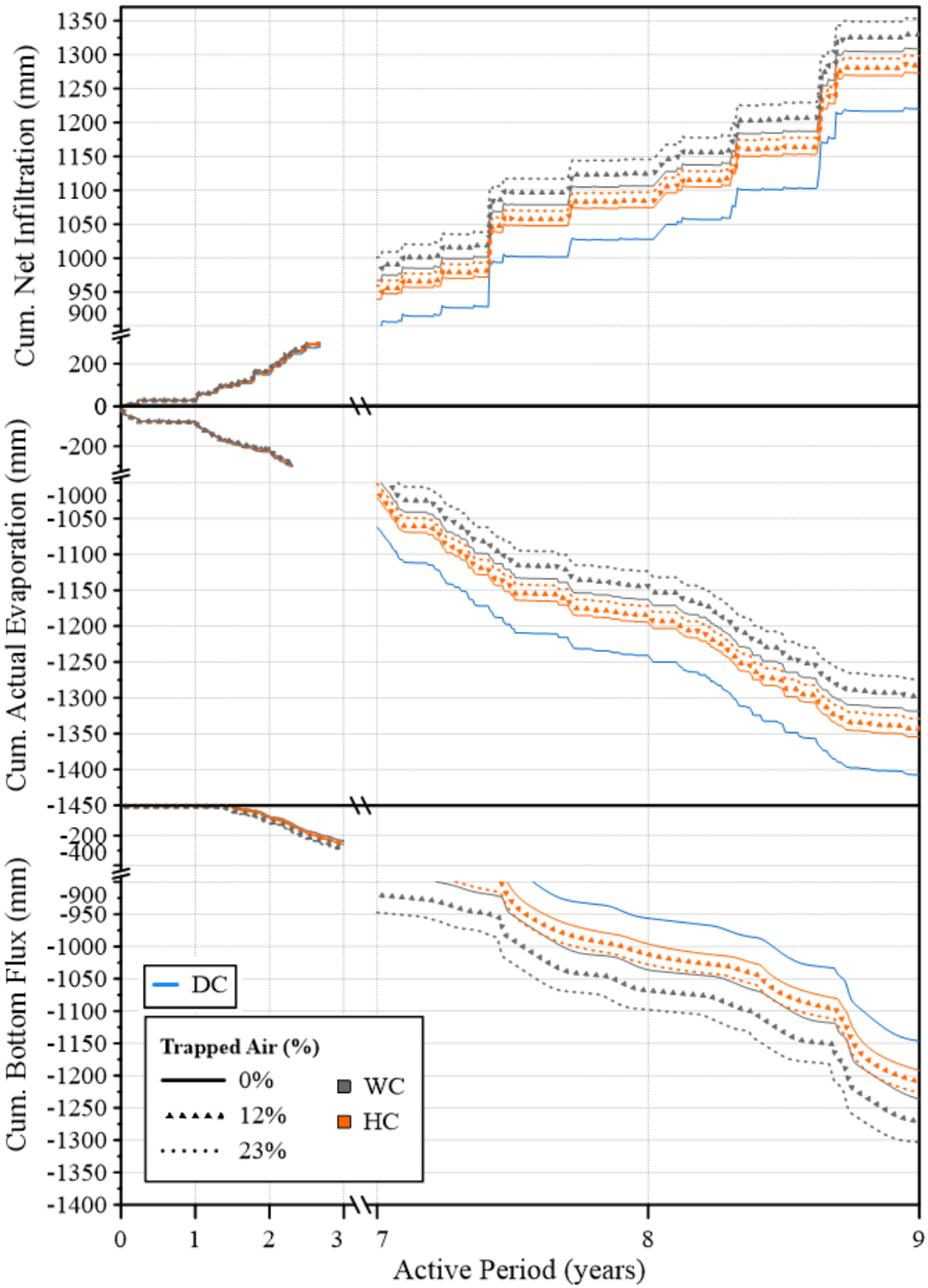

Figure A14 Estimated water balance at the surface of the sand profile – Calgary

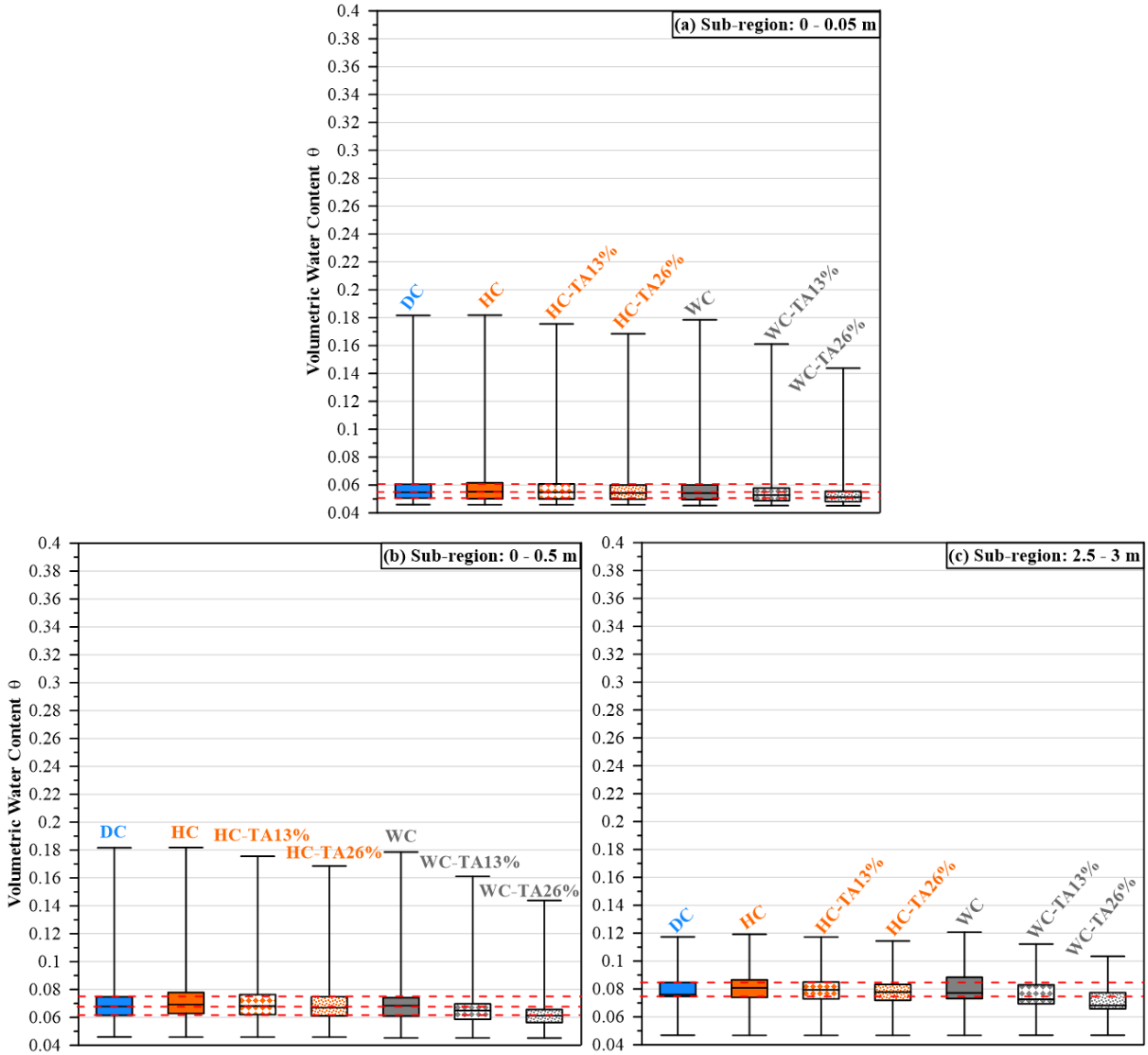

Figure A15 Box-whisker plot of volumetric water content from sub-regions within the sand domain: (a) 0-0.05 m, (b) 0-0.5 and (c) 2.5-3.0 m for Calgary climate

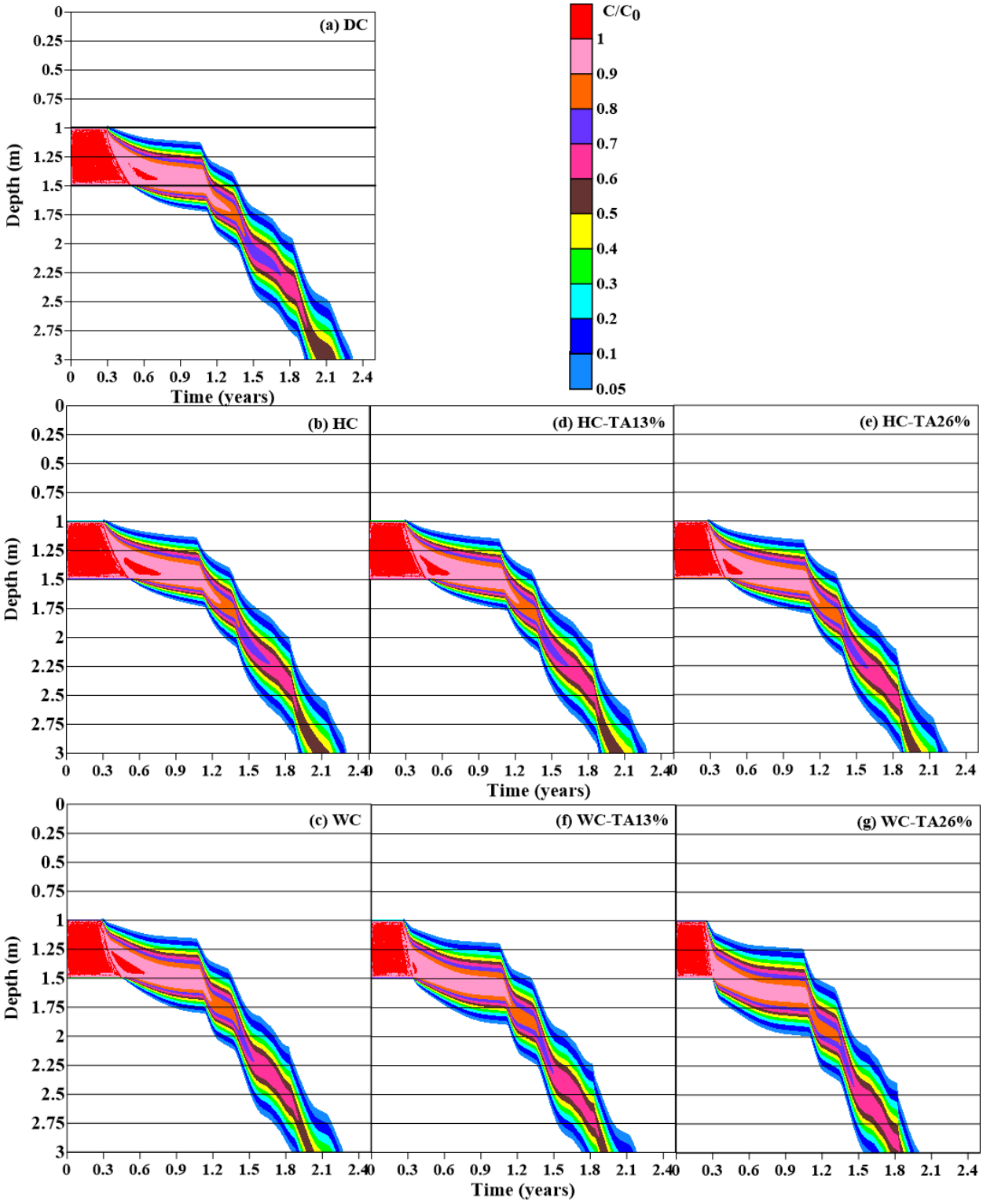

Figure A16 Temporal distribution of salt concentrations within the sand profile for Calgary climate

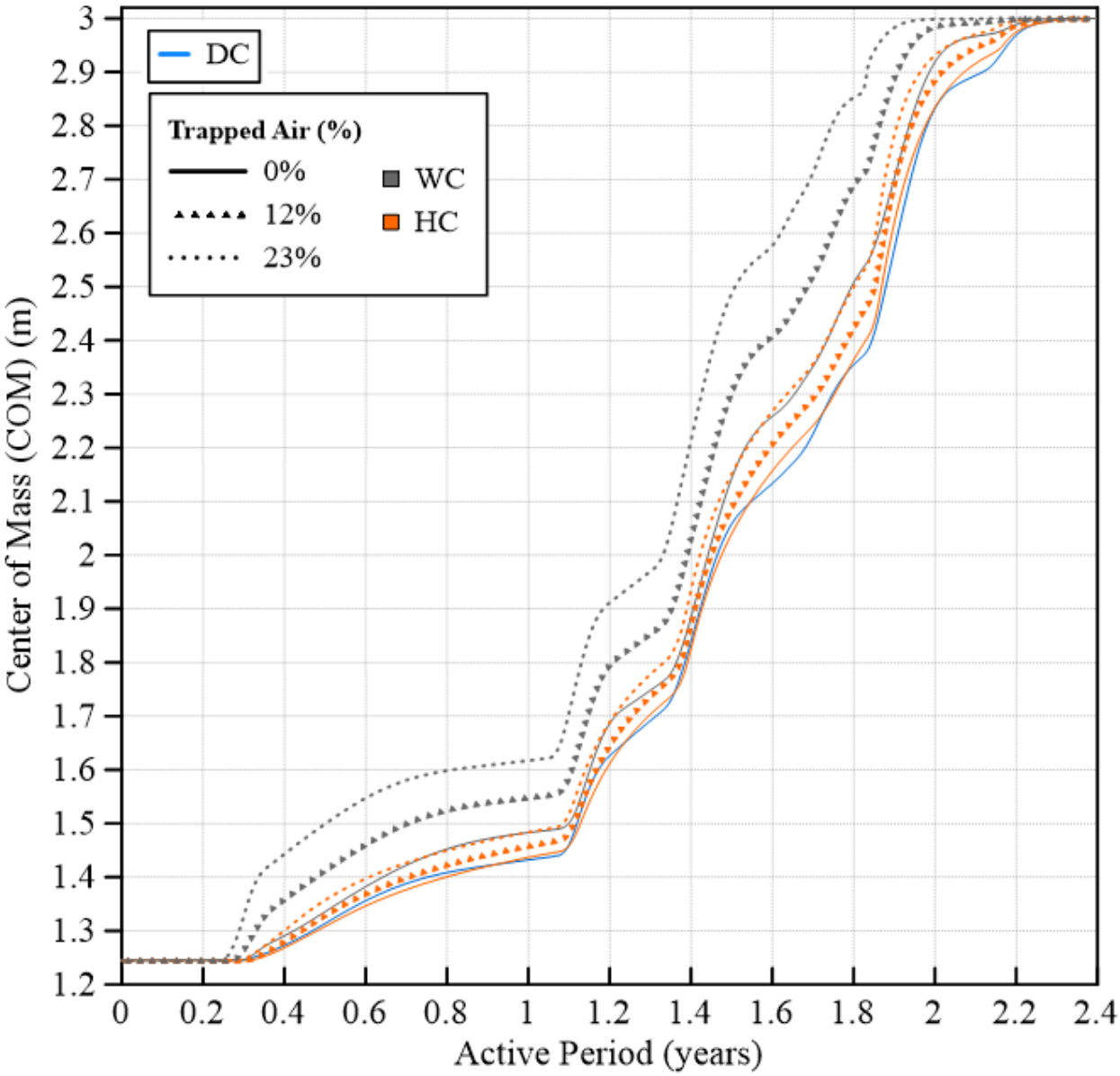

Figure A17 Temporal distribution of salt's Center of Mass (COM) within the sand profile – Calgary

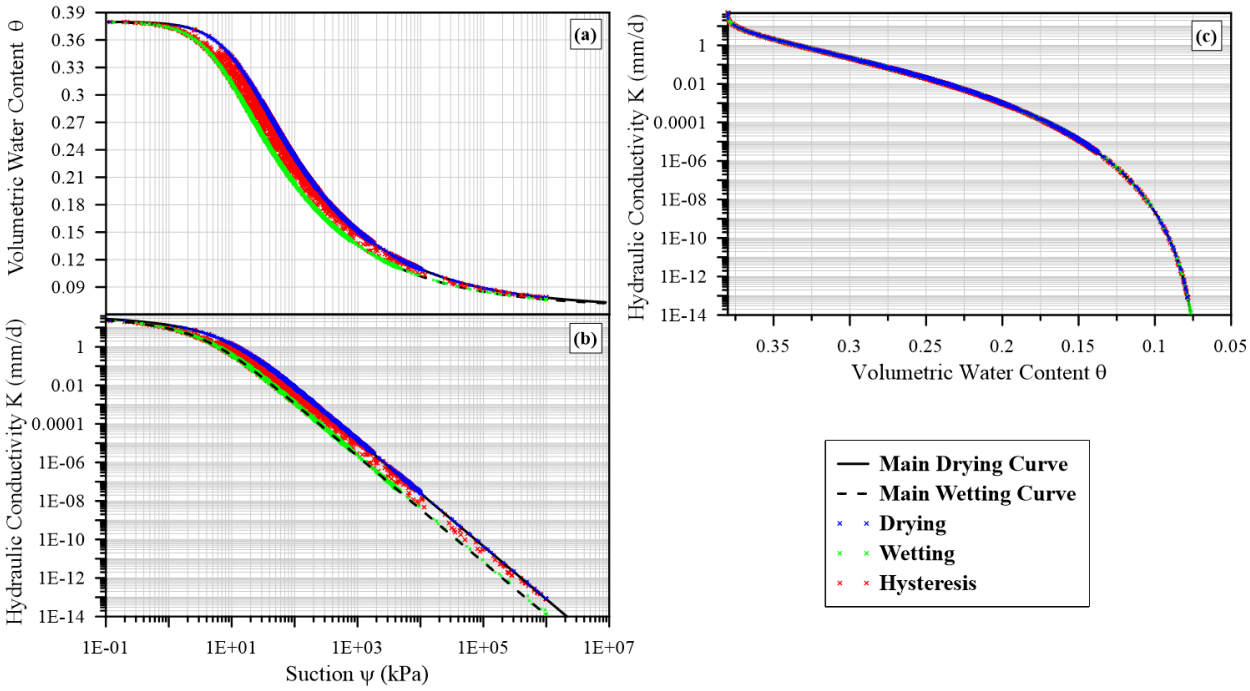

Figure A18 Soil water characteristic curve and unsaturated hydraulic conductivity function for clay used in simulations (data from Hydrus 1D simulations at nodes: 0 m, 0.01 m, 0.02 m, 0.03 m, 0.1 m, 0.3 m, 0.5 m, 1.0 m, 1.5 m, 3.0 m): with 0% air entrapment – Calgary

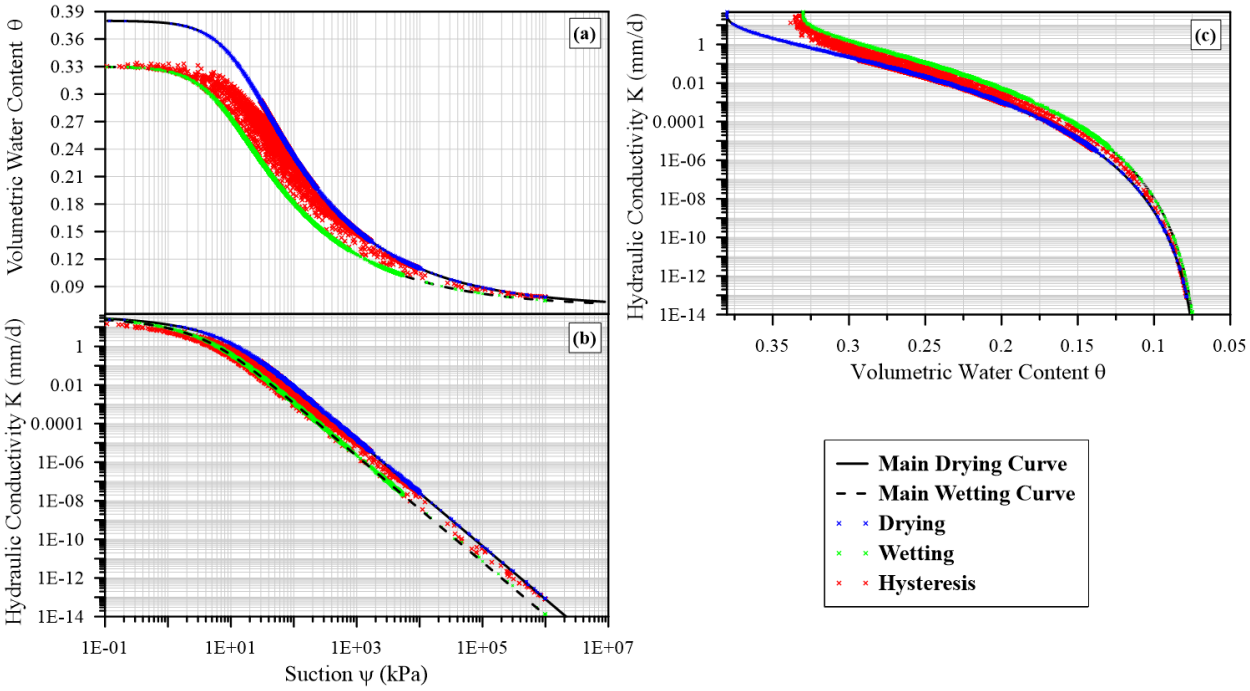

Figure A19 Soil water characteristic curve and unsaturated hydraulic conductivity function for clay used in simulations (data from Hydrus 1D simulations at nodes: 0 m, 0.01 m, 0.02 m, 0.03 m, 0.1 m, 0.3 m, 0.5 m, 1.0 m, 1.5 m, 3.0 m): with 13% air entrapment – Calgary

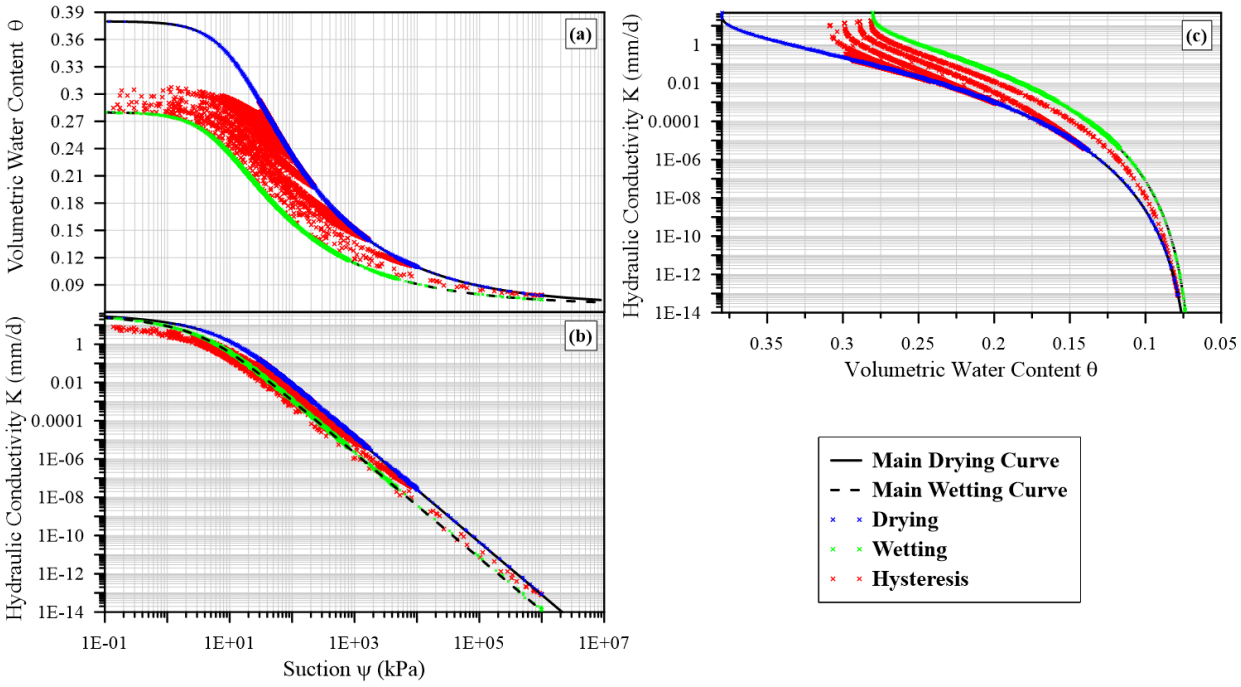

Figure A20 Soil water characteristic curve and unsaturated hydraulic conductivity function for clay used in simulations (data from Hydrus 1D simulations at nodes: 0 m, 0.01 m, 0.02 m, 0.03 m, 0.1 m, 0.3 m, 0.5 m, 1.0 m, 1.5 m, 3.0 m): with 26% air entrapment – Calgary

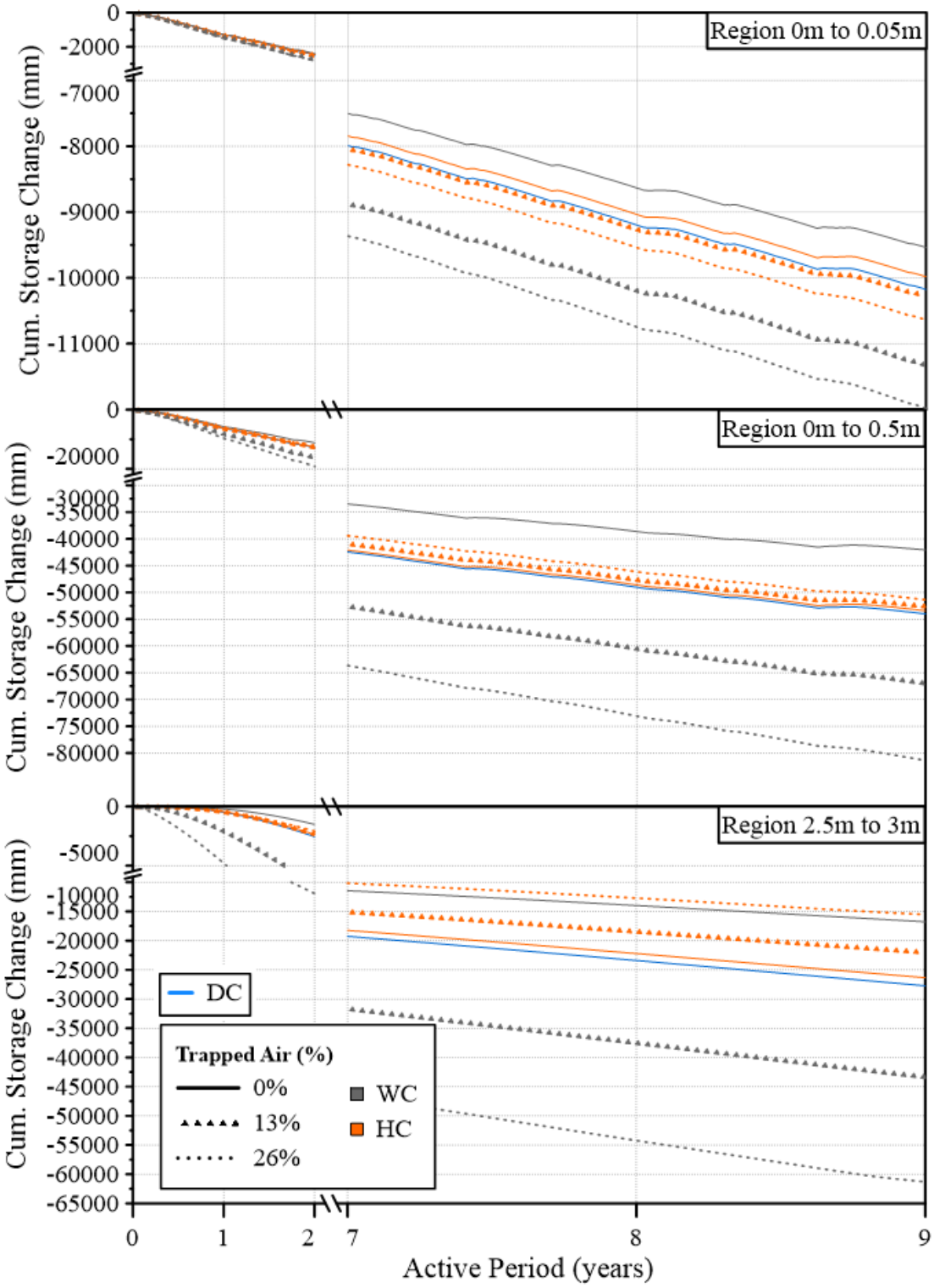

Figure A21 Cumulative storage change within three sub-regions of clay profile: 0-0.05 m, 0-0.5 m, and 2.5-3 m, using different hysteretic and nonhysteretic characteristics for Calgary climate

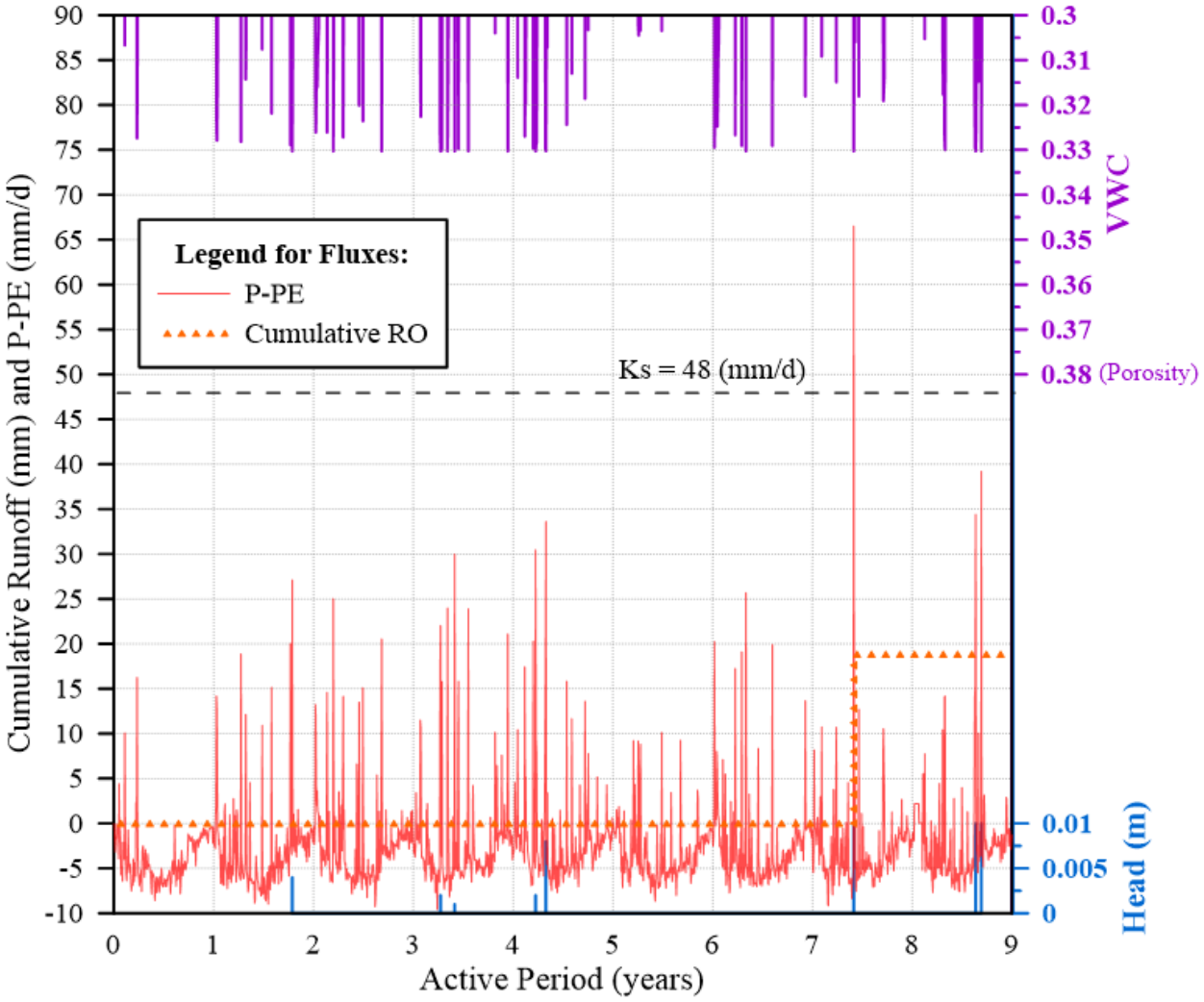

Figure A22 Temporal distribution of potential atmospheric flux (P-PE), cumulative runoff (RO), volumetric water content (VWC), at the ground surface of clay for the hysteretic simulation with 13% air entrapment for Calgary

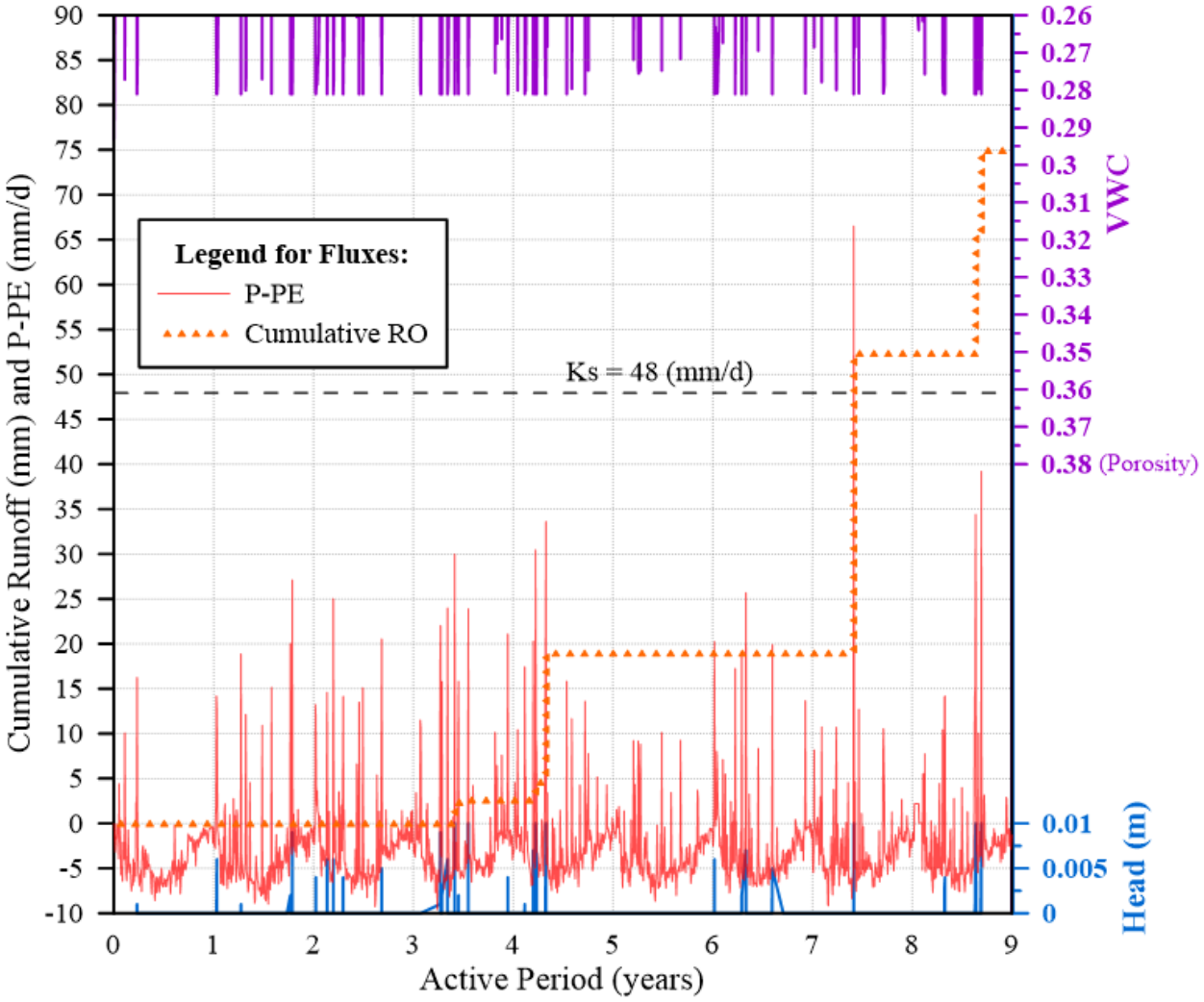

Figure A23 Temporal distribution of potential atmospheric flux (P-PE), cumulative runoff (RO), volumetric water content (VWC), at the ground surface of clay for the hysteretic simulation with 26% air entrapment for Calgary

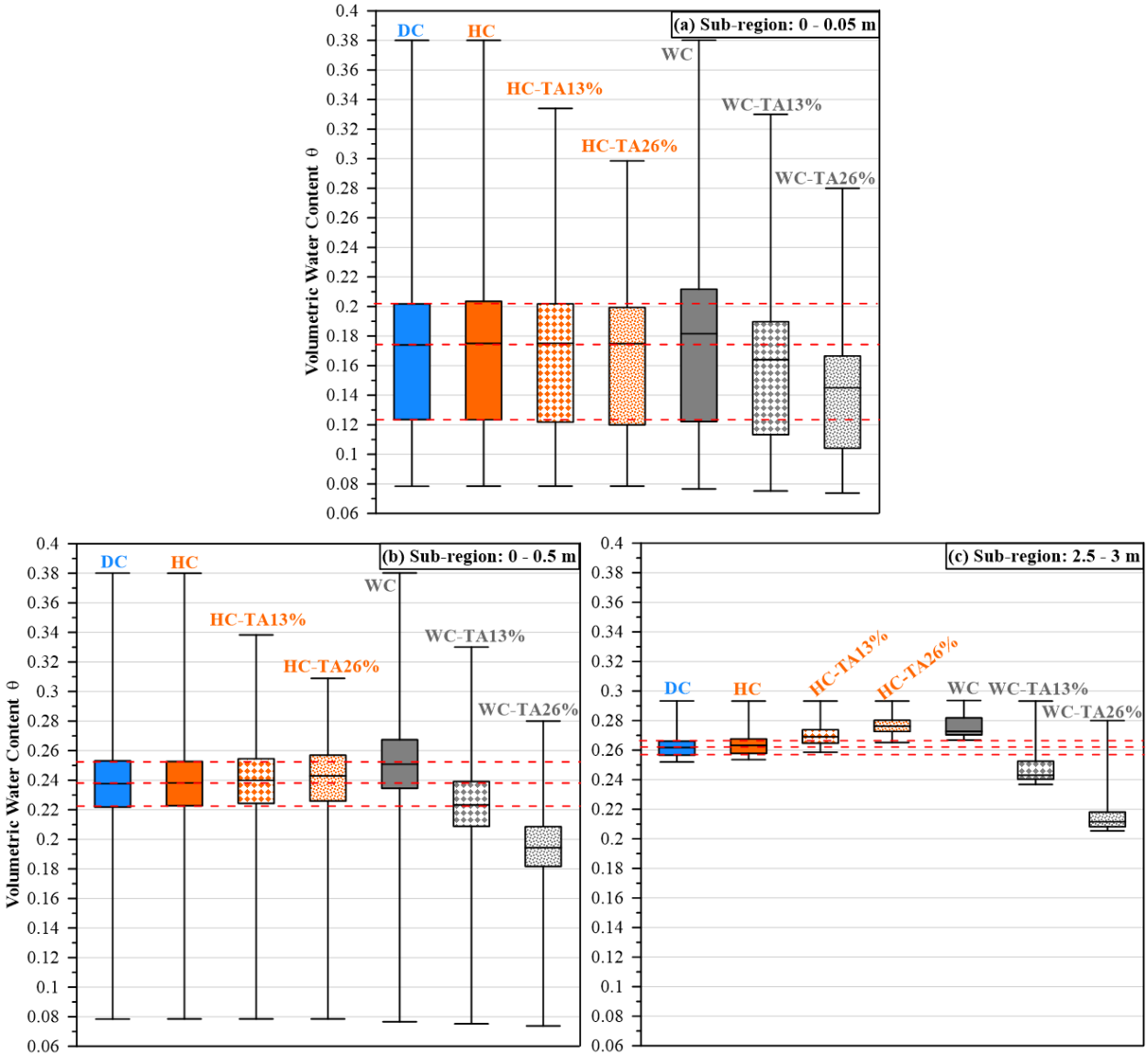

Figure A24 Box-whisker plot of volumetric water content from sub-regions within the clay domain: (a) 0-0.05 m, (b) 0-0.5 m (c) 2.5-3.0 m for Calgary climate

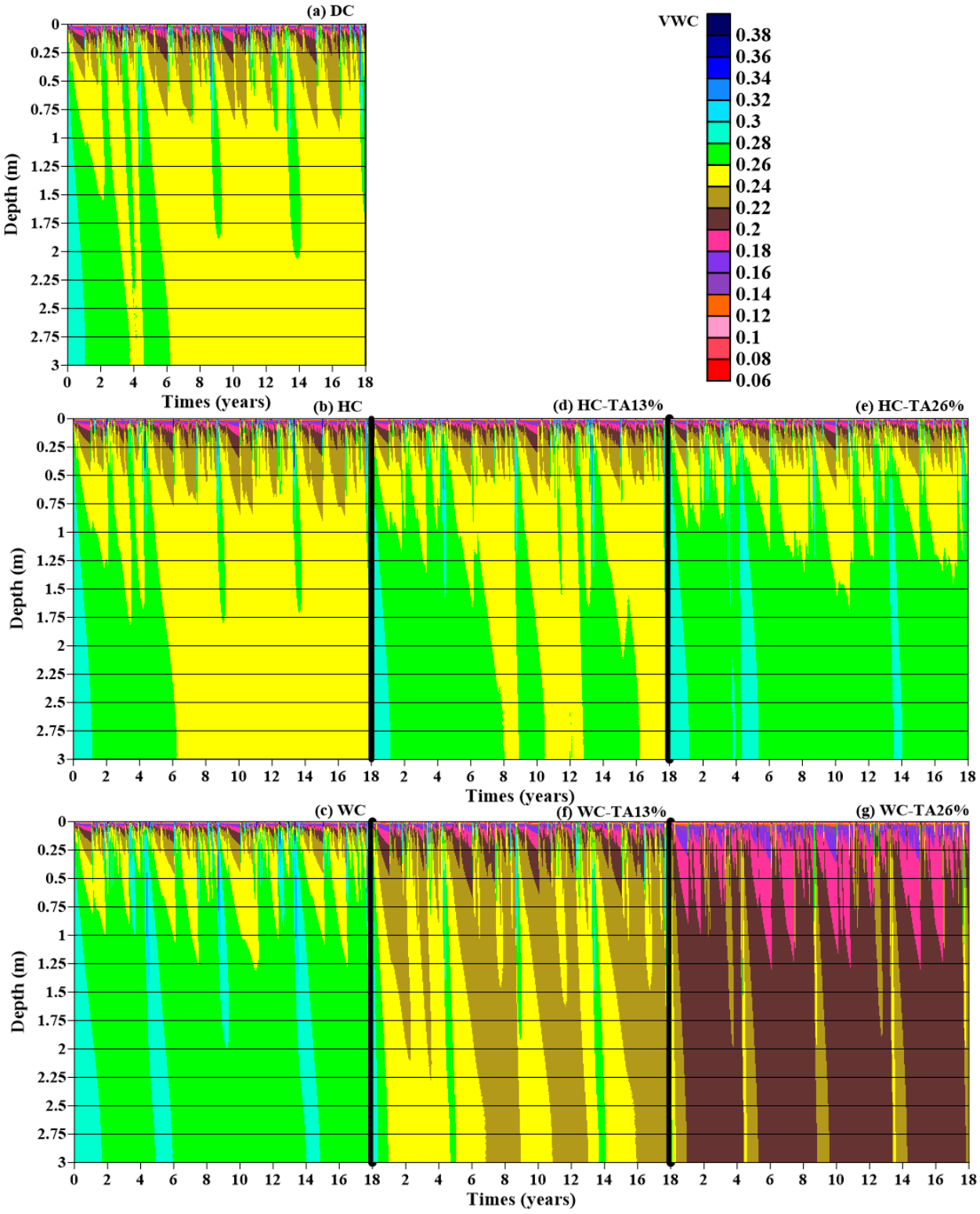

Figure A25 Temporal and spatial distribution of water within the clay profile using different hysteretic and nonhysteretic characteristics for Calgary climate

Appendix – B

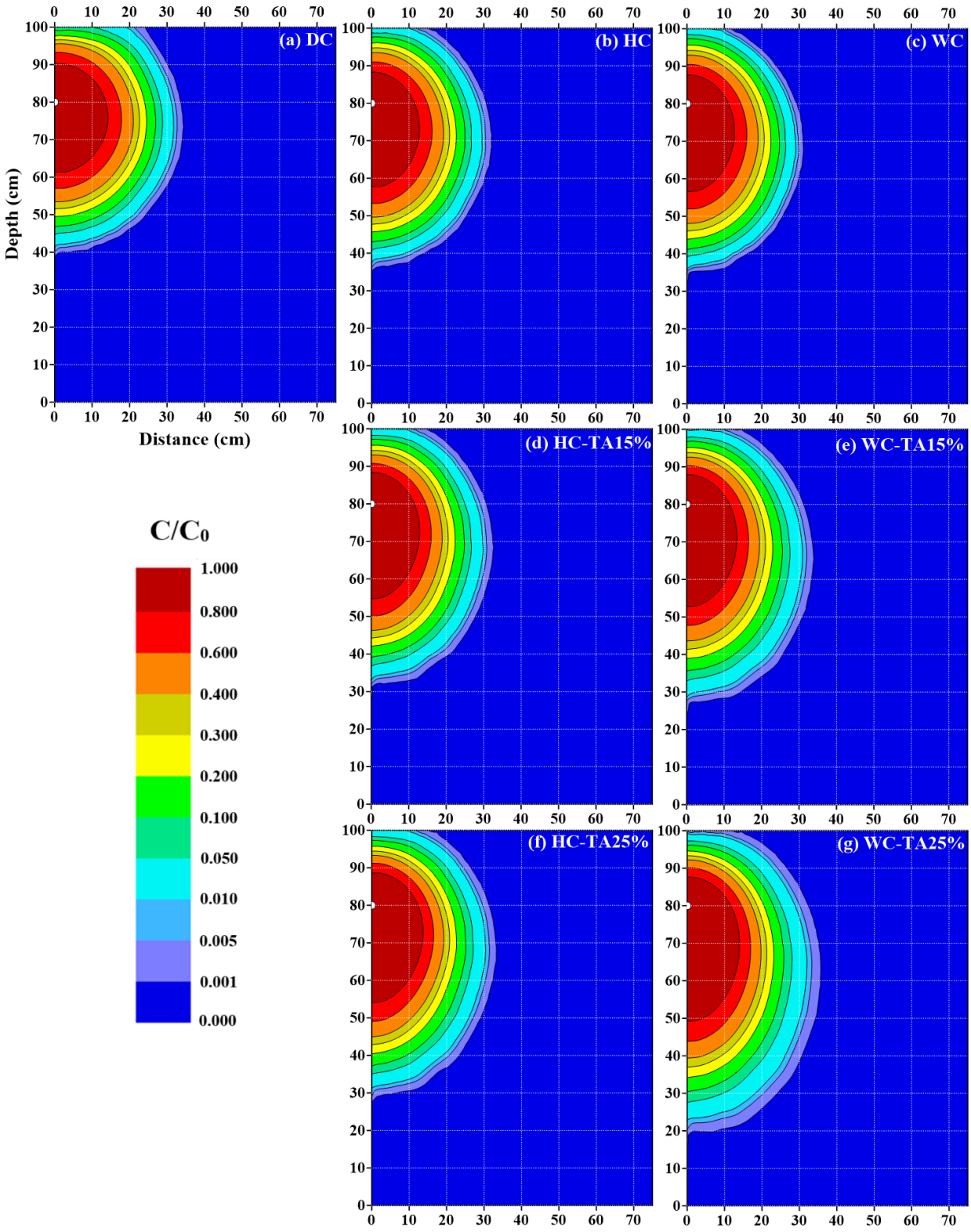

Figure B1 Distribution of solute after 2 days using different hysteretic and nonhysteretic characteristics - Case 1

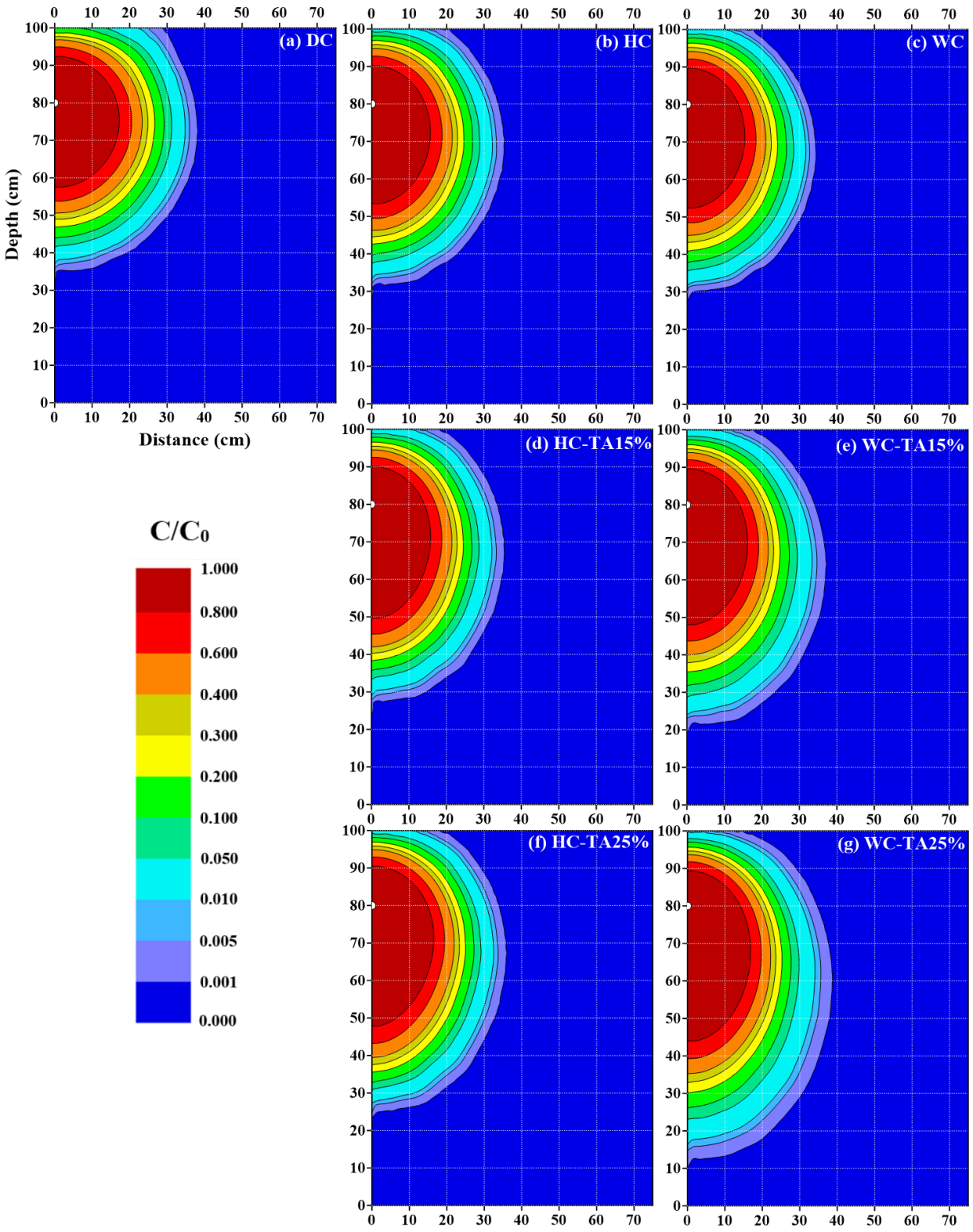

Figure B2 Distribution of solute after 4 days using different hysteretic and nonhysteretic characteristics - Case 1

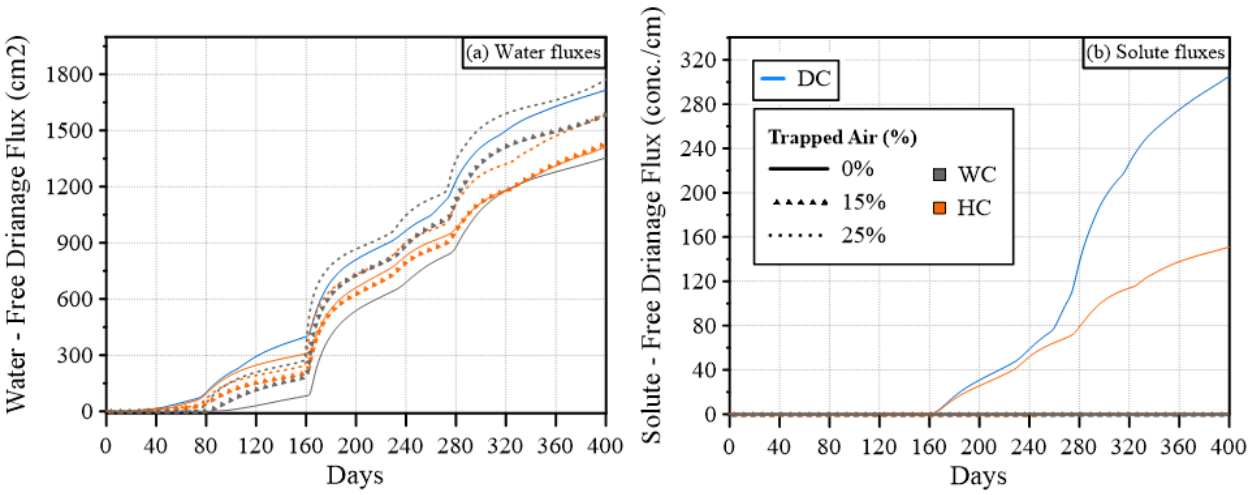

Figure B3 Cumulative free drainage fluxes of (a) water and (b) Solute - Case 2

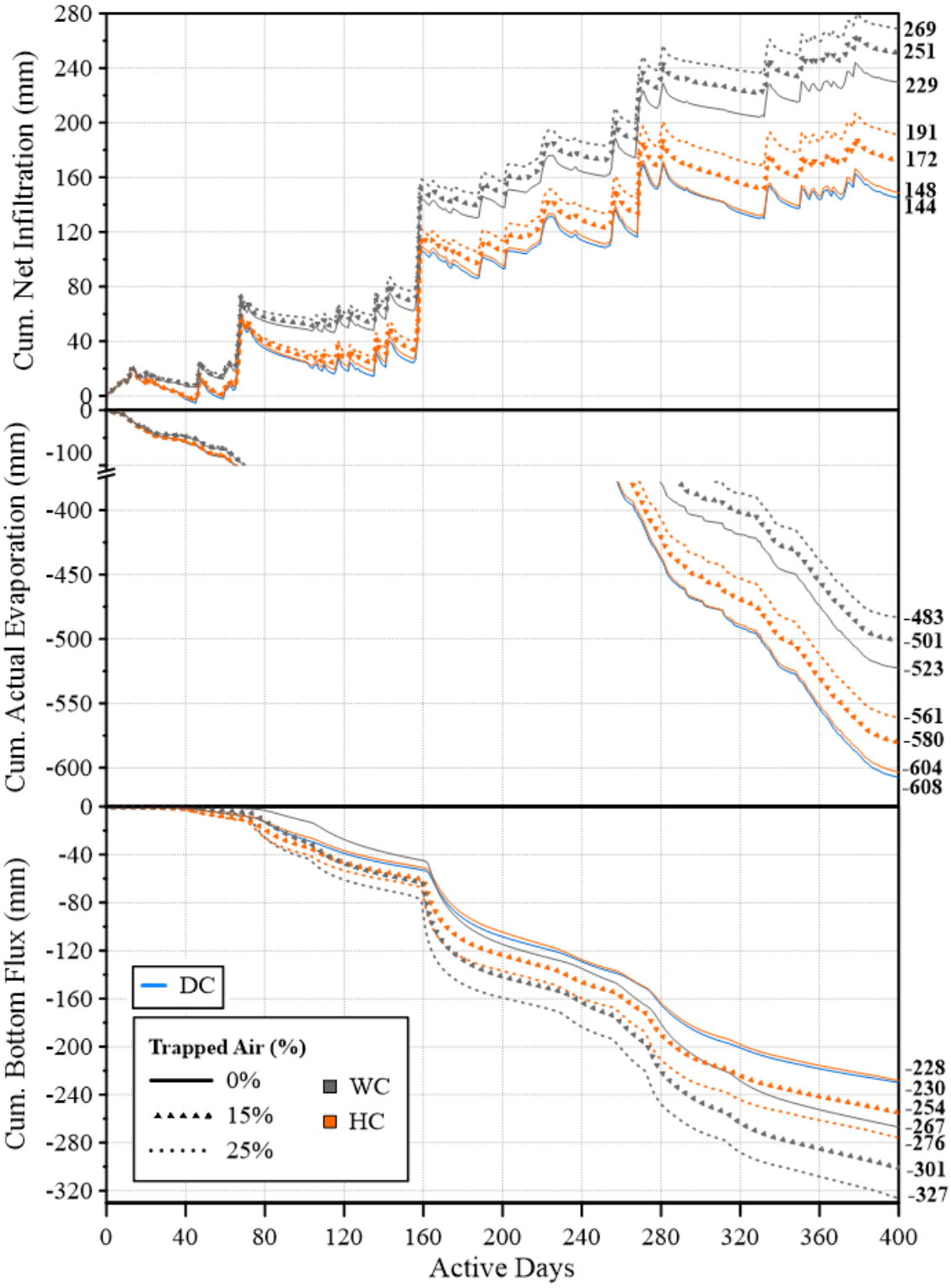

Figure B4 Estimated Water Balance at the surface and bottom flux of the Loam's profile – Case 3

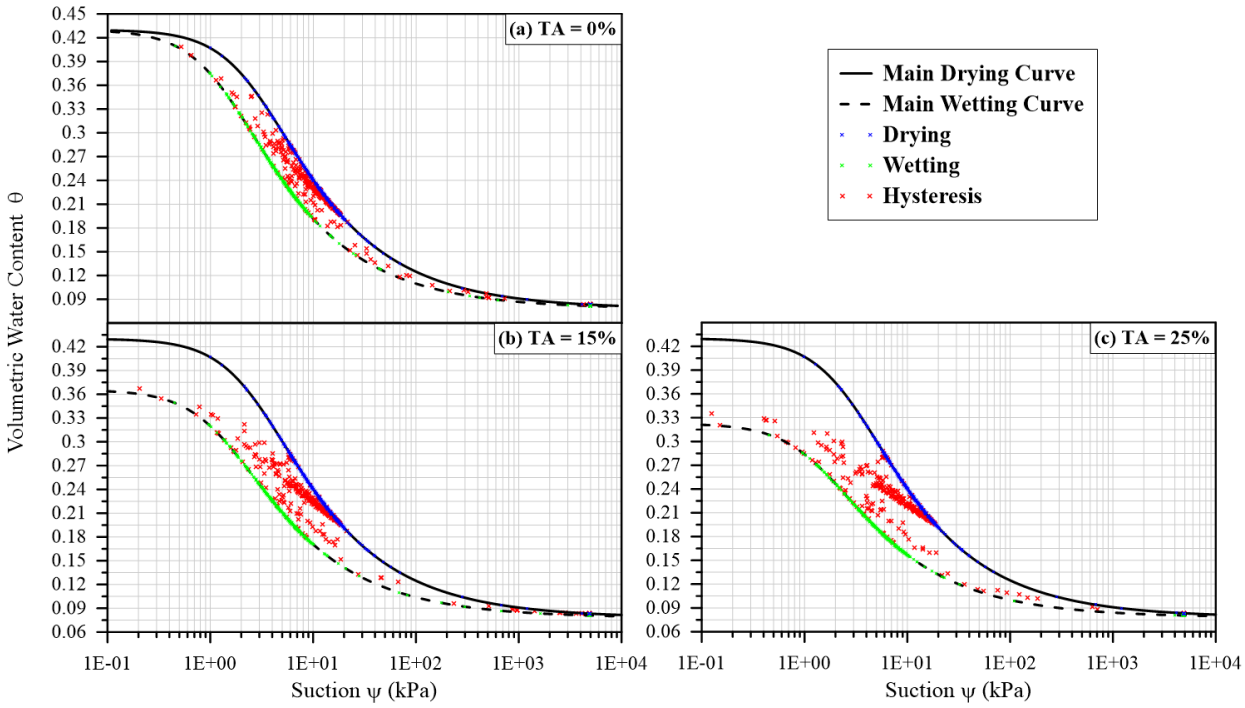

Figure B5 Loam's SWCC and paired water content and suction data at node (3.5 cm, 100 cm) and (3.5 cm, 90 cm) for different simulated hydraulic characteristics – Case 3

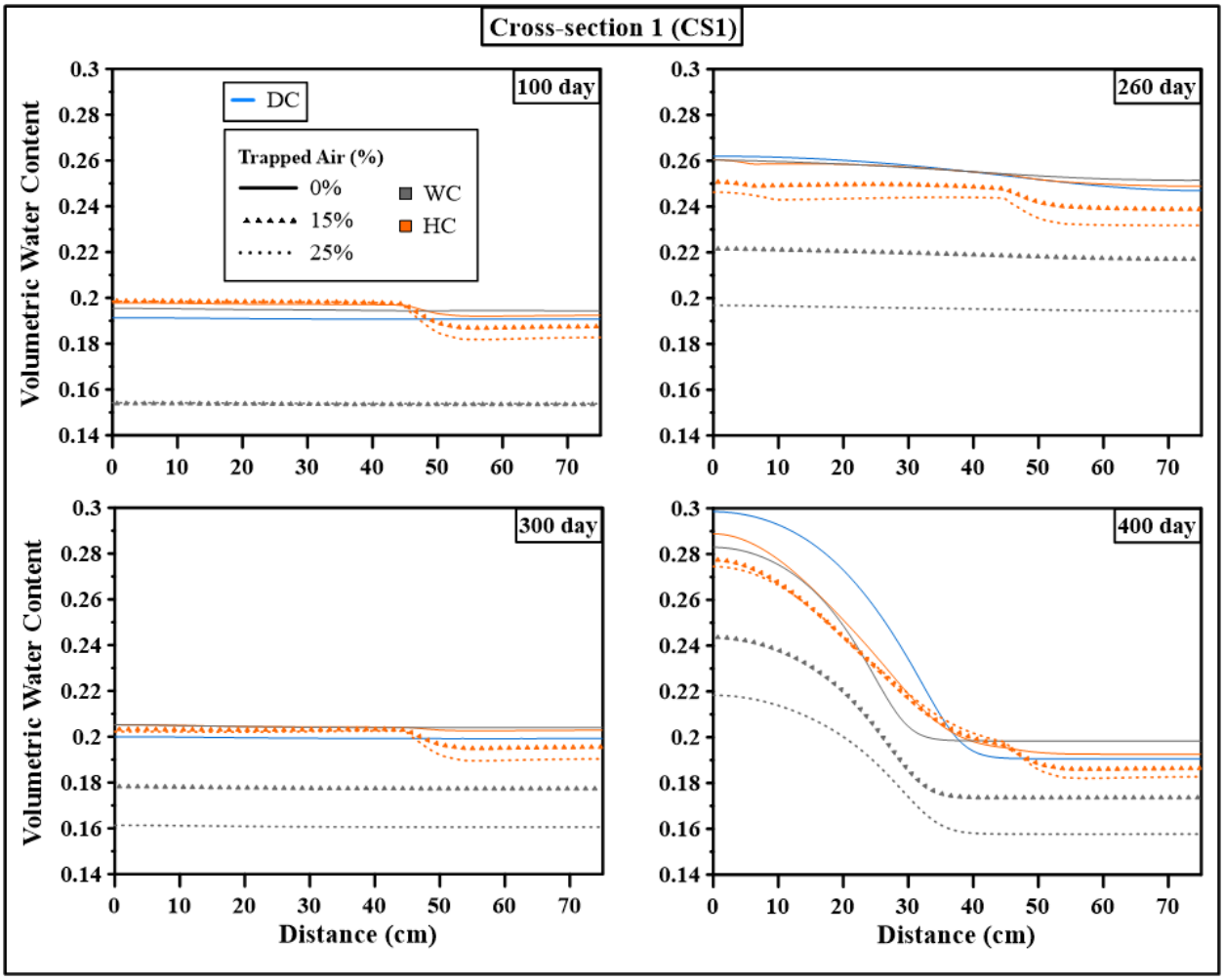

Figure B6 Distribution of volumetric water content at CS1 (10 cm below surface) at 4-time instances: 100 day, 260 day, 300 day, and 400 day – Case 3

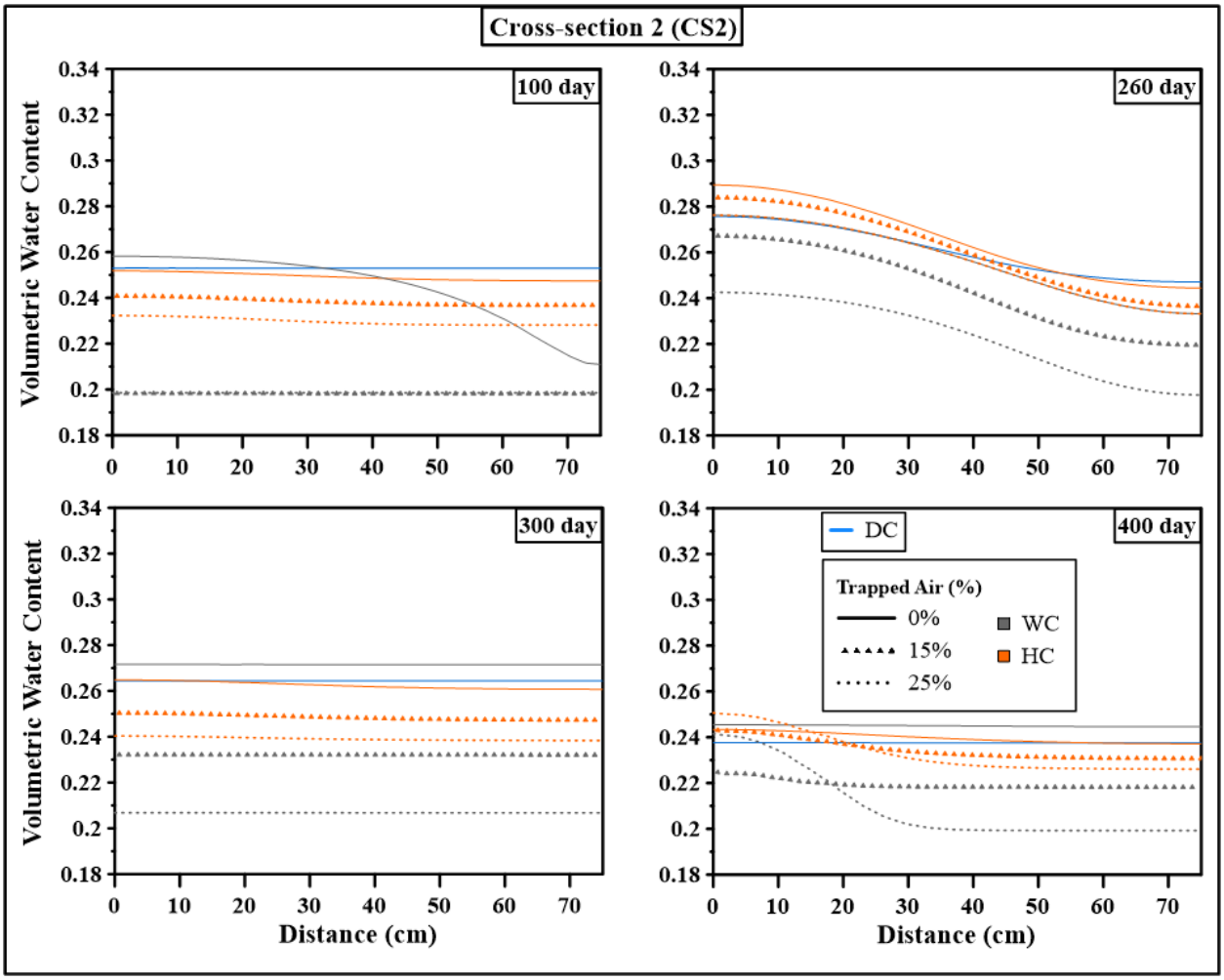

Figure B7 Distribution of volumetric water content at CS2 (98 cm below surface) at 4-time instances: 100 day, 260 day, 300 day, and 400 day – Case 3

Appendix – C

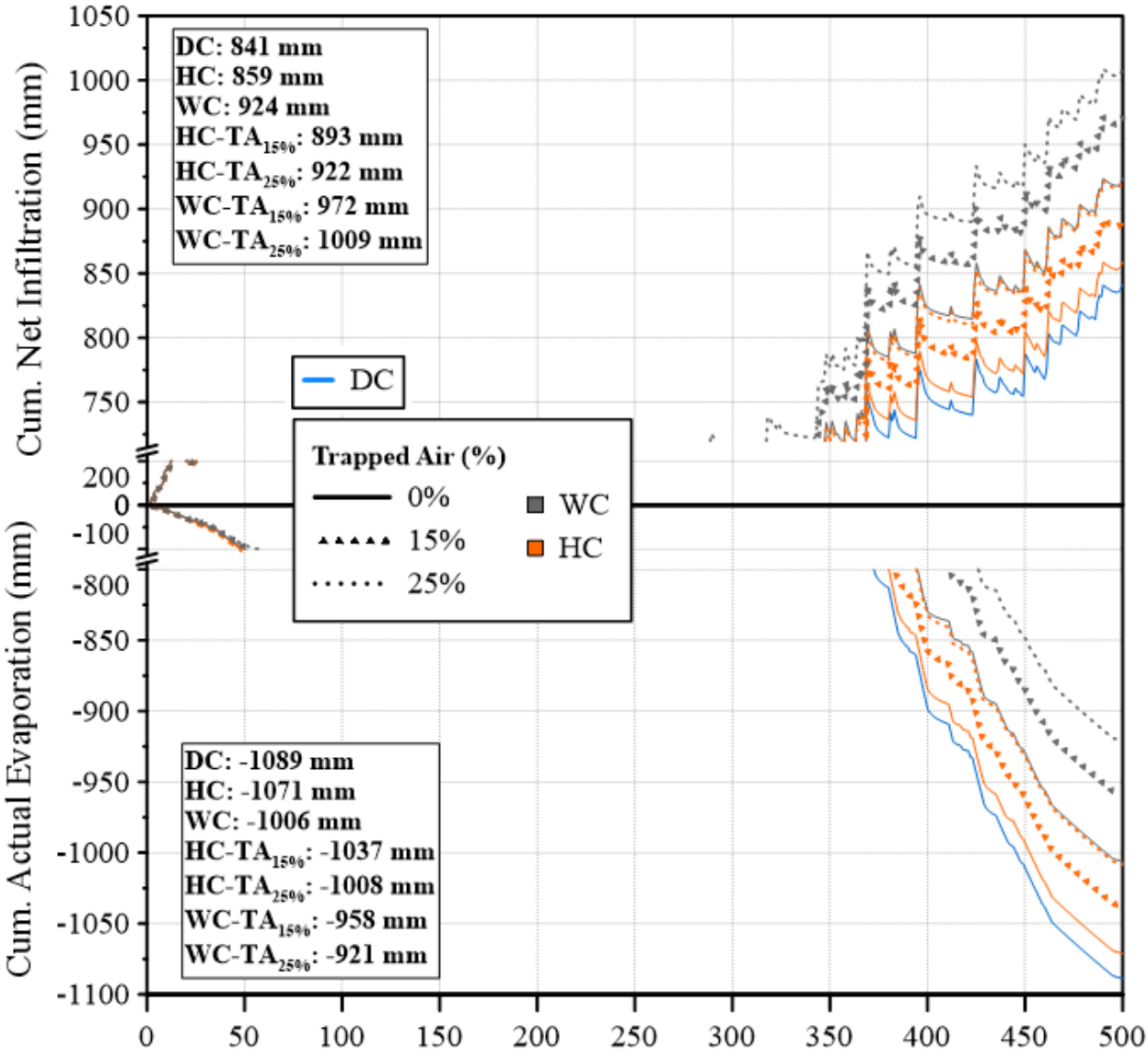

Figure C1 Estimated water balance at the surface of the sand profile – Toronto

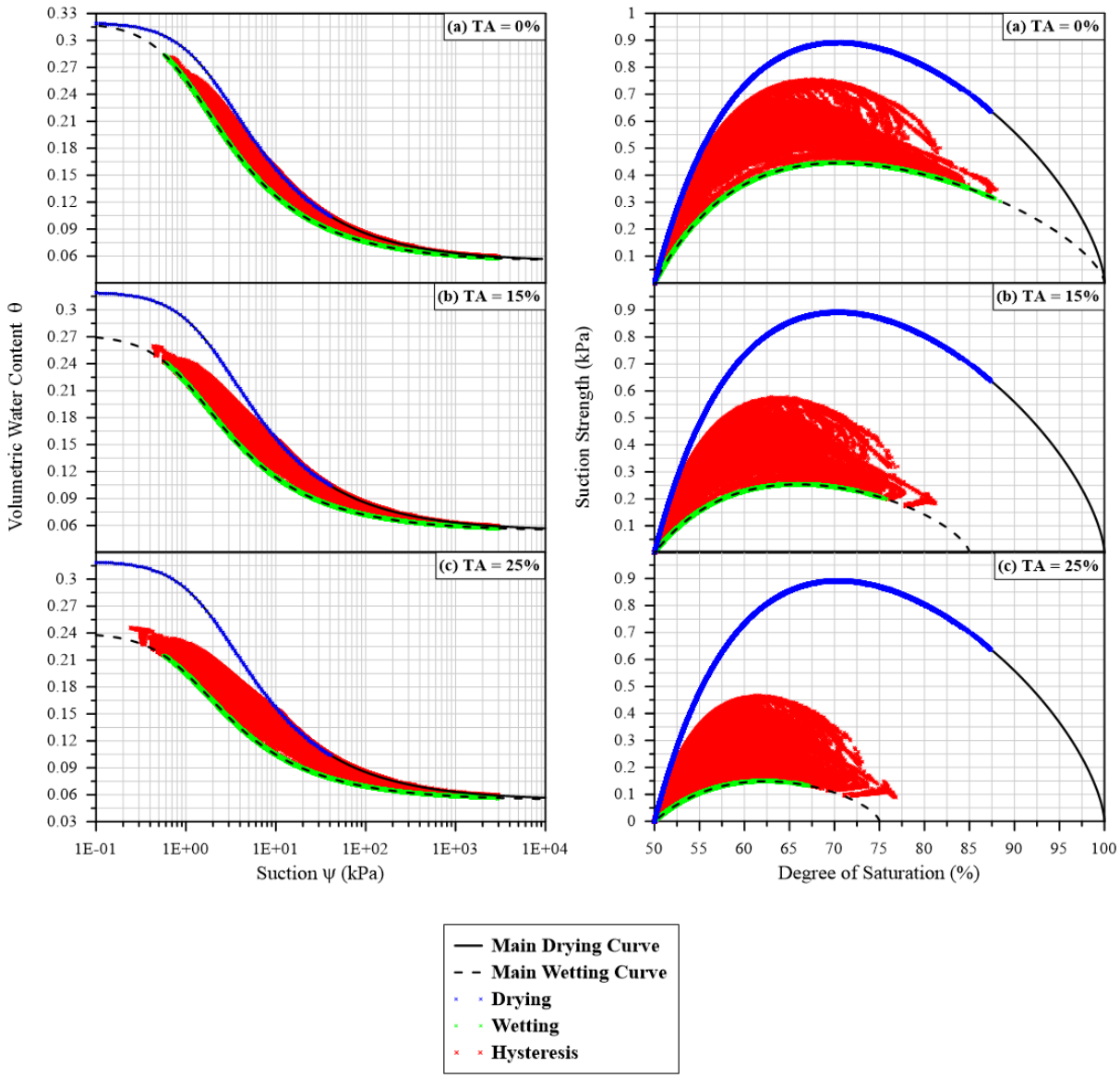

Figure C2 Hysteresis profiles of suction strength for sand, including data points from the hysteretic simulations with and without air entrapment– Toronto

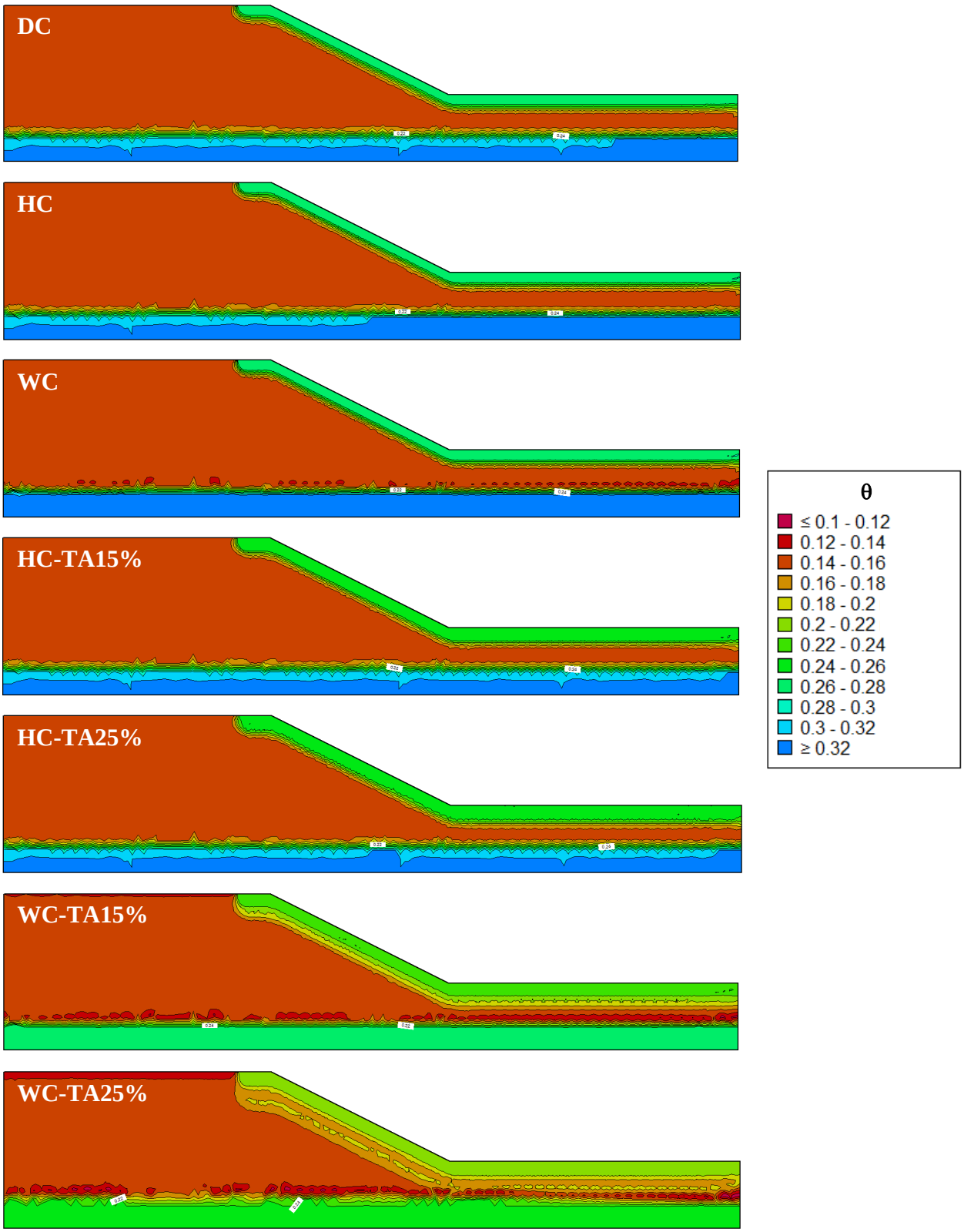

Figure C3 Volumetric water content distribution within sand slope at 9 d (*Max Sat*) – Toronto

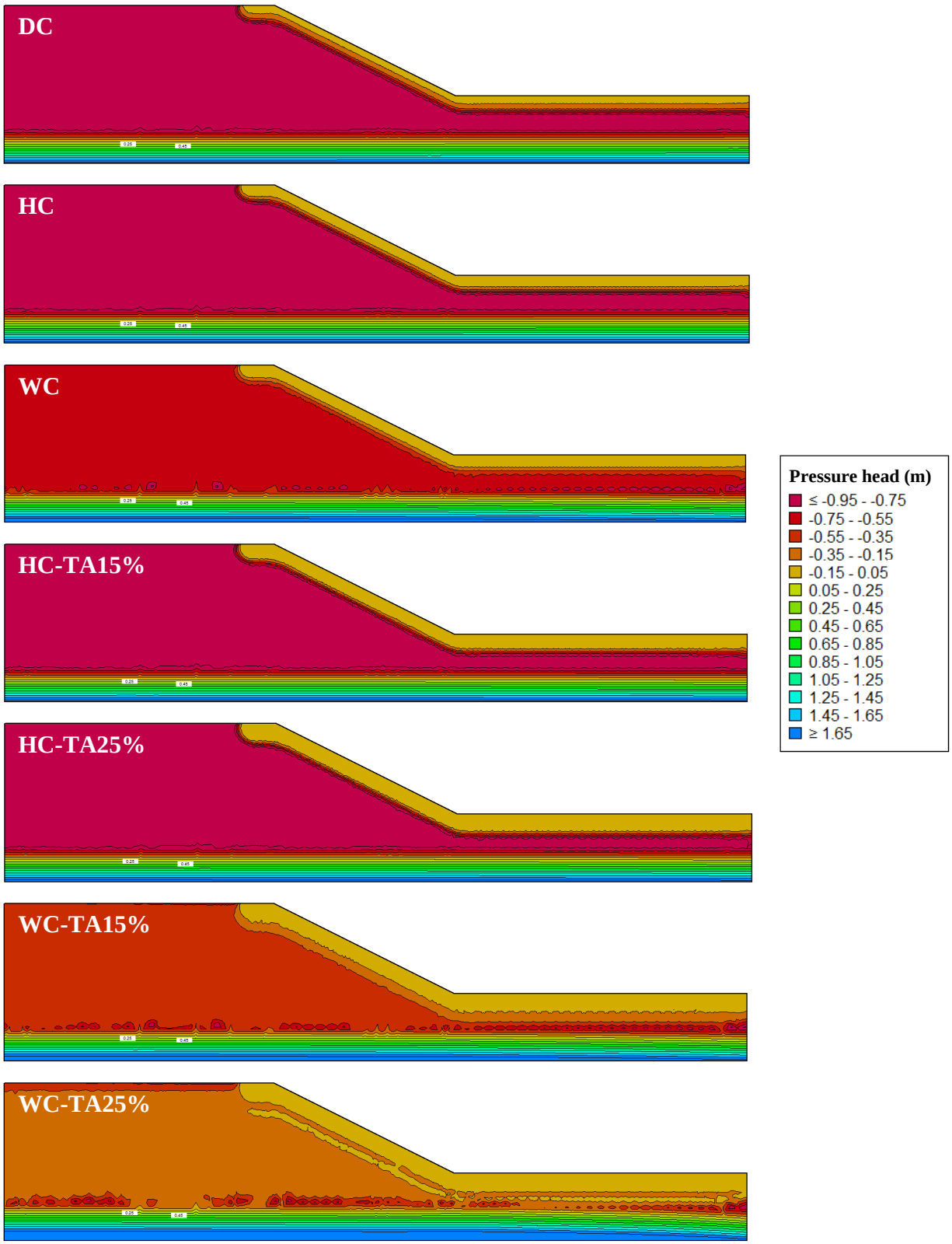

Figure C4 Pressure head distribution within sand slope at 9 d (*Max Sat*) – Toronto

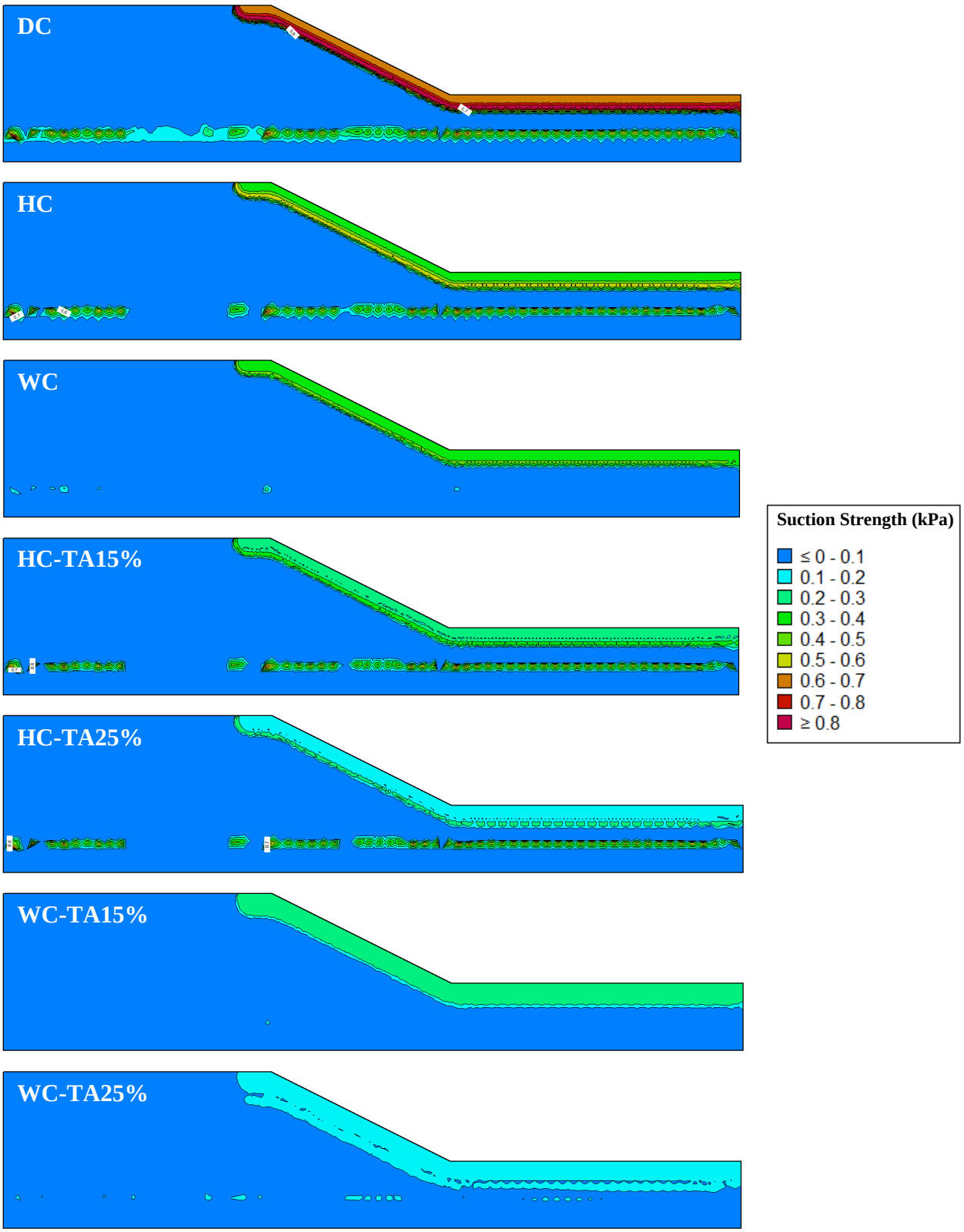

Figure C5 Suction strength distribution within sand slope at 9 d (*Max Sat*) – Toronto

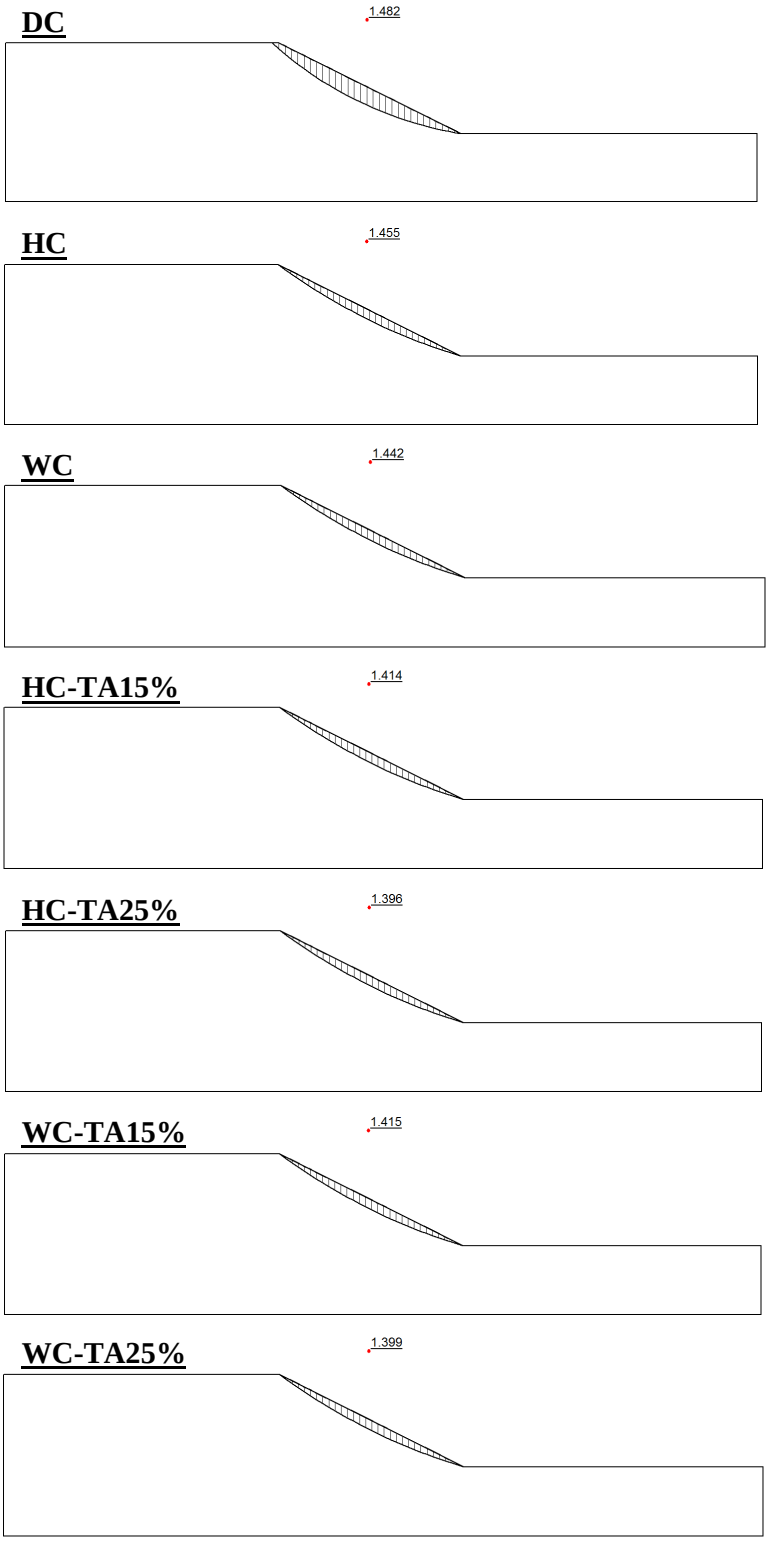

Figure C6 Sand slope's FOS and slip surface at 9 d (*Max Sat*) with minimum slip surface depth 0.3 m – Toronto

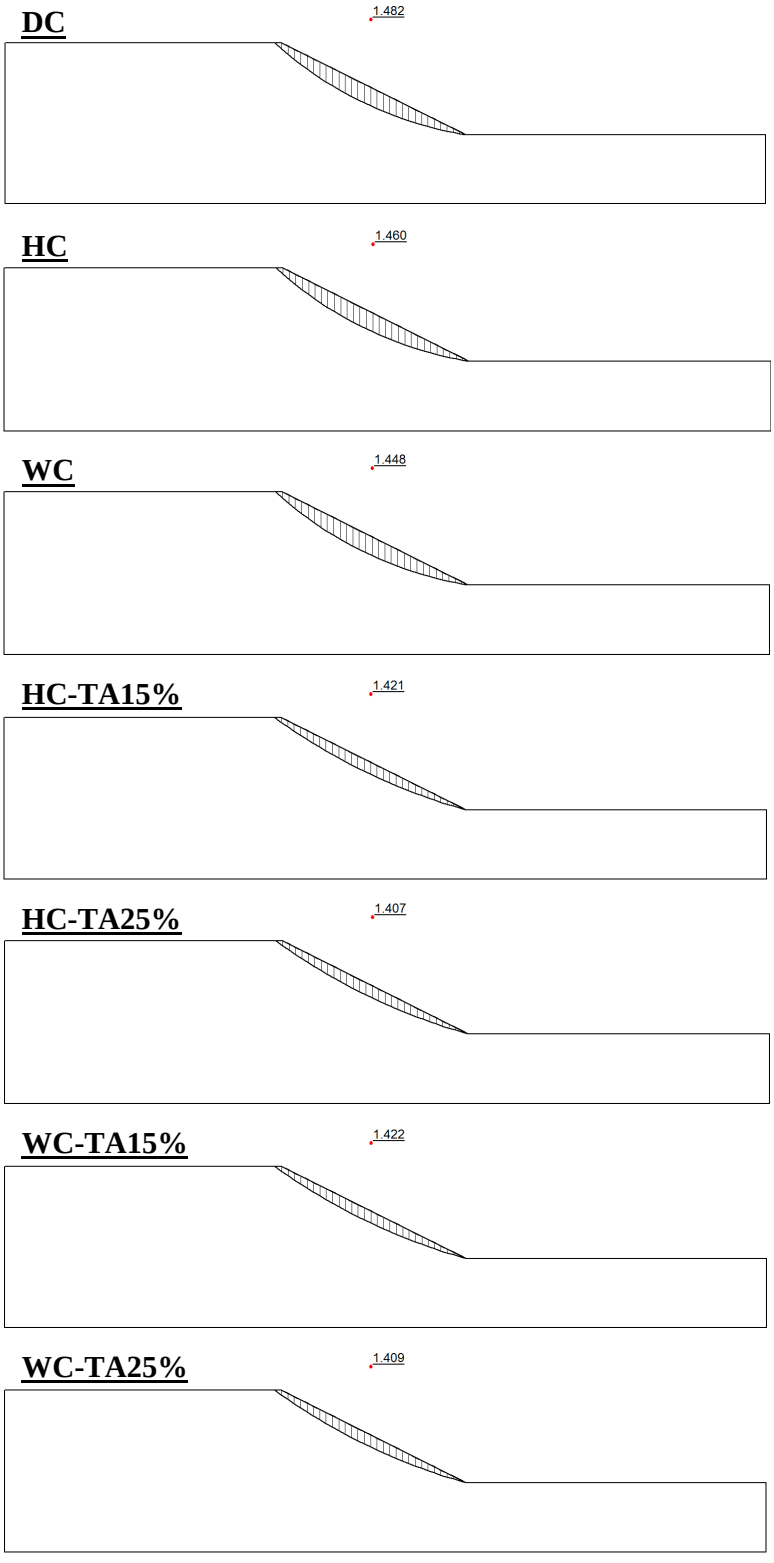

Figure C7 Sand slope's FOS and slip surface at 9 d (*Max Sat*) with minimum slip surface depth 1.0 m – Toronto

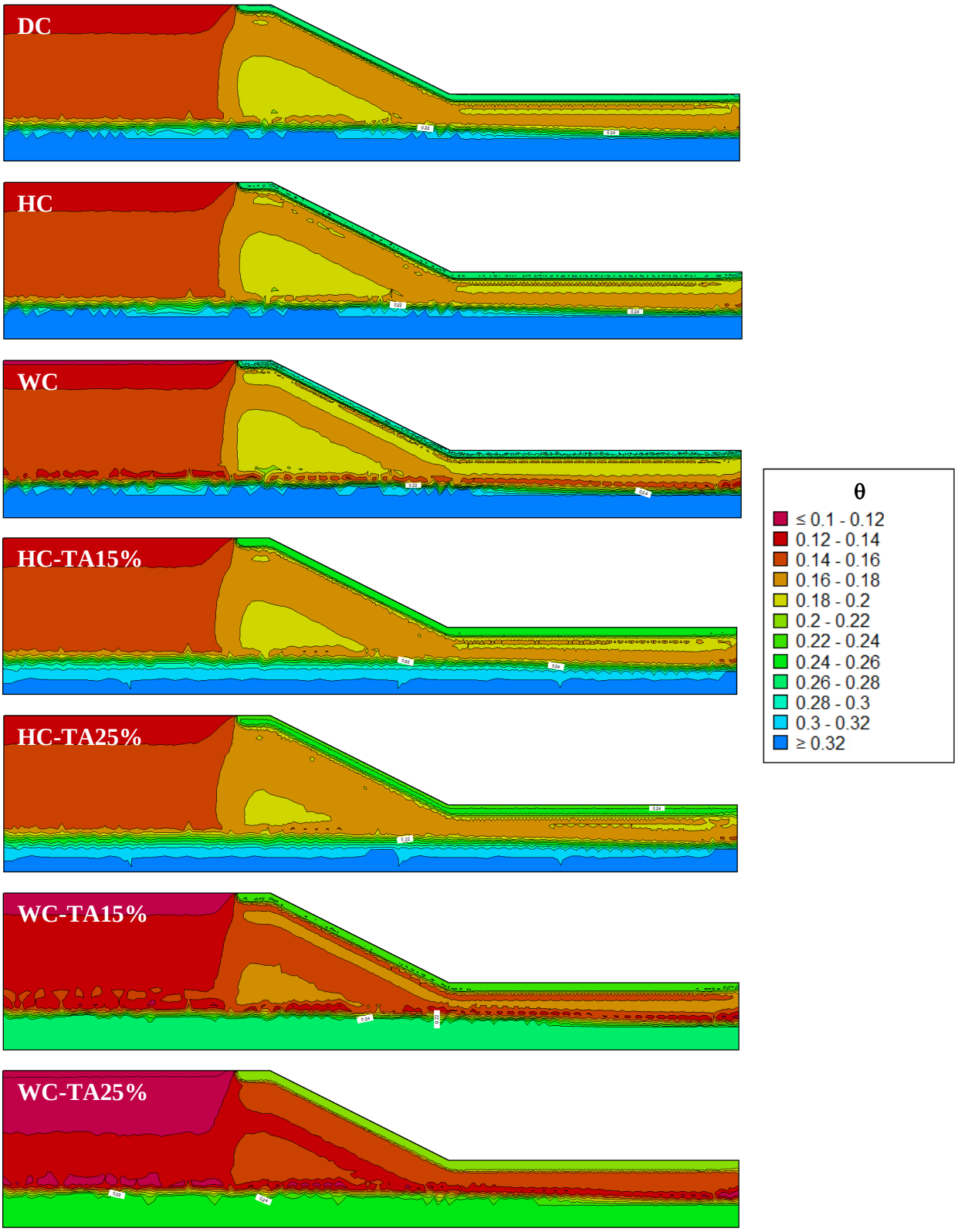

Figure C8 Volumetric water content distribution within sand slope at 369 d (*Max NI*) – Toronto

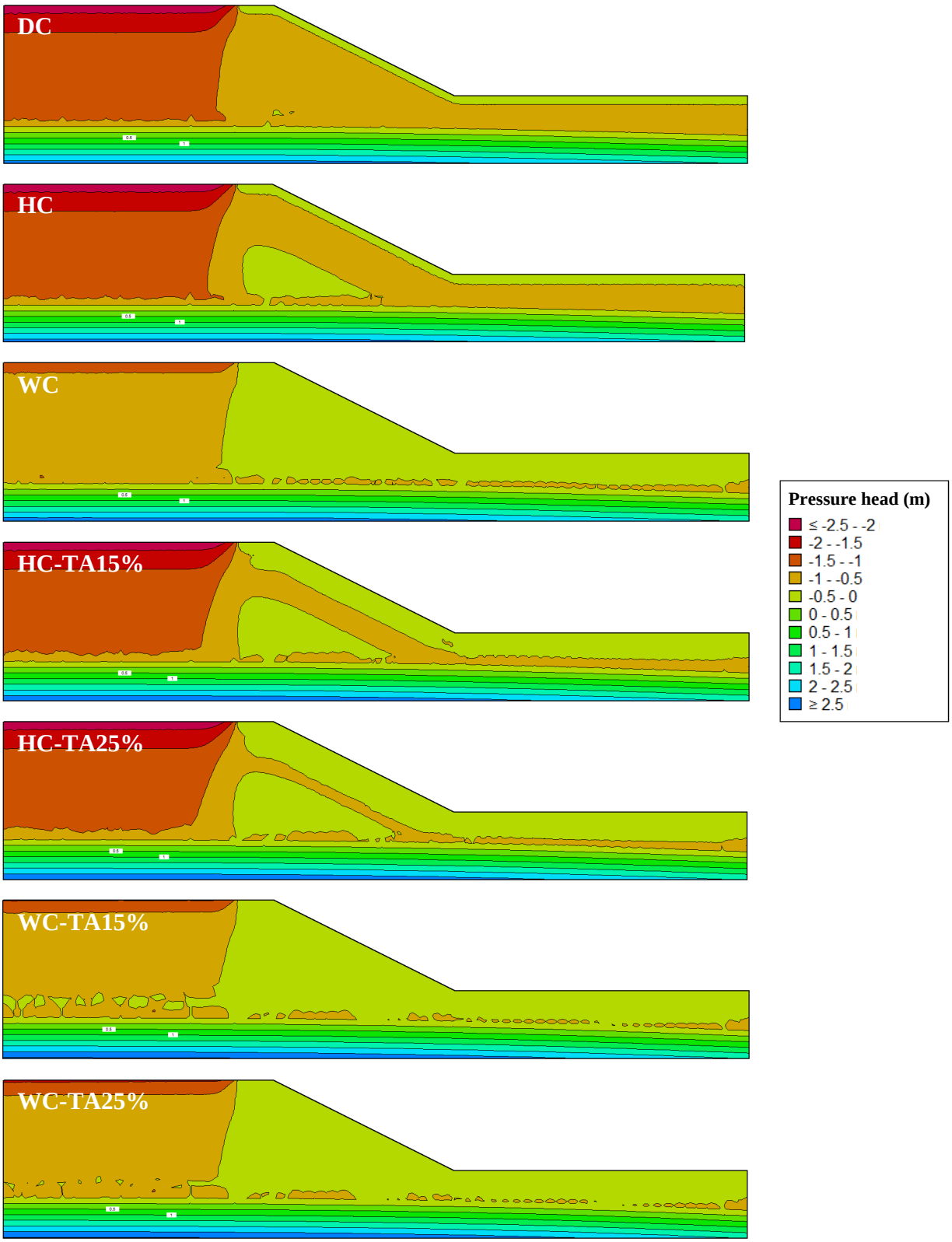

Figure C9 Pressure head distribution within sand slope at 369 d (*Max NI*) – Toronto

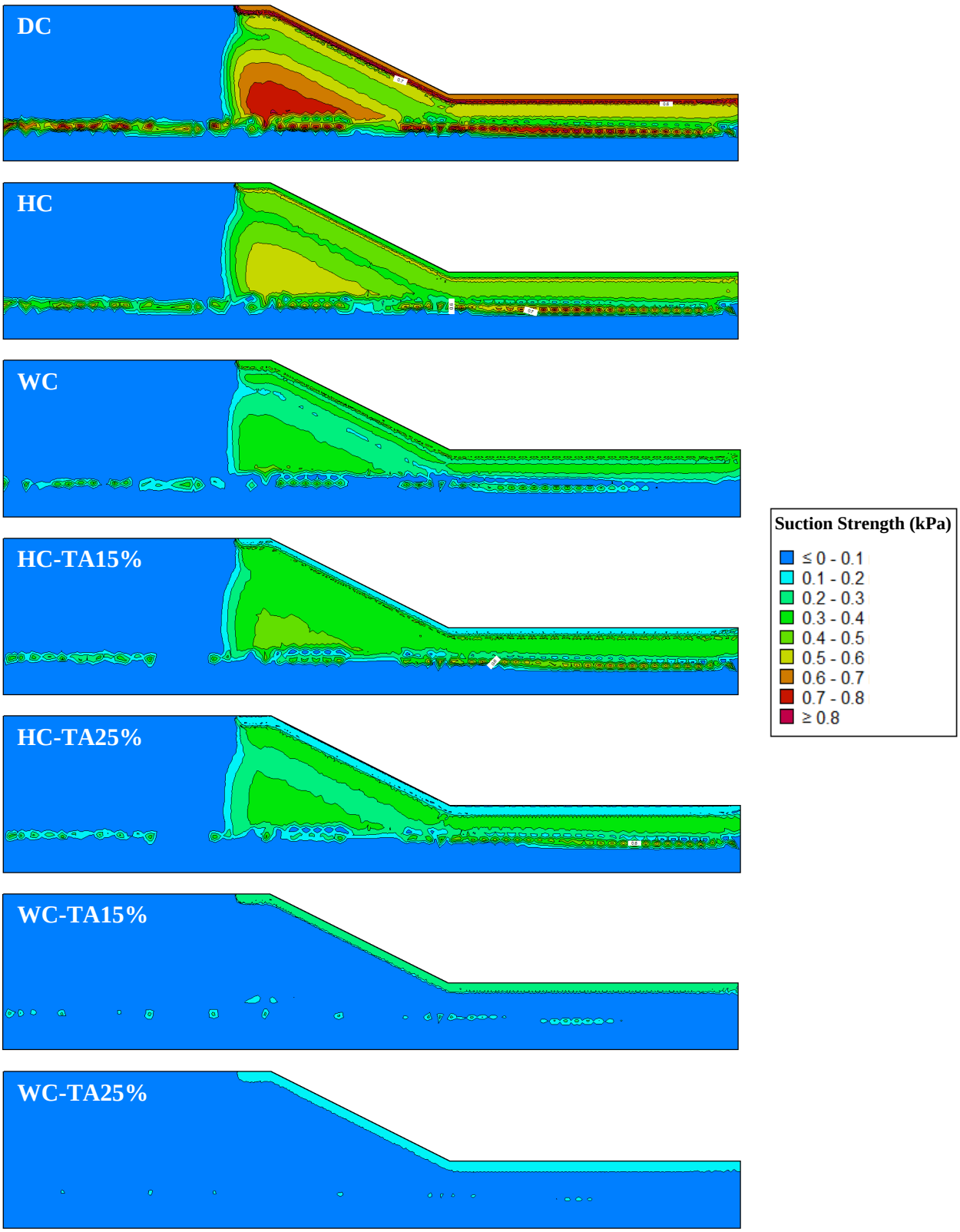

Figure C10 Suction strength distribution within sand slope at 369 d (*Max NI*) – Toronto

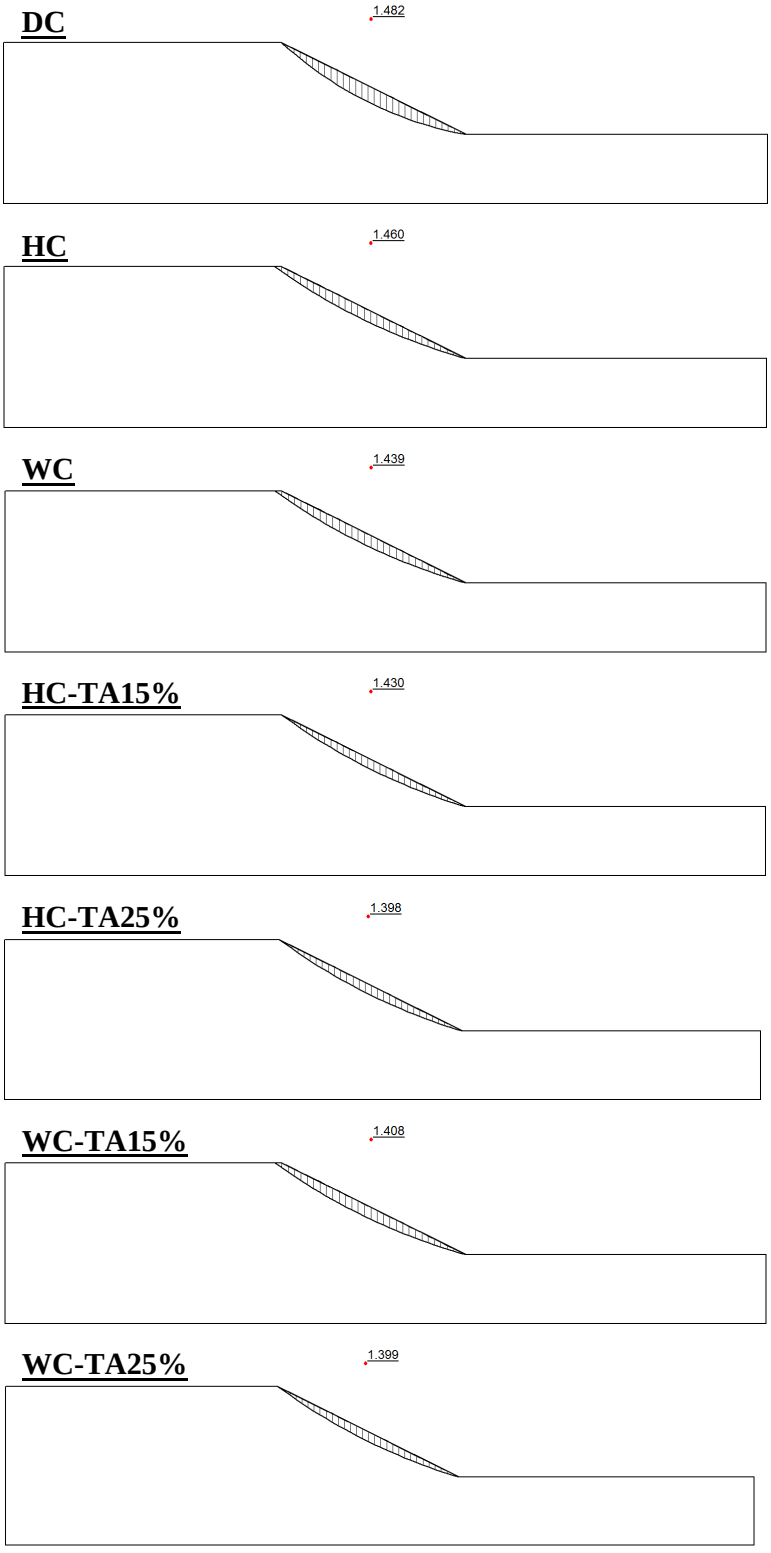

Figure C11 Sand slope's FOS and slip surface at 369 d (*Max NI*) with minimum slip surface depth of 0.3 m – Toronto

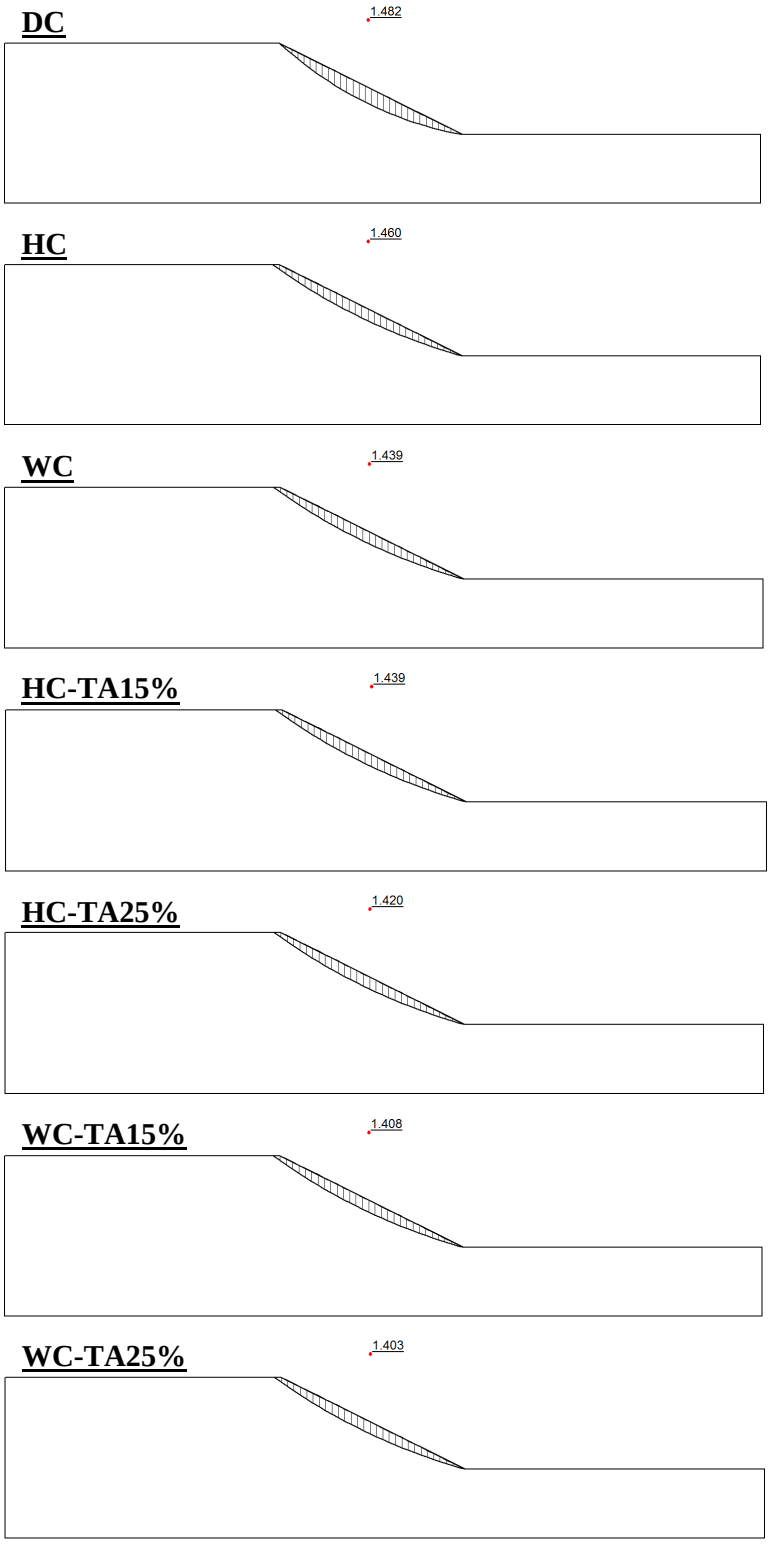

Figure C12 Sand slope's FOS and slip surface at 369 d (*Max NI*) with minimum slip surface depth of 1.0 m – Toronto

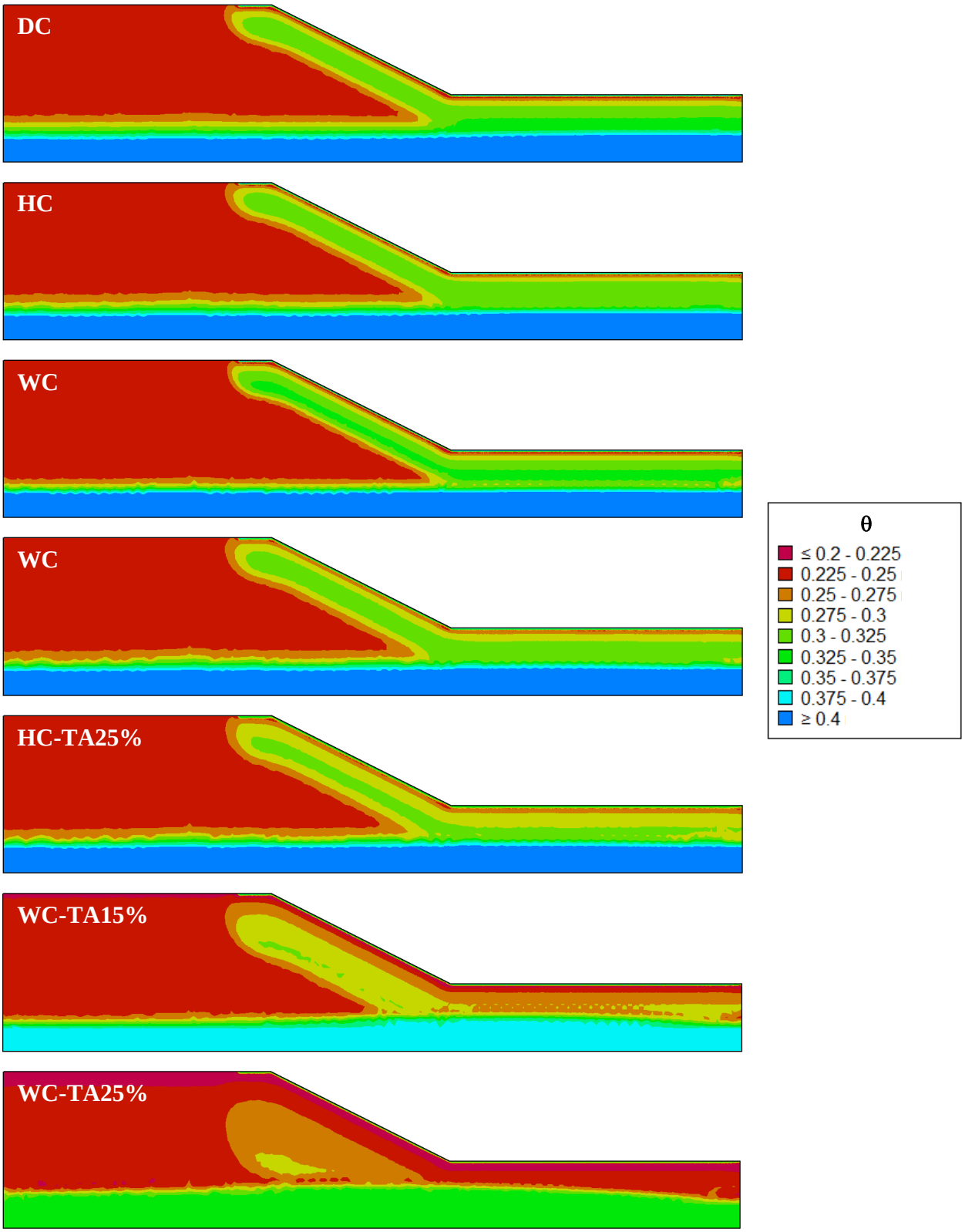

Figure C13 Volumetric water content distribution within silt slope at 120 d (*Max NI*) – Toronto

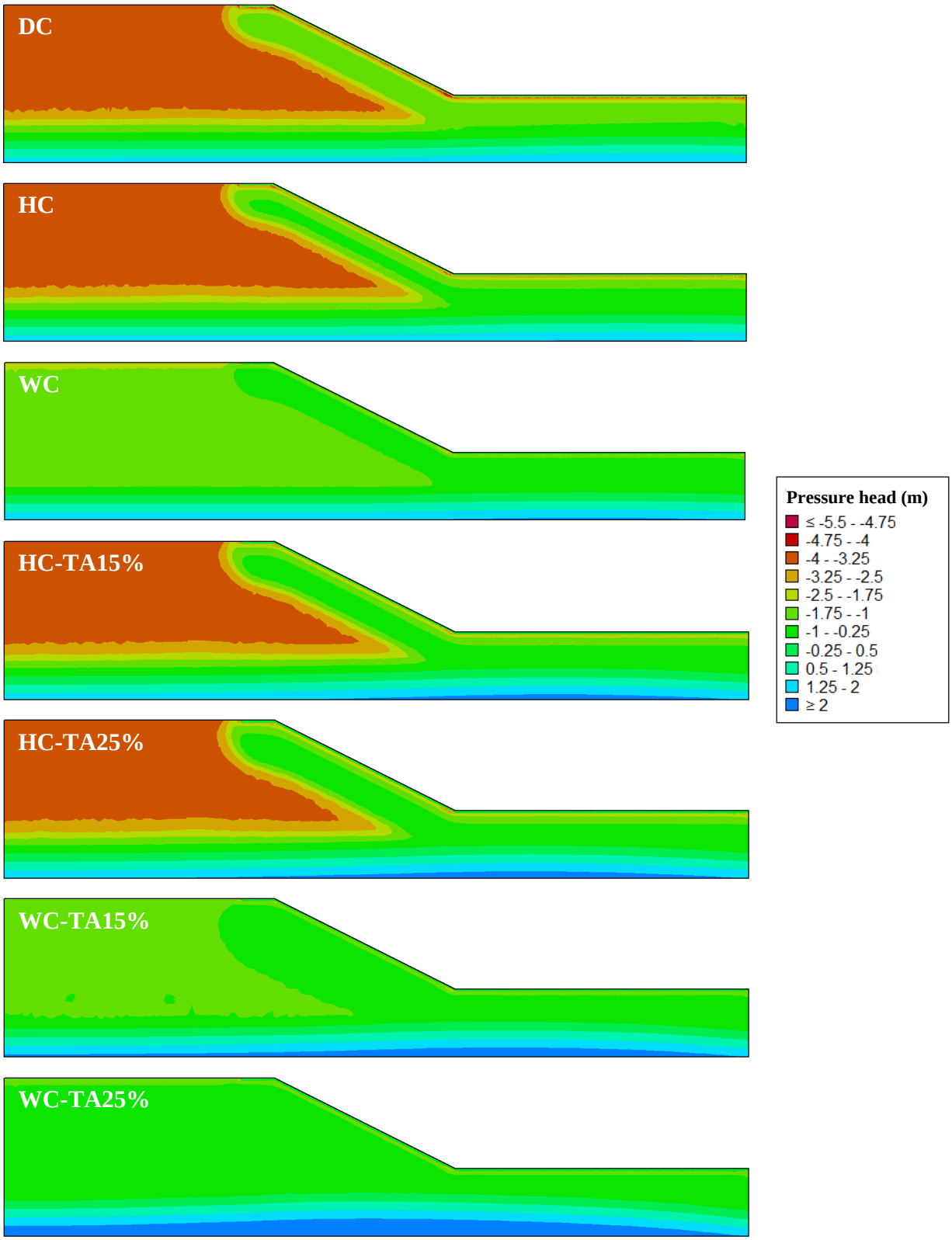

Figure C14 Pressure head distribution within silt slope at 120 d (*Max NI*) – Toronto

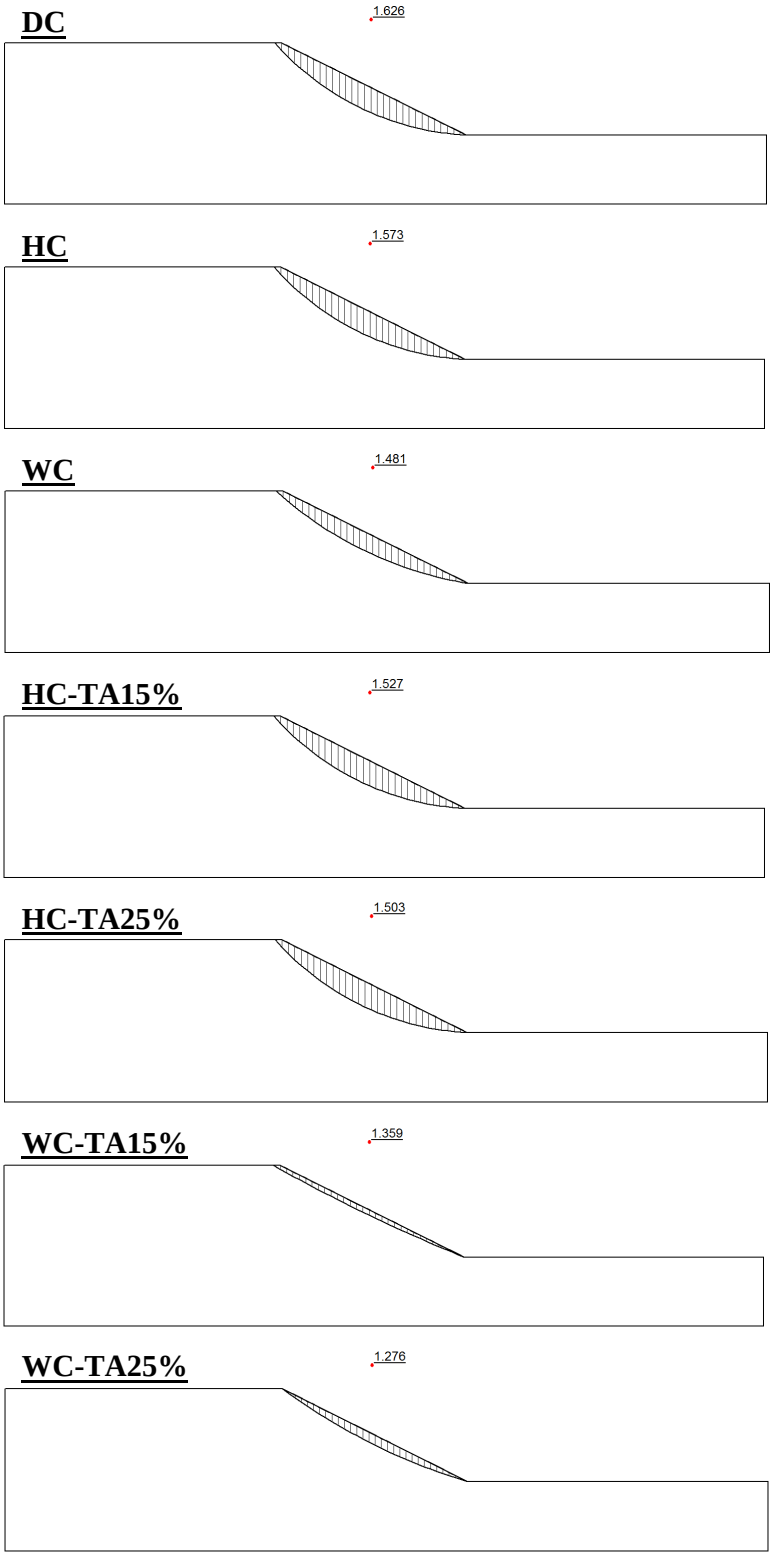

Figure C15 Silt slope's FOS and slip surface at 120 d (*Max NI*) with minimum slip surface depth of 0.3 m – Toronto

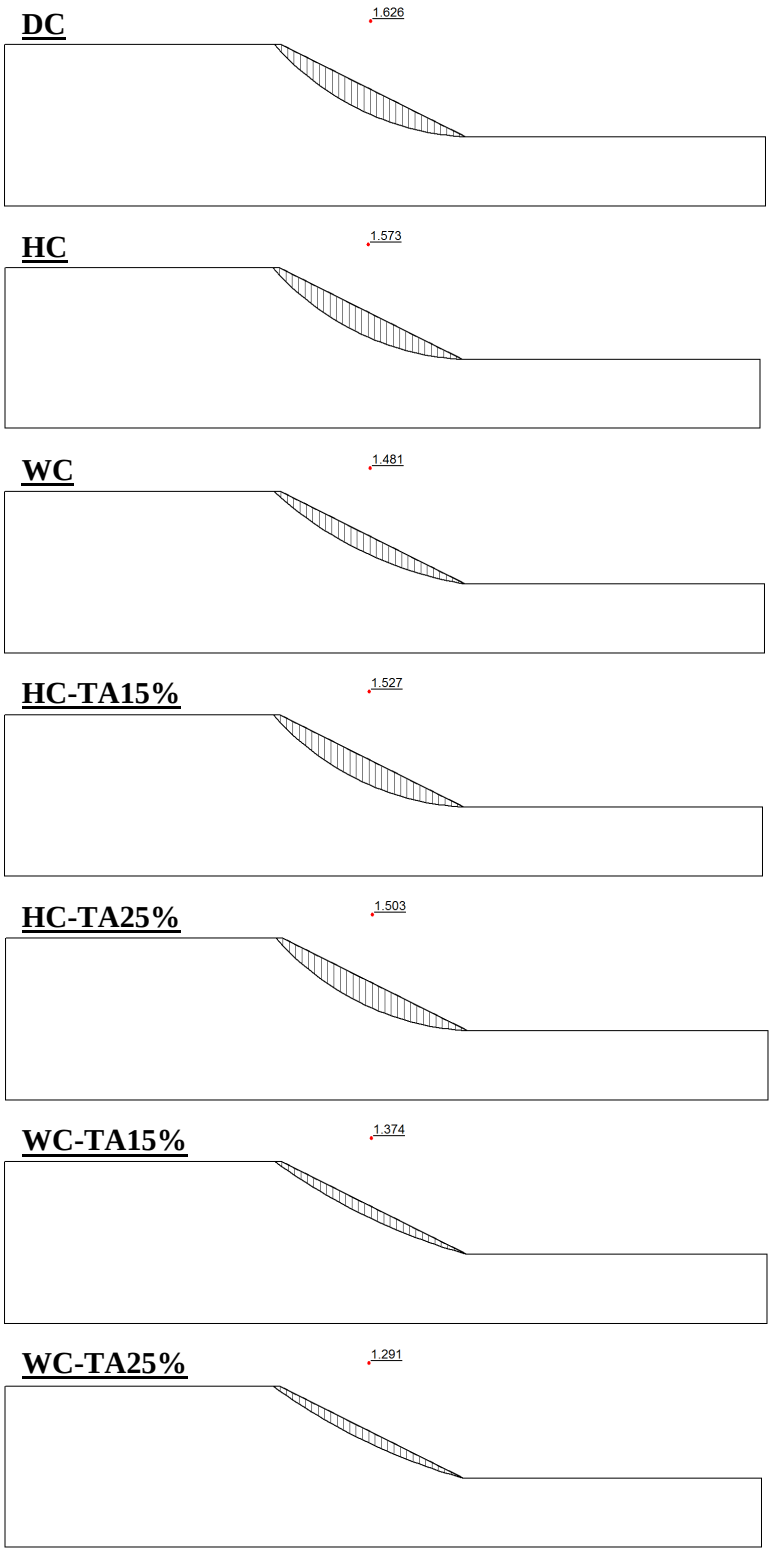

Figure C16 Silt slope's FOS and slip surface at 120 d (*Max NI*) with minimum slip surface depth of 1.0 m – Toronto

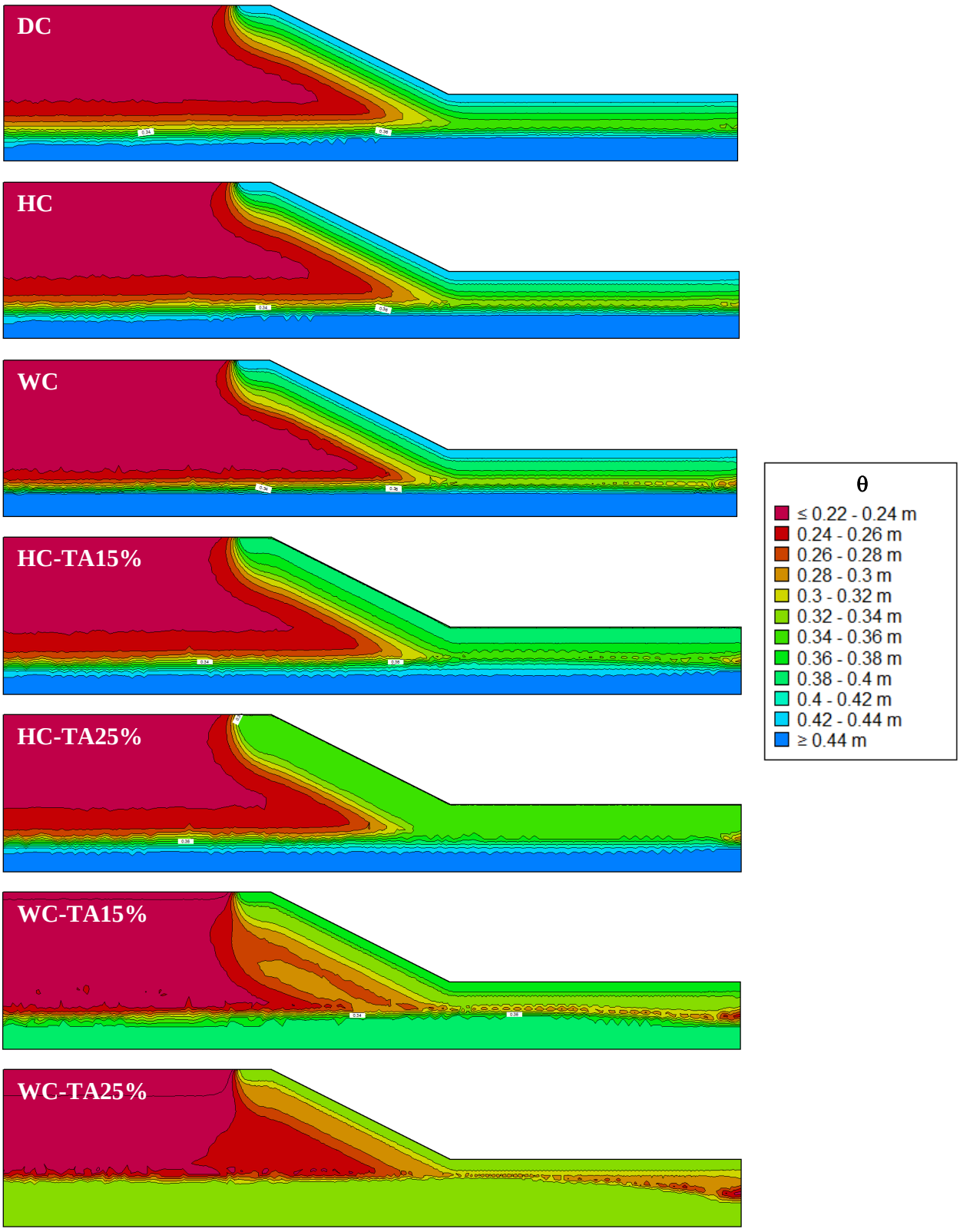

Figure C17 Volumetric water content distribution within silt slope at 289 d (*Max Sat*) – Toronto

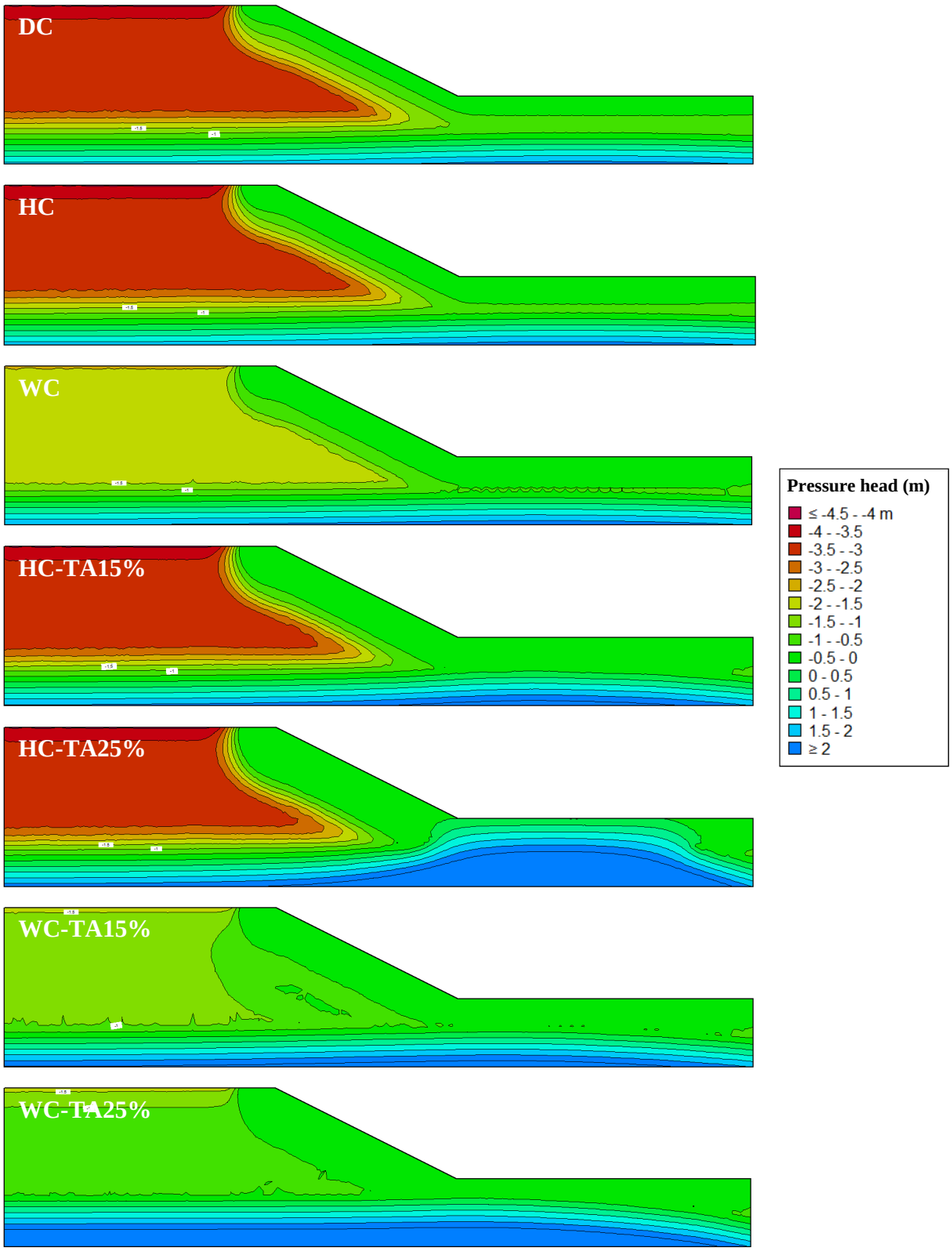

Figure C18 Pressure head distribution within silt slope at 289 d (*Max Sat*) – Toronto

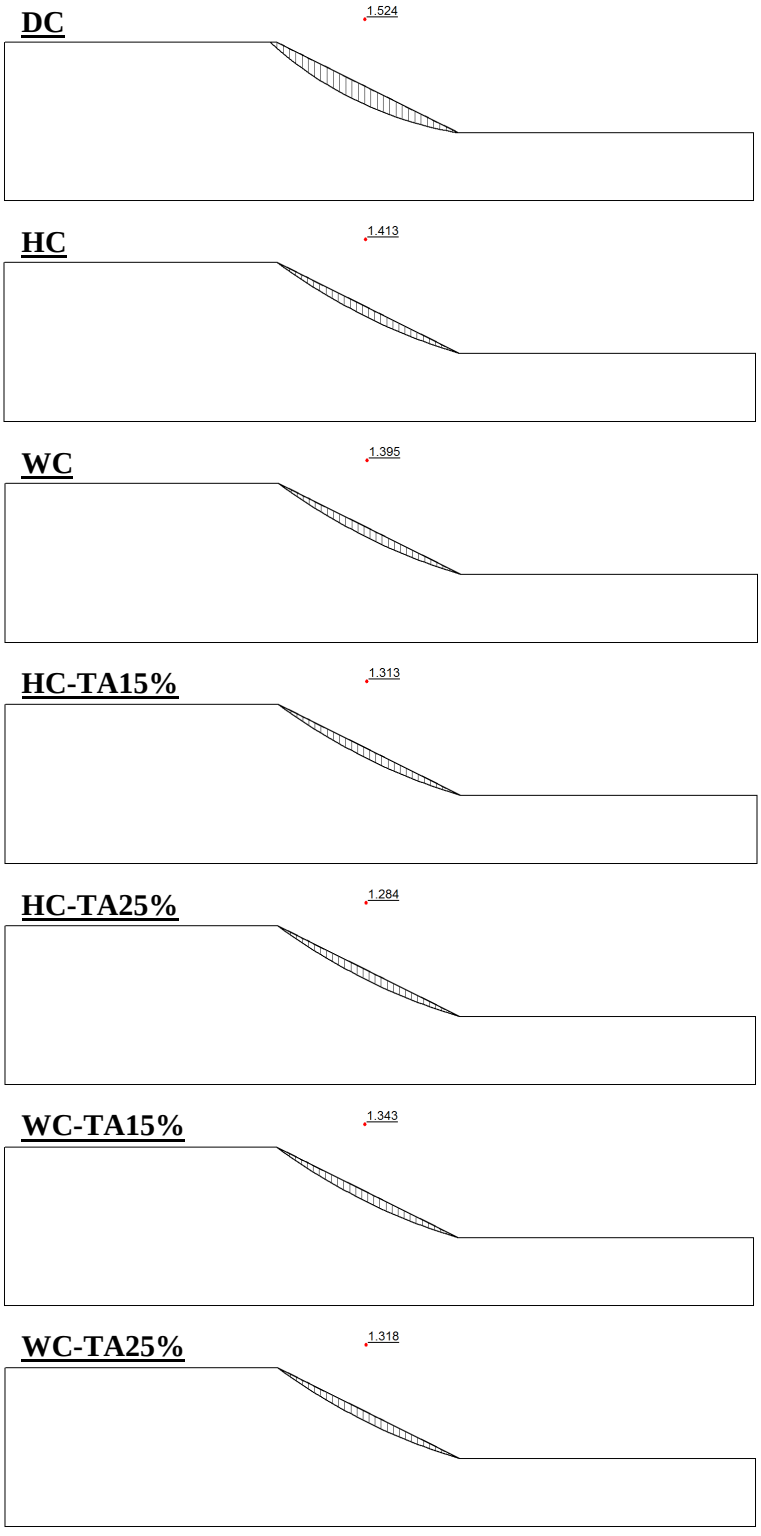

Figure C19 Silt slope's FOS and slip surface at 289 d (*Max Sat*) with minimum slip surface depth of 0.3 m – Toronto

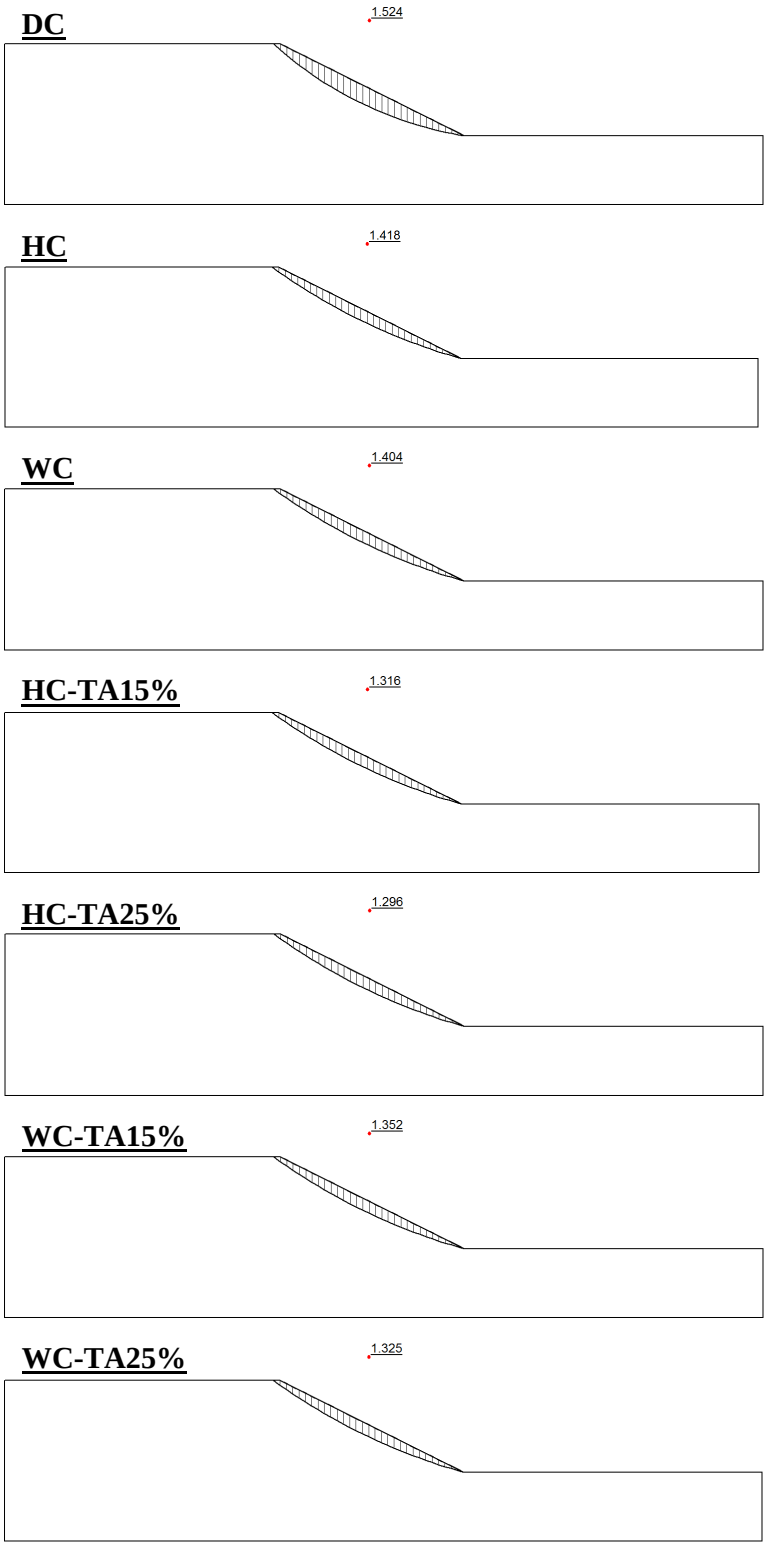

Figure C20 Silt slope's FOS and slip surface at 289 d (*Max Sat*) with minimum slip surface depth of 1.0 m – Toronto

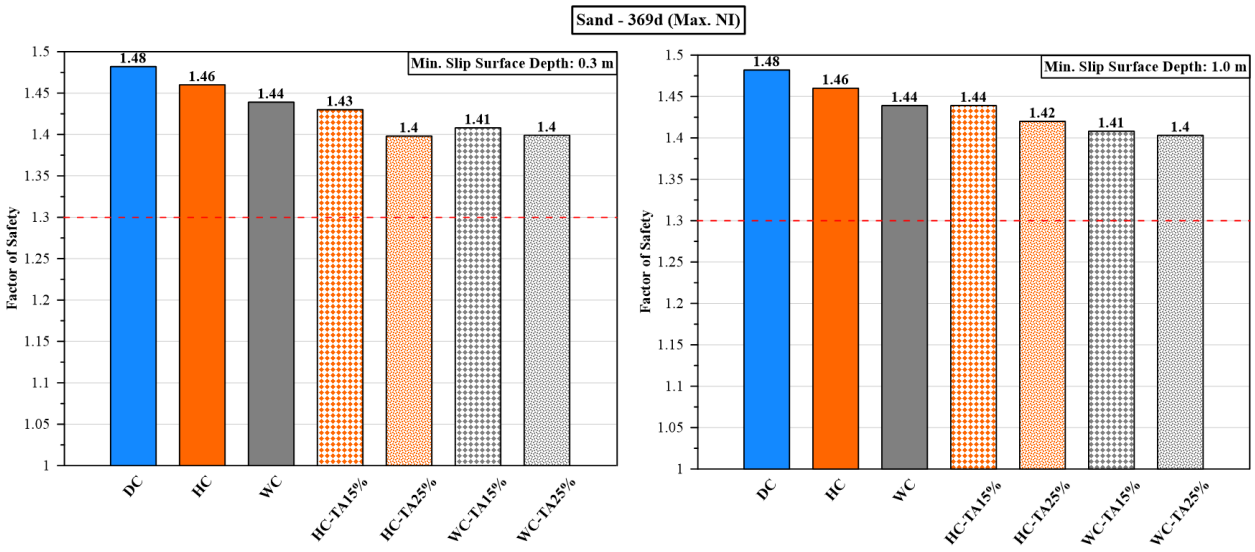

Figure C21 FOS of sand slope during *Max NI* occurrence (369 d) using different hydraulic characteristics, with two considered minimum slip surface depths: 0.3 m (left) and 1.0 m (right) – Toronto

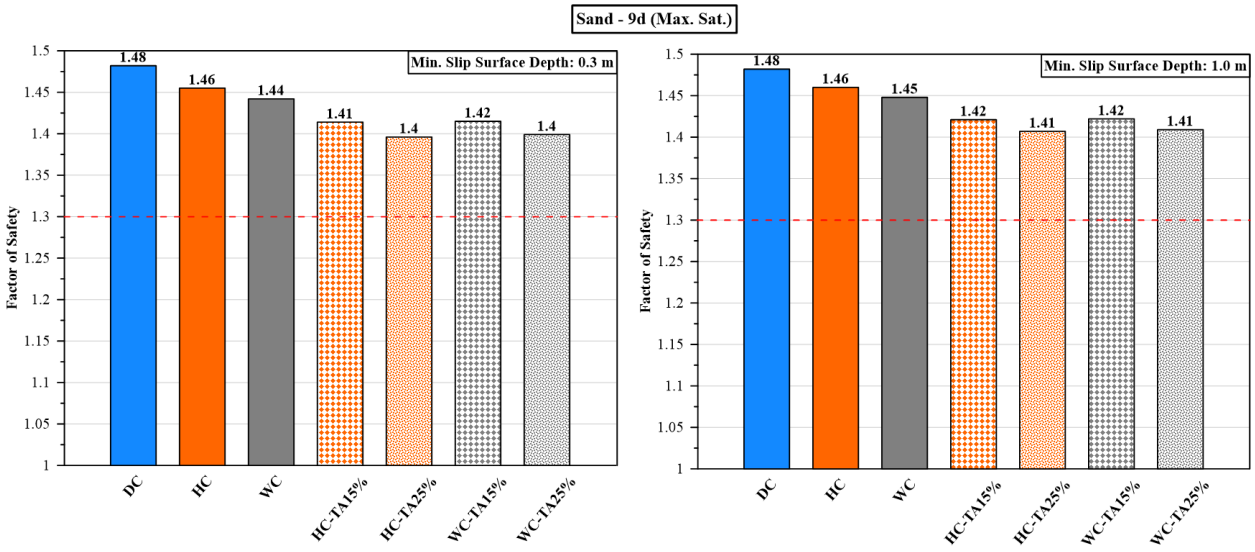

Figure C22 FOS of sand slope during *Max Sat* occurrence (9 d) using different hydraulic characteristics, with two considered minimum slip surface depths: 0.3 m (left) and 1.0 m (right) – Toronto

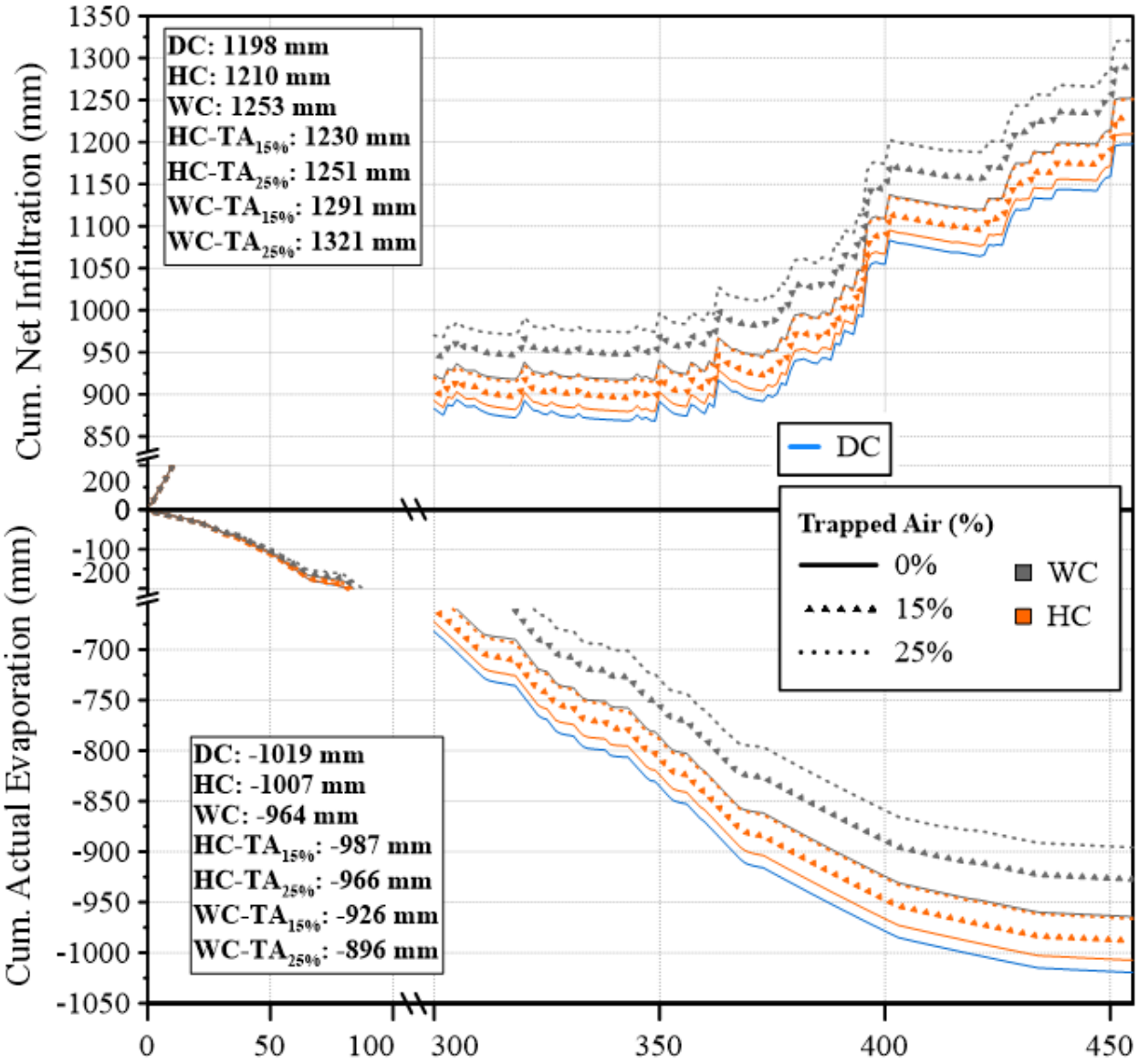

Figure C23 Estimated water balance at the surface of the sand profile – North Bay

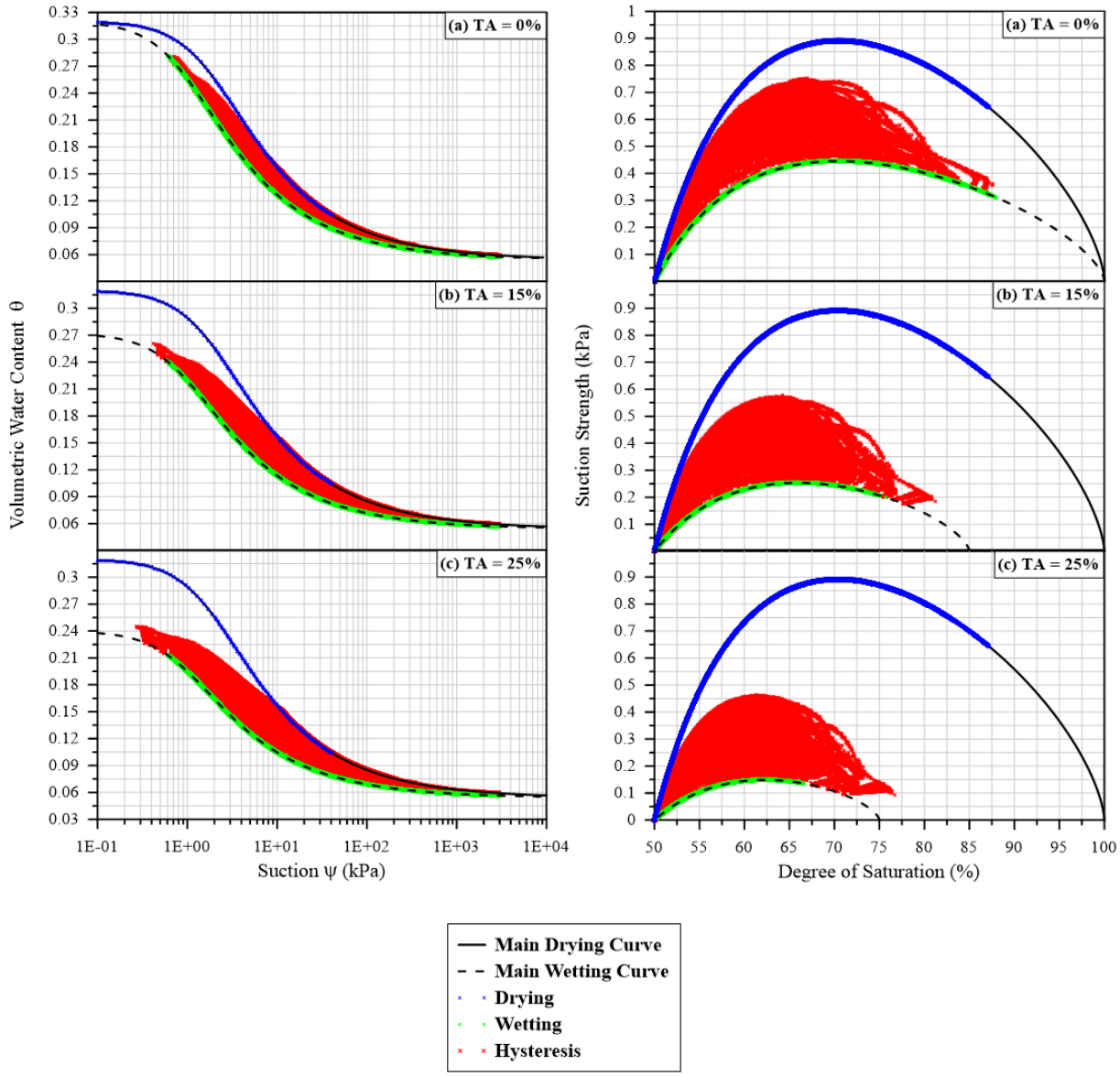

Figure C24 Hysteresis profiles of suction strength for sand, including data points from the hysteretic simulations with and without air entrapment– North Bay

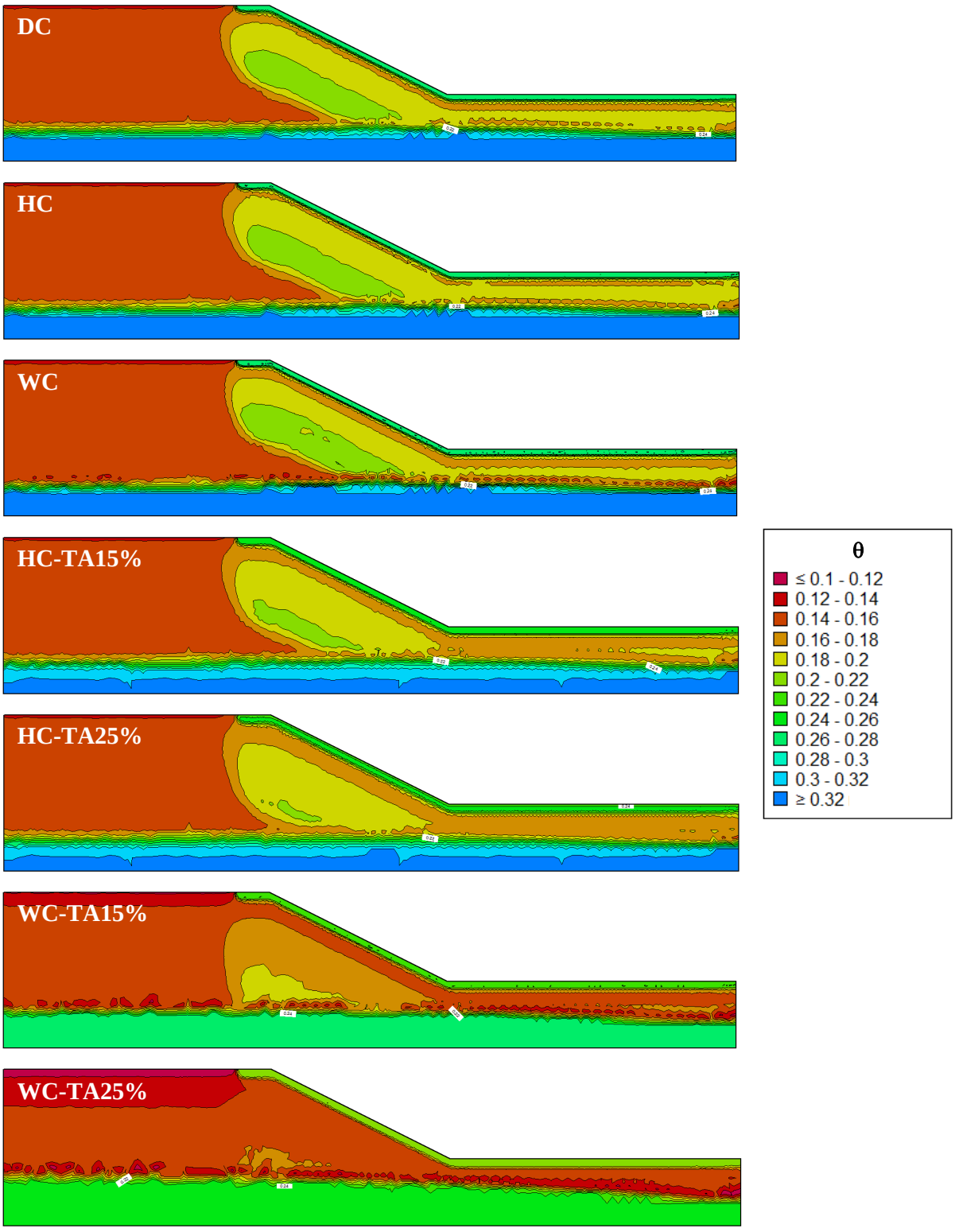

Figure C25 Volumetric water content distribution within sand slope at 50 d (*Max NI*) – North Bay

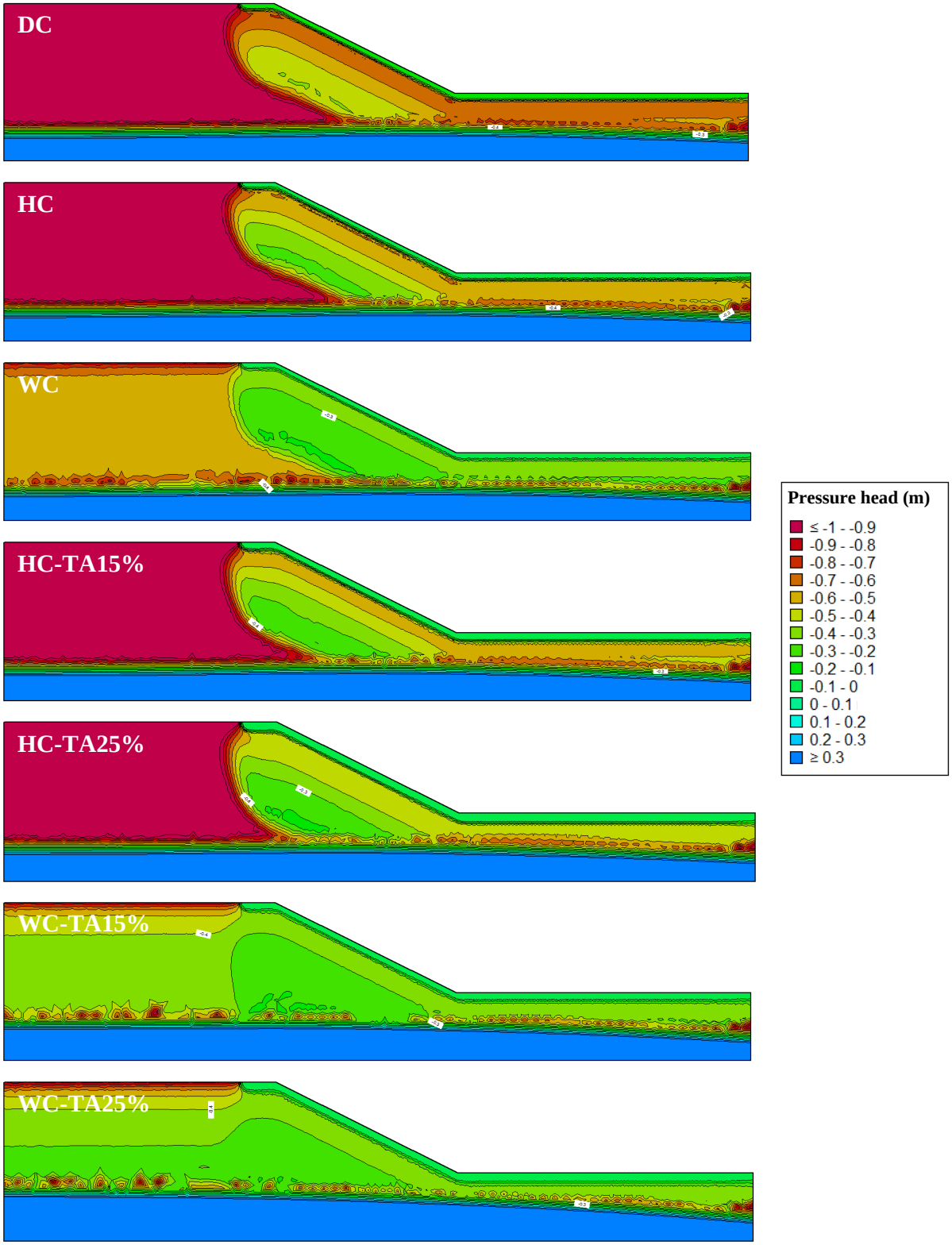

Figure C26 Pressure head distribution within sand slope at 50 d (*Max NI*) – North Bay

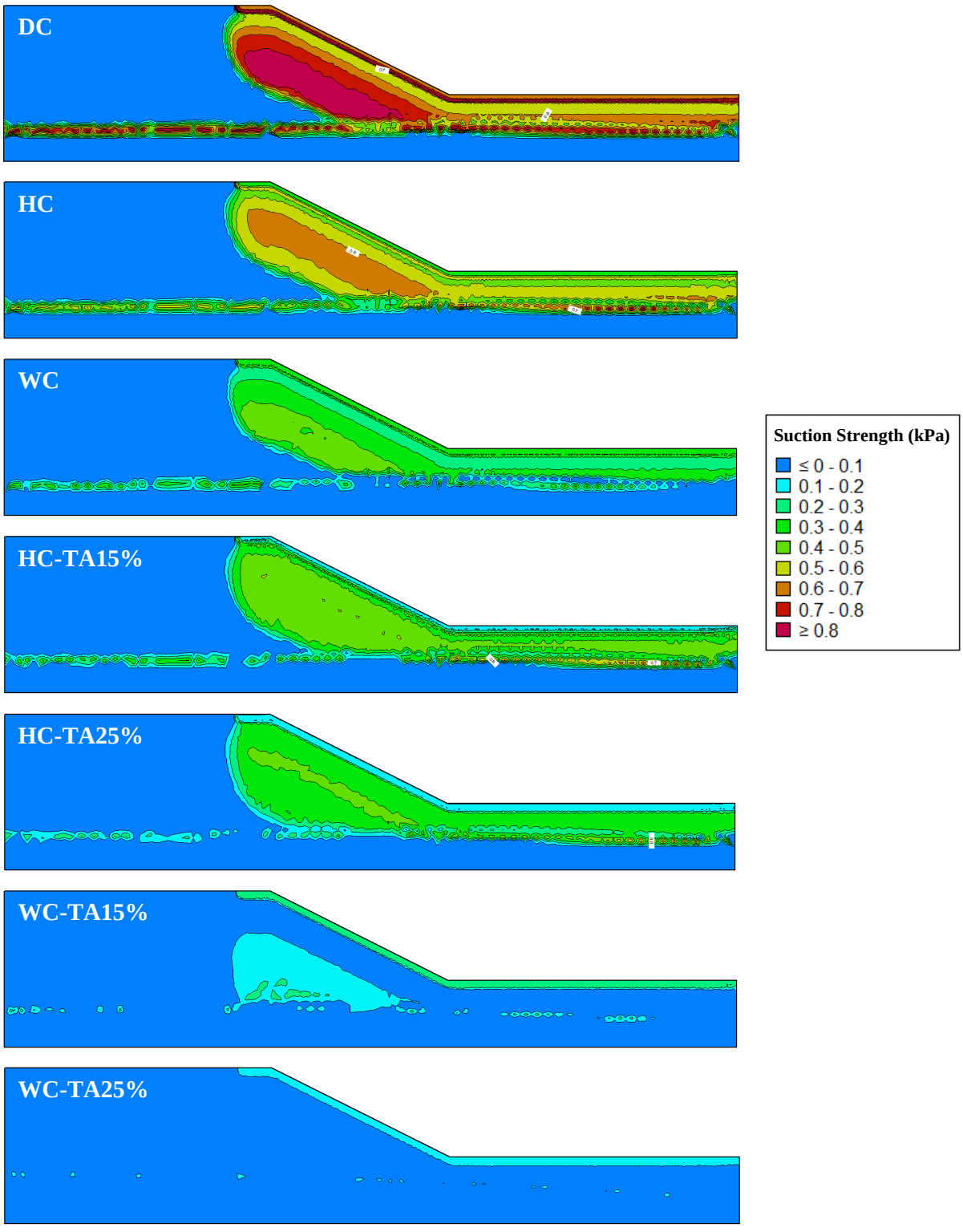

Figure C27 Suction strength distribution within sand slope at 50 d (*Max NI*) – North Bay

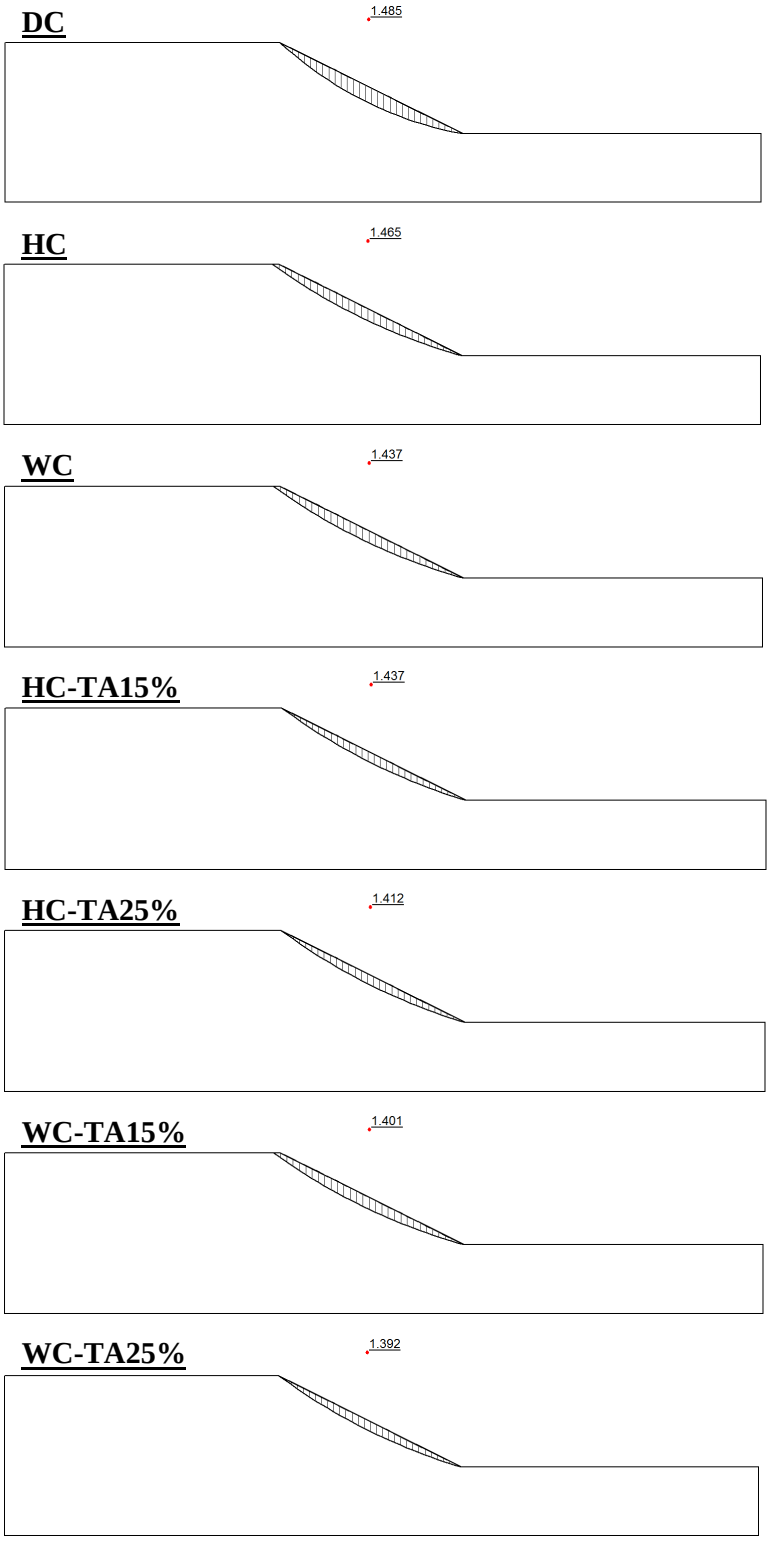

Figure C28 Sand slope's FOS and slip surface at 50 d (*Max NI*) with minimum slip surface depth of 0.3 m – North Bay

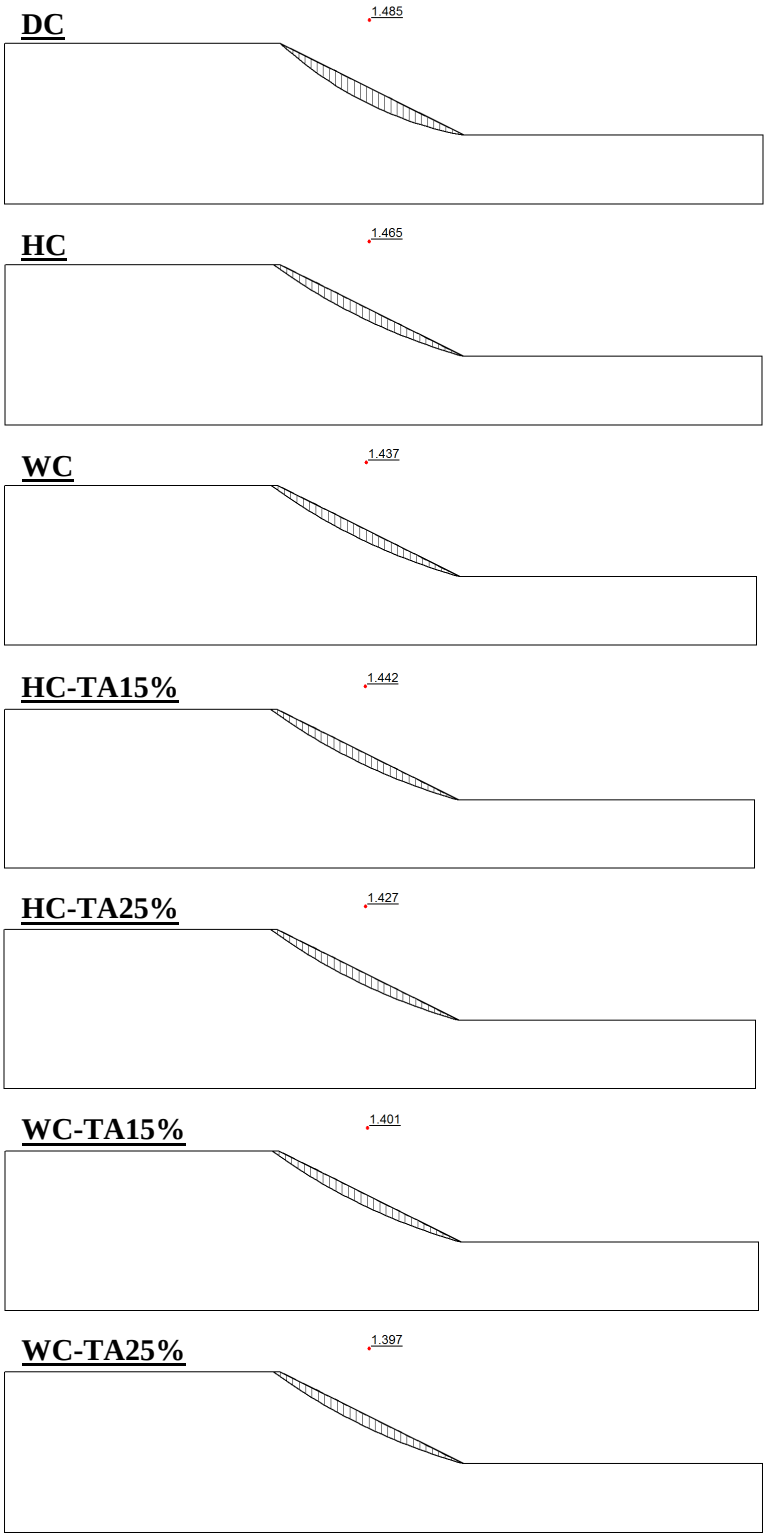

Figure C29 Sand slope's FOS and slip surface at 50 d (*Max NI*) with minimum slip surface depth of 1.0 m – North Bay

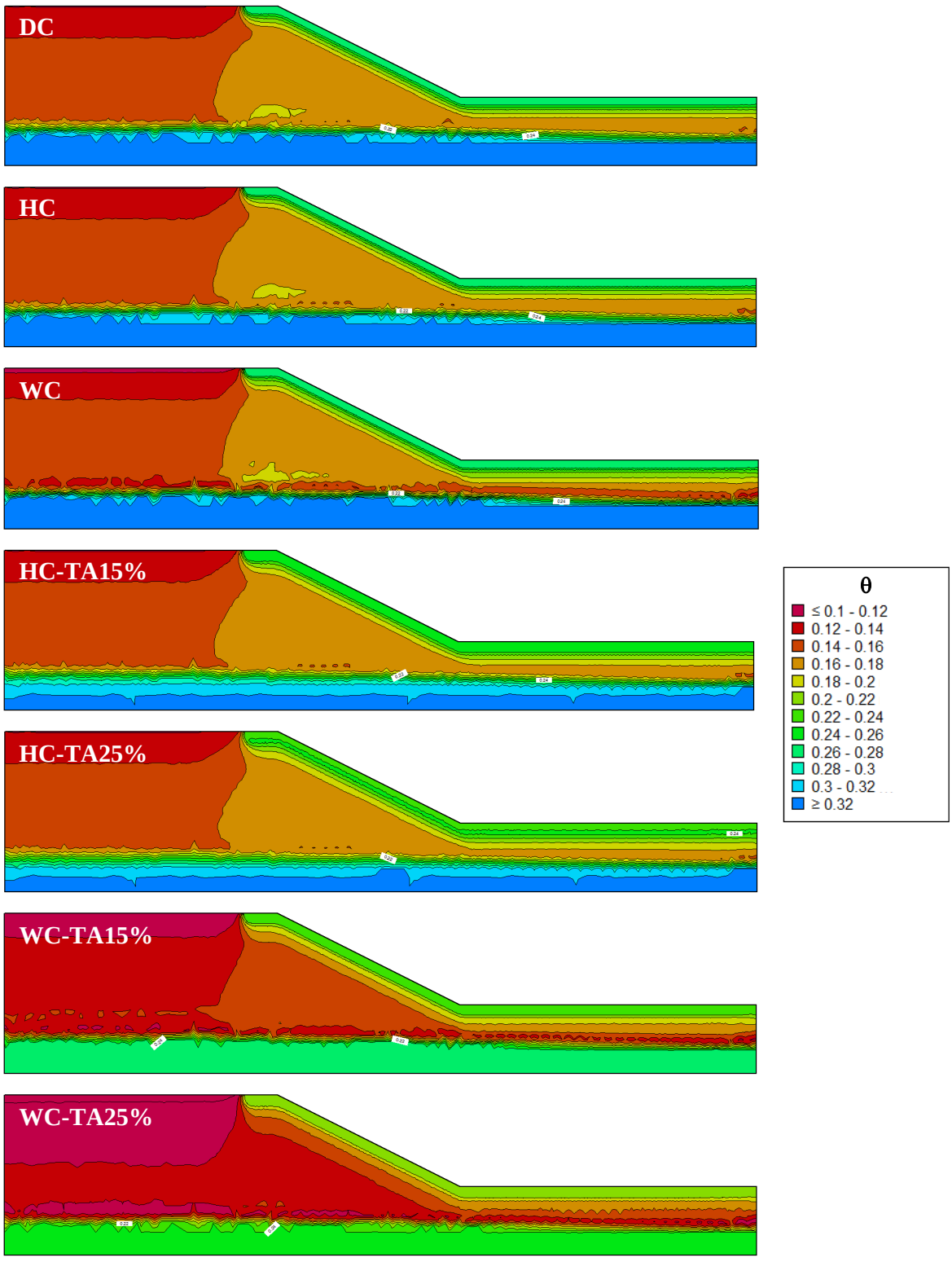

Figure C30 Volumetric water content distribution within sand slope at 396 d (*Max Sat*) – North Bay

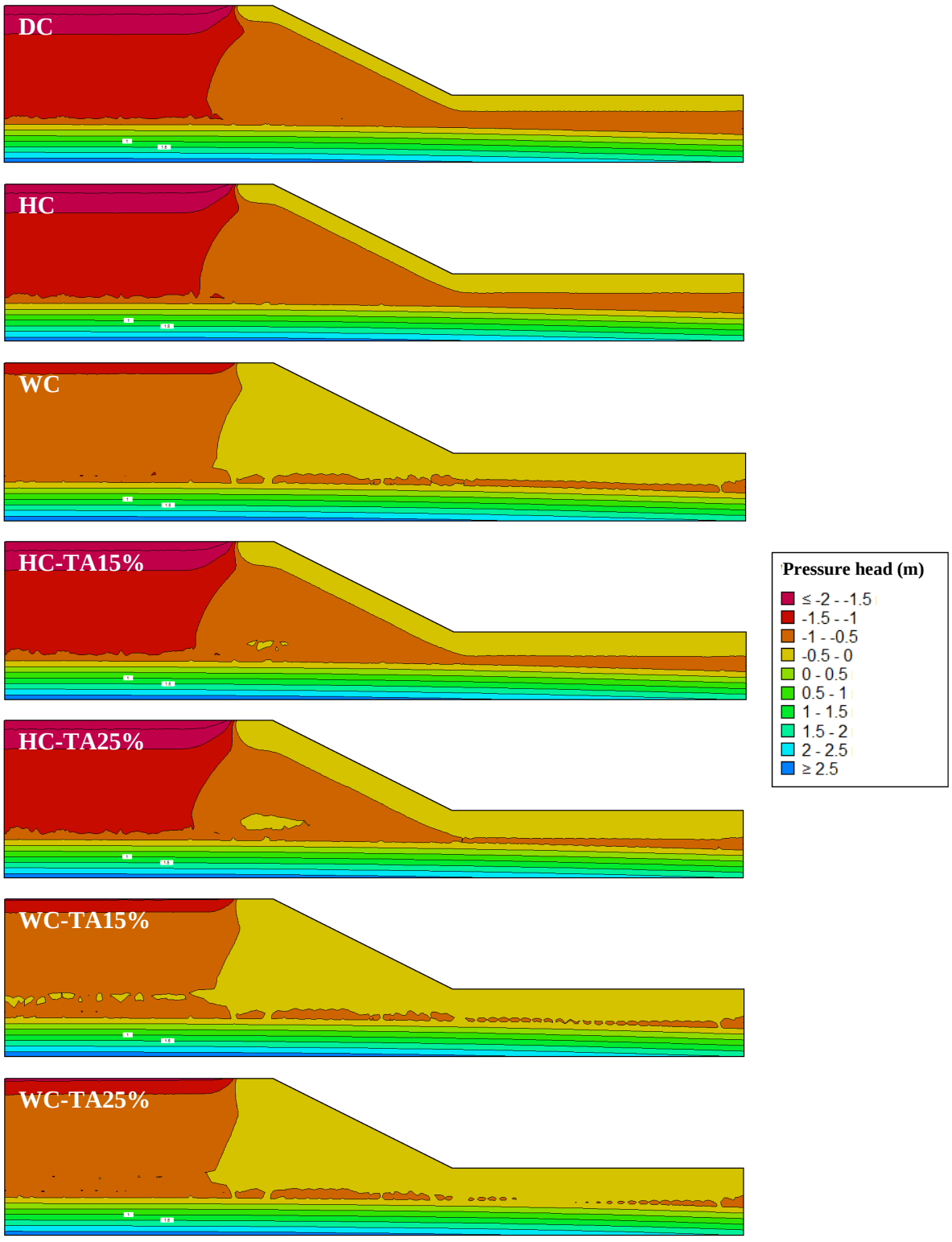

Figure C31 Pressure head distribution within sand slope at 396 d (*Max Sat*) – North Bay

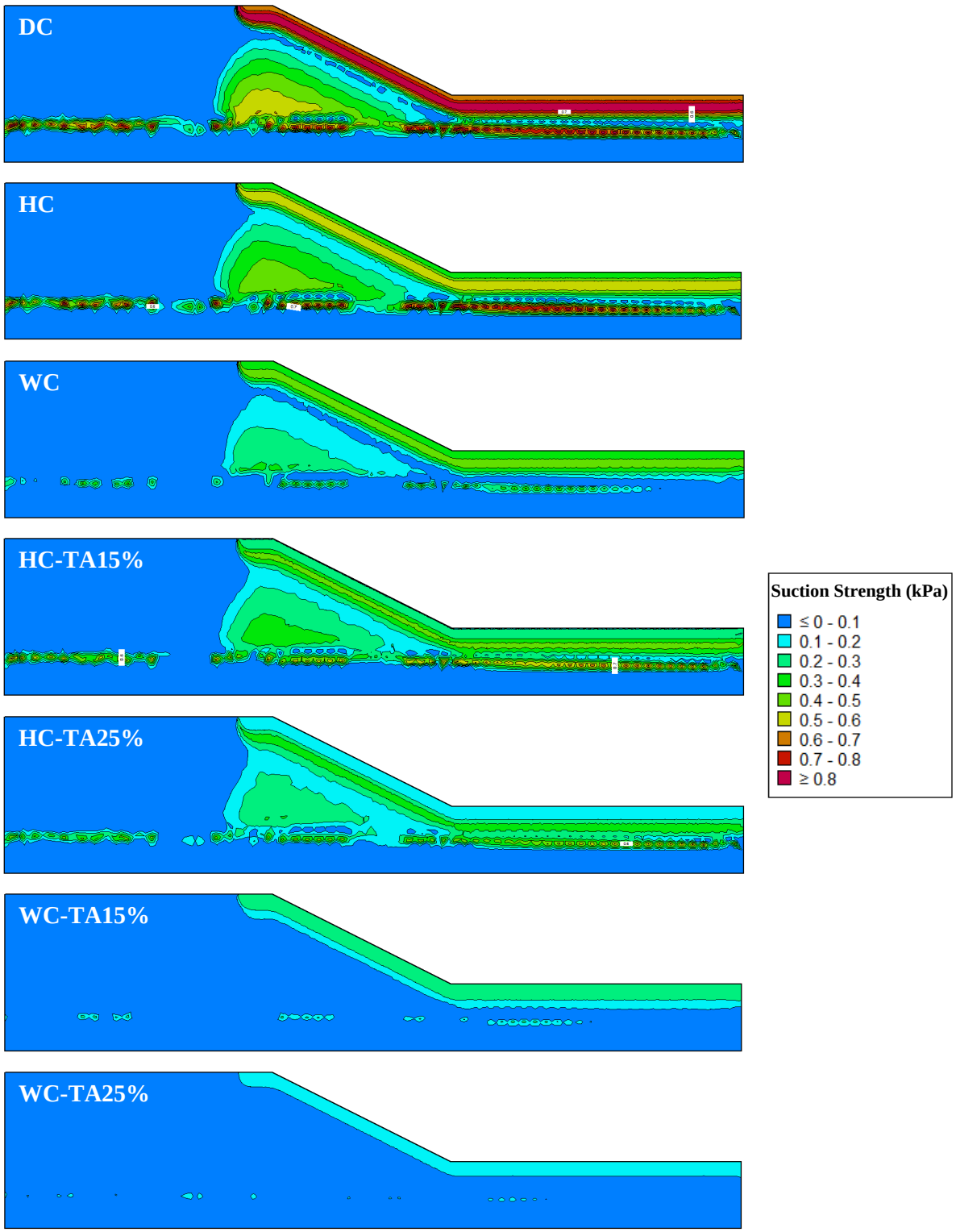

Figure C32 Suction strength distribution within sand slope at 396 d (*Max Sat*) – North Bay

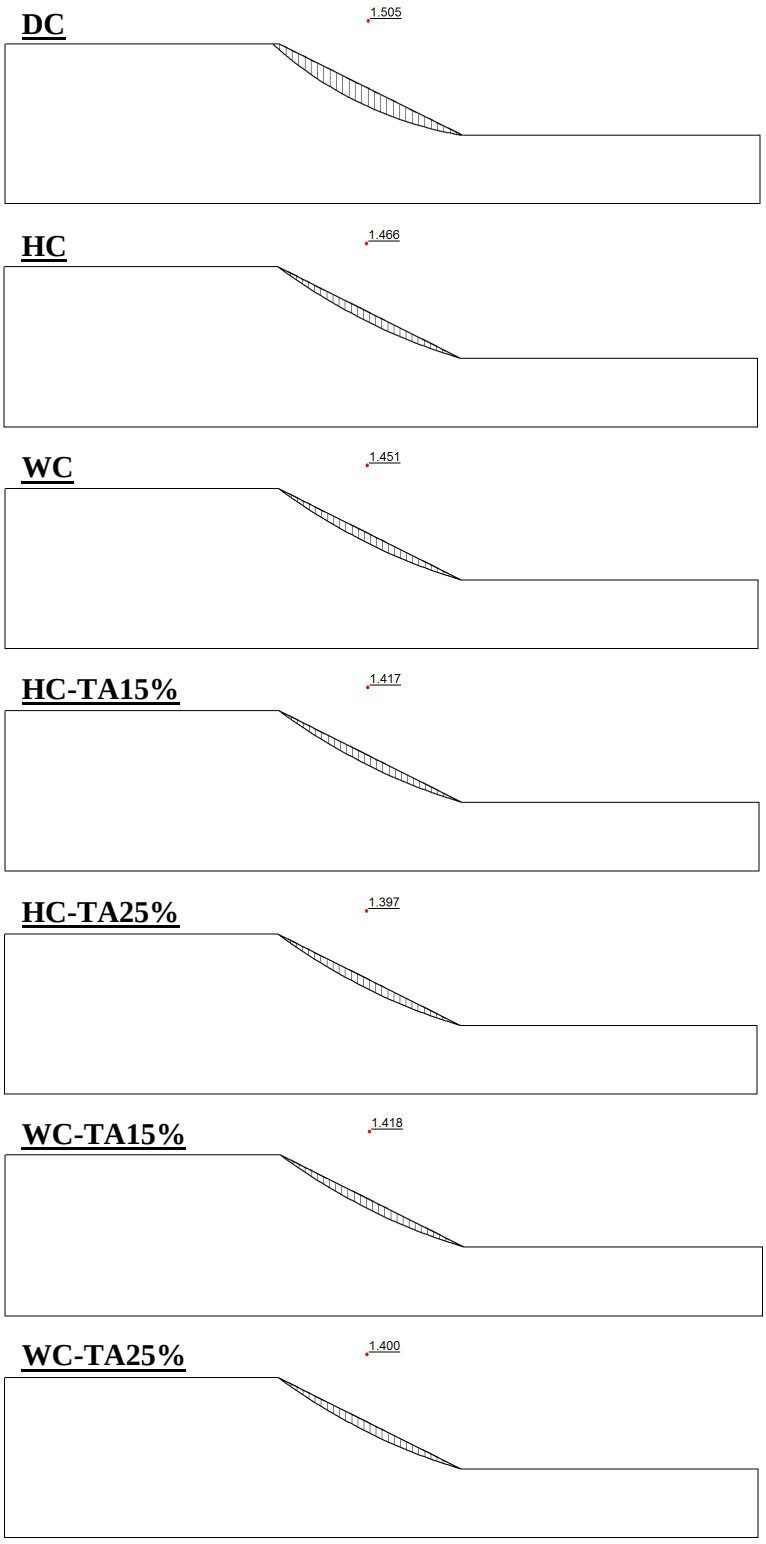

Figure C33 Sand slope's FOS and slip surface at 396 d (*Max Sat*) with minimum slip surface depth of 0.3 m – North Bay

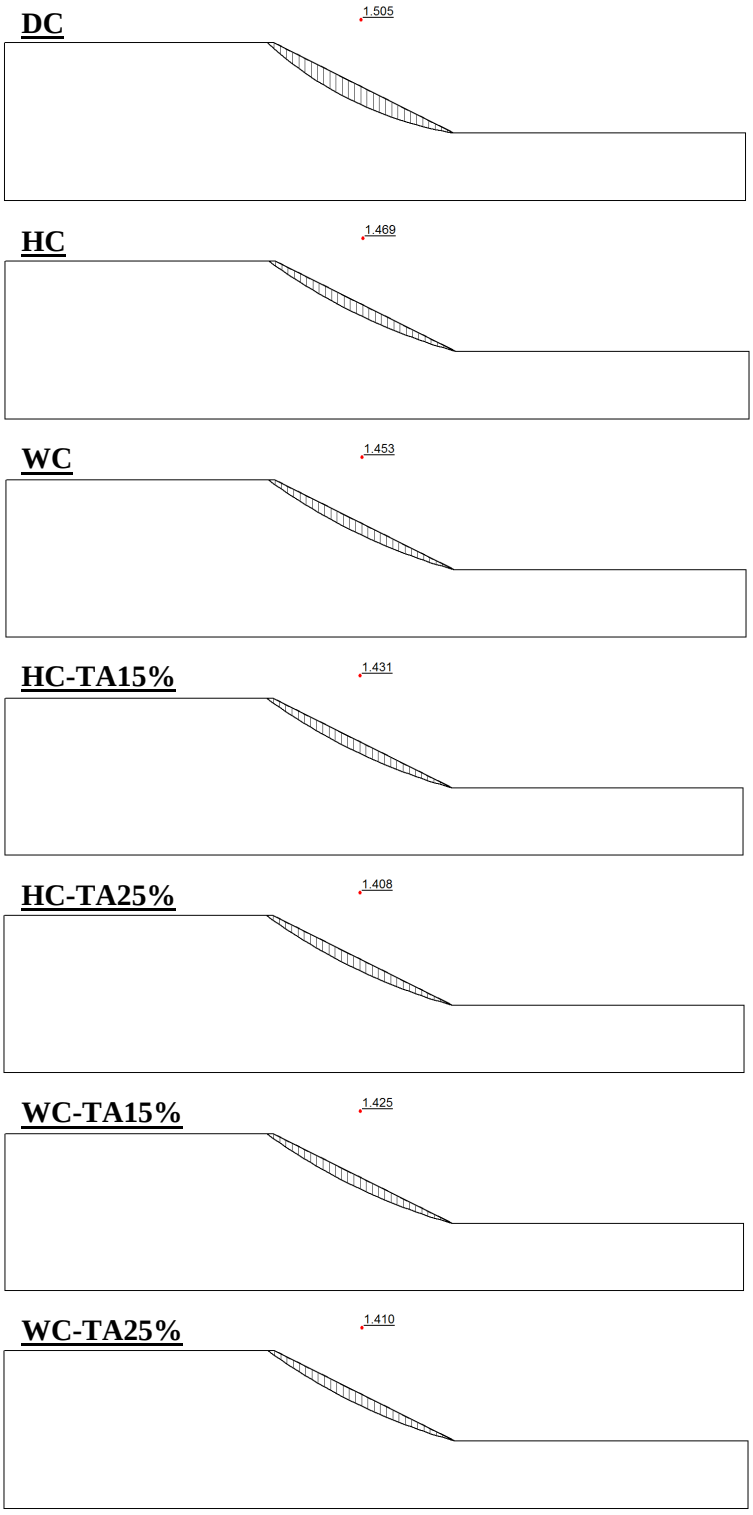

Figure C34 Sand slope's FOS and slip surface at 396 d (*Max Sat*) with minimum slip surface depth of 1.0 m – North Bay

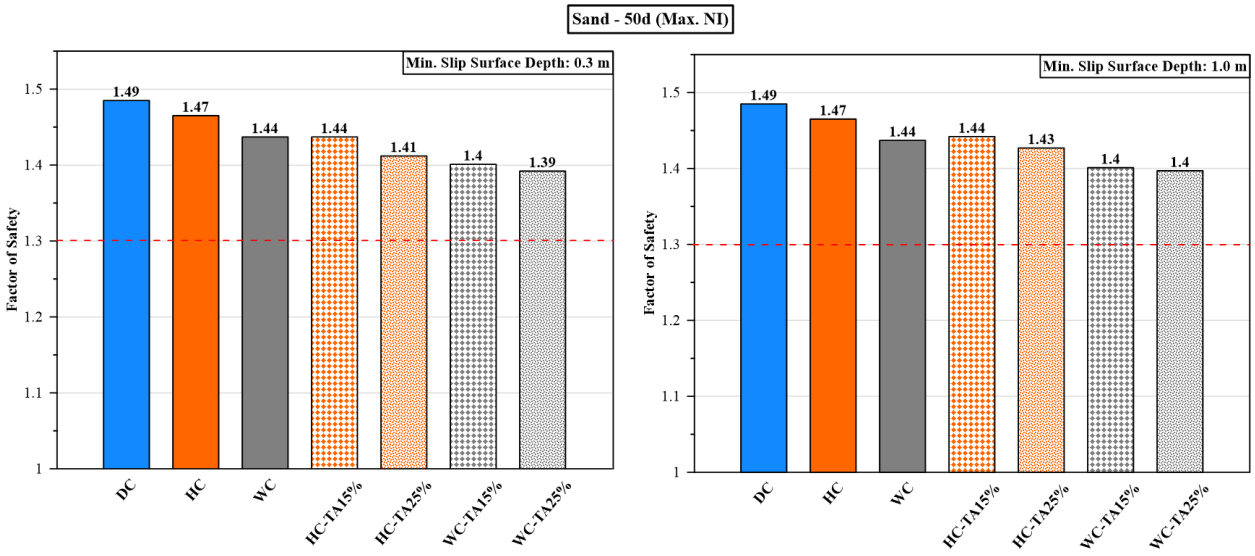

Figure C35 FOS of sand slope during *Max NI* occurrence (50 d) using different hydraulic characteristics, with two considered minimum slip surface depths: 0.3 m (left) and 1.0 m (right) – North Bay

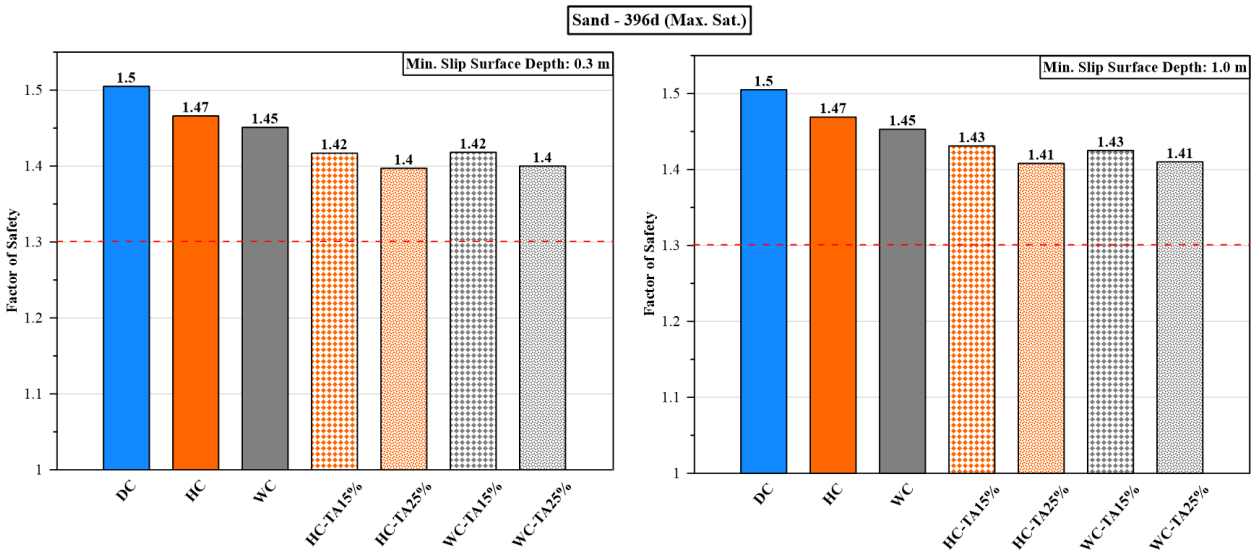

Figure C36 FOS of sand slope during *Max Sat* occurrence (396 d) using different hydraulic characteristics, with two considered minimum slip surface depths: 0.3 m (left) and 1.0 m (right) – North Bay

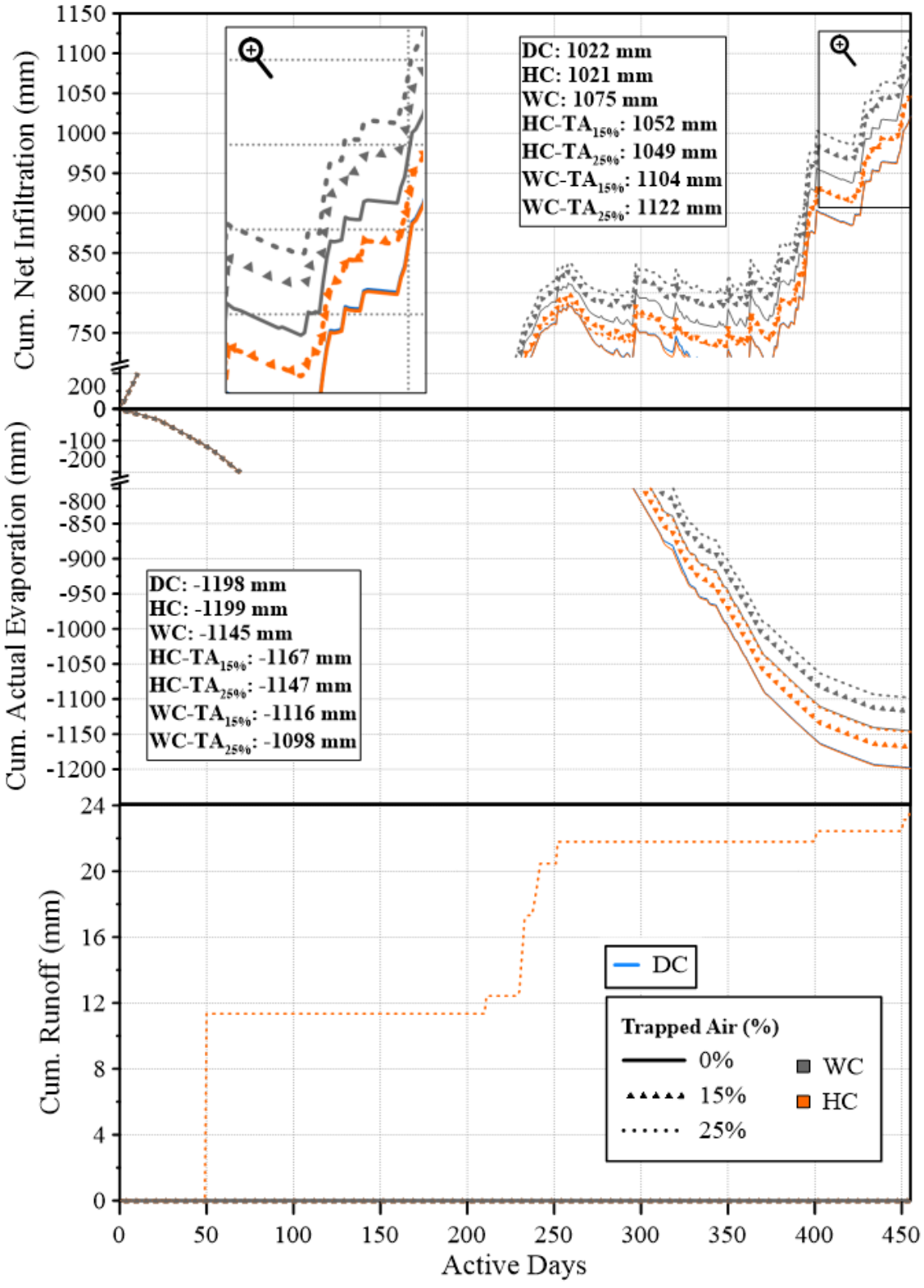

Figure C37 Estimated water balance at the surface of the silt profile – North Bay

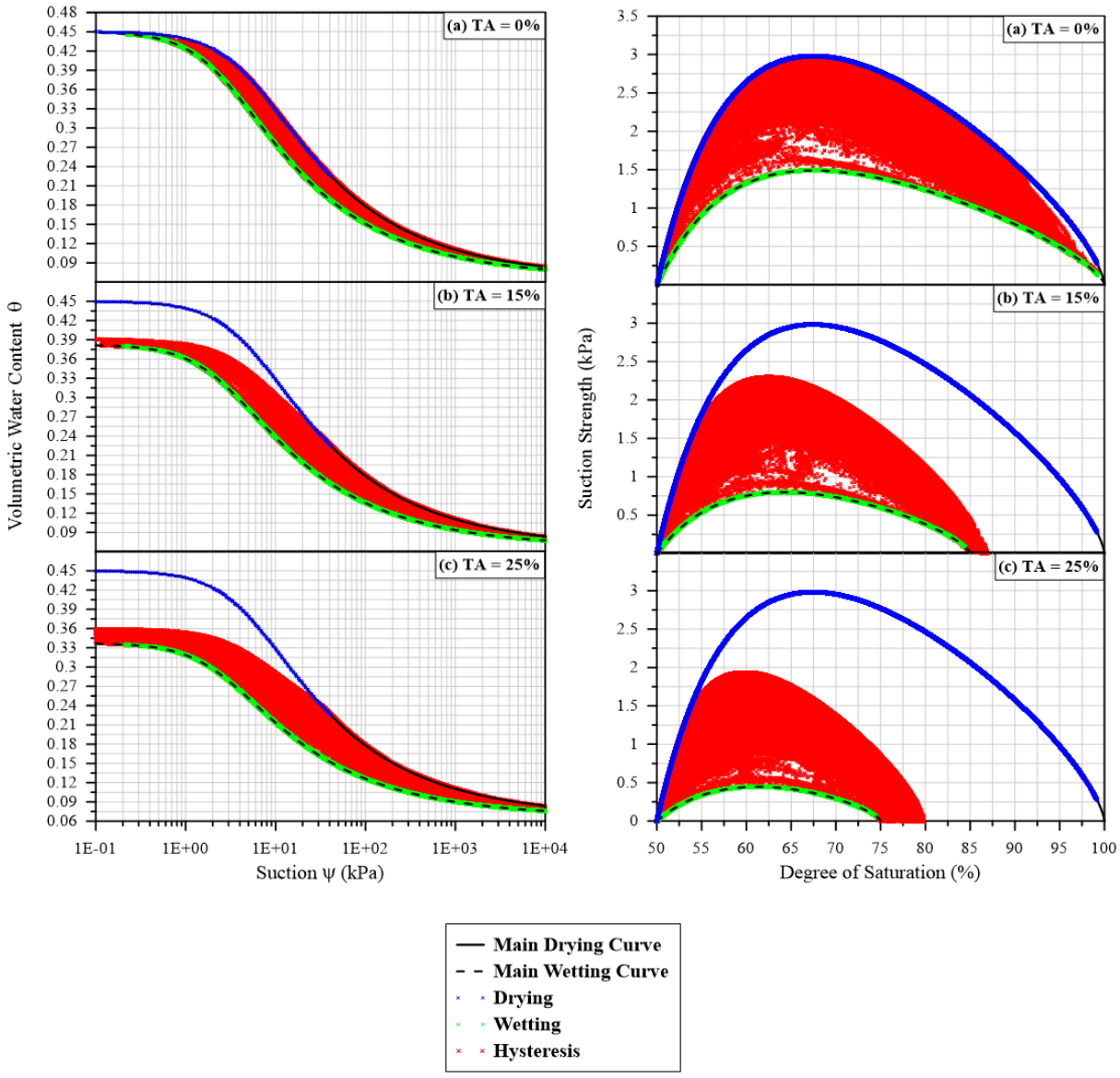

Figure C38 Hysteresis profiles of suction strength for silt, including data points from the hysteretic simulations with and without air entrapment– North Bay

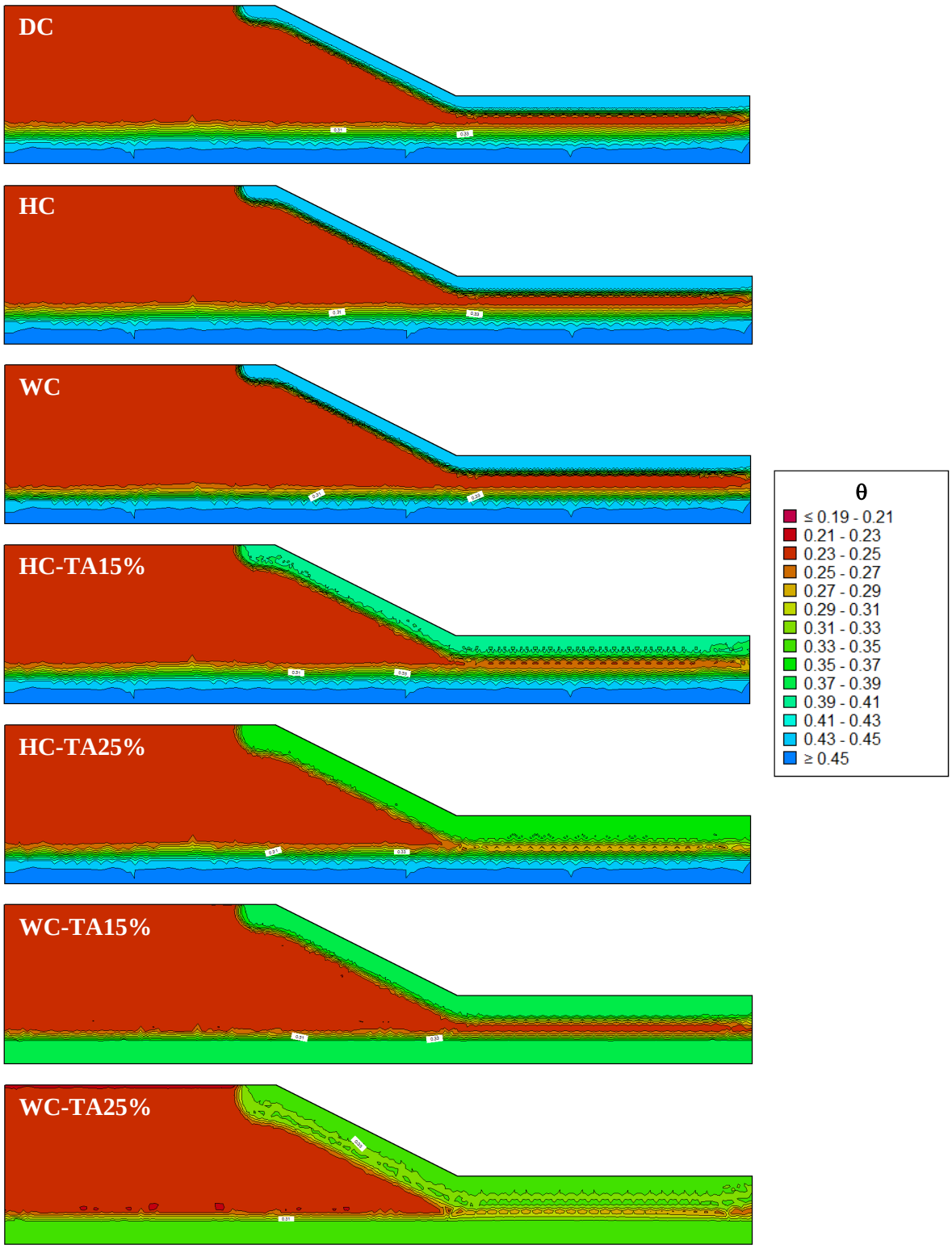

Figure C39 Volumetric water content distribution within silt slope at 14 d (*Max Sat*) – North Bay

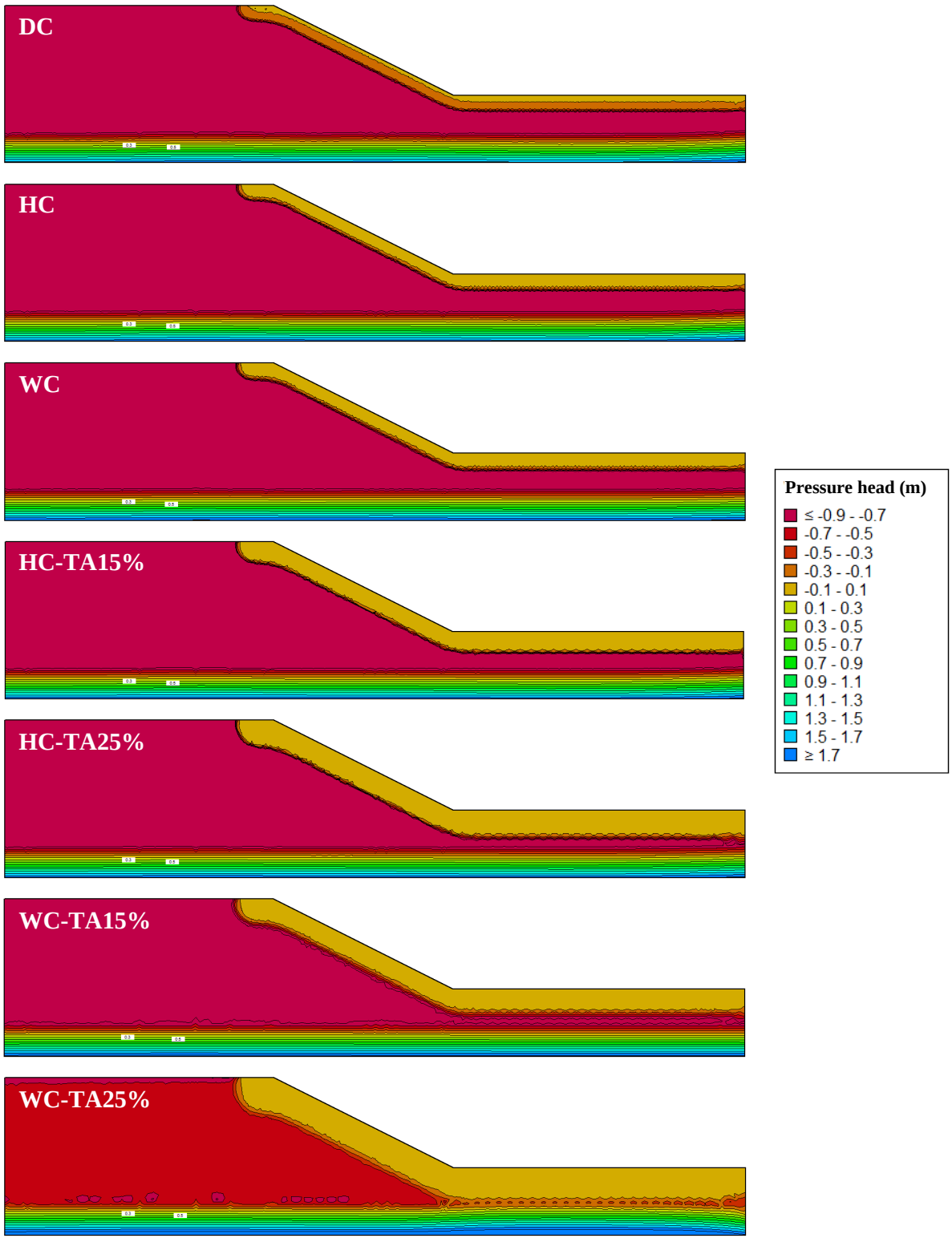

Figure C40 Pressure head distribution within silt slope at 14 d (*Max Sat*) – North Bay

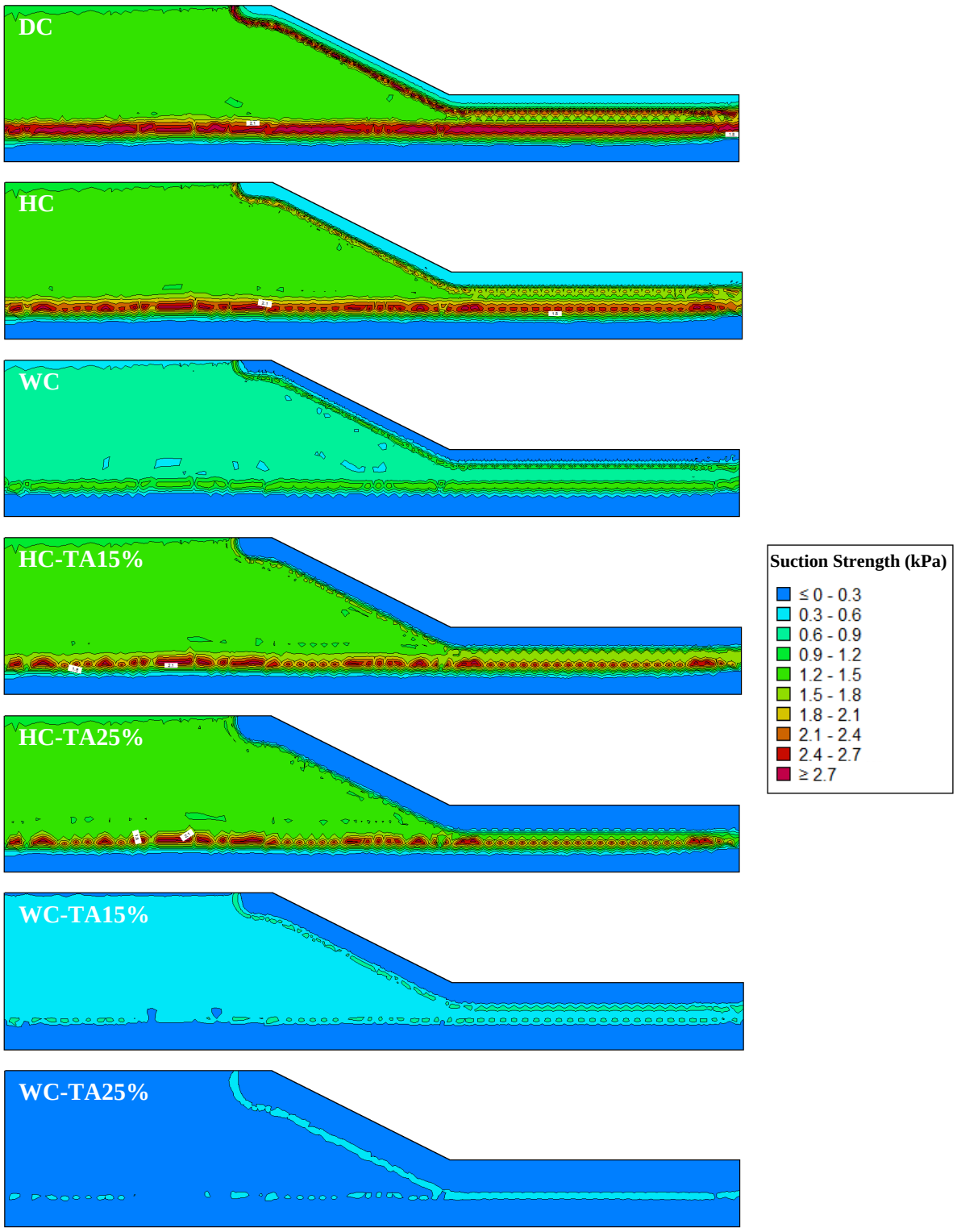

Figure C41 Suction strength distribution within silt slope at 14 d (*Max Sat*) – North Bay

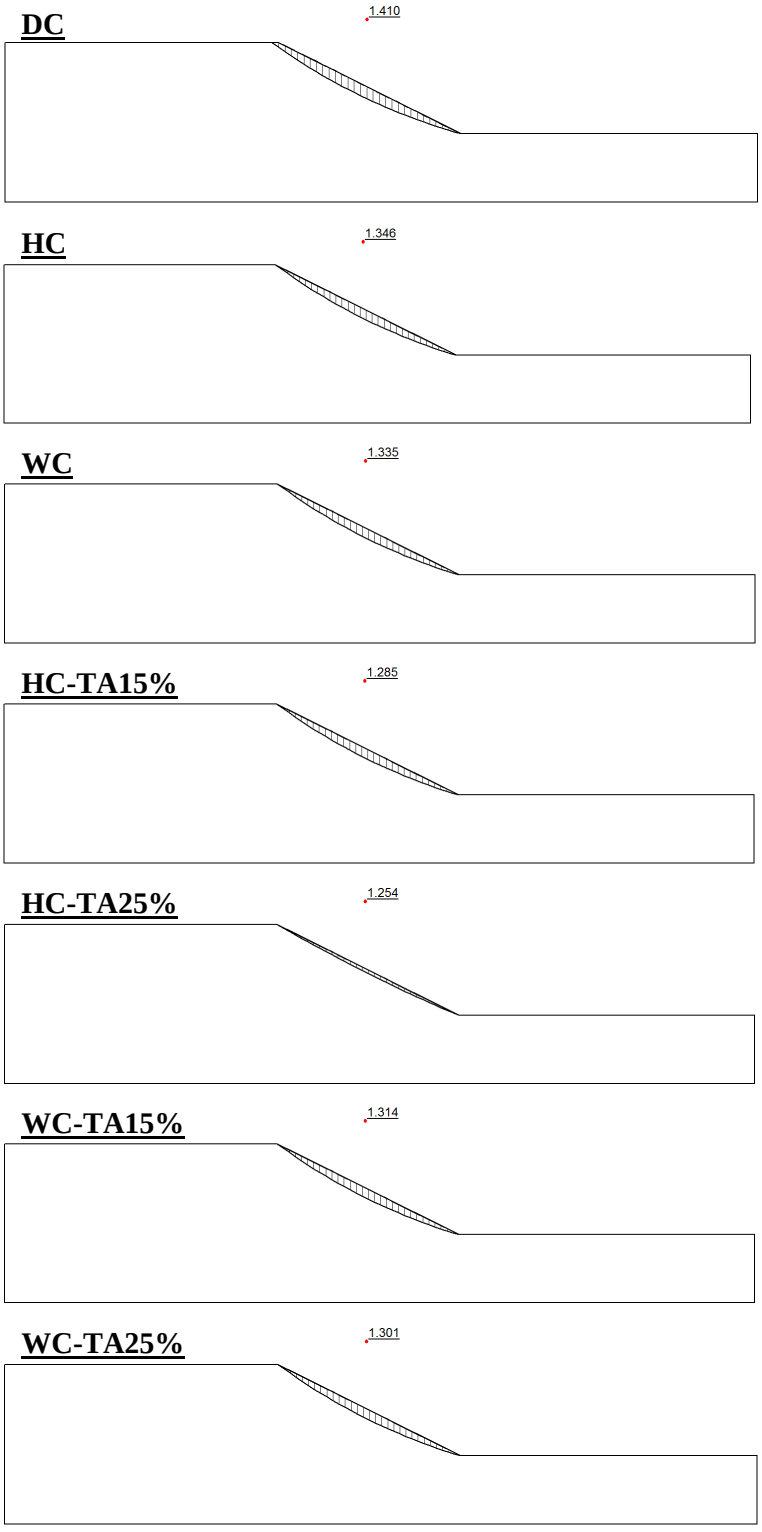

Figure C42 Silt slope's FOS and slip surface at 14 d (*Max Sat*) with minimum slip surface depth of 0.3 m – North Bay

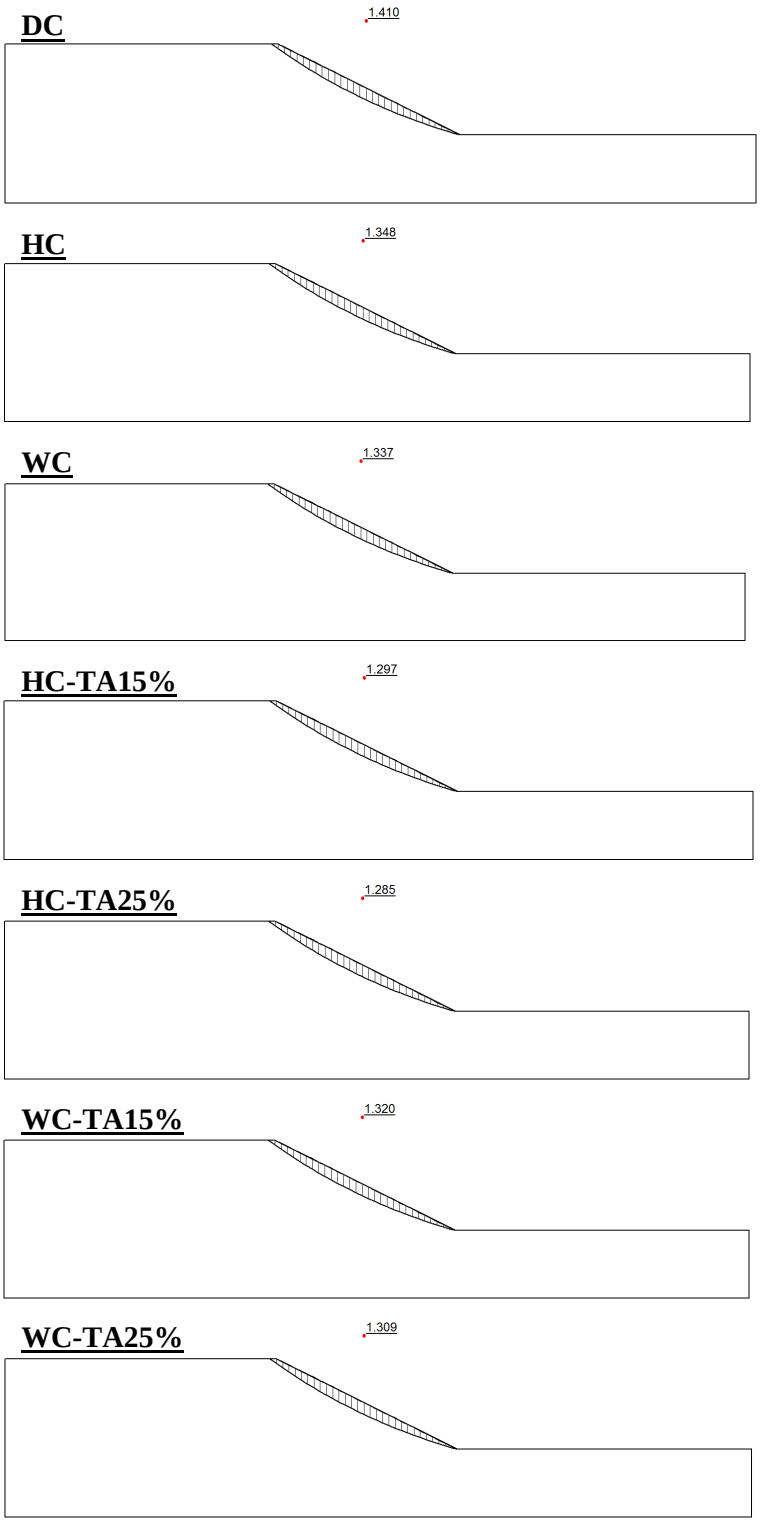

Figure C43 Silt slope's FOS and slip surface at 14 d (*Max Sat*) with minimum slip surface depth of 1.0 m – North Bay

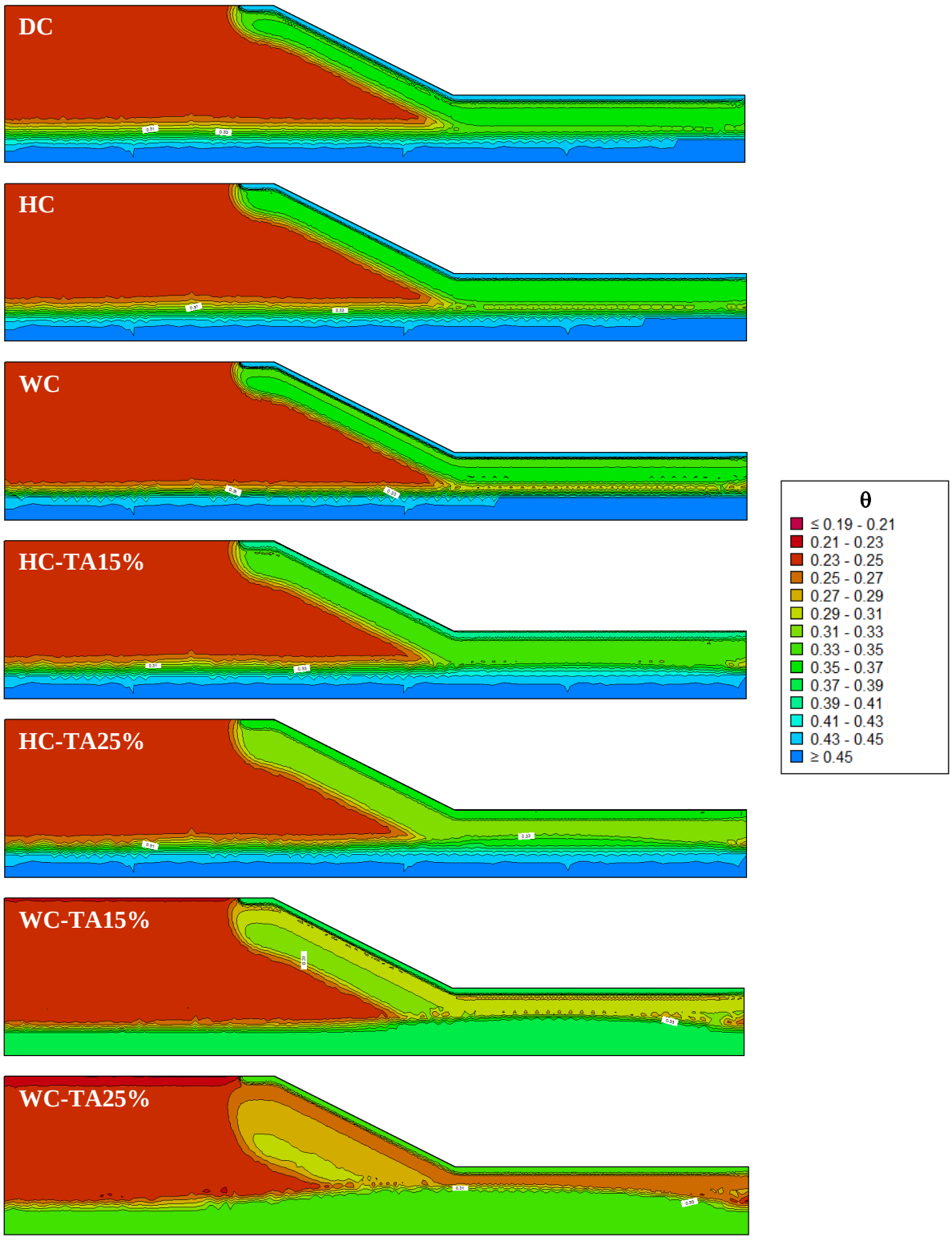

Figure C44 Volumetric water content distribution within silt slope at 50 d (*Max NI*) – North Bay

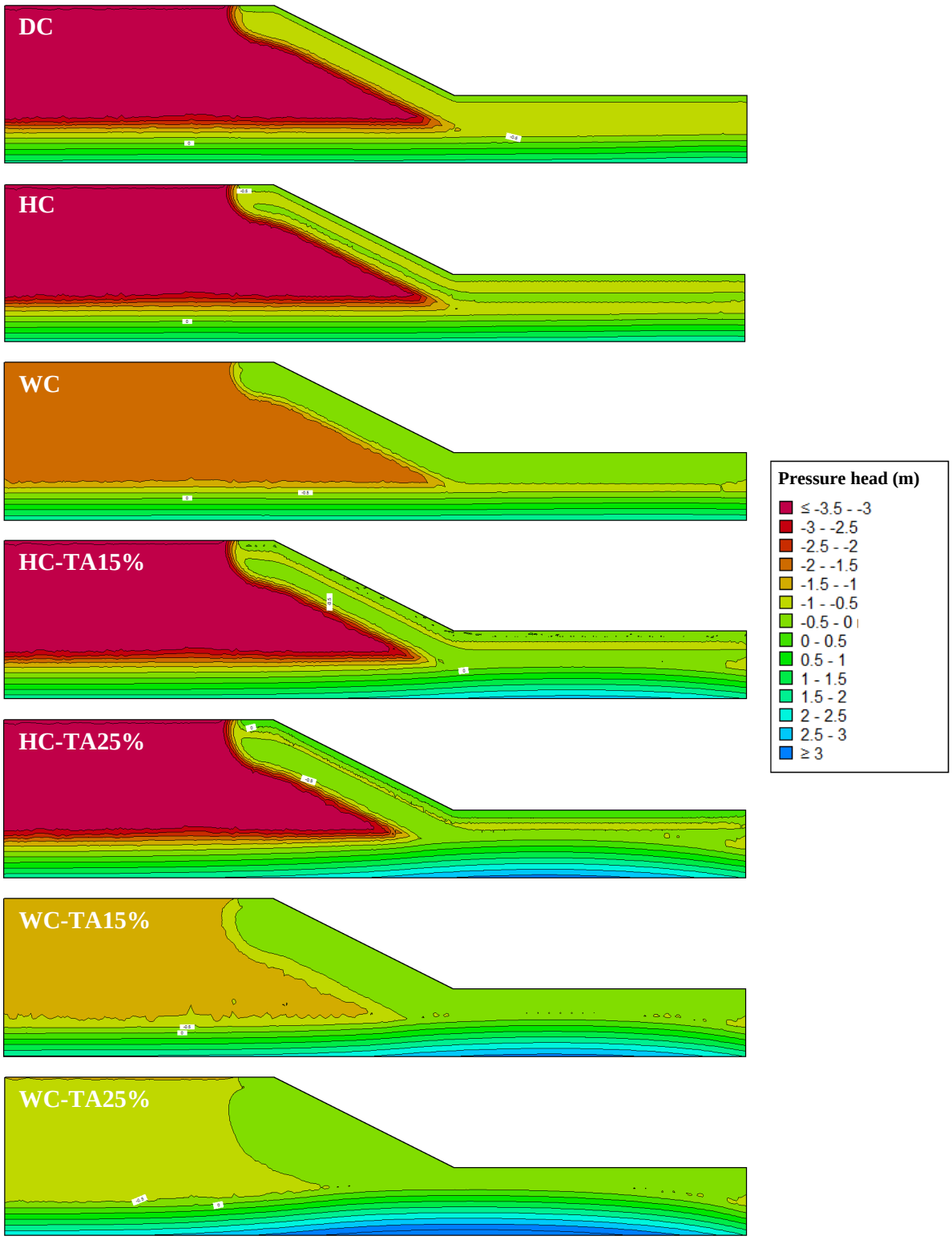

Figure C45 Pressure head distribution within silt slope at 50 d (*Max NI*) – North Bay

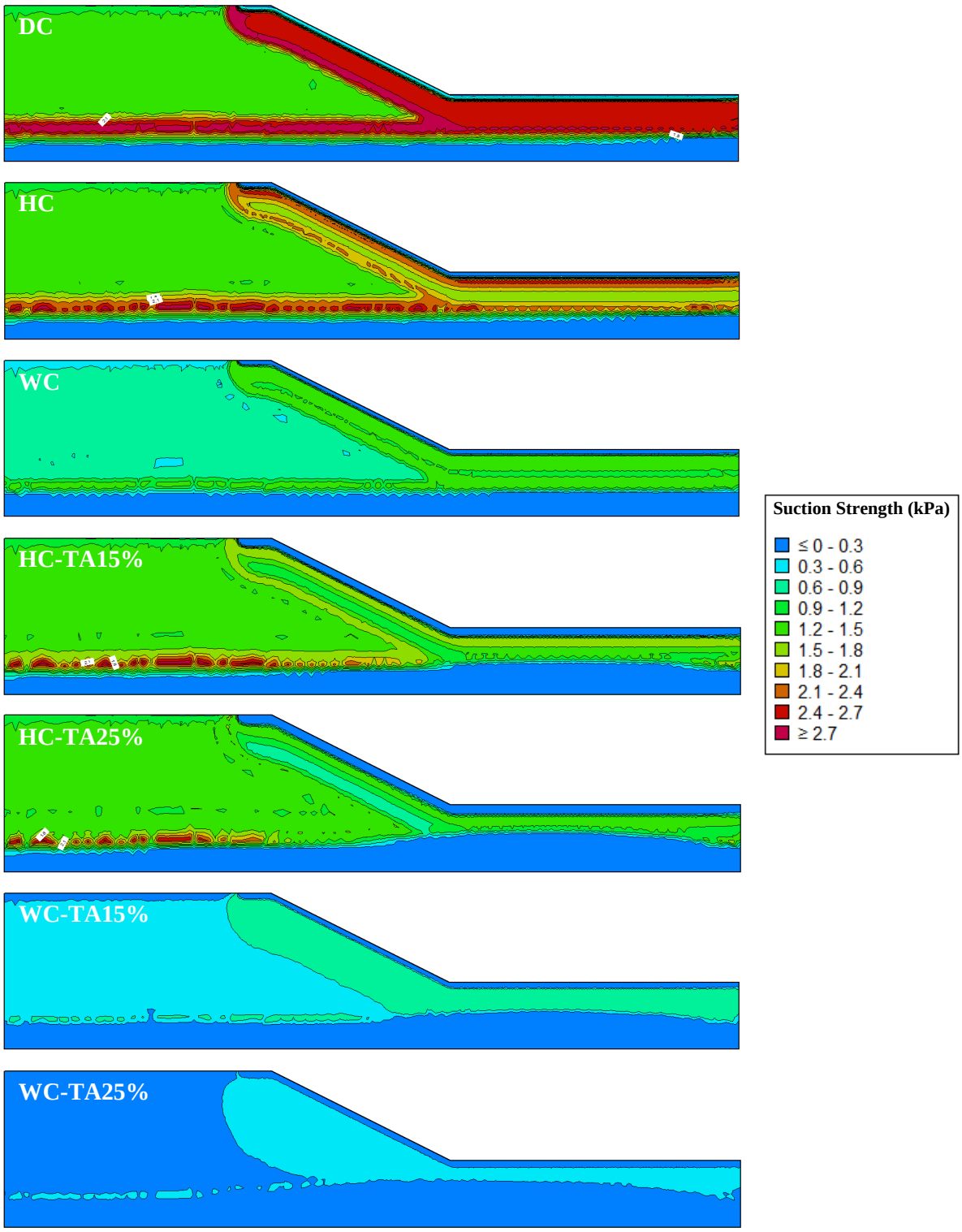

Figure C46 Suction strength distribution within silt slope at 50 d (*Max NI*) – North Bay

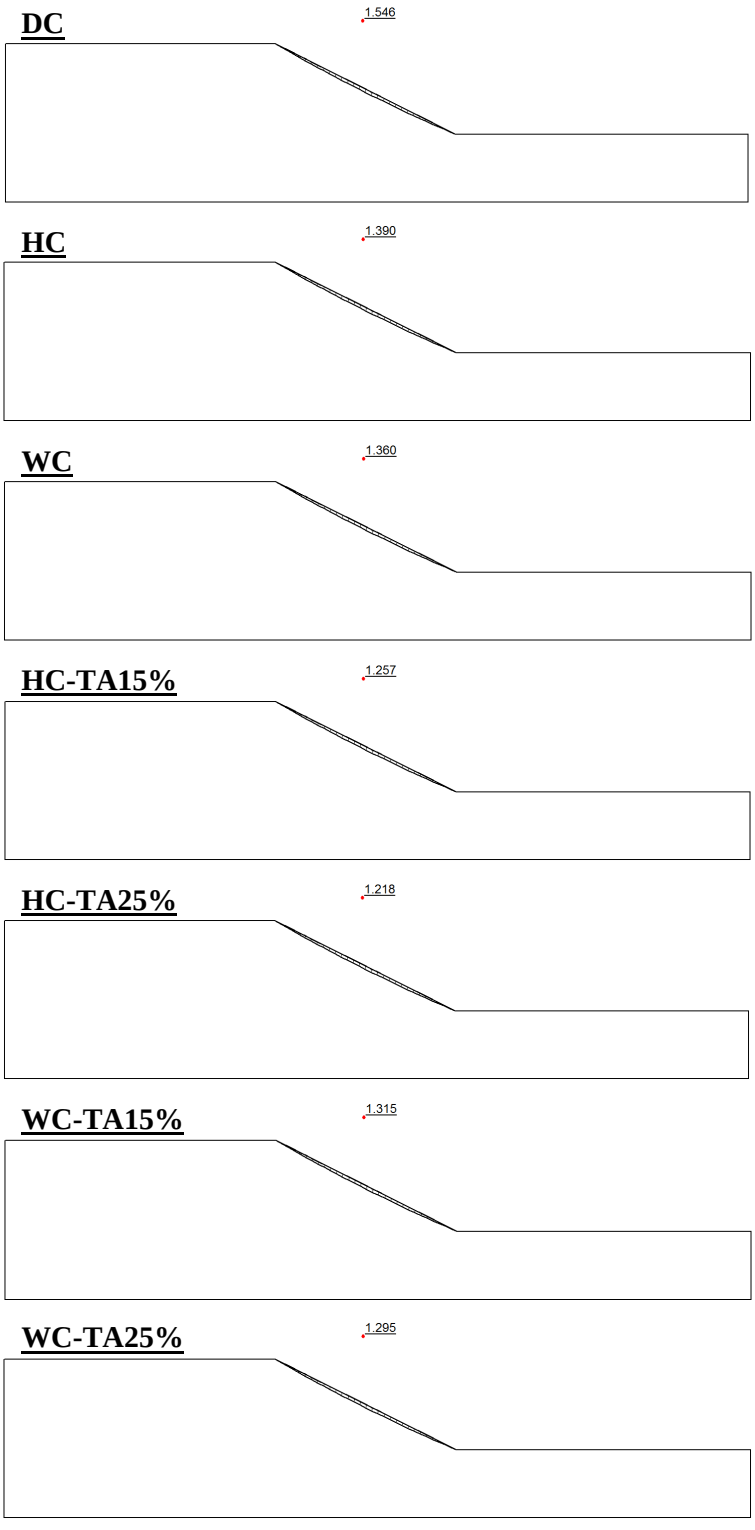

Figure C47 Silt slope's FOS and slip surface at 50 d (*Max NI*) with minimum slip surface depth of 0.3 m – North Bay

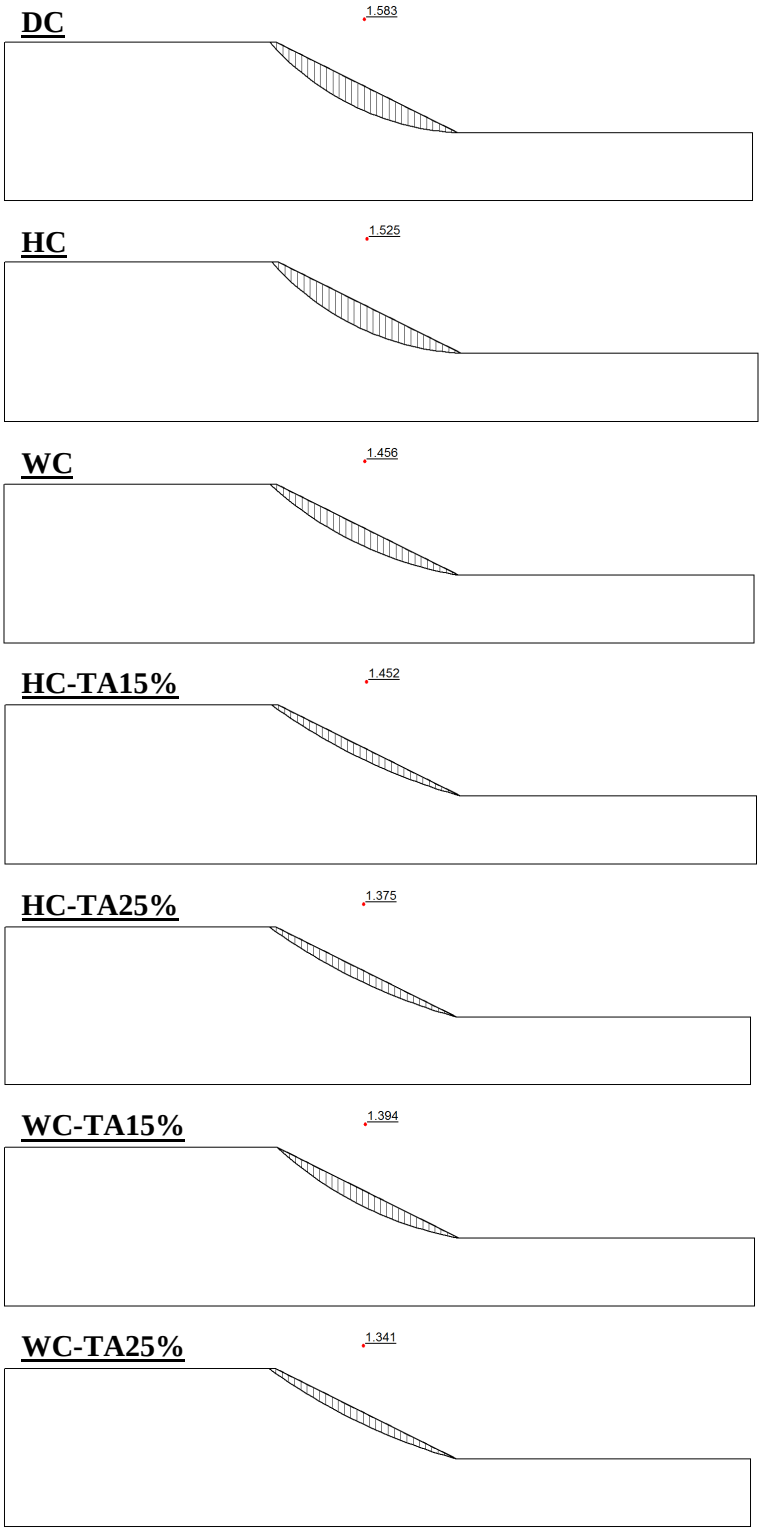

Figure C48 Silt slope's FOS and slip surface at 50 d (*Max NI*) with minimum slip surface depth of 1.0 m – North Bay

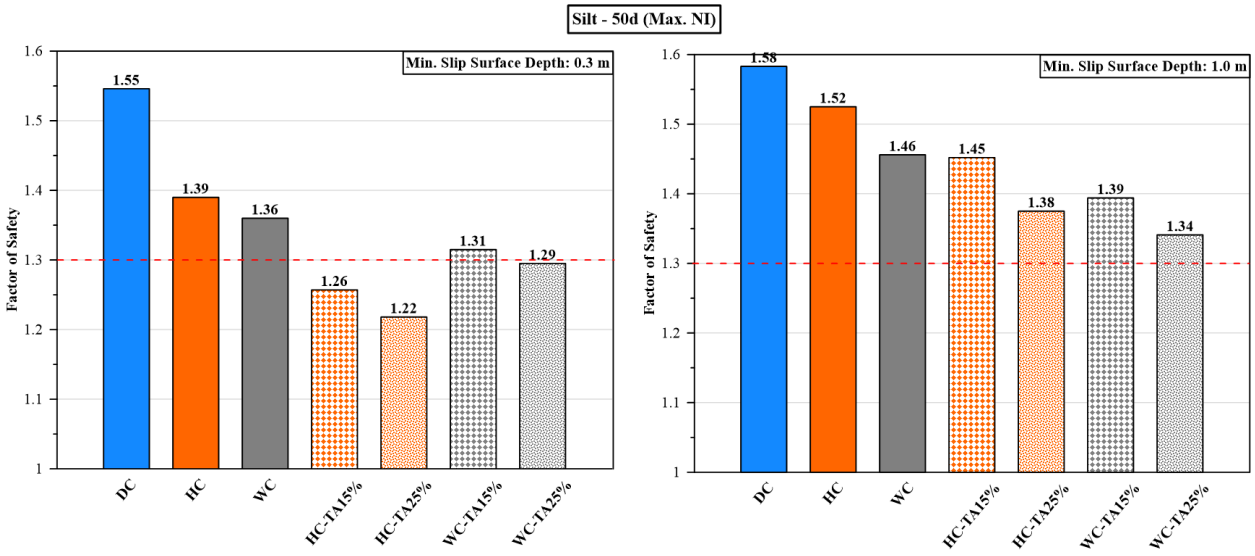

Figure C49 FOS of silt slope during *Max NI* occurrence (50 d) using different hydraulic characteristics, with two considered minimum slip surface depths: 0.3 m (left) and 1.0 m (right) – North Bay

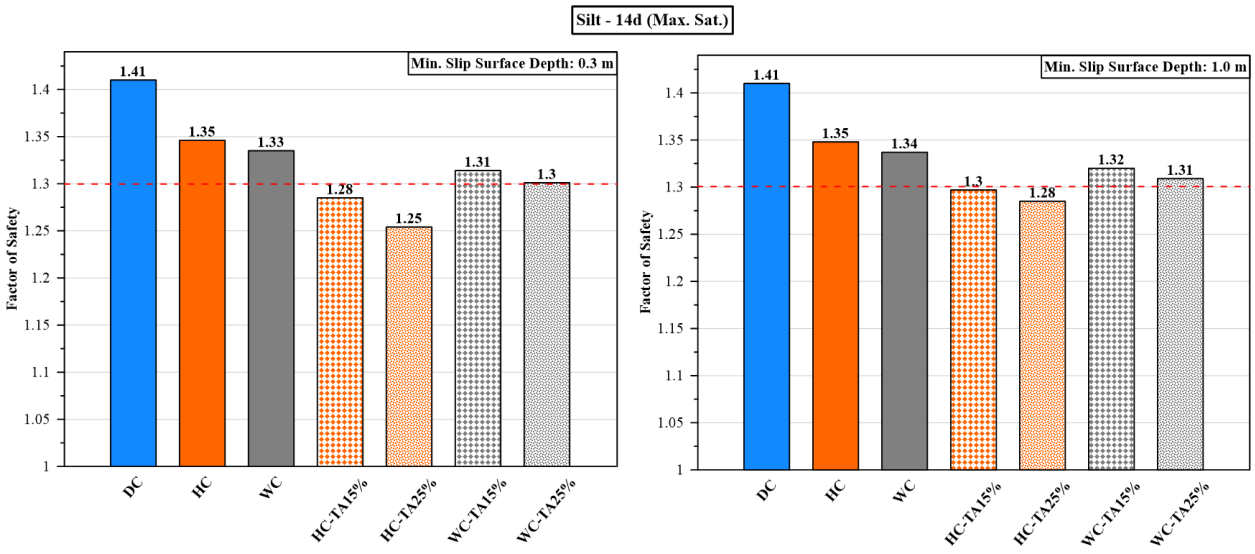

Figure C50 FOS of silt slope during *Max Sat* occurrence (14 d) using different hydraulic characteristics, with two considered minimum slip surface depths: 0.3 m (left) and 1.0 m (right) – North Bay